5-1-2014

Numerical study of a novel fin configuration of a high temperature ceramic plate fin heat exchanger

Vijaisri Nagarajan
University of Nevada, Las Vegas, vijaisri.n@gmail.com

NUMERICAL STUDY OF A NOVEL FIN CONFIGURATION OF A HIGH TEMPERATURE CERAMIC PLATE FIN HEAT EXCHANGER

by

Vijaisri Nagarajan

Bachelor of Science in Mechanical Engineering
Anna University, Chennai, India
2005

Master of Science in Mechanical Engineering
University of Nevada, Las Vegas
2008

A dissertation submitted in partial fulfillment
of the requirements for the

Doctor of Philosophy -Mechanical Engineering

Department of Mechanical Engineering
Howard R. Hughes College of Engineering
The Graduate College

University of Nevada, Las Vegas
May 2014

DISSERTATION APPROVAL PAGE PROVIDED BY THE GRADUATE COLLEGE

ABSTRACT

Numerical Study of a Novel Fin Configuration of a High Temperature Ceramic Plate Fin Heat Exchanger

by

Vijaisri Nagarajan

Dr. Yitung Chen, Advisory Committee Chair
Professor, Department of Mechanical Engineering
University of Nevada, Las Vegas

Compact heat exchangers are widely used in industries due to their compactness, reduced space, energy requirement and desired thermal performance. The proposed ceramic plate fin heat exchanger (PFHE) based on the offset strip fin design is used in applications which require extreme operating temperatures. It is well known that the compact heat exchanger requires small fins and channels to achieve high heat transfer rate and thermal performances. The fins in the ceramic heat exchanger ensure periodic restart of the boundary layer region which increases the thermal performance or heat transfer enhancement of the heat exchanger.

In this dissertation a novel fin configuration for high temperature ceramic plate fin heat exchanger is developed using three-dimensional computational fluid dynamics (CFD). The heat exchanger model developed in this dissertation is based on the conceptual design developed by Ceramatec, Inc. The working fluids used in the model are sulfur trioxide, sulfur dioxide, oxygen, helium and water vapor. The proposed material of the heat exchanger for this study is silicon carbide (SiC). The operational temperature of the heat exchanger used in the current study ranges from 973 K to 1173 K

and due to this high temperature, thermal stresses are induced in the heat exchanger components. The thermal and hydraulic analysis in this work is followed by finite element analysis (FEA) in ANSYS structural module to study the effect of principal stress on different types of fin designs and arrangements. The thermal and mechanical stress results obtained under steady and transient conditions are used for calculating the safety factor based on the Coulomb-Mohr failure criteria.

The goal of this research is to obtain a novel fin configuration that can be used in the ceramic plate fin heat exchanger with optimal stress, pressure drop and high heat transfer. After an extensive literature survey it is found that much work has been done on the standard rectangular and triangular fins. Hence in this dissertation, detailed three-dimensional analysis on fluid flow, heat transfer and stress analysis on many different configurations of fins are studied and analyzed. The ripsaw fin design with thickness of 0.05 mm gives the maximum heat transfer performance with less pressure drop and friction factor. Semi-analytical study is also carried out for different types of fins and is compared with the numerical results. In order to reduce the complexity, analysis is carried out on rectangular fin. The obtained fluid flow and heat transfer results from the numerical analysis are validated with the analytical results for all fin designs. The numerical analysis on chemical reaction is carried out to study the decomposition of sulfur trioxide to sulfur dioxide and oxygen. From the parametric studies it is found that the decomposition percentage of sulfur trioxide can be significantly enhanced by decreasing the reactant mass flow rate, increasing the length of the channel and the operation pressure. From the study it is found that the ripsaw fin design with thickness of

0.05 mm is found to be the best design with high heat transfer effectiveness, sulfur trioxide decomposition percentage, safety factor and less pressure drop.

ACKNOWLEDGEMENTS

I wish to express my deep sense of gratitude and heartfelt thanks to my esteemed research supervisor Dr. Yitung Chen for his excellent guidance, encouragement, valuable suggestions, cordial treatment and constructive criticism in the entire course of research. In addition to the academic guidance, Dr. Chen has been a motivating force in the development of my professional skills and perspective of research aside from my passion towards research. In the long road to my doctoral thesis, he provided me excellent direction and moral support when I faltered in my approach. I am extremely fortunate to have him as my advisor for my doctoral research.

I am thankful to Dr. Robert Boehm, Dr. Mohamed Trabia, Dr. Rama Venkat and Dr. William Culbreth, committee members for their critical reading and valuable suggestions during the course of this study.

I would like to thank my friends for their care and support during my stay in UNLV.

I would like to thank my parents Dr. M. Nagarajan and Mrs. Bagyalakshmi Nagarajan for their affection, constant encouragement and support. I take this opportunity to thank my sisters as well for their moral support, veritable criticism which helped me to finish this study successfully. I dedicate this thesis to my beloved periappa M. Srinivasan.

TABLE OF CONTENTS

ABSTRACT iii

ACKNOWLEDGEMENTS vi

TABLE OF CONTENTS vii

LIST OF TABLES x

LIST OF FIGURES xi

CHAPTER 1 INTRODUCTION AND LITERATURE SURVEY 1
1.1 Literature Review 4
1.1.1 Compact heat exchangers 4
1.1.2 Fluid flow and heat transfer enhancement in plate fin heat exchanger 8
1.1.3 Sulfur-iodine thermochemical cycle 11
1.1.4 Structural analysis 17
1.2 Motivation of the Dissertation 18
1.3 Outline of Dissertation 19

CHAPTER 2 PROBLEM DESCRIPTION AND METHODOLOGY 21
2.2 Types of Compact Heat Exchanger 21
2.2.1 Plate frame heat exchanger 21
2.2.2 Spiral heat exchanger 22
2.2.3 Brazed plate heat exchangers (BPHE) 23
2.2.4 Printed circuit heat exchanger (PCHE) 24
2.2.5 Plate fin heat exchanger (PFHE) 25
2.3 Numerical Method and Algorithm 32
2.3.1 Solution technique 32
2.3.2 Discretization 34
2.4 Boundary Conditions 36
2.4.1 Mass flow inlet boundary condition 36
2.4.2 Pressure outlet boundary condition 37
2.4.3 Thermal boundary condition 37
2.4.4 Wall boundary condition 38
2.4.5 Symmetry boundary condition 38
2.4.6 Solid condition 38
2.4.7 Fluid boundary condition 38
2.4.8 Under-relaxation factors 39
2.5 Governing Equations 39
2.6 Chemical Reaction and Kinetics 40
2.7 Structural Analysis 41

CHAPTER 3 FLUID FLOW AND HEAT TRANSFER 43
3.1 Material Properties 43
3.2 Boundary and Operating Conditions 44

3.3 Results and Discussions 45
3.4 Validation with Published Results 50
3.5 Uniform Arrangement 52
3.5.1 Case 1 (Single channel model with no fins) 52
3.5.2 Case 2 (Single channel model with rectangular fins) 54
3.5.3 Case 3 (Single channel model with triangular fins) 61
3.5.4 Case 4 (Single channel model with bolt fins) 64
3.5.5 Case 5 (Single channel model with inverted bolt fins) 70
3.5.6 Case 6 and Case 7 (Single channel model with eyelid type fin and ripsaw fan type fin) 74
3.5.7 Case 8 (Single channel model with ripsaw fin design with 0.0002 m thickness) 78
3.5.8 Case 9 (Single channel model with ripsaw fins with 0.00005 m thickness) 81
3.5.9 Conclusion 87
3.6 Staggered Arrangement 87
3.6.1 Case 1 (Single channel model with staggered rectangular and triangular fins) 87
3.6.2 Case 2 (single channel model with inverted bolt fins) 92
3.6.3 Case 3 (Single channel model with staggered ripsaw fin of thickness 0.00005 m) 96
3.6.4 Conclusion 101
3.7 Fins Arranged on the Top and the Bottom Solid 101
3.7.1 Case 1 (Single channel model with rectangular fins) 102
3.7.2 Case 2 (Single channel model with triangular fins) 106
3.7.3 Case 3 (Single channel model with inverted bolt type fins) 108
3.7.4 Case 4 (Single channel model with ripsaw fin thickness of 0.00005 m) 110
3.7.5 Conclusion 114
3.8 Parametric Study for Straight Ripsaw Fin with Thickness of 0.00005 m 115
3.9 Semi-Analytical Modeling 117
3.9.1 Continuity equation 118
3.9.3 Energy equation 119

CHAPTER 4 STEADY AND TRANSIENT STATE STRUCTURAL ANALYSIS 123
4.1 Principal Stress 123
4.2 Coulomb-Mohr Failure Criterion 125
4.3 Steady State Structural Analysis 128
4.3.1 Geometry and mesh generation. 129
4.3.2. Material properties. 130
4.3.3 Boundary and operating conditions. 132
4.4 Imported Thermal Load and Uniform Pressure of 1.5 MPa 134
4.4.1 Case 1 (single channel model with rectangular fins) 137
4.4.2 Case 2 (Single channel model with triangular fins) 142
4.4.3 Case 3 (Single channel model with inverted bolt fins) 145
4.4.4 Case 4 (Single channel model with ripsaw fins) 147
4.4.5 Case 6 (Single channel model with ripsaw fin with thickness of 0.0002 m, bolt fins, ripsaw fin fan type arrangement) 148

4.5 Imported Thermal Load and Imported Pressure Load from FLUENT 151
4.6 Imported Pressure Load 156
4.7 Transient Analysis of All the Fins 158
4.7.1 Startup process 160
4.7.2 Calculation at 0^+ seconds 160
4.7.3 Calculation at 10 seconds 163
4.7.4 Calculation at 50 seconds 164
4.7.5 Calculation at 80 seconds 165
4.7.6 Calculation at 100 seconds 166

CHAPTER 5 MODELING OF FLOW WITH CHEMICAL REACTIONS 169
5.1 Geometry and Boundary Conditions 169
The geometry of the model is similar to the geometry used in the previous chapters and chemical reaction is alone added in this chapter. Since the mass flow rate is assumed to be uniform a single channel model is developed to investigate the chemical reactions taking place inside the heat exchanger and the decomposer. Figure 5.1 shows the geometry and the calculation domain of the plate fin heat exchanger and decomposer. 169
5.2 Material Properties and Boundary Conditions 170
5.3 Chemical Reactions and Kinetics 171
5.4 Calculation of Results 172
5.5 Parametric Studies 179

CHAPTER 6 CONCLUSIONS AND FUTURE WORKS 185
6.1 Conclusions 185
6.2 Recommendations and Future Research 189

APPENDIX NOMENCLATURE 190

BIBLIOGRAPHY 194

VITA 204

LIST OF TABLES

Table 2.1 Dimensions of the current model and the model by Ponyavin et al.[48] 28
Table 2.2 Dimensions of various fins 31
Table 3.1 Thermal properties of gases.....44
Table 3.2 Fluid flow and heat transfer results for uniform arrangement of fins 84
Table 3.3 Pressure drop and the temperature difference between the inlet and the outlet of the flow channels 86
Table 3.4 Fluid flow and heat transfer values for the staggered flow arrangement 100
Table 3.5 Pressure drop and temperature difference between the inlet and the outlet for the flow channels 101
Table 3.6 Fluid flow and heat transfer results for the top and bottom fin arrangement ..112
Table 3.7 Pressure drop and temperature difference between the inlet and the outlet for the top and bottom fins 114
Table 3.8 Temperature results for the model 122
Table 3.9 Obtained percentage error between the semi-analytical modeling and the numerical result.....122
Table 4.1 Criterion requirements for different cases of principal stresses (Dowling [80]).....128
Table 4.2 Material properties of silicon carbide (Green, 1998) 131
Table 4.3 Principal stress and safety factor for all fin designs with imported thermal load and uniform pressure of 1.5 MPa 149
Table 4.4 Temperature gradient and grid dimensions for all the models 150
Table 4.5 Principal stress and safety factor for all fin designs.....156
Table 4.6 Principal stress and total deformation for all fin designs 158
Table 4.7 Maximum principal stress and safety factor for all fin designs at 0^+ second ..162
Table 4.8 Maximum principal stress and safety factor for all fins at 10 seconds 163
Table 4.9 Maximum principal stress and safety factor for all fins at 50 seconds 165
Table 4.10 Maximum principal stress and safety factor for all fin designs at 80 seconds 166
Table 4.11 Maximum principal stress and factor of safety for all fin designs at 100 seconds 167
Table 5.1 Fluid flow and chemical decomposition results for all fin designs 178

LIST OF FIGURES

Figure 1.1. Production of hydrogen at different temperatures (Thomas [3]).....3
Figure 1.2. Sulfur-iodine thermochemical water splitting cycle (Picard[5]). 4
Figure 2.1. Plate frame heat exchanger (Cheresources.com, [60]). 22
Figure 2.2. Spiral heat exchanger (Thermal Heat Transfer Systems Inc.[61]). 23
Figure 2.3. Brazed plate heat exchanger (Alfa Biz Limited. [62]).....24
Figure 2.4. Printed circuit heat exchanger (Heatric Inc. [63]). 25
Figure 2.5. Plate fin heat exchanger (Lytron Total Thermal Solutions [64]). 26
Figure 2.6. Geometry of the whole heat exchanger.....27
Figure 2.7. Geometry and dimensions of single channel.....28
Figure 2.8. Geometry and dimensions of rectangular and triangular fins. 29
Figure 2.9. Geometry and dimensions of bolt type fins. 30
Figure 2.10. Geometry and dimensions of ripsaw fins.....30
Figure 2.11. Geometry of staggered and top and bottom fin arrangement. 32
Figure 2.12. Segregated solver approach.....34
Figure 2.13. Two-dimensional staggered grid. 36
Figure 2.14. Mohr-Coulomb safety factor (Green [71]).....42
Figure 3.1. Boundary conditions of the single channel model.....45
Figure 3.2. Meshing in ANSYS workbench. 46
Figure 3.3. Grid independent study for fluid flow results.....46
Figure 3.4. Grid independent study for heat transfer results.....47
Figure 3.5. Velocity entrance length. 48
Figure 3.6. Outlet length of the velocity. 48
Figure 3.7. Velocity entrance length for 10% total length.....49
Figure 3.8. Velocity outlet length for 10% of total length.....49
Figure 3.9. Friction factor and heat transfer validation. 51
Figure 3.10. Contour of pressure and temperature for single channel model without fins. 53
Figure 3.11. Contour and streamline for velocity in m/s for single channel model without fins.....54
Figure 3.12. Contour of velocity and pressure for single channel model with straight rectangular fins. 55
Figure 3.13. Streamline along y-plane for velocity in m/s at y=0.0032 m. 56
Figure 3.14. Velocity along y-plane in m/s for single channel model with straight rectangular fins. 57
Figure 3.15. Streamline along z-plane for velocity in m/s.....58
Figure 3.16. Velocity and pressure along the mixture channel for the single channel model with straight rectangular fins. 59
Figure 3.17. Local temperature and heat transfer coefficient for single channel model with straight rectangular fins.....60
Figure 3.18. Pressure and temperature contours for single channel model with straight triangular fins. 61
Figure 3.19. Velocity vector plot in m/s at z=0.0047 m for single channel model with straight triangular fins. 62

Figure 3.20. Velocity streamline in m/s for single channel model with straight triangular fins at z=0.0047 m. 63
Figure 3.21. Velocity and local heat transfer coefficient plot for single channel model with triangular fins. 63
Figure 3.22. Pressure and velocity contour for single channel model with straight bolt fins. 65
Figure 3.23. Velocity streamline for the top cylinder along the y-plane at y=-0.00015 m. 66
Figure 3.24. Velocity streamline for the bottom cylinder along the Y-plane at y=0.000112 m. 67
Figure 3.25. Velocity streamline and vector distribution in m/s along the z-direction at .68
Figure 3.26. Velocity and pressure plot for single channel model with straight bolt fins. 68
Figure 3.27. Temperature and local heat transfer coefficient for single channel model with straight bolt type fins. 69
Figure 3.28. Pressure contour and velocity streamline for single channel model with straight inverted bolt fins at z=-0.0002 m. 71
Figure 3.29. Streamline for the large cylinder along the y-plane at y=-0.00014 m for single channel model with straight inverted bolt fins. 72
Figure 3.30. Streamline for the small cylinder along the y-plane at $y=-1.336\cdot10^{-6}$ m. 73
Figure 3.31. Velocity and local heat transfer coefficient for single channel model with straight inverted bolt fins. 73
Figure 3.32. Streamline for single channel model with eyelid type fin at y=0.00015 m. .75
Figure 3.33. Streamline for single channel model with straight ripsaw fan type fin design at $y=-5.002\cdot10^{-5}$ m. 76
Figure 3.34. Velocity for single channel model with eyelid fin and ripsaw fan type fins. 76
Figure 3.35. Heat transfer coefficient for single channel model with eyelid fin and ripsaw fan type fin. 77
Figure 3.36. Pressure contour for single channel model with straight ripsaw fin design of 0.0002 m thickness. 78
Figure 3.37. Velocity streamline in m/s for single channel model with straight ripsaw fins 1 at z=-0.00017 m and y=0.00013 m. 79
Figure 3.38. Pressure and local heat transfer coefficient for the ripsaw fin with thickness of 0.0002 m. 80
Figure 3.39. Contour for pressure in a single channel model with ripsaw fin with thickness of 0.00005 m. 82
Figure 3.40. Streamline velocity for a single channel model with ripsaw fins with thickness 0.00005 m at $y=1.336\cdot10^{-6}$ m and z=0.00027 m. 83
Figure 3.41. Pressure and temperature contour for single channel model with staggered rectangular fins. 88
Figure 3.42. Velocity streamline for single channel model with staggered rectangular fins along y-plane at y=0.003 m. 89
Figure 3.43. Velocity streamline for single channel model with staggered rectangular fins along z-plane at z=0.0015 m. 90

Figure 3.44. Velocity and local heat transfer coefficient for single channel model with staggered rectangular fins. 91
Figure 3.45. Pressure and velocity contour for single channel modelwith staggered inverted bolt fins. 93
Figure 3.46. Velocity streamlines for the single channel model with staggered rectangular fins at y=0.003 m and z=0.0048 m. 94
Figure 3. 47 Temperature in K along y=0.00302037 m for a single channel model with staggered inverted bolt fins. 95
Figure 3.48. Velocity and local heat transfer coefficient for single channel model with staggered inverted bolt fins. 95
Figure 3.49. Pressure and velocity contour for single channel model with staggered ripsaw fins with thickness of 0.00005 m. 97
Figure 3.50. Velocity streamline for single channel model with staggered ripsaw fin with thickness of 0.00005 m at y=0.0037 m and z=0.0047 m. 98
Figure 3.51. Pressure and local heat transfer coefficient for staggered ripsaw fin with thickness 0.0005 m. 98
Figure 3.52. Pressure in Pa and velocity in m/s contour for single channel model with rectangular fins arranged on the top and bottom solid regions. 102
Figure 3.53. Velocity streamline for the single channel model with rectangular fins arranged on the top and bottom solid regions at y=0.0032 m and z=0.0053 m. 103
Figure 3.54. Pressure and velocity for single channel model with rectangular fins arranged on the top and bottom solid regions. 104
Figure 3.55. Temperature and local heat transfer coefficient of single channel model with rectangular fins arranged in the top and bottom solid regions. 105
Figure 3.56. Pressure and velocity distribution for single channel model with triangular fins arranged on the top and bottom solid regions. 106
Figure 3.57. Velocity streamline for single channel model with triangular fins arranged on the top and bottom solid regions at y=0.0045 m and z=0.0059 m. 107
Figure 3.58. Velocity streamline for the single channel model with inverted bolt fins arranged on the top and bottom solid regions at y=0.0036 m and z=0.0045 m. 109
Figure 3.59. Velocity and local heat transfer coefficient for the single channel model with inverted bolt fins arranged on the top and bottom solid regions. 109
Figure 3.60. Velocity streamline for single channel model with ripsaw fin of thickness 0.00005 m arranged on the top and bottom solid regions at y=0.0032 m and y=0.0046 m. 111
Figure 3.61. Parametric study for uniform arrangement of ripsaw fin with thickness of 0.00005 m. 117
Figure 3.62. Geometry of the rectangular channel. 118
Figure 3.63. Subdivided geometry for the rectangular channel. 120
Figure 3.64. Temperature profile obtained from FLUENT. 121
Figure 4.1. Principal normal stresses (Dowling [80]). 124
Figure 4.2. Coulomb-Mohr fracture criterion as related to the Mohr's circle (Dowling[80]). 125

Figure 4.3. ANSYS 20 nodes solid structural element types. 129
Figure 4.4. Meshing and grid independent study. 130
Figure 4.5. Displacement restrictions along z-direction. 133
Figure 4.6. Displacement restrictions along y-direction. 133
Figure 4.7. Whole body restriction along vertices. 134
Figure 4.8. Imported thermal load in K for the single channel model with rectangular fins. 135
Figure 4.9. Imported thermal load in K for the single channel model with triangular fins. 135
Figure 4.10. Imported thermal load in K with the single channel model for inverted bolt fins. 136
Figure 4.11. Imported thermal load in K with the single channel model for ripsaw fins of 0.00005 m thickness. 136
Figure 4.12. Uniform pressure load of 1.5 MPa. 137
Figure 4.13 .Maximum principal stress (Pa) for single channel model with straight rectangular fins. 139
Figure 4.14. Maximum principal stress (Pa) for single channel model with staggered rectangular fins. 139
Figure 4.15. Maximum principal stress (Pa) for single channel model with top and bottom arrangement of rectangular fins. 140
Figure 4 16. Total deformation (m) for single channel model with straight rectangular fins. 141
Figure 4.17. Total deformation (m) for single channel model with staggered rectangular fins. 141
Figure 4.18. Total deformation (m) for single channel model with top and bottom rectangular fins. 141
Figure 4.19. Maximum principal stress (Pa) for single channel model with straight triangular fins. 142
Figure 4.20. Maximum principal stress (Pa) for single channel model with staggered triangular fins. 143
Figure 4.21. Maximum principal stress (Pa) for single channel model with top and bottom triangular fin arrangement. 143
Figure 4.22. Total deformation (m) for single channel model with uniform triangular fins. 144
Figure 4.23. Total deformation (m) for single channel model with staggered triangular fins. 144
Figure 4 24. Total deformation (m) for single channel model with top and bottom triangular fins. 144
Figure 4.25. Maximum principal stress (Pa) for single channel model with straight inverted bolt fins. 146
Figure 4.26. Maximum principal stress (Pa) for single channel model with staggered inverted bolt fins. 146
Figure 4.27. Maximum principal stress (Pa) for single channel model with top and bottom arrangement of inverted bolt fins. 146
Figure 4.28. Maximum principal stress (Pa) for straight ripsaw fin with thickness of 0.00005 m. 147

Figure 4.29. Maximum principal stress (Pa) for staggered ripsaw fin with thickness of 0.00005 m. 148
Figure 4.30. Maximum principal stress (Pa) for top and bottom arrangement of ripsaw fin with thickness of 0.00005 m. 148
Figure 4.31. Imported pressure load (Pa) for top and bottom ripsaw fin arrangement from FLUENT [13] 151
Figure 4.32. Maximum principal stress (Pa) for single channel model with top and bottom rectangular fins. 152
Figure 4.33. Maximum principal stress (Pa) for the single channel model with top and bottom triangular fin arrangement. 153
Figure 4.34. Maximum principal stress (Pa) for single channel model with top and bottom arrangement of inverted bolt fins. 154
Figure 4.35. Maximum principal stress (Pa) for the single channel model with top and bottom ripsaw fins. 155
Figure 4.36. Total deformation (m) for the single channel model with top and bottom ripsaw fins. 155
Figure 4.37. Maximum principal stress (Pa) for single channel model with top and bottom ripsaw fins. 157
Figure 4.38. Total deformation (m) for single channel model with top and bottom ripsaw fins. 157
Figure 4.39. Fluid-structure interaction setup in ANSYS WORKBENCH. 160
Figure 4.40. Maximum principal stress (Pa) for single channel model with straight triangular fins at 0^+ second. 161
Figure 4.41. Maximum principal stress (Pa) for single channel model with top and bottom rectangular fins at 0^+ second 161
Figure 4.42. Maximum principal stress (Pa) for the straight triangular fins at 50 seconds. 164
Figure 4.43. Maximum principal stress (Pa) for the top and bottom triangular fins at 50 seconds. 164
Figure 4.44 Time vs. the principal stress for all the fin designs in transient analysis. 167
Figure 5.1. Geometry of the heat exchanger and decomposer. 169
Figure 5.2. Pressure distribution in Pa for single channel staggered rectangular model 173
Figure 5.3. Temperature distribution in K for single channel model with staggered rectangular fins. 173
Figure 5.4. Mass fraction of SO_3 for single channel model with staggered rectangular fins. 174
Figure 5.5. Mass fraction of SO_2 for single channel model with staggered rectangular fins. 174
Figure 5 6. Mass fraction of O_2 for single channel model with staggered rectangular fins. 175
Figure 5.7. Pressure distribution in Pa for single channel model with top and bottom ripsaw fins. 176
Figure 5.8. Mass fraction of SO_3 in single channel model with top and bottom ripsaw fins. 176

Figure 5.9. Mass fraction of SO_2 for a single channel model with top and bottom ripsaw fins. 177
Figure 5.10. Pressure distribution in Pa for long staggered rectangular fins. 179
Figure 5.11. Mass fraction of SO_3 for single channel model with long staggered rectangular fins. 180
Figure 5.12. Mass fraction of SO_2 for single channel model with long staggered rectangular fins. 180
Figure 5.13. Mass fraction of O_2 for a single channel model with long staggered rectangular fins. 181
Figure 5.14. Percentage decomposition of SO_3 vs operation pressure for top and bottom ripsaw fins for channel length of 0.0064648 m. 182
Figure 5.15. Percentage decomposition of SO_3 versus different mass flow rates of the reacting channel for top and bottom ripsaw fins for channel length of 0.0064648 m. 183
Figure 5.16. Sulfur dioxide production or throughput vs mass flow rate of the reacting channel for channel length of 0.0064648 m. 184
Figure 5.17. Sulfur dioxide production or throughput vs operating pressure of the reacting channel for channel length of 0.0064648 m. 184

CHAPTER 1

INTRODUCTION AND LITERATURE SURVEY

Hydrogen is widely seen as the future energy carrier due to the growth of the global energy demand and the necessity to reduce greenhouse gas emissions. Energy carriers are used to store, move and deliver energy in usable form. Hydrogen is one of the two natural elements that combine to produce water. There are both advantages and disadvantages of using hydrogen as the energy carrier. Though they are renewable and have less environmental impacts, non-renewable sources like coal, oil and natural gases are still needed to separate it from oxygen. Most of the energy that is used today comes from fossil fuels. From the work done by Odum [1] it is found that only eight percent of hydrogen production comes from renewable energy sources. The renewable sources are usually cleaner and can be replenished in a short period time. Hydrogen is produced from both renewable and non-renewable resources. Hydrogen is one of the most promising energy carriers for the future. It is a high efficiency, low polluting fuel that can be used in transportation, heating and power generation facilities.

The primary challenge to the increased use of hydrogen is the cost associated with its production, storage and delivery. Hydrogen may be produced by several methods. The cheapest source of hydrogen production is natural gas which is both an energy source and hydrogen source. The disadvantage of this process is that the resulting hydrogen has only 50% of the chemical energy of the original gas. Hydrogen obtained from fossil fuel produces greenhouse gases. The other method for producing hydrogen is steam reforming where the high temperature steam separates hydrogen from the carbon atoms in methane. Though it is the most cost-effective way to produce hydrogen, it uses fossil

fuels in both the manufacturing and chemical production process and also as a heat source. Hence the existing hydrogen production methods are either insufficient or produce greenhouse gases. Nuclear energy can produce high quality hydrogen in large quantities at a relatively low cost and without any air emissions. There are two main categories of hydrogen production technologies using high temperature gas reactors (HTGRs) namely thermochemical water splitting cycles and high temperature water electrolysis. Like conventional electrolysis both technologies separate water into hydrogen and oxygen. Both technologies use high temperature heat for economical, emission-free hydrogen.

High temperature or steam electrolysis involves the separation of water into hydrogen and oxygen through electrolysis at high temperatures. The temperatures involved in this reaction are usually above 1000°C (Vitart et al. [2]). In the thermochemical water splitting cycle hydrogen is separated from water into hydrogen and oxygen through chemical reactions at high temperatures (450°C to 1000°C). The thermochemical water splitting cycle involves a series of chemical reactions, some at a higher temperature than the others. In this cycle all the reactants and the products are regenerated and recycled. Energy as heat is given as an input to the thermochemical cycle via one or more endothermic chemical reactions. Heat is rejected via one or more exothermic low temperature chemical reactions. Among the available thermochemical cycles, the sulfur family consisting of sulfur-iodine cycle (S-I) cycle and hybrid sulfur (H-S) cycle are found to be the most promising candidates for hydrogen production. Figure 1.1 shows the production of hydrogen using the sulfur-iodine thermochemical cycle at different temperatures (Thomas [3]).

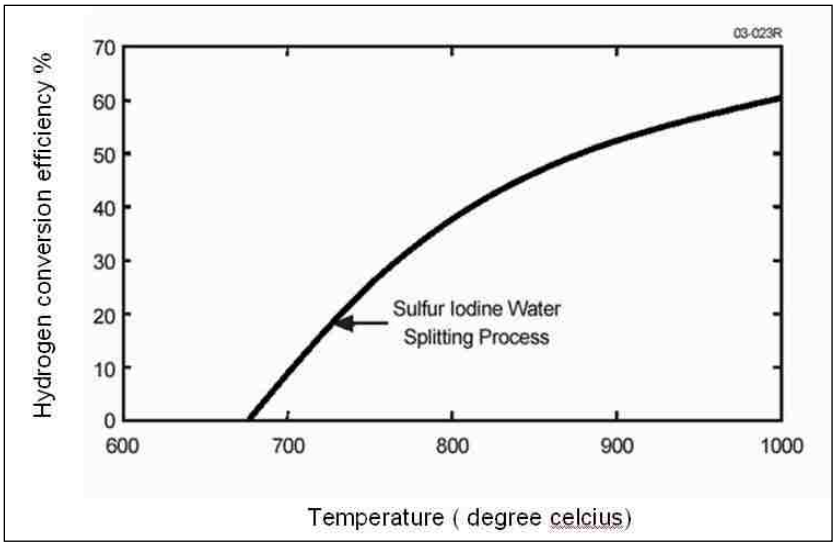

Figure 1.1. Production of hydrogen at different temperatures (Thomas [3]).

The sulfur-iodine water splitting cycle proposed by General Atomics (GA) is a promising candidate for thermochemical hydrogen production (Norman et al. [4]). It consists of three chemical reactions that sum to the dissociation of water.

$$I_2 + SO_2 + 2H_2O \rightarrow 2HI + H_2SO_4 \quad (120°C)\ (\text{Exothermic}) \qquad (1.1)$$

$$H_2SO_4 \rightarrow H_2O + SO_2 + 1/2O_2 \quad (850°C)\ (\text{Endothermic}) \qquad (1.2)$$

$$2HI \rightarrow I_2 + H_2 \quad (450°C)\ (\text{Endothermic}) \qquad (1.3)$$

The net reaction is the decomposition of water to hydrogen and oxygen. The first equation also known as the Bunsen reaction proceeds exothermally in liquid phase and produces two immiscible aqueous acids. The whole process takes in water and high temperature heat particularly in the decomposition steps (Eqn 1.2 and 1.3) and releases hydrogen and oxygen. High temperature heat is provided either by nuclear source or solar source. The sulfuric acid is decomposed at about 850°C releasing the oxygen and recycling the sulfur dioxide. The hydrogen iodide is decomposed at 450°C releasing

hydrogen and recycling the iodine. Much of the heat source is used for the dissociation of sulfuric acid to sulfur dioxide and oxygen. The inputs for the whole process are water and high temperature heat and the outputs are hydrogen, oxygen and low temperature heat. The sulfur-iodine thermochemical water splitting cycle is shown in Figure 1.2 (Picard [5]).

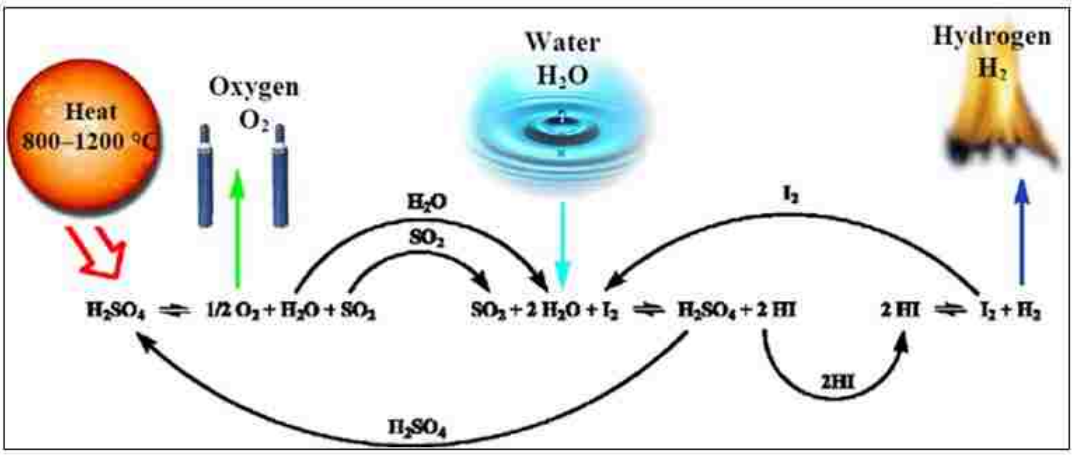

Figure 1.2. Sulfur-iodine thermochemical water splitting cycle (Picard[5]).

1.1 Literature Review

1.1.1 Compact heat exchangers

Compact heat exchangers (CHE) plays an important role in the field of aerospace, transportation and other industries. The need for lightweight, space saving and economical heat exchangers has driven to the development of compact surfaces. Compact heat exchangers are widely in demand due to their improved effectiveness, smaller volume, higher surface density and power savings. Surface area density greater than 700 m^2/m^3 is achieved by incorporating fins, ribs etc. There are many types of

compact heat exchangers like plate heat exchangers, tube fin heat exchangers, printed circuit heat exchangers, spiral heat exchangers etc. The impact of compact heat exchangers on refrigeration technology has been studied by Hesselgreaves [6]. In this paper the study has been done to find out the effects of using fewer refrigerants for a given thermal duty by increasing its compactness. Different types of compact heat exchangers have been studied and it was found that plate fin heat exchanger (PFHE) is likely to make an increasing market impact.

Plate fin heat exchanger is a type of heat exchanger design that uses plates and finned chambers to transfer heat between fluids. A plate fin heat exchanger is a form of compact heat exchanger made of block of alternating layers of corrugated fins separated by parting sheets. Surface interruption prevents the continuous growth of the thermal boundary layer by periodically interrupting it. Thus the thicker thermal boundary layer which offers high thermal resistance to heat transfer are maintained thin and their resistance to heat transfer is reduced In a plate fin heat exchanger fins are easily rearranged resulting in cross-flow, counterflow, cross-counterflow or parallel flow arrangement. The cost of plate fin heat exchanger is slightly higher compared to conventional heat exchangers due to higher level of detail required during manufacture. However the cost can be outweighed by the added heat transfer enhancement. The widely used plate fin heat exchanger has a variety of augmented surfaces such as plain fins, wavy fins, offset strip fins, perforated fins, pin fins, louvered fins etc. (Shah & Webb [7]). Najafi et al. [8] published the optimization studies done on plate and fin heat exchanger using the genetic algorithm. Total rate of heat transfer and total annual cost of the system were considered as the objective function. The main advantage of this work is

providing a set of optimal solutions each of which satisfies the objective function in an appropriate level. Sahin et al. [9] studied the experimental investigations on fluid flow characteristics in a plate fin and tube heat exchanger model composed of single cylinder located between two parallel plates. Particle image velocimetry (PIV) was employed to obtain instantaneous time-averaged and phase-averaged turbulence flow characteristic in the heat exchanger flow passage. Zhang [10] studied flow maldistribution and thermal performance deterioration in air-to-air heat exchanger with plate fin cores. Computational fluid dynamics (CFD) analysis was used to calculate the flow distribution by treating the plate fin cores as porous media. From the study it was found that when the channel pitch is more than 2 mm the flow maldistribution is slightly high and 10-20% thermal deterioration factor could be found.

From the research done by Kayansayan [11] the effect of the performance of plate fin-tube cross-flow heat exchangers due to the outer surface geometry was considered. In this study 10 geometrical configurations were tested and the Reynolds number was varied from 2,000 to 30,000. The results showed that the heat transfer coefficient strongly depends on the finning factor ε and the value of ε increases with decrease in j-factor. Ismail et al. [12] studied three compact plate fin heat exchangers using FLUENT ANSYS [13] software for quantification of flow maldistribution effects with ideal and real cases.

Ranganayakaulu & Seetharamu [14] carried out an analysis of a cross-flow compact plate fin heat exchanger for the combined effects of two-dimensional longitudinal heat conduction through the exchanger wall, flow non-uniformity and temperature distribution was carried out using the finite element method. The exchanger effectiveness and thermal deterioration due to these effects were studied for various

design and operating conditions. Fernandez-Seara [15] carried out an experimental analysis of a titanium brazed plate fin heat exchanger with offset strip-fin in liquid-liquid heat transfer process. Pressure drop and heat transfer characteristics were determined and the Wilson plot was used for the reduction of the experimental heat transfer data. It was found that the experimental results agree well with the correlation equation obtained from the Wilson plot technique. An experimental investigation was carried out by Dubrovsky [16] for a new convective rational heat transfer augmentation law in a plate fin heat exchanger. The results indicated that the fundamental character and causes limiting the rational heat transfer augmentation depend upon the heat transfer surface corrugation.

Jiao et al. [17] carried out an experimental investigation on the effects of inlet pipe diameter, the first header's diameter of equivalent area, the second header's diameter of equivalent flow area on the flow maldistribution in plate fin heat exchanger. From the experimental studies it was found that the performance of flow distribution in PFHE is effectively improved by the optimum design of the header configuration. Wen & Li [18] proposed a study in order to enhance the uniformity of flow distribution. In their study an improved header configuration of plate fin heat exchanger was proposed. The results showed that the fluid flow maldistribution was very severe in the direction of header length for the conventional header used in the industry due to poor header configuration. It was also found that when the baffle is installed properly with optimum length, the ratio of maximum velocity to minimum velocity drops for various Reynolds number. Hence it was concluded that improved header configuration can prominently improve the performance of the plate fin heat exchanger.

1.1.2 Fluid flow and heat transfer enhancement in plate fin heat exchanger

Numerical and experimental investigation of plate fin and tube heat exchanger for fluid flow and heat transfer with inclined block shape vortex generators mounted behind the tubes was studied by Leu et al. [19]. The effects of different span angles for the Reynolds number varying from 400 to 3000 were studied. It was found that the vortex generator arranged at 45° provides the best heat transfer enhancement with 8.30% increase in the Colburn factor and 11.15% increase in the fanning friction factor. Sinha et al. [20] performed a numerical investigation for heat transfer enhancement in the plate fin heat exchanger using two rows of winglet type vortex generators (VGs). In their study the Reynolds number was varied from 250 to 1580. It was found that from the five different strategic placements of VGs, common-flow up (CFU) in series configuration of vortex generator has the best heat transfer and quality factor.

Manglik & Bergles [21] studied the heat transfer and pressure drop correlations for the rectangular offset strip-fin compact heat exchanger. The *f* and j parameters were also found for laminar, transition and turbulent flow regimes. Steady state three-dimensional numerical model was used to study the heat transfer and pressure drop characteristics of an offset strip-fin heat exchanger by Bhowmik & Lee [22]. In this paper *f* and j factor correlations have been used to analyze fluid flow and heat transfer characteristics of offset strip-fins in the laminar, transition and turbulent flow regions. Three different performance criteria for heat exchangers were tested for different fluids and the appropriate performance criteria for Pr = 7 and Pr = 50 were found to be *JF* (thermal-hydraulic performance factor) and $j/f^{1/3}$. Martinez et al. [23] investigated four different semi-empirical models of heat transfer and pressure drop for helically

segmented finned tubes arranged in staggered layout. From the results the optimum pressure drop and heat transfer were found for the Reynolds number of 10,000. The comparison between the predicted and the experimental data shows a precision of greater than 95% in heat transfer for a combination of the Kawaguchi and Gnielinski models at the flue gas Reynolds number.

Research has been carried out by Ma et al. [24] to find heat transfer and pressure drop performances of ribbed channels in the high temperature heat exchanger. The effects of inlet temperature and rib height on the ribbed channel have been studied. From the results it was found that the Nusselt number and the friction factor were unsuitable to compare heat transfer and pressure drop performances at different temperature conditions. Yakut et al. [25] studied the effects of the heights and widths of the hexagonal fins, streamwise and spanwise distances between the fins. The flow velocity on the heat transfer and pressure drop characteristics was investigated using the Taguchi experimental design method. From the results it was found that the heat transfer results were mostly influenced by the fin height, fin width and flow velocity. The fin width was found to be the most effective parameter on the friction factor. Naik & Probert [26] investigated the steady state heat transfer from an array of rectangular uniform duralumin fins constructed with various inter-fin spacings, heights and lengths. It was found that increasing fin height increases heat transfer rates from the fin arrays and decreasing the length of the fins resulted in lower steady-state rates of dissipation per unit base area. Dong et al. [27] conducted a series of test for the Reynolds number ranging from 200 to 2500 based on the louver pitch with different fin pitch, fin height and fin thickness. The results showed that the heat transfer coefficients decrease with fin length and fin width

and increase with fin pitch. The pressure drop decreases with decrease in fin length and increase in fin pitch.

Ngo et al. [28] studied and developed a new microchannel model with s-shaped fins using three-dimensional computational fluid dynamics. It was found that the microchannel heat exchanger provided 6 to 7 times lower pressure drop while maintaining heat transfer performance. The microchannel heat exchangers with s-shaped fins were found to have higher heat transfer performance compared to other conventional heat exchangers. A ceramic microchannel heat exchanger has been modeled by Alm et al. [29]. The performance of the heat exchanger was checked using water in the temperature range up to 95ºC. The performance has been tested using water as a test fluid with maximum flow rates of $120 kg \cdot h^{-1}$. The device shows stronger heat transfer and pressure loss than predicted by theoretical calculations.

Peng & Peterson [30] showed that the cross-sectional aspect ratio has a great influence on the heat transfer in microchannels. It was reported that even if the length to hydraulic diameter ratio (L/d_h) and other parameters are identical, the Nusselt numbers in microchannels are slightly different for different cross-sectional aspect ratios. A theoretical model that predicts the thermal and fluid characteristics of a micro cross-flow heat exchanger was developed by Kang & Tseng [31]. The analytical results showed that the average temperature of the flow significantly affects the heat transfer rate and the pressure drop at the same effectiveness.

The heat transfer behavior of a cross-flow micro SiC heat exchanger in the temperature range up to 340ºC was studied in detail experimentally and numerically by Meschke et al. [32]. It was found that such a heat exchanger has very high thermal

conductivity, resulting in a superior gas-to-gas heat transfer with reasonable efficiency at high loads.

Schulte-Fischedick et al. [33] proposed a ceramic high temperature plate fin heat exchanger for externally fired combustion process. Thermal performance and pressure drop in ceramic heat exchanger was evaluated using CFD simulations by Monteiro et al. [34]. Correlations for the Colburn and the friction factors for the Reynolds number ranging from 500 to 1500 were evaluated. Simulations with conjugate heat transfer were conducted and the results show the influence of mass flow rate on pressure drop and effectiveness of the heat exchanger. A novel bayonet tube high temperature heat exchanger with inner and outer fins was studied by Ma et al [24]. Numerical and experimental investigation of heat transfer performance on the inside of the bayonet element was studied.

1.1.3 Sulfur-iodine thermochemical cycle

Many works have been conducted for the sulfuric acid decomposition process using high temperature heat exchangers and chemical decomposers. Thermochemical water splitting cycles have been studied at various levels of effort for the past 35 years. Extensive studies were done in the late 70s and early 80s, but only little attention was received in the past 10 years as indicated by Brown et al. [35]. Over 100 cycles have been proposed and the interest in thermochemical water splitting cycles varied greatly with time.

The Bunsen reaction for the production of hydriodic and sulfuric acids from water, iodine and sulfur dioxide has been studied by Giaconia et al. [36]. The results showed that the operative temperatures have a minor effect on the phase behavior.

Huang & T-Rassi [37] used ASPEN Technologies HYSYS chemical process simulator to develop flowsheets for sulfuric acid decomposition that include all mass and energy balances. Based on the HYSYS analyses, a new process flowsheet has been developed. The developed sulfuric acid decomposition process is simpler and more stable than previous processes, and yields higher conversion efficiencies for sulfuric acid decomposition, sulfur dioxide and oxygen formation. A study on sulfur-iodine cycle for hydrogen production by a water splitting reaction has been done by Barbarossa et al. [38]. Experiments have been done in a homogenous gas phase in the presence of solid catalysts Ag-Pd intermetallic alloy and Fe_2O_3 supported on SiO_2 in the temperature range of 773 K to 1373 K. From the results it was observed that the thermal dissociation of sulfuric acid is strongly affected by temperature and hence a suitable catalytic material must be selected to decrease decomposition temperature.

A design study of the sulfur trioxide decomposition reactor encompassing the thermodynamics, reaction kinetics, catalyst, heat transfer and mechanical design was performed by Lin & Flaherty [39]. Numerical simulation of shell-and-tube heat exchanger and chemical decomposer with straight tube configuration and porous media was studied to find the decomposition percentage of sulfur trioxide by Kuchi et al. [40]. From the results it was found that the decomposition percentage of SO_3 is 93% for counterflow arrangement and 92% for parallel flow arrangement.

The research carried out at Westinghouse Electric Corporation by Brecher et al. [41] describes the design of one of the most critical components which is the sulfur trioxide decomposition reactor. A shell and tube heat exchanger with packed bed catalyst was used where the catalyst is located on the shell side and helium along the tube side.

The preheat section is loaded with a packed bed of spheres or rings without catalyst just to enhance heat transfer. The percentage decomposition obtained was low at temperature below 1000 K and satisfactory conversion is achieved above 1073 K. Ozturk et al. [41] studied a new design and thermodynamic and engineering analysis of the H_2SO_4 decomposition section of the sulfur-iodine thermochemical cycle for producing hydrogen. In this process all the equipment is operated adiabatically at a maximum pressure of 0.7 MPa. The thermodynamic result shows that the first law efficiency is 64.2% and the exergetic efficiency is 64%. The cost of kmol of SO_2 is $1.8 based on the currency in 1990 for a nuclear energy cost of $3.0 per GJ to $3.0 based on the currency in 1990 for the nuclear energy cost of $6.0 per GJ.

Perkins & Weimer [43] did research on thermodynamic and material considerations for two-step and three-step thermochemical cycles to split water using solar thermal processing. From the study it was found that solar thermal processing was ideal for sulfur-iodine (S-I) cycle, as it would allow operation in optimal temperature range (~1900 K), not easily accessible by other processing methods. H_2SO_4 dissociation in the presence of SiC (protective SiO_2 layer) is stable over the desirable temperature range.

Kubo et al. [44] showed that Japan Atomic Energy Research Institute (JAERI) has carried out thermochemical hydrogen production using the water splitting sulfur-iodine process, as part of the research programs aimed at utilizing heat from a high temperature gas-cooled reactor (HTGR). The process is limited to the bench-scale stage, and only covers several fields including the evaluation of structural materials in corrosion environments, the improvement in thermal efficiency and the techniques for operation in

closed-loop continuous hydrogen production. In their experimental study, hydrogen production at the rate of 32 l/h for 20 h was successfully accomplished.

In the work done by Wang et al. [45] the HI catalytic decomposition for the lab scale H_2 producing apparatus of IS-10 in Institute of Nuclear and New Energy Technology (INET) was studied. The experimental results showed that the active carbon and carbon molecular sieve had the higher catalytic activity for HI decomposition. The results of X-ray diffractometer (XRD), transmission electron microscopy (TEM) and Brunauer-Emmett-Teller (BET) specific surface area about the fresh and used Pt/AC showed that the stability of active carbon supported Pt catalyst should be improved. In the work done by Kane et al. [46] the analysis of hydrogen iodide (HI) decomposition based on the flow sheet developed by General Atomics (GA) was performed. The whole HI decomposition section was flow sheeted and simulated with Aspen Plus. The results showed a correlation between the boil-up rate and the pressure of the distillation column.

Research has been done for materials to be used in the sulfur-iodine thermochemical water splitting cycle for the hydrogen production by Wong et al. [47]. The immersion coupon corrosion tests have been performed and only Ta and Nb-based refractory metals and ceramic mullite can stand up to the corrosive environment. A compact ceramic high temperature heat exchanger has been proposed as sulfuric acid decomposer for hydrogen production within the sulfur iodine thermo-chemical cycle by Ponyavin et al. [48]. The results of this research provide the basis for optimal design of the decomposer that provides maximum chemical decomposition while maintaining the stresses within desired limits. The research has been conducted on the sulfur trioxide

decomposer which includes reaction kinetics, catalyst, heat transfer and mechanical design.

In the work done by Liberatore et al. [49] sulfur recovery from flue gas in industrial plants has been considered and analyzed. Therefore two configurations for the S-I process have been considered in order to identify the better solution in terms of energy consumption and equipment costs. The cost production is mainly due to gains derived from the sale of the process products and from the absence of both $CaCO_3$ supply and $CaSO_4$ disposal costs.

In the research done by Subramanian et al. [50] ceramic high temperature heat exchanger was used as a sulfuric acid decomposer for hydrogen production within the sulfur-iodine thermochemical cycle. Hot helium from nuclear reactor is used to heat the S-I (sulfuric acid) feed components (H_2O, H_2SO_4, SO_3) to obtain appropriate conditions for the S-I decomposition reaction. The inner walls of the S-I decomposition channels of the decomposer are coated by a catalyst to decompose sulfur trioxide into sulfur dioxide and oxygen. The activity and stability of several metal oxide supported platinum catalysts were explored for sulfuric acid decomposition reaction. In the study by Ginosar [51] reactions were carried out using a feed of concentrated sulfuric acid (96 wt%) at atmospheric pressure at temperatures between 800 and 850ºC. The influence of exposure to reaction conditions were observed for three catalysts namely zirconia, titania and 0.1-0.2 wt% Pt supported on alumina. The results showed that the higher surface area catalysts namely Pt/Al_2O_3 and Pt/ZrO_2 had the highest activity but deactivated rapidly. The lower surface area catalyst like Pt/TiO_2 had good stability in short term tests.

Sandia National Lab (SNL) (Gelbard [52]) developed silicon carbide integrated decomposer (SID) for hydrogen production using high temperature heat. It has a sulfuric acid section which receives dilute acid from the adjacent reaction section, concentrates and decomposes the acid to SO_2, O_2 and H_2O. The problem of corrosion is solved by using non-metal wetting components. The low temperature regions are made of teflon and viton seals while the high temperature region is made up of silicon carbide. Platinum is used as a catalyst to decompose sulfur trioxide to sulfur dioxide. The SID or bayonet heat exchanger combines the boiler, superheater, decomposer and recuperator in a single unit without any connections that have the potential for leaking. From the shakedown test performed on the SID, the flow rate is varied from 5-15 $ml \cdot min^{-1}$ and the acid conversion fraction is about 0.6. Another test was performed by coupling the concentrator at 0.1 bar with the SID operating between 3 and 5 bar and the acid conversion fraction obtained is 0.37.

In the work done by Nagarajan et al. [53] a bayonet heat exchanger used as silicon carbide integrated decomposer (SID) produces sulfuric decomposition product- sulfur dioxide. The study was carried out under constant wall temperature and by applying measured values obtained from the thermocouples placed along the outer wall of the lab scale model of the bayonet heat exchanger. The investigation of different types of pellets in the packed bed region was carried out and the obtained decomposition percentage of sulfur trioxide is in good agreement with the experimental results from SNL. In another study done by Nagarajan et al. [54] decomposition percentage of sulfur trioxide was studied in the packed bed region of the bayonet heat exchanger. Cylindrical, spherical, cubical and hollow cylindrical pellets were used for packing. The spherical pellets gave

decomposition percentage of 61% which is in close agreement with the experimental results obtained from SNL.

1.1.4 Structural analysis

In the study done by Ponyavin et al. [48] a three-dimensional computational model is developed to investigate fluid flow, heat transfer, chemical reaction and stress analysis within the decomposer. Fluid/thermal/chemical analysis of the decomposer was conducted using FLUENT [13] software. Thermal results were exported to ANSYS to perform the probabilistic failure analysis. From the results it was found that all the considered designs have zero probability of failure as SiC has an extremely high thermal conductivity which eliminates large thermal gradients.

Barreau et al. [55] studied the failure strength of silicon carbide ceramic disks under biaxial flexure when exposed to elevated temperatures and concentrated sulfuric acid. The heat exchanger materials are subjected to temperatures in the range of 930°C and sulfuric acid. The discs are tested in their manufactured condition or after ninety-six hours exposure to sulfuric acid vapor or after ninety-six hours immersion in 100% concentrated sulfuric acid. The Weibull statistical analysis has been done. It is concluded that testing under a temperature of 930°C has no noticeable effect on the strength of the specimens. Similarly immersing the specimens in sulfuric acid or exposing them to sulfuric acid vapor has no appreciable effect. The results indicate that the strength of the tested specimens below the standard values due to sintering problems.

In the work done by Borger et al. [56] a finite element analysis (FEA) of the stress state in a ball on three balls tested disc was performed. It was found that the stress fields

with the maximum principal stress occur in the center of the tensile surface. An analytical approximation has been derived which accounts for the influence of all relevant geometrical and material parameters. Danzer et al. [57] performed a biaxial strength test for brittle rectangular plates. A disc shaped plate is symmetrically supported by the three balls at one plane and loaded by the fourth ball in the center of the opposite plane. Finite element analysis of the stress fields was performed and the maximum tensile stress amplitude and the effective volume in the specimen were determined. It was found that the ball over three balls (B3B) strength data determined on rectangular plate specimen fits to test results determined on disc specimens and to conventional bending test results.

The statistical approach to brittle failure in ceramic was done by Lamon [58]. In this paper the Weibull approach, the Batdorf's approach and the multiaxial elemental strength model were studied. It was found that the Weibull approach presents important limitation on the ability to treat multiaxial failure under complex stress fields involving compressive components. The Batdorf's approach was found to be mathematically complex. The multiaxial elemental strength model overcomes the difficulties of the other two models. The Weibull discussed the applicability of statistics to a wide field of problems for both simple and complex distributions.

1.2 Motivation of the Dissertation

Though hydrogen can be produced by many methods much of the current hydrogen production comes from fossil fuels. But technology for large scale hydrogen production with low cost hasn't been developed yet. So now there is a very high urgency

to create a relatively cheap and reliable technological cycle for hydrogen production that is compatible with the environment and independent of foreign fuels. The most promising of these cycles is the sulfur-iodine process, from which sulfuric acid decomposition is one of the most important and difficult parts.

The microchannel heat exchangers proved their high efficiency and heat transfer rate in numerous investigations, and they are widely used now in a high range of industrial applications. To improve heat transfer rate with optimum pressure drop, microchannel heat exchangers with different designs have been developed in this study. High temperature corrosion resistant ceramic can be used as a material for the microheat exchangers for the sulfuric acid decomposition.

1.3 Outline of Dissertation

The focus of this dissertation is on the development of a three-dimensional computational model of a high temperature heat exchanger and decomposer for hydrogen production, based on the sulfur-iodine thermochemical water splitting cycle. Chapter 2 explains the details of the problem, geometry and operating conditions, associated governing equations and methodology of solution. The fluid flow and heat transfer of different fin designs are studied in this chapter. Validation of fluid flow and heat transfer model with the published results is shown in Chapter 3. Chapter 4 discusses the structural analysis of different fin designs. The failure criteria of ceramic on all the fin designs are studied in Chapter 4. Chapter 5 shows the calculations with chemical reactions and parametric studies were performed with the purpose of increasing of the

reaction decomposition percentage. Chapter 6 concludes the current research and suggestions for future work are provided.

CHAPTER 2

PROBLEM DESCRIPTION AND METHODOLOGY

A heat exchanger is a device which is used to transfer energy from one fluid medium to the other. The medium may be separated by a solid wall to prevent mixing or they may be in direct contact. The heat exchangers are widely used in refrigeration, space heating, power plants, chemical plants, nuclear industry, sewage treatment etc. An efficient heat exchanger can be designed by considering several important factors like heat transfer, pressure drop, size and weight, required life, cost and resistance to fouling and contamination. Compact heat exchangers (CHE) are now widely being used in order to reduce pressure drop, minimize size and weight and obtain higher heat transfer rate. CHE are a class of heat exchanger that incorporates a large amount of heat transfer surface area per unit volume. A typical compact heat exchanger has an area density of 700 m^2/m^3 for gas and greater than 300 m^2/m^3 for liquid or two-phase streams. The most important characteristics of CHEs are large extended surfaces, high surface area density and small hydraulic diameter. There are many types of compact heat exchangers employed in the industry namely plate frame heat exchanger, spiral heat exchanger, brazed plate heat exchanger, printed circuit heat exchanger, plate fin heat exchanger etc.

2.2 Types of Compact Heat Exchanger

2.2.1 Plate frame heat exchanger

Plate and frame heat exchanger was commercially successfully introduced in 1923 by Dr. Richard Seligman (Thulukkanam [59]). The plate and frame heat exchanger consists of a frame in which closely spaced metal plates are clamped between head and

follower. The plates have corner ports and are sealed by gaskets around the ports and along the plate edges. The plates are grouped into passes with each fluid being directed evenly between the paralleled passages in each pass. An important feature of plate heat exchanger is that by use of special connector plates it is possible to provide connections for alternative fluids so that a number of duties can be done in same frame. They are used for temperatures from -35°C to 220°C, pressures up to 25 bar and flow rate up to 5000 $m^3 \cdot h^{-1}$ (Cheresources.com, [60]). The advantages of plate heat exchanger are high thermal effectiveness, low fabrication cost, ease of cleaning and temperature control and the disadvantages are due to pressure and leakage. Figure 2.1 shows the schematic of plate frame heat exchanger.

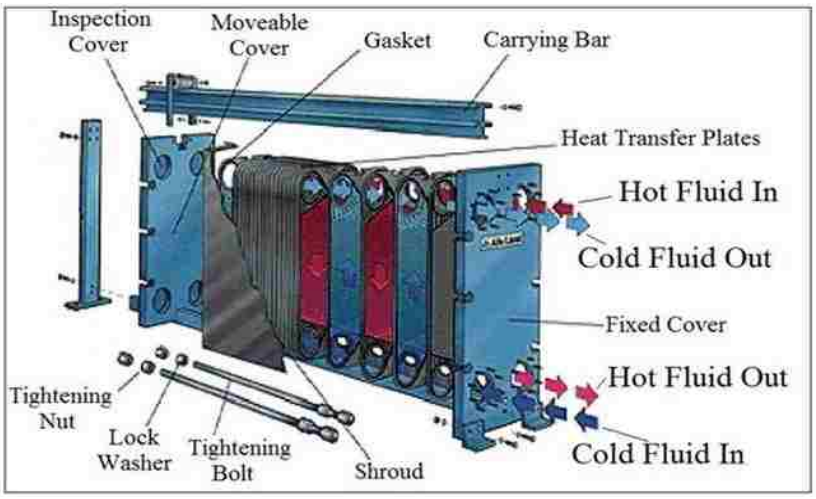

Figure 2.1. Plate frame heat exchanger (Cheresources.com, [60]).

2.2.2 Spiral heat exchanger

A spiral heat exchanger is a coiled tube arrangement with two channels coiled one around another. These two channels operate in a counter-flow arrangement, offering

excellent turn down ratios and enhancing heat transfer. They are used for temperatures up to 400°C and pressure up to 25 bars (Thermal Heat Transfer Systems Inc. [61]). The advantages of spiral heat exchanger are overall heat transfer coefficient, easy maintenance and leakage. Serious fouling and corrosion are some of the limitations of spiral heat exchanger. Spiral heat exchanger is shown in Figure 2.2.

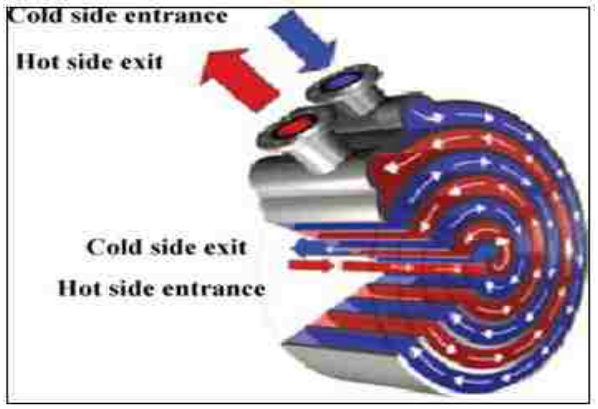

Figure 2.2. Spiral heat exchanger (Thermal Heat Transfer Systems Inc.[61]).

2.2.3 Brazed plate heat exchangers (BPHE)

The compact brazed plate heat exchanger is constructed as a plate package of corrugated channel plates with a filler material between each plate. The BPHE allows media at different temperatures to come into close proximity separated only by channel plates that enable heat from one media to be transferred to the other with very high efficiency. The brazed plate fin heat exchanger is similar to plate and frame technology but without gaskets and frame parts. They are used for temperatures from -195°C to 200°C and pressure up to 30 bar (Alfa Biz Limited. [62]). Figure 2.3 shows the schematic of BPHE.

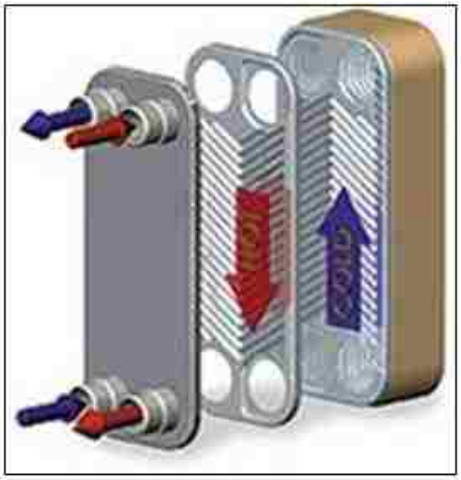

Figure 2.3. Brazed plate heat exchanger (Alfa Biz Limited. [62]).

The advantages of BPHE are compactness, durability, easy maintenance, requires less investment cost requirements etc. and the disadvantage is that they are difficult to clean.

2.2.4 Printed circuit heat exchanger (PCHE)

PCHEs are characterized as high integrity plate type heat exchangers. They are formed by diffusion bonding of a stack of plates with fluid flow channels chemically etched on one side of each plate. PCHEs are four to six times smaller than conventional shell and tube heat exchangers. PCHEs are highly compact, robust and achieve high thermal effectiveness. They are used for temperature range from -200°C to 900°C and pressure capability in excess of 600 bar (Heatric Inc. [63]). Due to the presence of microchannels the working fluid should be extremely clean and blockages can easily occur. Figure 2.4 shows the Heatric design of printed circuit heat exchanger.

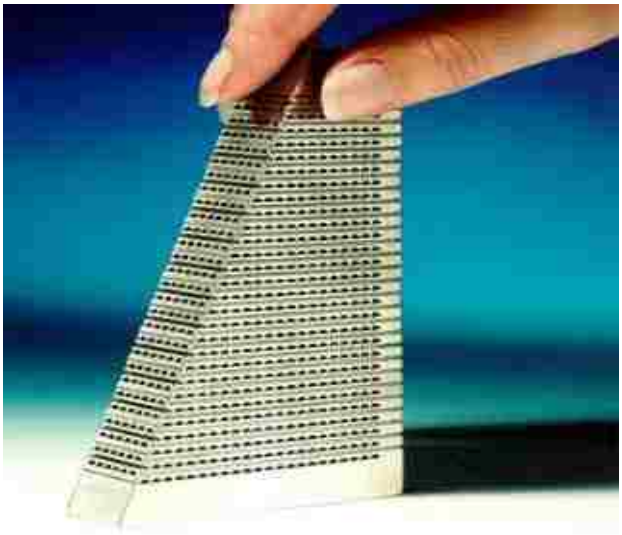

Figure 2.4. Printed circuit heat exchanger (Heatric Inc. [63]).

2.2.5 Plate fin heat exchanger (PFHE)

Plate fin heat exchanger uses plates and finned chambers to transfer heat between fluids. It is a type of heat exchanger with relatively high heat transfer surface area to volume ratio. In this heat exchanger hot fluid and cold fluid streams flow through alternating layers and are enclosed at the edges by the side bars. The fluid streams usually are gas, liquid or two-phase fluids. Heat transfer between multiple process streams is also accommodated. It can be used in wide operating range and high overall heat transfer coefficient is obtained. The major disadvantage of plate fin heat exchanger is that they are prone to fouling due to their small channel size. They cannot be mechanically cleaned and requires chemical cleaning (Lytron Total Thermal Solutions [64]). The plate fin heat exchanger is shown in Figure 2.5.

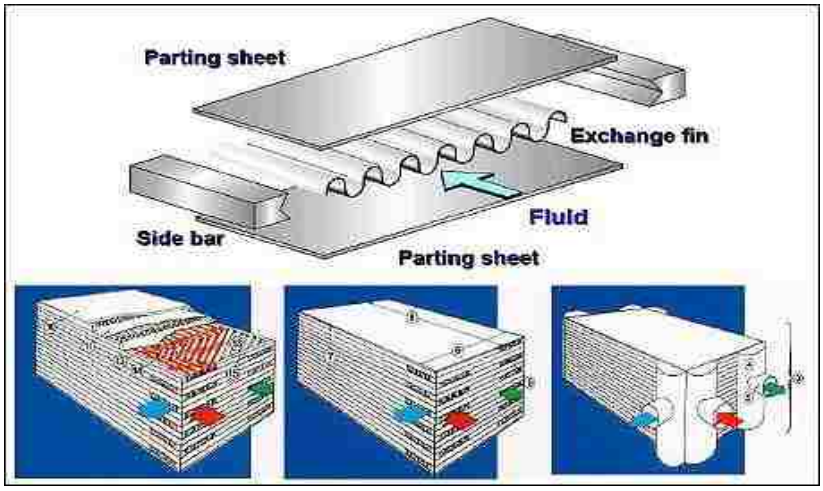

Figure 2.5. Plate fin heat exchanger (Lytron Total Thermal Solutions [64]).

In this study a novel fin configuration for high temperature ceramic plate fin heat exchanger (PFHE) is analyzed using finite volume method (FVM). Nine typical PFHE design configurations are studied in detail in this research. The computer aided geometry (CAD) geometry for all the models are modeled in Solidworks [65] and simulations are carried out in ANSYS FLUENT 14.5 [13]. The geometry and dimensions for the current study is taken from the work done by Ponyavin et al. [48]. In their study the geometry was designed according to the process design proposed by General Atomics (GA). Figure 2.6 shows the geometry of the whole model of plate fin heat exchanger modeled in Solidworks.

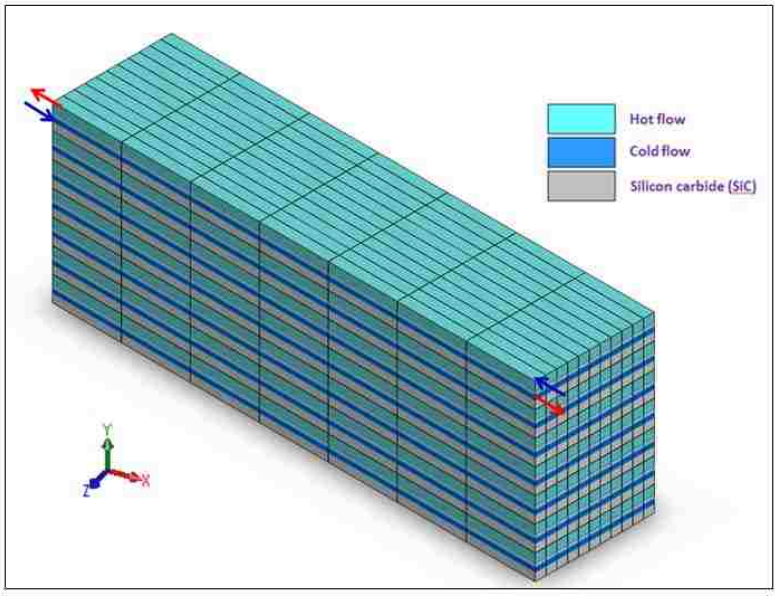

Figure 2.6. Geometry of the whole heat exchanger.

From the previous study by Ponyavin et al. [48] it was found that mass flow rate in all channels can be made almost uniform with a proper design of manifold channels. Hence by applying that concept a single channel model is developed to reduce computational time and memory. Single-banking configuration is used where in the hot and the cold plates are stacked alternatively. The current study has hot fluid channel, cold fluid channel and two silicon carbide (SiC) solid regions. Helium fluid flows through the hot channel placed above the solid region and mixture of sulfur trioxide, sulfur dioxide, oxygen and water vapor flows through the cold fluid channel which is placed between the two solid regions. The flow is counter flow where the hot and the cold fluids enter the model from –x and +x directions and exit in the +x and –x directions, respectively. Figure 2.7 shows the geometry and dimensions of the single channel of plate fin heat exchanger.

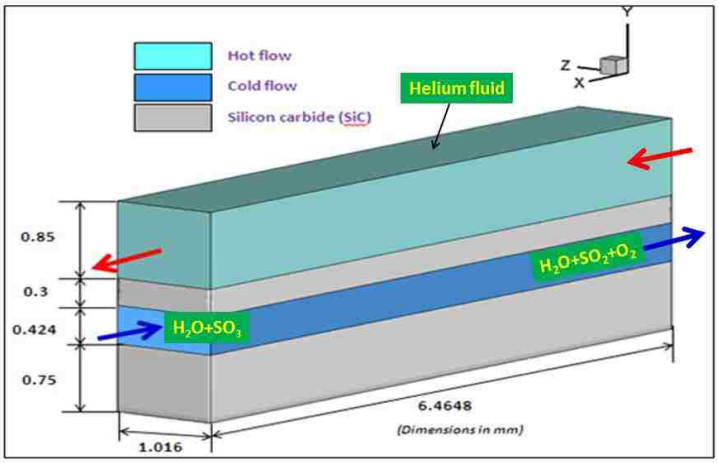

Figure 2.7. Geometry and dimensions of single channel.

The dimensions of the heat exchanger are obtained from Ponyavin et al.[48]. Table 2.1shows the dimension for the current study and the study done by Ponyavin et al.[48].

Table 2.1

Dimensions of the current model and the model by Ponyavin et al.[48]

	Dimensions used by Ponyavin et al.[48]			Dimensions used in the current study		
	Height (mm)	Width (mm)	Length (mm)	Height (mm)	Width (mm)	Length (mm)
Hot fluid channel	0.850	1.016	52.2324	0.850	1.016	6.4648
Cold fluid channel	0.424	0.635	52.2324	0.424	1.016	6.4648
Solid region between the hot and cold channel	0.300	1.016	52.2324	0.300	1.016	6.4648
Solid region below the cold channel	0.750	1.016	52.2324	0.750	1.016	6.4648

The novelty of this type of configuration is that new design of fins is modeled and studied by Nagarajan et al. [66]. To enhance the thermal performance of the PFHE many fin designs are explored and studied. The heat exchanger design with no fins is selected as the baseline design. The other designs differ from the baseline design only in the geometry of the cold channel. The geometry and the dimensions of the rectangular and triangular fins are shown in Figure 2.8.

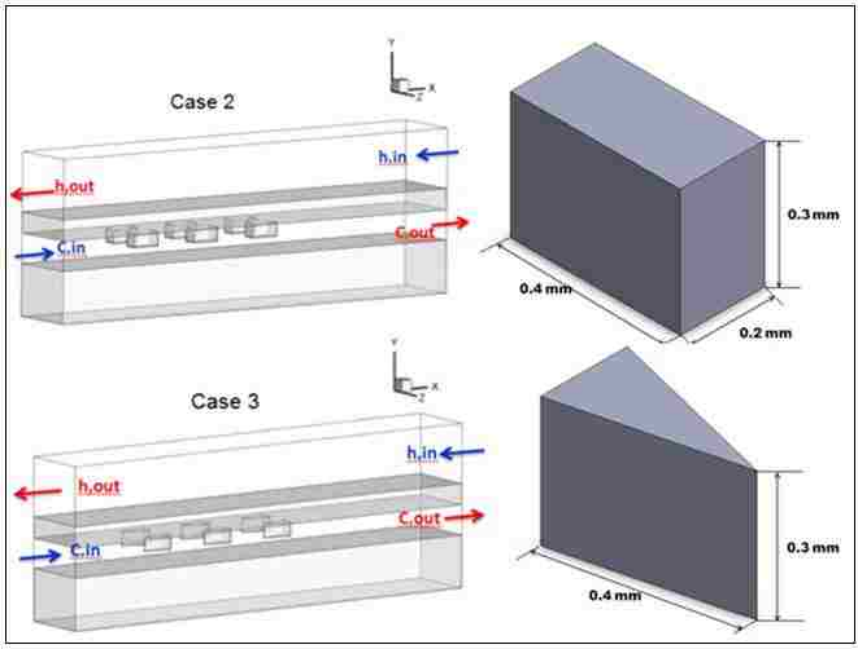

Figure 2.8. Geometry and dimensions of rectangular and triangular fins.

In addition to the conventional fins (rectangular and triangular) fluid flow and heat transfer analysis are carried out on bolt type fins, ripsaw fins and eyelid type fins. The geometry of the inverted bolt and bolt type fins are shown in Figure 2.9.

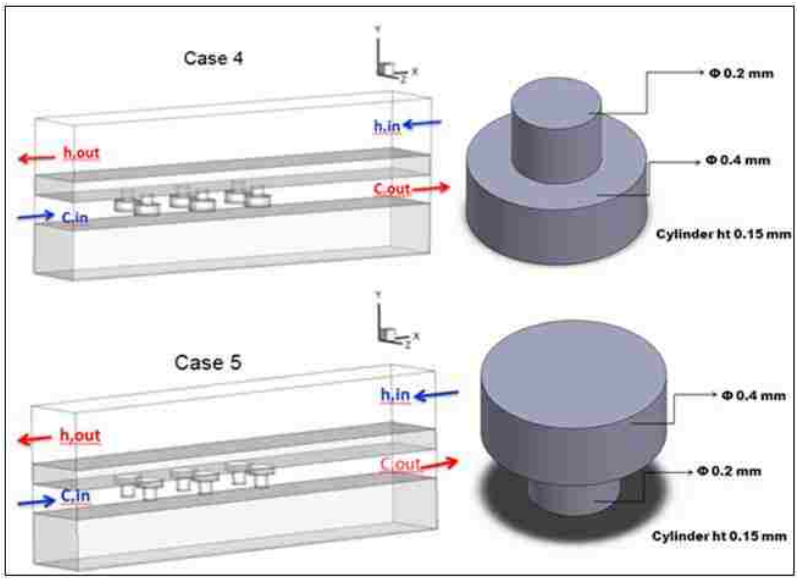

Figure 2.9. Geometry and dimensions of bolt type fins.

Another fin type called ripsaw fin type is selected to enhance heat transfer. Ripsaw fins with 0.2 mm thickness and 0.05 mm thickness are selected to study the fluid flow and heat transfer. Figure 2.10 shows ripsaw fin geometry and dimensions.

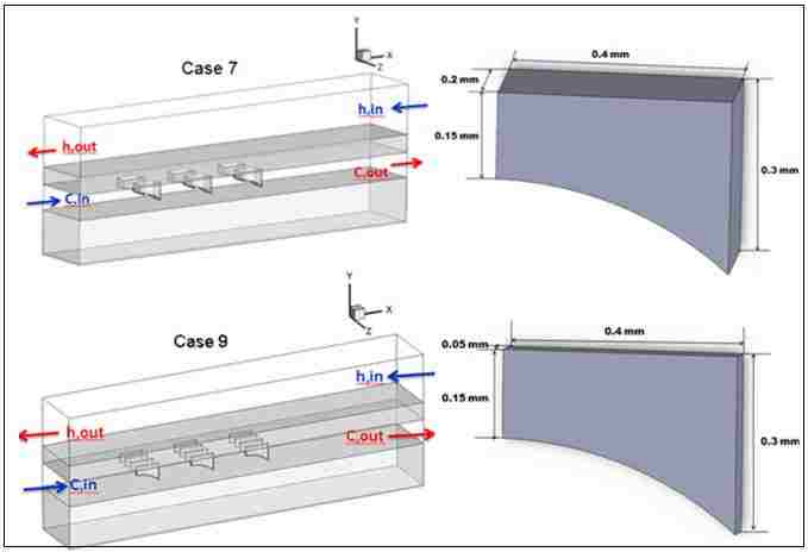

Figure 2.10. Geometry and dimensions of ripsaw fins.

Table 2.2 shows the dimensions of all fin types.

Table 2.2

Dimensions of various fins

Geometry	Definition
Rectangular fins (Case 2)	Height = 0.4 mm, length = 0.4 mm, width = 0.2 mm
Triangular fins (Case 3)	Height = 0.3 mm, breadth = 0.2 mm, length = 0.4 mm
Inverted bolt type fins (Case 4)	Diameter of top cylinder = 0.2 mm, diameter of bottom cylinder = 0.4 mm
Bolt type fins (Case 5)	Diameter of top cylinder = 0.4 mm, diameter of bottom cylinder = 0.2 mm
Eyelid type fins (Case 6)	Height = 0.4 mm, radius of semi-circle = 0.3 mm
Ripsaw fins (Case 7,8,9)	Larger height of the rectangle = 0.3 mm, smaller height of the rectangle = 0.15 mm

In addition to the uniform arrangement, analysis is done for the staggered arrangement of the fins. Staggered arrangement of fins is done for rectangular, triangular, inverted bolt type and ripsaw fins with thickness of 0.05 mm. Another study is carried out with fins on both top and bottom solid regions. The main reason for this arrangement is to enhance the heat transfer coefficient of the heat exchanger. Figure 2.11 shows different arrangements for rectangular fins.

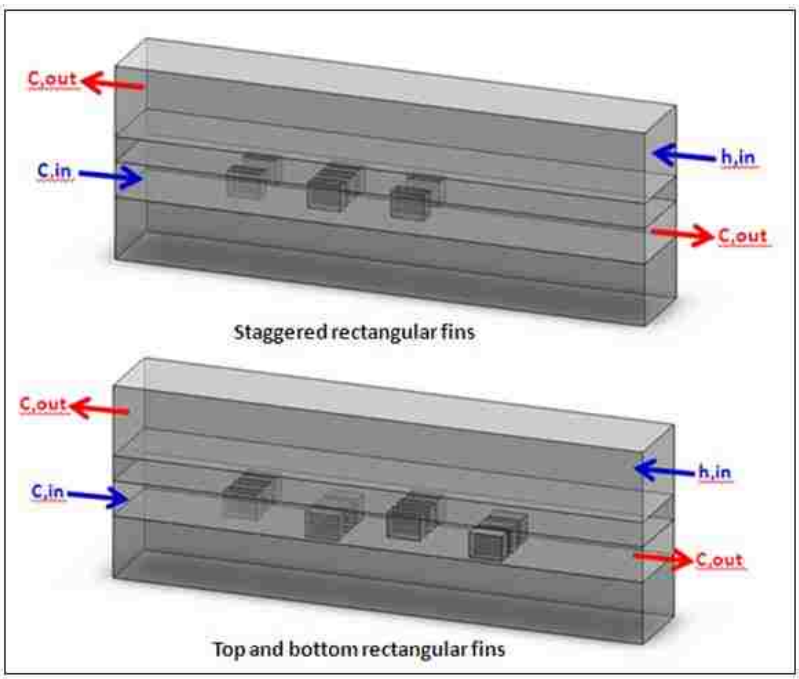

Figure 2.11. Geometry of staggered and top and bottom fin arrangement.

2.3 Numerical Method and Algorithm

2.3.1 Solution technique

The finite volume method is one of the most versatile discretization techniques used in CFD. Based on the control volume formulation of analytical fluid dynamics, the first step in the FVM is to divide the domain into a number of control volumes where the variable of interest is located at the centroid of the control volume. The next step is to integrate the differential form of the governing equations over each control volume. The resulting equation is called the discretized equation. Physically, the conservation of mass, momentum and energy are assured in the formulation of FVM via the finite difference method (FDM) itself. The governing equations are solved in the Cartesian coordinate system using a control volume finite difference method that is similar to the

approach introduced by Patankar [67]. ANSYS FLUENT [13] a commercial CFD program based on the finite volume method is among the most powerful packages of existing software used for solving fluid flow and heat transfer problems.

The pressure-based segregated solution algorithm is used for the given problem. It can be simply described as the process of solving the governing equations in a sequential order as opposed to simultaneously as with a coupled solver. The segregated solution algorithm is memory efficient since it only needs to store the discretized equations in memory sequentially. All fluid properties such as density, specific heat, viscosity etc., are updated.

1. Each individual momentum equation is solved using the previously updated pressure and fluxes.
2. A pressure correction is obtained using the previously obtained velocity and mass fluxes.
3. Mass fluxes, velocity and pressure are updated using the obtained pressure correction.
4. Conservation equations are solved for energy and species terms.
5. Source terms are evaluated for the generation/depletion of energy and species due to chemical reaction.
6. Convergence is checked to determine if more iterations are required.

The governing equations which are discrete and non-linear are linearized to produce a system of equations for the dependent variables in every computational cell. The governing equations are linearized by the semi-implicit method with respect to the set of dependent variables. By this method the unknown value in each cell is computed

using a relation that includes both existing and unknown values from neighboring cells. The methodology of the segregated solver that is executed in each iterative step is shown in Figure 2.12.

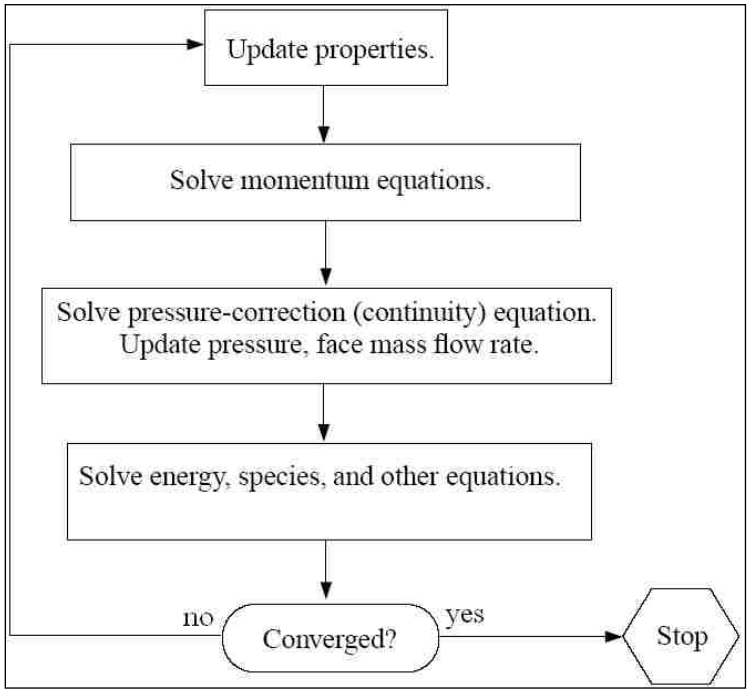

Figure 2.12. Segregated solver approach.

2.3.2 Discretization

This control volume technique used by ANSYS FLUENT (Patankar [67]) consists of integrating the governing equations about each control volume, yielding discrete equations that conserve each quantity on a control-volume basis. By default the solver stores the discrete values of the scalar quantities at the cell center. However, when the face values of the scalar quantities are required the values are interpolated from the cell center values. This is accomplished using an "upwind" scheme. Upwinding means that

the face values are derived from quantities in the cell upstream, relative to the direction of the normal velocity.

The process of simply assigning the value of the upwind grid point to the cell face value is known as a first-order-upwind-differencing. The first-order discretization equation is used for momentum and continuity equation. The SIMPLE (Semi-Implicit Method for Pressure Linked Equations) is used to introduce pressure into continuity equations. The SIMPLE algorithm uses the relationship between velocity and pressure corrections to enforce mass conservation and to obtain the face flux. If the resulting flux does not satisfy the continuity equation a correction face flux is added to obtain the corrected flux, thus satisfying the continuity equation. The pressure correction equation may be solved using the algebraic multigrid method (AMG) method. The SIMPLE algorithm proposed by Patankar & Spalding [67] is used in the finite volume method. The discretization of the primitive variables is performed on a two-dimensional staggered grid as shown in. Figure 2.13. The shaded part shows the control volume associated with (i,j). Pressure, temperature and other scalar occupy the center of the control volume, the velocity components u and v are at the center of the upstream and downstream cell faces of the control volume in the x and y directions respectively. In Figure 2.13 the main grid is shown in solid lines and the staggered grid is shown in broken lines. The horizontal and vertical arrows indicate the grid points for the u and v velocity components.

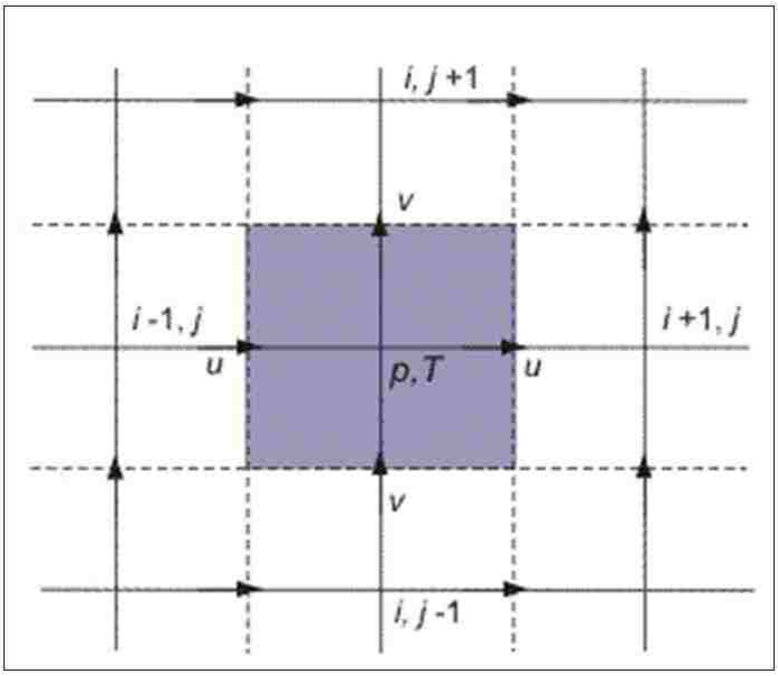

Figure 2.13. Two-dimensional staggered grid.

2.4 Boundary Conditions

2.4.1 Mass flow inlet boundary condition

Mass flow boundary conditions can be used in ANSYS FLUENT [13] to provide a prescribed mass flow rate at the inlet. A mass flow rate inlet is often used when it is more important to match a prescribed mass flow rate than to match the total pressure of the inflow stream. When the mass flow boundary condition is used for an inlet zone, a velocity is used to compute the fluxes of all relevant solution variables into the domain. With each iteration, the computed velocity is adjusted so that the correct mass flow rate value is maintained. If total mass flow rate is specified at the inlet, FLUENT converts it internally to a uniform mass flux by dividing the mass flow rate by the total inlet area.

$$\rho v_n = \frac{\dot{m}}{A} \tag{2.1}$$

Once the value of ρv_n at a given face has been determined, the density ρ at the face must be determined in order to find the normal velocity, v_n. For incompressible flow, the density at the inlet is either constant or readily computed as the function of the temperature and the species mass fractions.

2.4.2 Pressure outlet boundary condition

The pressure outlet boundary condition requires the specification of gauge pressure at the outlet. The value of the static pressure is used only when the flow is sub-sonic, as in this case. All other flow quantities are extrapolated from the interior. A set of the "backflow" conditions are also specified, should reverse flow occur at the exit during the solution process. To set the static pressure the appropriate gauge pressure should be entered. At the pressure outlets ANSYS FLUENT [13] uses the boundary condition pressure input as the static pressure of the fluid at the outer plane and extrapolates all other conditions from interior of the domain.

2.4.3 Thermal boundary condition

When choosing to solve an energy equation, it is required to define the thermal boundary condition at the walls. Since the wall zone in three-dimensional modeling is a fluid/solid interface a conjugate heat transfer problem is encountered. FLUENT allows us an option to choose whether or not the two sides of the wall are "coupled". When the coupled option is chosen no other thermal boundary conditions are required, because the solver will calculate heat transfer directly from the solution in the adjacent cells.

2.4.4 Wall boundary condition

Wall boundary conditions are used to bound fluid and solid regions. Since the flow is modeled as viscous flow, the no-slip boundary condition is enforced at wall. The catalytic surface reaction is enabled at the wall which allows fluid to react when it comes in contact with the wall.

2.4.5 Symmetry boundary condition

Symmetry boundary conditions are used when the physical geometry of interest and the expected pattern of the flow/thermal solution have mirror symmetry. ANSYS FLUENT [13] assumes zero flux of all quantities across a symmetry boundary. There is no convective flux across a symmetry plane: the normal velocity component at the symmetry plane is thus zero. There is no diffusion flux across a symmetry plane. Since the shear stress is zero at a symmetry boundary, it can also be interpreted as a "slip" wall when used in viscous flow calculations.

2.4.6 Solid condition

A "solid" zone is a group of cells for which only a heat conduction problem is solved, no flow equations are solved. The only required input for a solid zone is the type of solid material.

2.4.7 Fluid boundary condition

A fluid zone is a group of cells for which all active equations are solved. The only required input for the fluid zone is the type of fluid material. The type of fluid and the properties of the individual fluid and the mixture properties are defined in the material panel of ANSYS FLUENT [13].

2.4.8 Under-relaxation factors

The segregated solver uses under-relaxation to control the update of computed variables after each iteration. All the equations solved using the segregated solver will have the under-relaxation factor. In ANSYS FLUENT [13], the default under-relaxation parameters for all variables are set to values that are near optimal for the largest possible number of cases. The calculations are performed with the default under-relaxation factor for all parameters except temperature. Since the residual of energy started increasing the under-relaxation factor for energy is reduced from 1.0 to 0.8. As reversed pressure flow is seen during the iterations the under-relaxation factor for pressure was decreased to 0.1. Once the residuals started to stabilize it was then increased to 0.9 which results in faster convergence.

2.5 Governing Equations

The governing equations for the continuity, momentum and energy for laminar flow are expressed as follows:

$$\frac{\partial}{\partial w_i}\left(\rho u_i\right) = 0 \tag{2.2}$$

$$\frac{\partial}{\partial w_i}\left(\rho u_i u_k\right) = \frac{\partial}{\partial w_i}\left(\mu \frac{\partial u_k}{\partial w_i}\right) - \frac{\partial p}{\partial w_k} \tag{2.3}$$

$$\frac{\partial}{\partial w_i}\left(\rho u_i T\right) = \frac{\partial}{\partial w_i}\left(\frac{K}{Cp}\frac{\partial T}{\partial w_i}\right) + S_h \tag{2.4}$$

The governing equation for different species involved in the reaction model is written as:

$$\frac{\partial}{\partial w_j}\left(\rho D_{i,m}\frac{\partial X_i}{\partial w_j}-\rho u_j X_i\right)+R_{rxni}+S_i=0 \tag{2.5}$$

2.6 Chemical Reaction and Kinetics

The wall surface reaction model is implemented to determine the mass fraction of SO_3, SO_2 and O_2 as a result of sulfur trioxide decomposition: $SO_3 \rightarrow SO_2+0.5O_2$. The chemical reaction is highly temperature and pressure dependent.

Assuming that the reaction is the first order homogeneous reaction (Spewock [68]), the rate equation for the reaction is written as:

$$R_{rxn}=-kC_{SO_3} \tag{2.6}$$

The reaction rate constant (k) is obtained by using the Arrhenius equation (Scott [69]):

$$k = A\,e^{\left(\frac{-E_a}{RT}\right)} \tag{2.7}$$

A platinum catalyst is used to enhance the chemical decomposition. The activation energy (E_a) and pre-exponential factor (A) for the chemical reaction are obtained from the experimental data of (Ginosar [51]). For 1 wt % Pt catalyst pre-exponential factor A is 0.16 $1\cdot s^{-1}$, E_a is 32.67 $kJ\cdot mol^{-1}$. There are both exothermic (Eqn 1.1) and endothermic (Eqn 1.2 and Eqn 1.3) reactions in the mechanism and the heat generated or consumed by these reactions needs to be accounted in the energy equation.

2.7 Structural Analysis

In this research finite element analysis model is created to analyze the induced stresses due to the applied load. The FEA model is divided into smaller components called elements and each element has number of nodes. The Coulomb-Mohr failure criterion is applied to study the safety of factor in the heat exchanger. Since the Coulomb-Mohr failure criterion deals with the state of stress at each point the nodal solution will be used for Coulomb-Mohr failure. From the FEA model it will be possible to extract the nodal solution of the corresponding principal stresses. The output of using the Coulomb-Mohr failure criterion is the factor of safety (SF). The component is considered to be safe if the factor of safety is greater than 1. The Coulomb-Mohr failure theory is calculated based on the ultimate tensile and ultimate compressive strength for brittle materials. The mechanical properties of ceramics change with the changes in temperature and hence this should be incorporated while solving for stress analysis. For the FEA model the temperature distribution for the solid part is imported to ANSYS STRUCTURAL [13] from ANSYS FLUENT [13] by using the fluid-structure interaction (FSI). The variation in ultimate strength of the heat exchanger material with temperature is given by the following equation (Munro [70]). The ultimate tensile strength is given by

$$\sigma_{ut} = 0.0142857T + 200 \text{ MPa} \tag{2.8}$$

where T is the temperature in K. The ultimate compressive strength is given by

$$\sigma_{uc} = -3\sigma_{ut} \text{ MPa} \tag{2.9}$$

The factor of safety is the ratio between the state of stress (A) and the point where the line starting at origin (O) and passing through (A) intersects the Mohr-Coulomb envelope.

$$SF = \frac{OB}{OA} \tag{2.10}$$

The graphical representation of safety factor is shown in Figure 2.14.

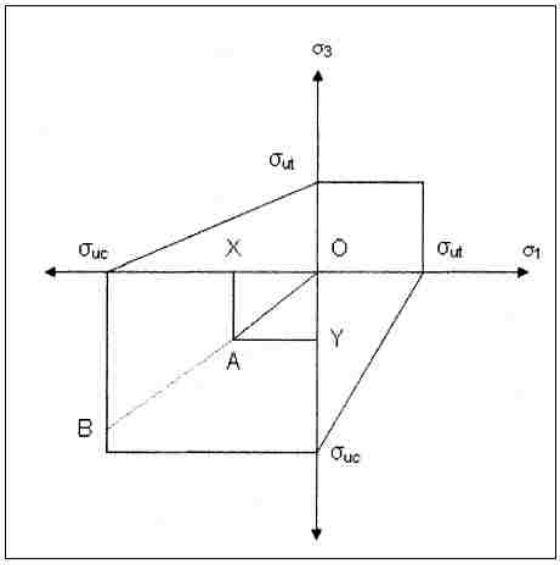

Figure 2.14. Mohr-Coulomb safety factor (Green [71]).

CHAPTER 3

FLUID FLOW AND HEAT TRANSFER

In this chapter fluid flow and heat transfer distribution for high temperature ceramic plate fin heat exchanger is studied. From the study carried out by Ponyavin et al. [48] it has been found that the mass flow rate in all the channels can be made uniform by properly designing the channel manifolds. Hence a single channel model of the helium and the reacting flow is developed to reduce computational load without sacrificing the accuracy of the calculations. The results of fluid flow and heat transfer without the initiation of chemical reactions is discussed in this chapter.

3.1 Material Properties

Silicon carbide (SiC) is used as the material for the solid regions. Density and specific heat are not strongly temperature dependent within the considered temperature (Ponyavin et al [48]) range (973 K-1223 K) and hence they are assumed as constants. The density and specific heat values are 3130 $kg \cdot m^{-3}$ and 1200 $J \cdot kg^{-1} \cdot K^{-1}$. The thermal conductivity of SiC varies with temperature. The fluids used in the current model are sulfur trioxide, sulfur dioxide, oxygen and water vapor. Helium flows inside the hot fluid channel and a mixture of sulfur trioxide, sulfur dioxide, oxygen and water vapor flows inside the cold fluid channel (mixture side). In this chapter there is no chemical reaction taking place inside the cold channel (mixture fluid side). The gas properties of the flow areas do not depend on the temperature significantly. Therefore the properties are taken as constants for the areas with mean temperatures and pressure of 1.5 MPa. The thermal

properties of the gases for the helium and mixture flow channel are calculated from FLUENT and they are shown in Table 3.1

Table 3.1

Thermal properties of gases

Parameters	Helium flow	Mixture flow
Density ($kg \cdot m^{-3}$)	0.591	9.03800
Thermal conductivity ($W \cdot m^{-1} \cdot K^{-1}$)	0.388	0.04184
Specific heat ($J \cdot kg^{-1} \cdot K^{-1}$)	5193	1142.69

3.2 Boundary and Operating Conditions

The thermal boundary conditions for the front and back sides are adiabatic boundary conditions. The boundary conditions on the top, bottom, left and right sides are planes of symmetry. Mass flow rate is the inlet boundary condition and pressure outlet boundary condition is chosen for the outflow boundary. Pressure outlet boundary conditions require the specification of the static gage pressure at the outlet boundary. The inlet mass flow rate for the mixture fluid is $3.148 \cdot 10^{-6}$ $kg \cdot s^{-1}$ and the helium fluid is $1.409 \cdot 10^{-6}$ $kg \cdot s^{-1}$ for a single channel model. The inlet temperature of the hot fluid channel (helium) is 1223.15 K and the cold fluid channel (mixture fluid) is 974.9 K. The Reynolds number obtained for the reacting flow channel is 244 and hence the flow is laminar for all the fin cases studied in this research. Figure 3.1 shows the boundary conditions for the single channel model.

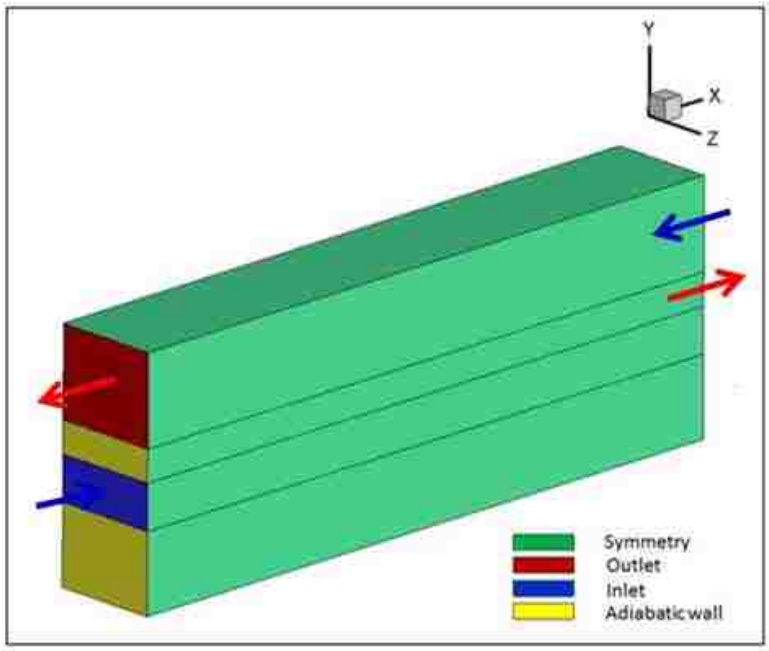

Figure 3.1. Boundary conditions of the single channel model.

3.3 Results and Discussions

The geometry of the model is meshed in ANSYS WORKBENCH mesh generator. Hexahedral elements are used for meshing. The mesh is refined near the walls for both laminar and turbulent flows (two turbulent cases are done for parametric studies) particularly for the cold flow channel with fins. The mesh refinement near the wall helps in calculating the fluid flow and heat transfer properties accurately. The elements of large aspect ratio are found in the bottom solid SiC region. In order to check the mesh dependence on fluid flow and heat transfer properties, a grid independent study was done for all the nine cases of the uniform fin arrangement. From the study, optimum nodes with difference in pressure drop and heat transfer of less than 5% is selected for further study. Around 481,558 cells, 1,496,152 faces and 532,599 nodes are selected for further study for all the cases. The meshing and the grid independent study are shown in Figure 3.2, Figure 3.3 and Figure 3.4, respectively.

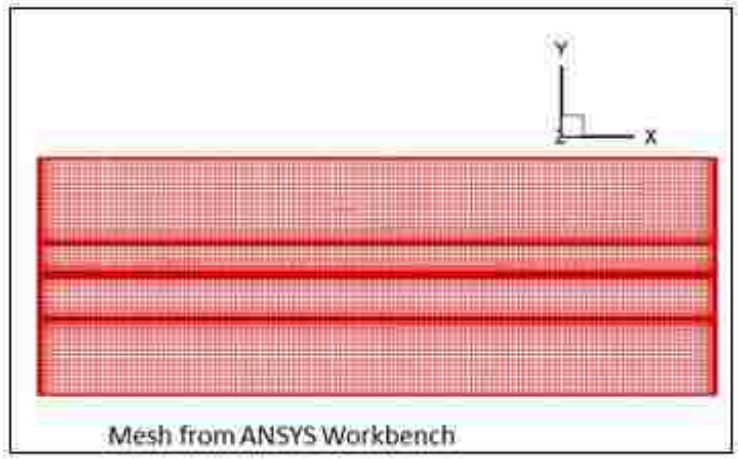

Figure 3.2. Meshing in ANSYS workbench.

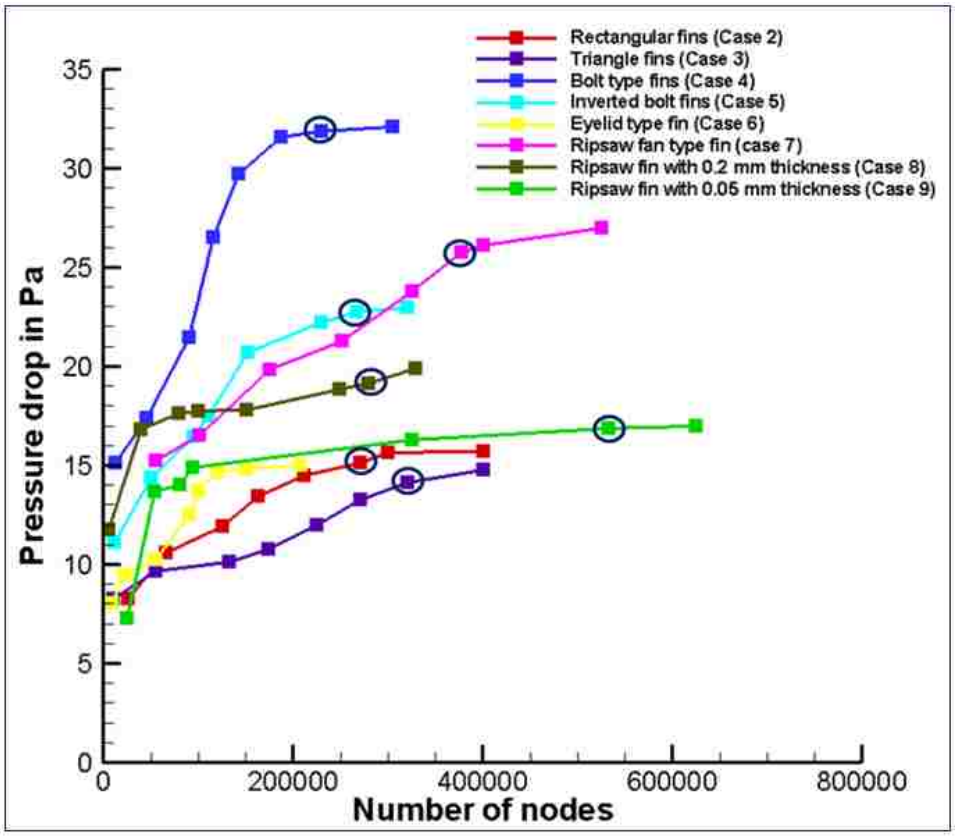

Figure 3.3. Grid independent study for fluid flow results.

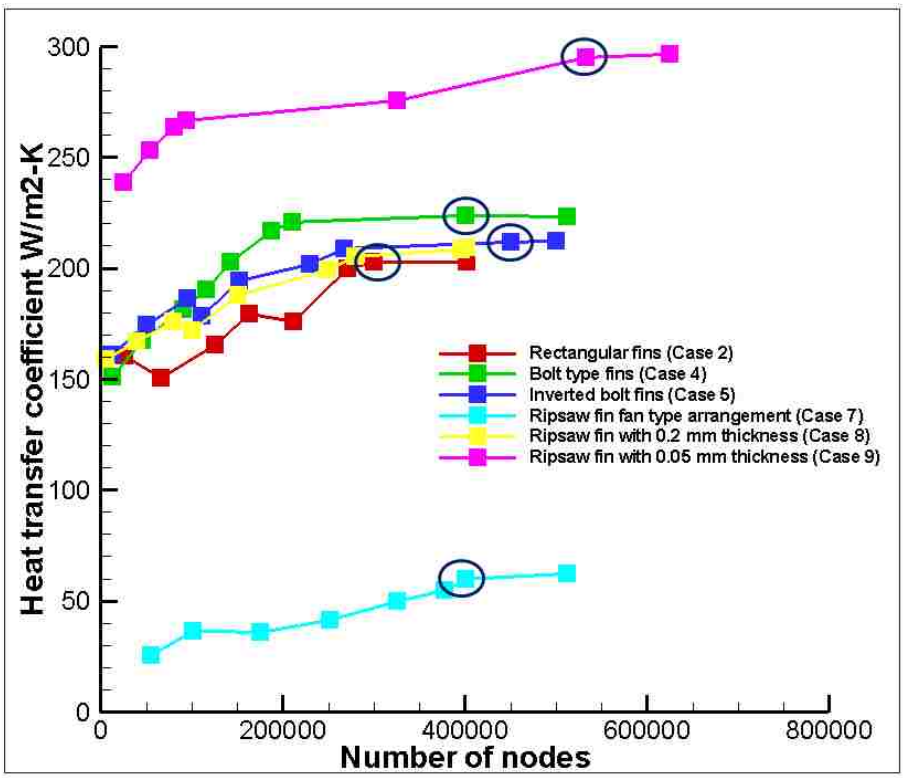

Figure 3.4. Grid independent study for heat transfer results.

In this study fins are not placed near the inlet and the outlet regions of the cold channel in order to avoid backflow and provide an entrance zone. Studies are carried out by increasing the length of the inlet and the outlet parts to 10 times the hydraulic diameter. It is found that the flow becomes fully developed before it reaches the fins and hence the entrance length is taken to be 10 times the hydraulic diameter. Also another study is carried out by increasing the inlet length to 5%, 10% and 15% of the total length of the heat exchanger. It is found that the flow is not fully developed at 5% and it becomes fully developed when it reaches 10%. In this study the entrance length is taken to be 10 times the hydraulic diameter of the heat exchanger. The fins are mostly used to increase the heat transfer by breaking up of the boundary layer. However the fins

increase the pressure drop and the friction factor. Figure 3.5, Figure 3.6, Figure 3.7 and Figure 3.8 show the fully developed velocity profile with 10 times the hydraulic diameter and 10% of total length.

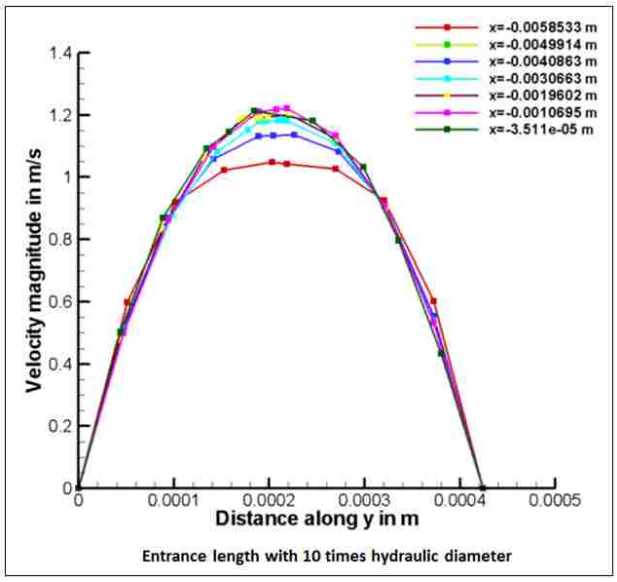

Figure 3.5. Velocity entrance length.

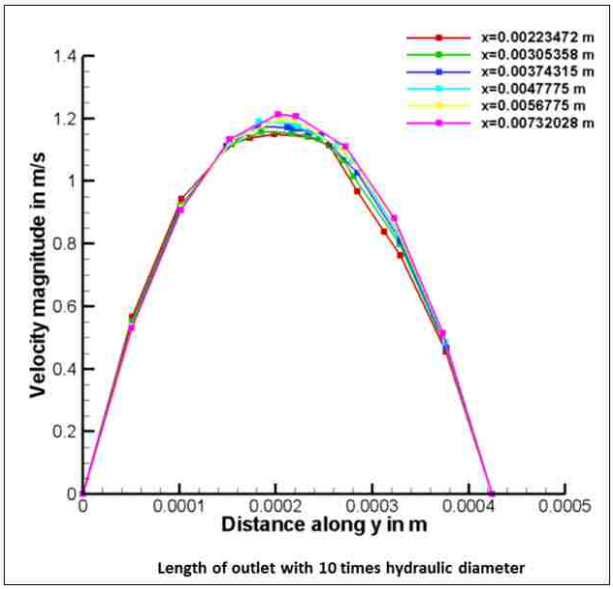

Figure 3.6. Outlet length of the velocity.

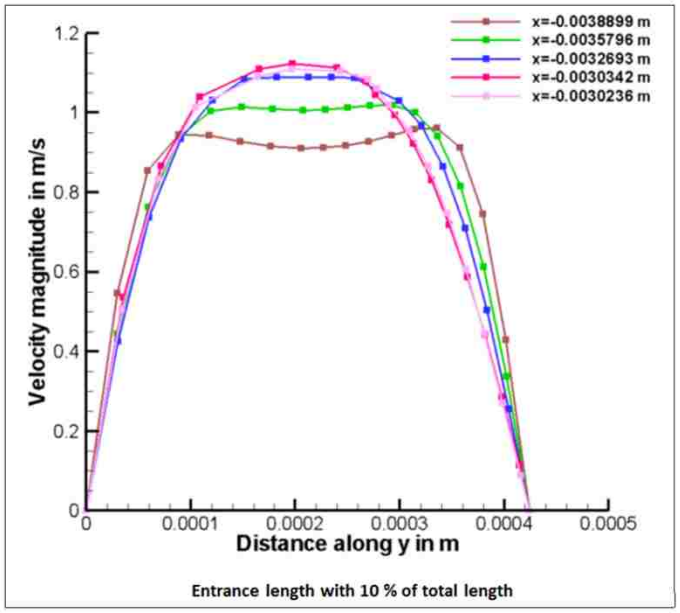

Figure 3.7. Velocity entrance length for 10% total length.

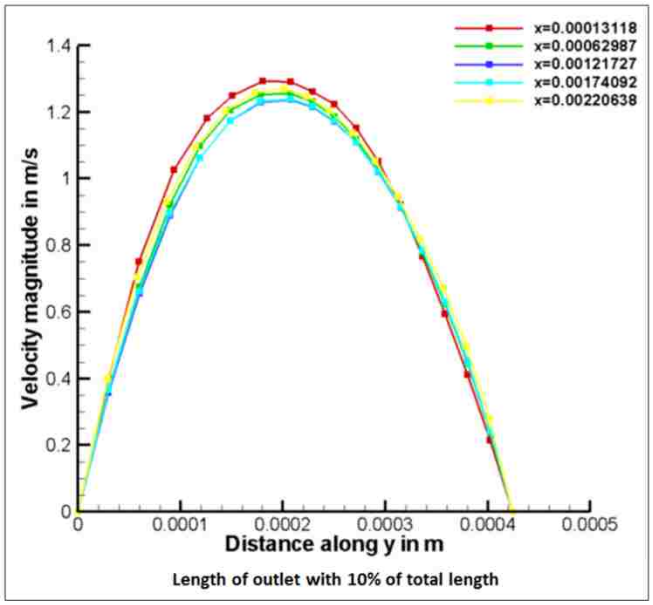

Figure 3.8. Velocity outlet length for 10% of total length.

Physical parameters like the Reynolds number, the average Nusselt number and the heat transfer coefficient are described as follows:

$$\mathrm{Re} = \frac{\rho v D_h}{\mu} \tag{3.1}$$

$$\overline{Nu} = \frac{\bar{h}.\overline{D_h}}{K} \tag{3.2}$$

$$\bar{h} = \frac{q''}{(T_w - T_b)} \tag{3.3}$$

where D_h ($D_h=4A_s \cdot P^{-1}$) is the hydraulic diameter, A_s is the cross-sectional area and P is the wetted perimeter of the cold channel. T_w is the wall temperature, T_b is the weighted average bulk mean temperature of the fluid used to calculate the average Nusselt number and U is the velocity at the inlet of the cold channel. The average bulk mean temperature T_b is calculated by $T_b=(T_i+T_o)/2$ where T_i and T_o are the inlet and outlet temperature of the fluid. For the local Nusselt number T_w and T_b are dependent along the x-direction.

The friction factor, the Colburn factor and the Prandtl number are calculated using the formula shown below:

$$f = \frac{\left(\frac{\Delta P}{L}\right) * D_h}{(0.5 \cdot \rho \cdot U^2)} \tag{3.4}$$

$$j = \frac{\overline{Nu}}{Re \cdot Pr^{\frac{1}{3}}} \tag{3.5}$$

$$Pr = \frac{\mu \cdot C_p}{K} \tag{3.6}$$

3.4 Validation with Published Results

In order to validate the model, the friction factor and the Colburn factor for the selected ripsaw fin design with thickness of 0.00005 m (Case 9) and rectangular fin (Case 2) are compared with the available published data from (Manson [72]). Few assumptions are made during the aforementioned numerical analysis. A friction factor correlation has been proposed by (Manson [72]) for the Reynolds number above and below 3500 based

on the fin passage hydraulic diameter. The flow is laminar and hence the laminar friction factor correlation is used for validating the current model. The correlation equation proposed by (Manson [72]) used for the Reynolds number up to 3500 is given by the following equation.

$$f = \frac{11.8}{\left(\frac{\lambda}{D_h}\right)\left(\frac{GD_h}{\mu}\right)^{0.67}} \tag{3.7}$$

where $\frac{\lambda}{D_h} \leq 3.5$. Figure 3.9 shows the comparison of the numerical results with published data from (Manson [72]) for the friction factor and (Wieting [73]) for the Colburn factor.

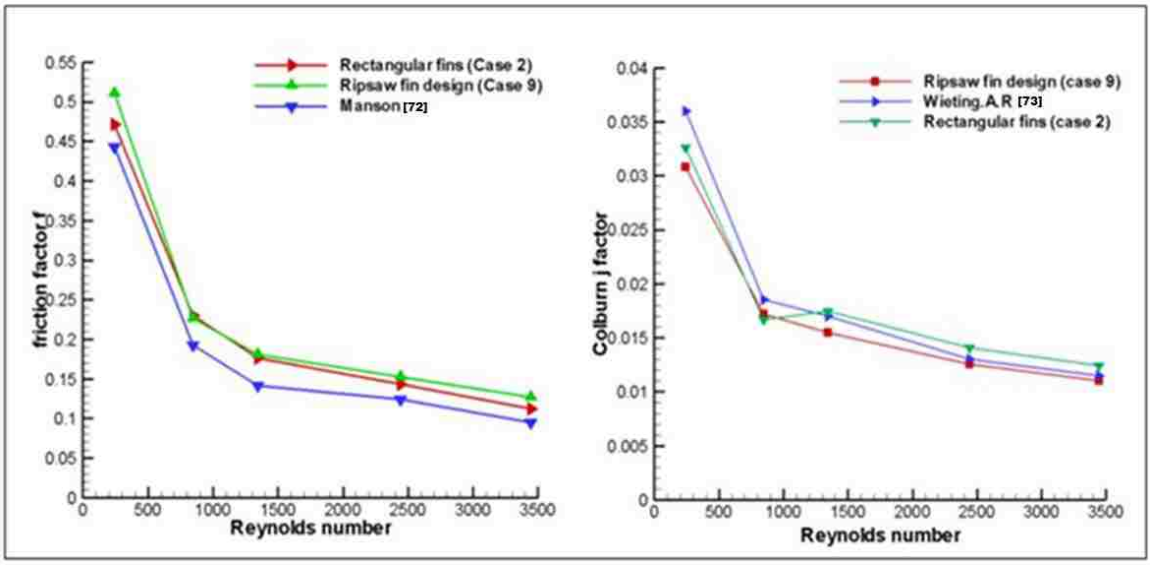

Figure 3.9. Friction factor and heat transfer validation.

The obtained CFD results for the friction factor are in agreement with the published data. The reason for the slight offset is due to the difference in the dimensions of the heat exchanger. In the work done by Manson [72], the dimensions of the

rectangular fins are not exactly same as the dimensions used in this current study. The ratio of length of the fin to the hydraulic diameter is 0.606 in the work done by Manson [72] and 0.6685 in the current study.

The heat transfer results are validated with the empirical correlations obtained for the heat transfer by (Wieting [73]). An empirical correlation equation for the Colburn factor was proposed for the Reynolds number shown below. The equations mentioned below for the Colburn factor are used for validating the obtained numerical heat transfer results.

$$j = 0.483\left(\frac{x}{D_h}\right)^{-0.162}(\alpha)^{-0.184}(Re)^{-0.536} \qquad (Re \leq 1000) \qquad (3.8)$$

$$j = 0.242\left(\frac{x}{D_h}\right)^{-0.322}\left(\frac{t}{D_h}\right)^{0.089}(Re)^{-0.368} \qquad (Re \geq 2000) \qquad (3.9)$$

The numerical results for the Colburn factor agree well with the empirical correlation results from (Wieting [73]) for rectangular (Case 2) and ripsaw fin (Case 9). From Figure 3.9 it can be seen that the numerical results obtained for the high Reynolds number region are in well accordance with the published results and variations of 5 to 10% are found for the low Reynolds number region. Since the numerical results agree closely and follow the same trend further research is carried out for the selected design.

3.5 Uniform Arrangement

3.5.1 Case 1 (Single channel model with no fins)

The heat exchanger with no fins is selected as the baseline design. The Reynolds number calculated based on the hydraulic diameter is 244 and hence laminar flow is used for all the models. The pressure drop obtained for the base case is 8.0 Pa and the friction factor is 0.247. Case 1 has the least pressure drop and friction factor due to the absence

of fins. However the heat transfer rate obtained is also very less. Figure 3.10 shows the contour plot for the pressure and temperature.

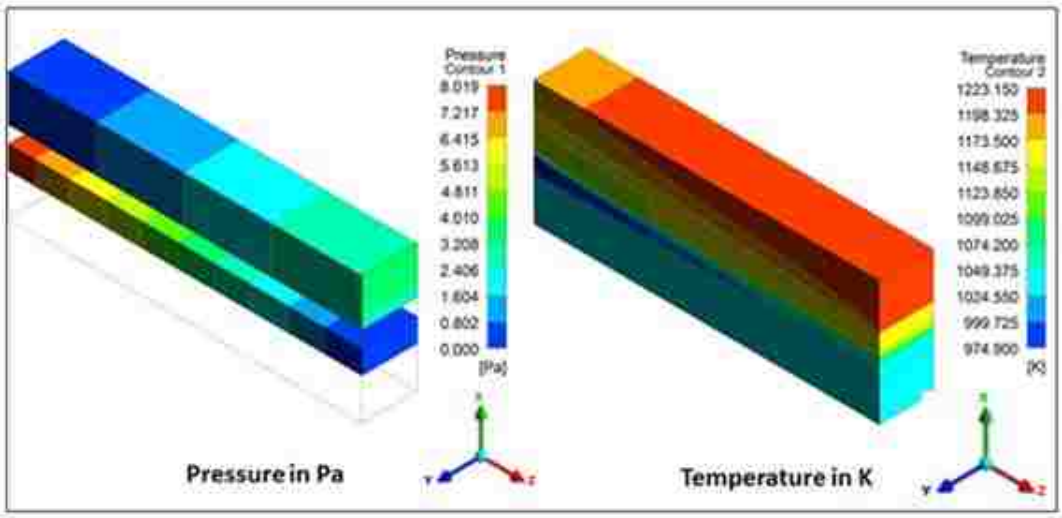

Figure 3.10. Contour of pressure and temperature for single channel model without fins.

The heat transfer surface area is $1.948 \cdot 10^{-5}$ m^2 which is less compared to the other cases. The heat transfer rate of 0.3616 W and the average Nusselt number of 2.312 are obtained for Case 1. For the baseline design the streamlines are always to parallel to the flow direction (x-direction) because of the rectangular geometry of the channel without fins. There are no obstacles found in this case and hence recirculation is not formed on the baseline design case without fins. Figure 3.11 shows the velocity contour and streamline plot for Case 1.

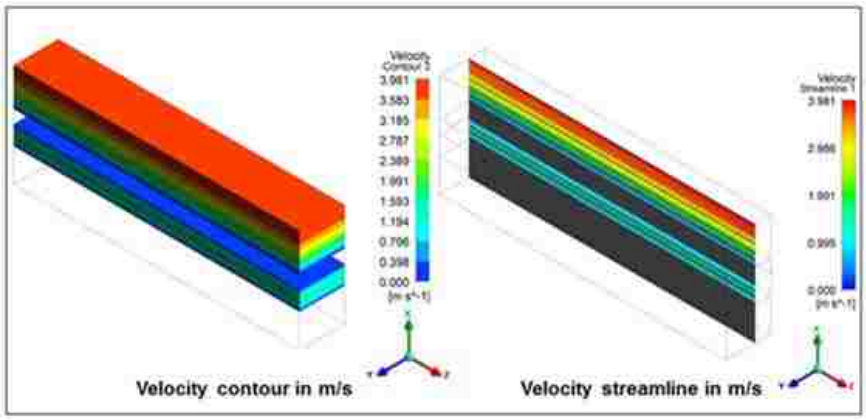

Figure 3.11. Contour and streamline for velocity in m/s for single channel model without fins.

3.5.2 Case 2 (Single channel model with rectangular fins)

The rectangular fins are placed in the reacting channel of the heat exchanger. Six rectangular fins are arranged in a uniform arrangement. The height of the fins is around 70% of the channel height. Due to the presence of fins the pressure drop and heat transfer rate obtained are higher than the base case results. The pressure drop is 20.386 Pa and the friction factor is 0.645. The heat transfer surface area is $2.212 \cdot 10^{-5}$ m^2 and the obtained heat transfer rate is 0.476 W. The obtained temperature plot is similar to the base case. The pressure and velocity plot are shown in Figure 3.12.

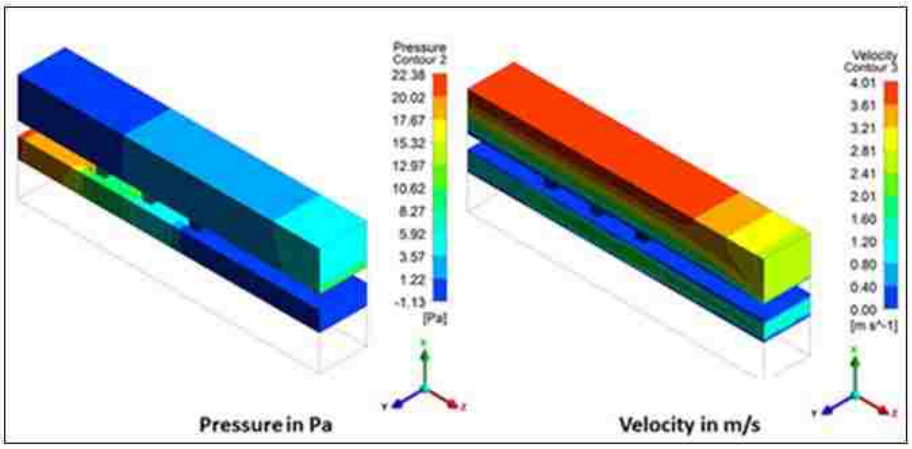

Figure 3.12. Contour of velocity and pressure for single channel model with straight rectangular fins.

The streamline plot along the y-plane for the rectangular fins is shown in Figure 3.13. It can be seen that in the upstream of the obstacles no vortices are formed due to the lower blockage effect produced by the rectangular fins. As the fluid flows towards the fins the boundary layer breaks away from the surface. The fluid is sucked in from behind in the opposite direction. There is a buildup of positive pressure on the front and negative pressure at the back which is called the form drag or pressure drag. The blockage effect is quite moderate and the separation structure formation is very small before the fins. The recirculation in the figure looks asymmetrical due to the position where the slice is taken. The slice is taken at y=0.0032 m.

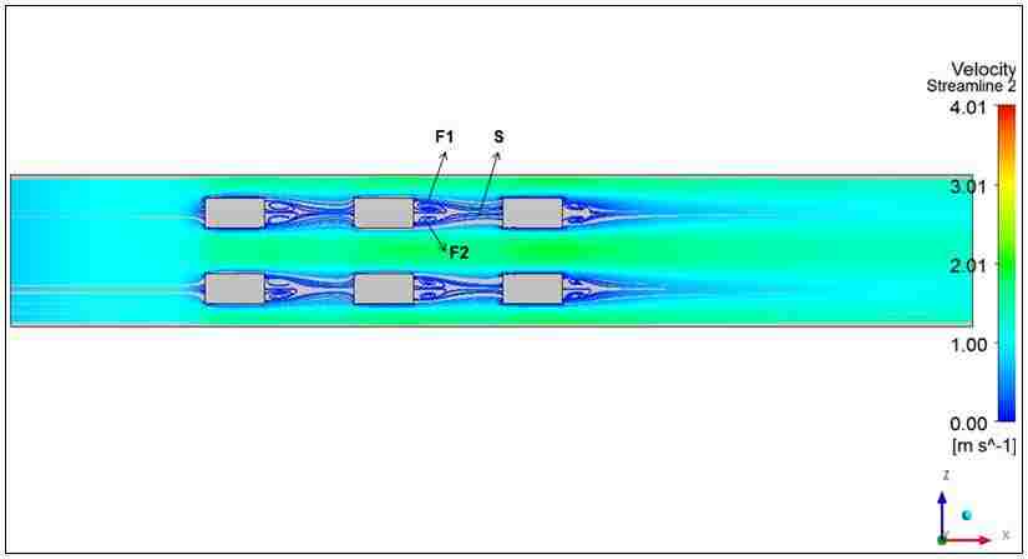

Figure 3.13. Streamline along y-plane for velocity in m/s at y=0.0032 m.

A broad wake region is formed in the downstream of the fins and flow recirculation is found in the wake region. Closer to the fin surface foci F1 and F2 are developed in between the saddle point S showing the interaction between the shear layers and the vortices. This interaction simulates circulatory motion where high rate of fresh fluid flow from the main core flow region gets entrained in the wake flow regions. This entrainment increases the pressure drop and friction factor in the rectangular fins.

Figure 3.14 shows the separation point and the wake region for the single channel model with straight rectangular fins. Separation of the boundary layers occurs whenever the flow tries to decelerate or when the adverse pressure gradient occurs. Due to the formation of the adverse pressure gradient the fluid separates from the surface and a recirculating region is created in the wake.

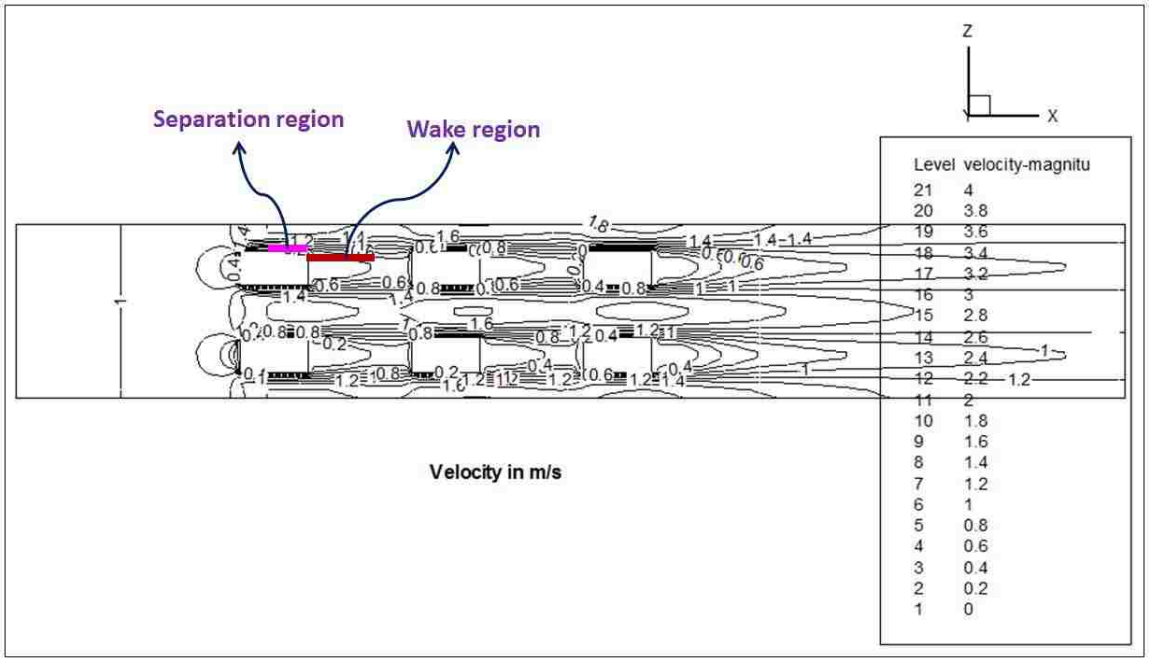

Figure 3.14. Velocity along y-plane in m/s for single channel model with straight rectangular fins.

A three-dimensional recirculation flow can be found in the wake region where it extends over almost the whole channel length and height as shown in the Figure 3.15. The recirculation occurs behind each fin and flow becomes continuous in the downstream of the third fin. The recirculation length is located at about 0.00166 m and the reattachment of the shear layer is located at a distance of 0.00213 m

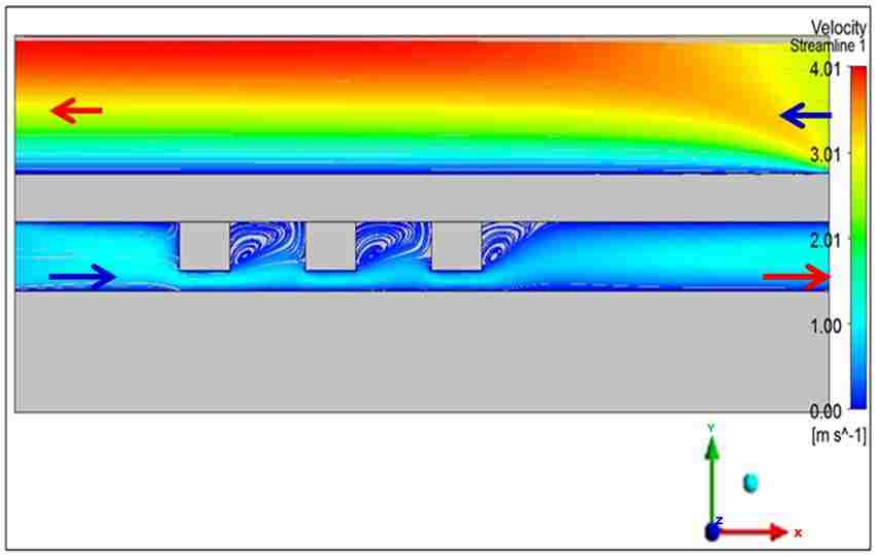

Figure 3.15. Streamline along z-plane for velocity in m/s.

The fluid flow initially has no recirculation and the pressure difference in the fluid flow is responsible for accelerating the fluid. Since both $\nabla^2\omega = 0$ and $\omega \cdot \nabla v = 0$ the vorticity equation for the flow before reaching the fins will be $\frac{D\omega}{Dt} = 0$. The fluid particle receives its initial rotation by viscous diffusion. The velocity decreases as the fluid flows from the inlet and it reaches a minimum at P1 where the first fin start. Figure 3.16 shows the pressure and velocity distribution for the single channel model with straight rectangular fins.

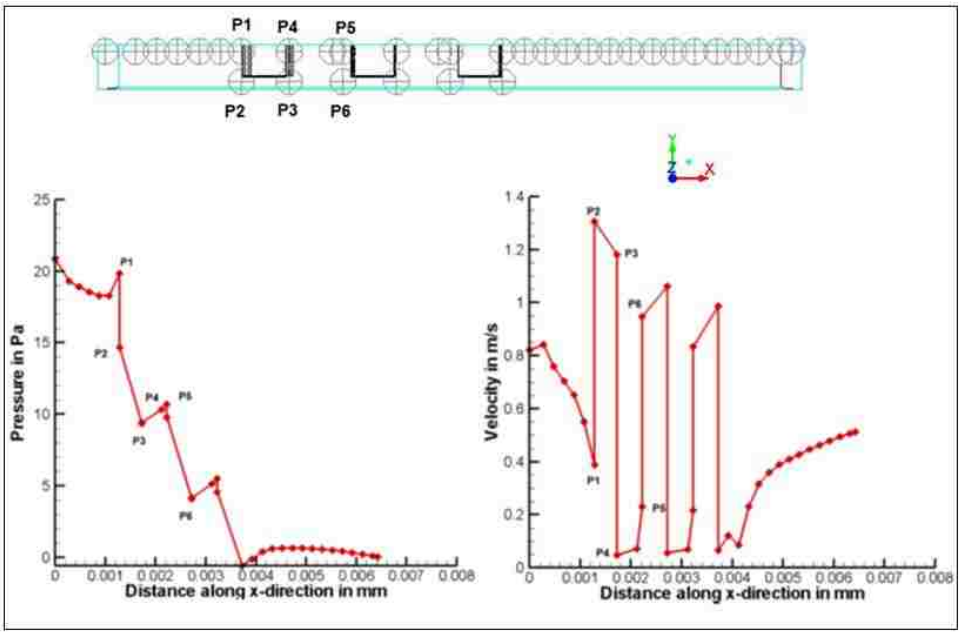

Figure 3.16. Velocity and pressure along the mixture channel for the single channel model with straight rectangular fins.

The velocity is maximum at P2 where the fluid travels without obstacles. Since P2 is placed before the first fin, the velocity is maximum compared to other points. After the first fin the velocity decreases as the fluid flows through P3. In the wake region there is three-dimensional recirculation and hence the velocity decreases at P4. The velocity again increases and becomes maximum at the end of second fin. The process repeats till the end of the third fin. The velocity then increases without much fluctuation till the fluid reaches the outlet.

Similarly the pressure fluctuations are less till the fluid reaches the fin and it becomes maximum before the first in at P1. The pressure decreases at place where there are no obstacles and it becomes high at the end of the first fin. The pressure again decreases at P6 before the start of the second fin. The process repeats till the end of the

third fin and becomes stable thereafter.

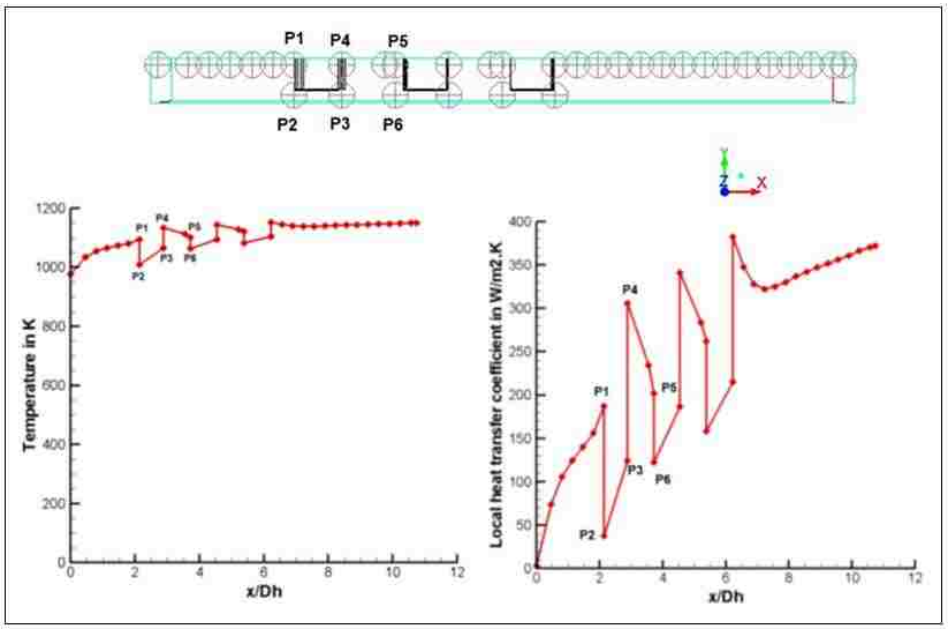

Figure 3.17. Local temperature and heat transfer coefficient for single channel model with straight rectangular fins.

From Figure 3.17 it can be seen that the temperature and local heat transfer coefficient increases till the flow reaches P1. The points which are closer to the top surface have high temperature and the heat transfer coefficient. Heat is convected from the hot helium fluid to the solid wall and the heat is conducted from the solid wall to the top surface of the fluid wall. Hence the points which are near the wall have high temperature and heat transfer coefficient values. At points P2, P3, P6 etc. the temperature and the heat transfer coefficient are less due to the fluid mixing and the temperature dissipation. Another reason is that these points are away from the hot wall surface. Due to the recirculation formed behind the first fin the temperature and heat

transfer coefficient at P5 is less compared to P4. After the third fin the temperature profile becomes stable without much fluctuation.

3.5.3 Case 3 (Single channel model with triangular fins)

The obtained fluid flow and heat transfer results for triangular fins are similar to the rectangular fins. The heat transfer surface area of triangular fin is slightly lesser than rectangular fins. The front tip of the triangular fin is slightly curved to prevent skewness and to decrease the friction factor. The obtained pressure drop and friction factor for the triangular fins are 16.84 Pa and 0.530 respectively. The heat transfer surface area is $2.169 \cdot 10^{-5}$ m^2 and the obtained heat transfer rate is 0.472 W. Figure 3.18 shows the pressure and temperature distributions for the triangular fins.

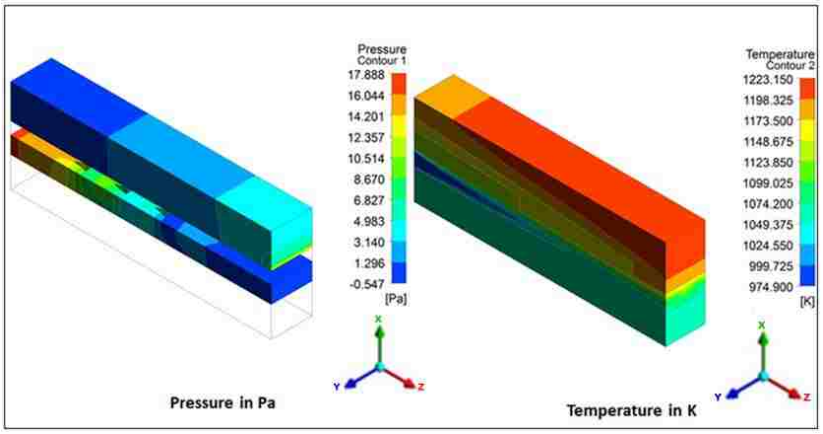

Figure 3.18. Pressure and temperature contours for single channel model with straight triangular fins.

It is found that similar to rectangular fins, a strong recirculation zone is formed in the wake region. Due to the triangular shape of the fin no horseshoe vortex is formed at the front end of the fins. The recirculation formed is similar to the rectangular fins and

they have circulatory motion which entrains the fluid flowing from the main flow region. Figure 3.19 shows the velocity vector plot.

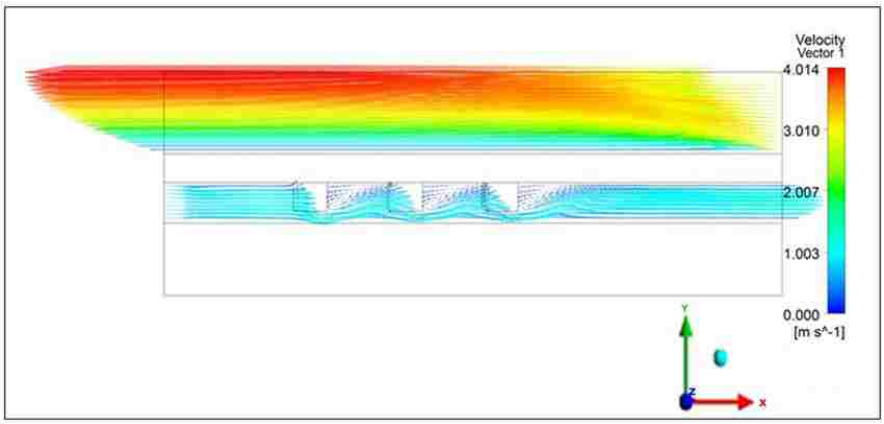

Figure 3.19. Velocity vector plot in m/s at z=0.0047 m for single channel model with straight triangular fins.

Figure 3.20 shows the velocity streamline plot for the triangular fins. Since there are no fins placed in the hot fluid channel no vortices are formed and the streamlines are parallel to the fluid flow direction. It can be seen that the velocity is around zero near the top and bottom wall due to no-slip boundary condition. Due to the shape of the triangular fins, the recirculation region does not occupy the full space between the fins as found in rectangular fins. Hence the pressure drop and the friction factor obtained are less than the triangular fins. The heat transfer coefficient obtained is similar to the rectangular fins. The recirculation region of the triangular fins is located at 0.0016 m and the reattachment region is located at 0.0022 m.

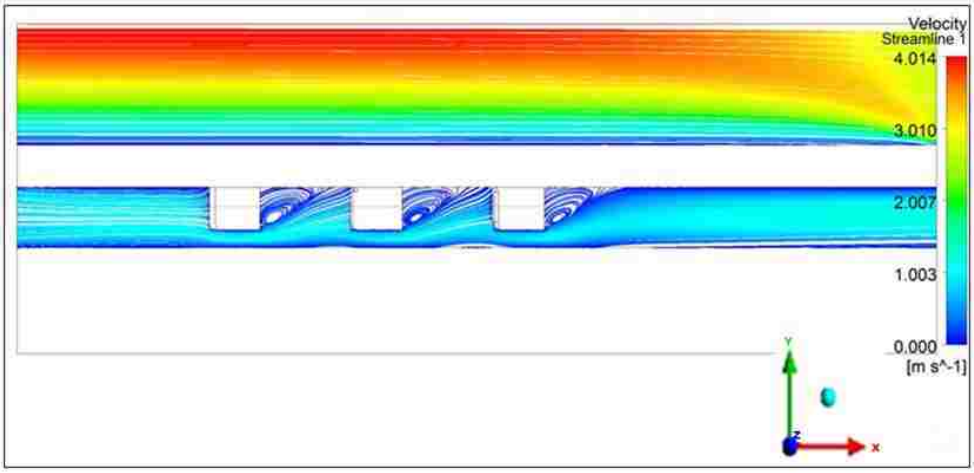

Figure 3.20. Velocity streamline in m/s for single channel model with straight triangular fins at z=0.0047 m.

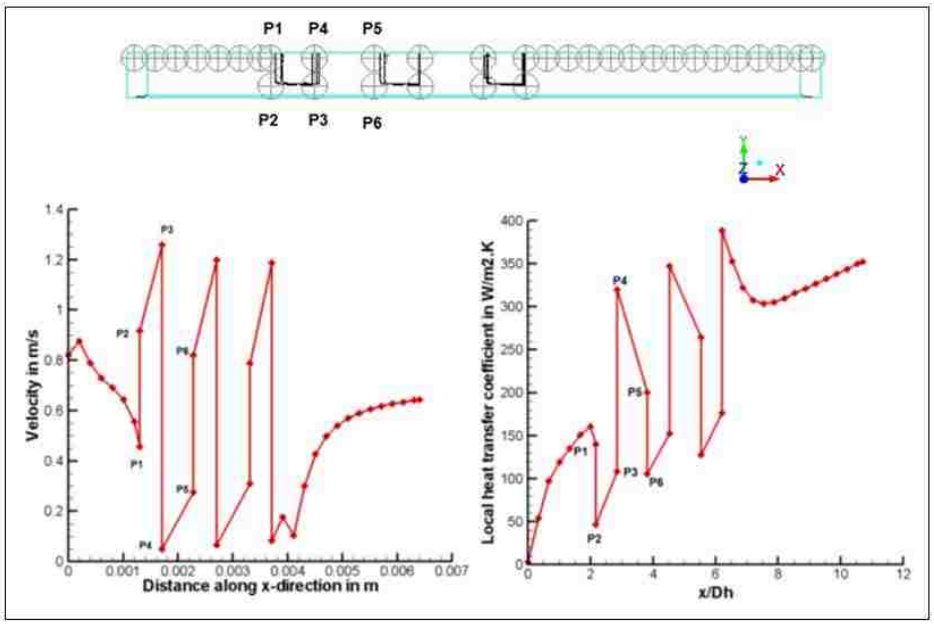

Figure 3.21. Velocity and local heat transfer coefficient plot for single channel model with triangular fins.

Figure 3.21 shows velocity and local heat transfer coefficient plot for the triangular fins. The velocity decreases along the flow direction and it reaches minimum

at P1 before the start of the fins. At this point the pressure is high and hence the velocity is low. The velocity increases from P1 to P2 as there is no obstacle for the fluid flow path. The velocity further increases and reaches maximum at P3. In the wake region recirculation is formed and hence velocity at P4 reaches minimum and then increases along P4, P5 and reaches maximum at the next point. At P4 the pressure is very high due to recirculation. The process repeats till the end of the third fin and thereafter the velocity increases without much fluctuation as the fluid progresses towards the outlet. The local heat transfer coefficient increases from the inlet and it reaches maximum as the fluid reaches the first fin. Similar to the rectangular fins the heat transfer coefficient is high near the hot solid wall (P1, P4, P5 etc.) and low at the points away from the wall (P2, P3 P6 etc.).

3.5.4 Case 4 (Single channel model with bolt fins)

Bolt type fins are selected to enhance the heat transfer in the single channel model of the heat exchanger. The obtained pressure drop for bolt fins is 22.24 Pa and the friction factor is 0.7002. The heat transfer surface area is $2.2119 \cdot 10^{-5}$ m^2 and the average heat transfer coefficient is 229.63 $W/m^2 \cdot K$. The average Nusselt number is 3.283 and the obtained Colburn factor is 0.017. Due to the shape of the fins large pressure drop and friction factor are obtained. The bolt type fins have larger heat transfer surface area than rectangular and triangular fins. Figure 3.22 shows the contour for pressure and velocity of bolt fins.

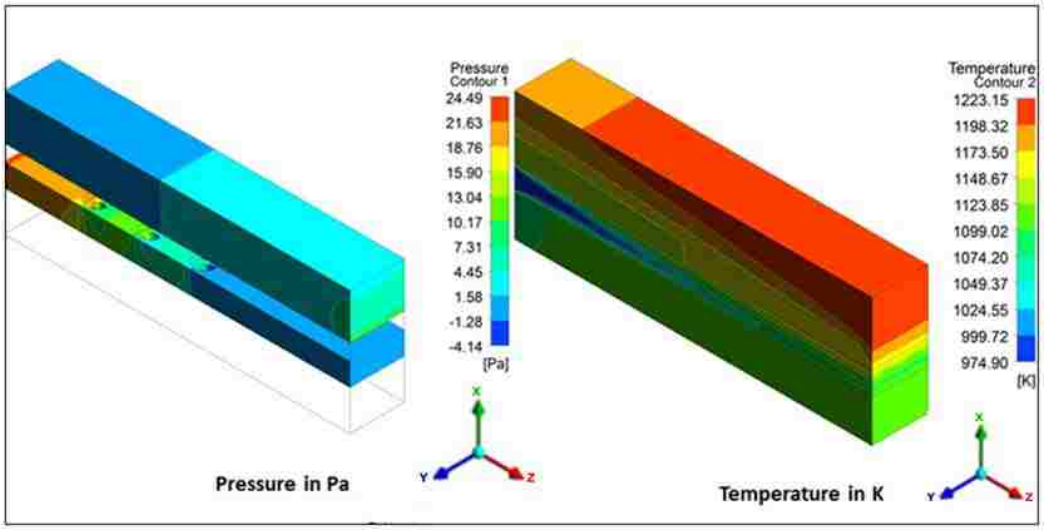

Figure 3.22. Pressure and velocity contour for single channel model with straight bolt fins.

At very low Reynolds numbers no separation occurs. When the Reynolds number increases the wake becomes unstable and gives rise to the phenomenon of vortex shedding. The boundary layer over the cylinder surface will separate due to adverse pressure gradient imposed by the divergent geometry at the rear side of the cylinder. The boundary layer formed along the cylinder has a significant amount of vorticity. This vorticity is fed into the shear layer formed downstream of the separation point and causes the shear layer to roll up into a vortex. Similarly a vortex rotating in the opposite direction is formed in the other side of the cylinder. The recirculation region formed behind the cylinder is located at 0.00105 m and the reattachment length is located at 0.00206 m. Figure 3.23 shows the velocity streamline for the single channel model with inverted bolt fins and formation of twin vortex street in the near wake.

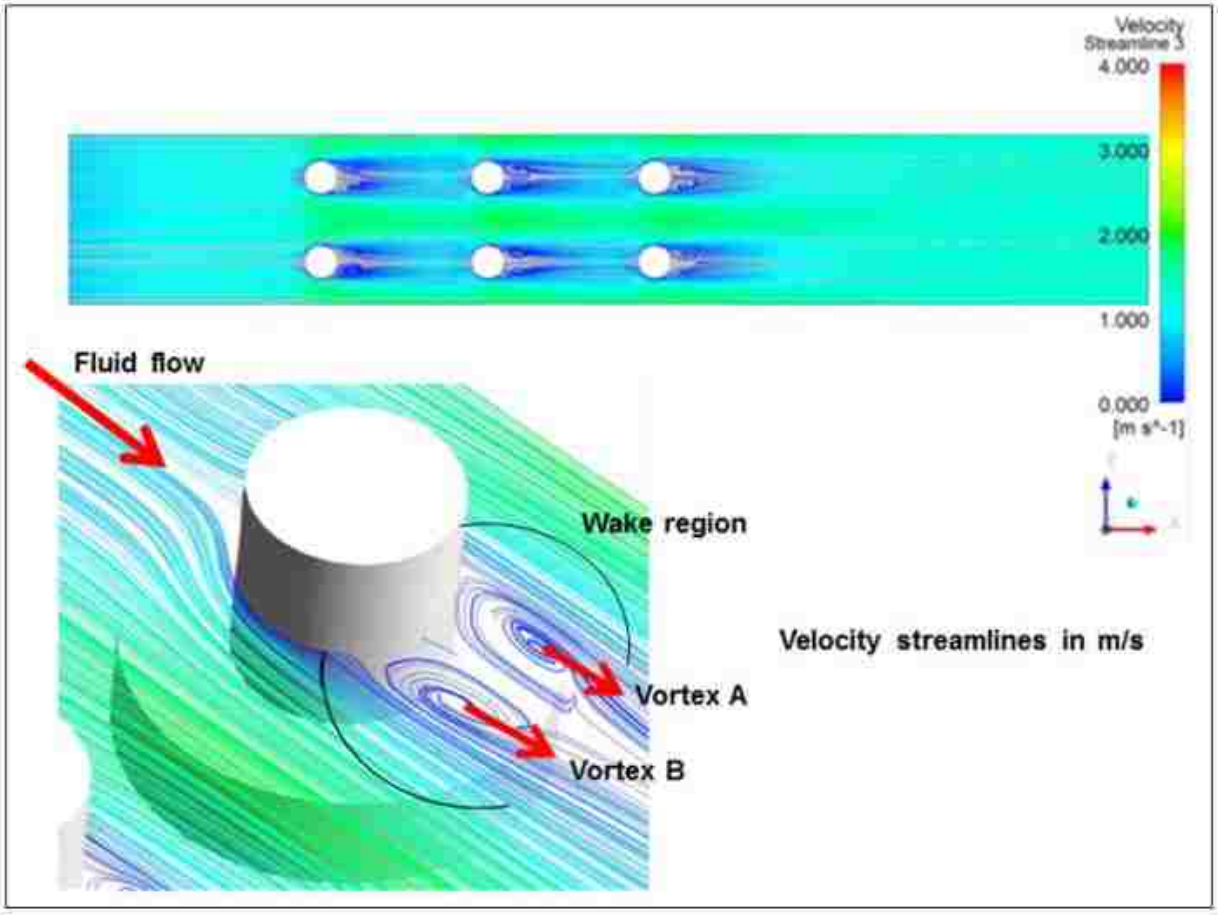

Figure 3.23. Velocity streamline for the top cylinder along the y-plane at y=-0.00015 m.

Figure 3.24 shows the streamline for the bottom cylinder along the y-plane. Similar to the top cylinder twin symmetrical vortices are formed. The influence of aspect ratio i.e., the ratio of cylinder length (H) to characteristic width (d) on the near wake plays an important role in vortex shedding. It has been found that for short obstacle $H/d \leq 4$ the free-end shear layer reattaches to the wall. The bottom cylinder has an aspect ratio of 4 and the top cylinder has an aspect ratio of 1 and the reattachment of shear layer to the wall can be seen in Figure 3.24.

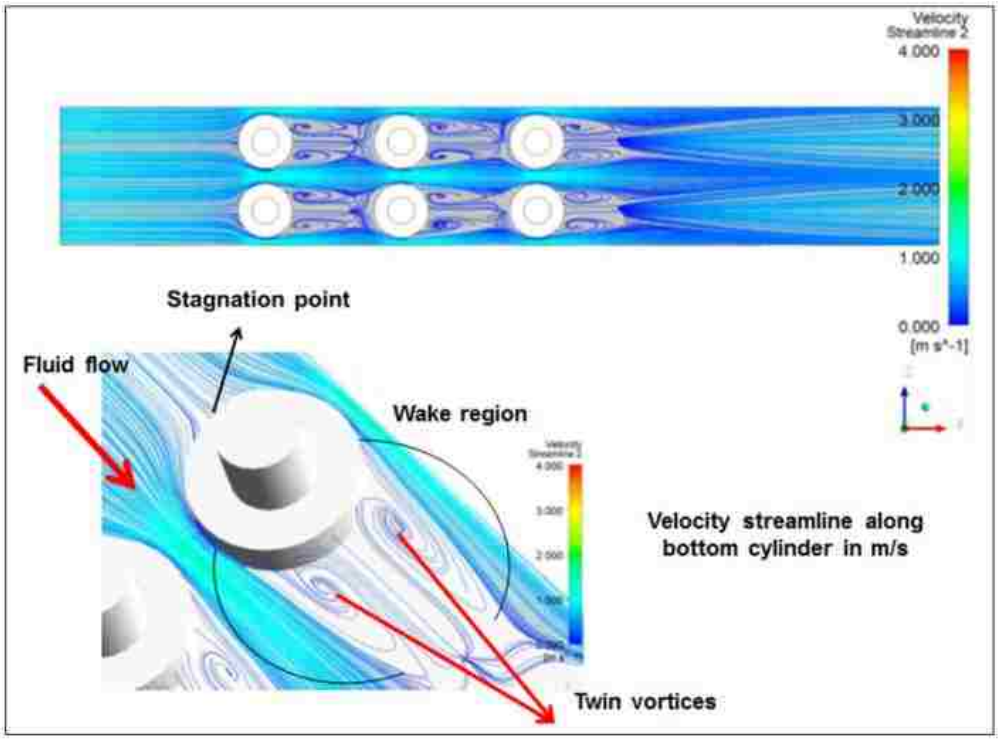

Figure 3.24. Velocity streamline for the bottom cylinder along the Y-plane at y=0.000112 m.

Three-dimensional recirculation is found at the end of each bolt fin. The recirculation occupies the entire height of the fins and more than three-fourth of the channel distance. The velocity is very low near the fins and zero at the no-slip wall boundary. Figure 3.25 shows the streamline and velocity vector along the z-direction.

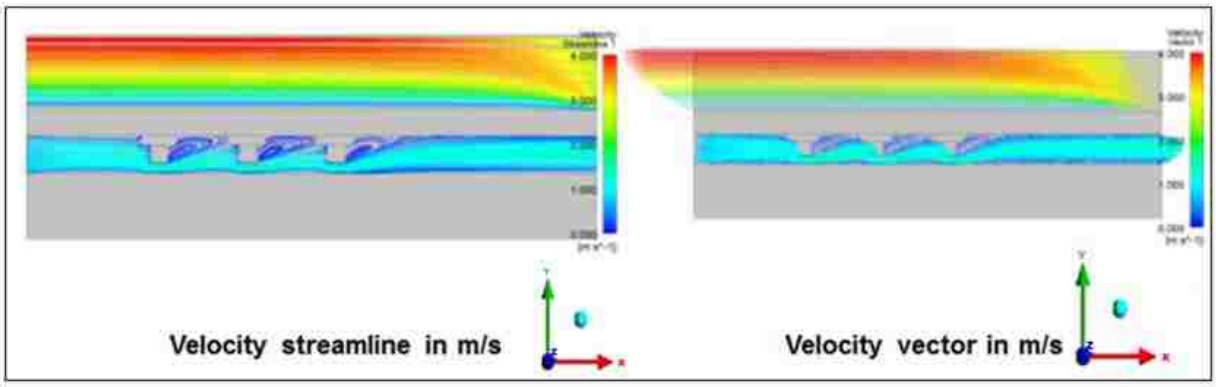

Figure 3.25. Velocity streamline and vector distribution in m/s along the z-direction at $z=-1.17\cdot10^{-5}$ m.

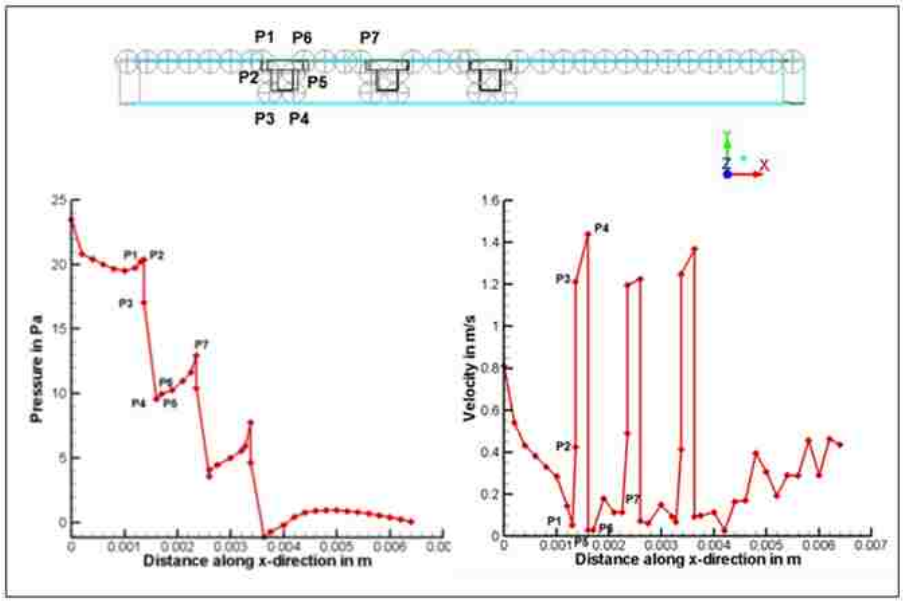

Figure 3.26. Velocity and pressure plot for single channel model with straight bolt fins.

Figure 3.26 shows the velocity and pressure plot for the bolt fins. There is no big fluctuation in the pressure distribution until the fluid reaches the fins. The pressure becomes high at the stagnation point P1, P2 and gradually decreases along the front half of the cylinder. The velocity starts increasing along the front half of the cylinder and

becomes maximum at P4. At this point the pressure is minimum. The pressure starts to increase in the rear half of the cylinder and the particle now experiences an adverse pressure gradient. Consequently the flow separates from the surface creating a recirculating region behind the cylinder called wake. At the rear end of the cylinder the velocity decreases and again it starts to increase after P7. The process repeats till the end of the third fin. Due to the bolt shape of the fin the velocity distribution is not uniform. As a result of this high pressure drop is obtained.

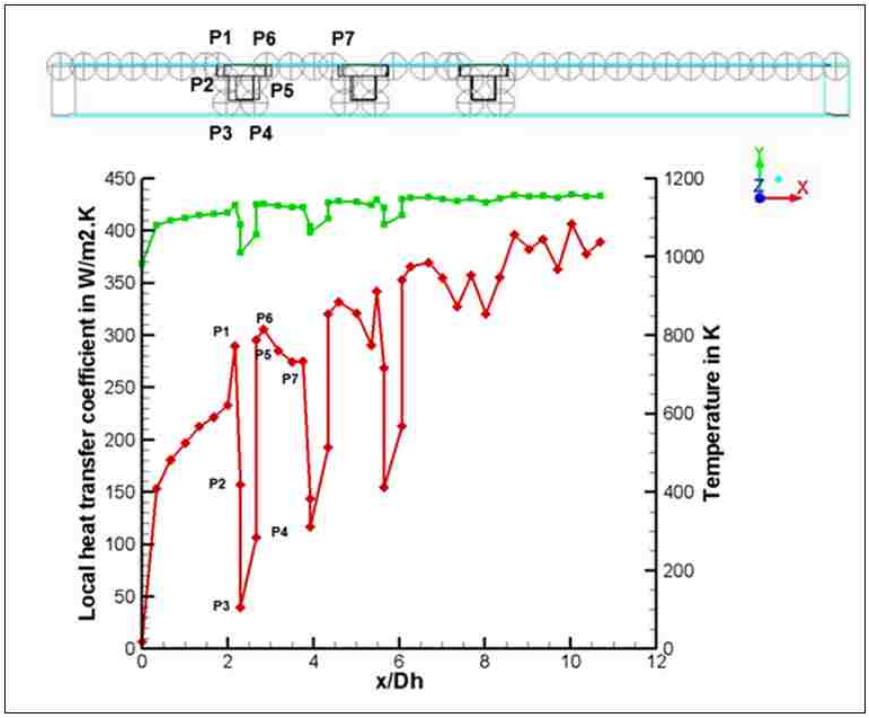

Figure 3.27. Temperature and local heat transfer coefficient for single channel model with straight bolt type fins.

Figure 3.27 shows the temperature and local heat transfer coefficient of bolt type fins. The local heat transfer coefficient and temperature increases gradually and it

becomes maximum at P1 before the start of the fins. The temperature and heat transfer coefficients are high at points which are closer to the hot solid wall. Temperatures at points P2 and P5 are in between P1 and P3. At a distance away from the wall and heat dissipation the temperatures at point P3 and P4 are less. The obtained heat transfer coefficient for the bolt fin is higher compared to the rectangular and triangular fins due to increased heat transfer surface area and recirculation between cylinders.

3.5.5 Case 5 (Single channel model with inverted bolt fins)

The inverted bolt type fin has the same geometry as bolt type fins but is attached to the solid wall on the reverse side. The height of the smaller and larger cylinder is 0.00015 m. The heat transfer surface area of the inverted bolt fins is $2.2873 \cdot 10^{-5}$ m^2 which is higher than bolt type fins. Due to the increase in the cylinder height and the inverted shape the pressure drop and friction factor are high compared to the above mentioned four fins. The obtained pressure drop is 31.4 Pa and the friction factor is 0.988. There is an increase in heat transfer surface area and the average Nusselt number of 3.318 is obtained. A horseshoe vortex is formed around each fin. One of the major features of this complex flow is the horseshoe vortex which loops around the cylinder and gradually trails off. The vortex next to the wall continuously entrains more fluid as it proceeds around the cylinder and downstream. Figure 3.28 shows the pressure contour and velocity streamline along the z-direction.

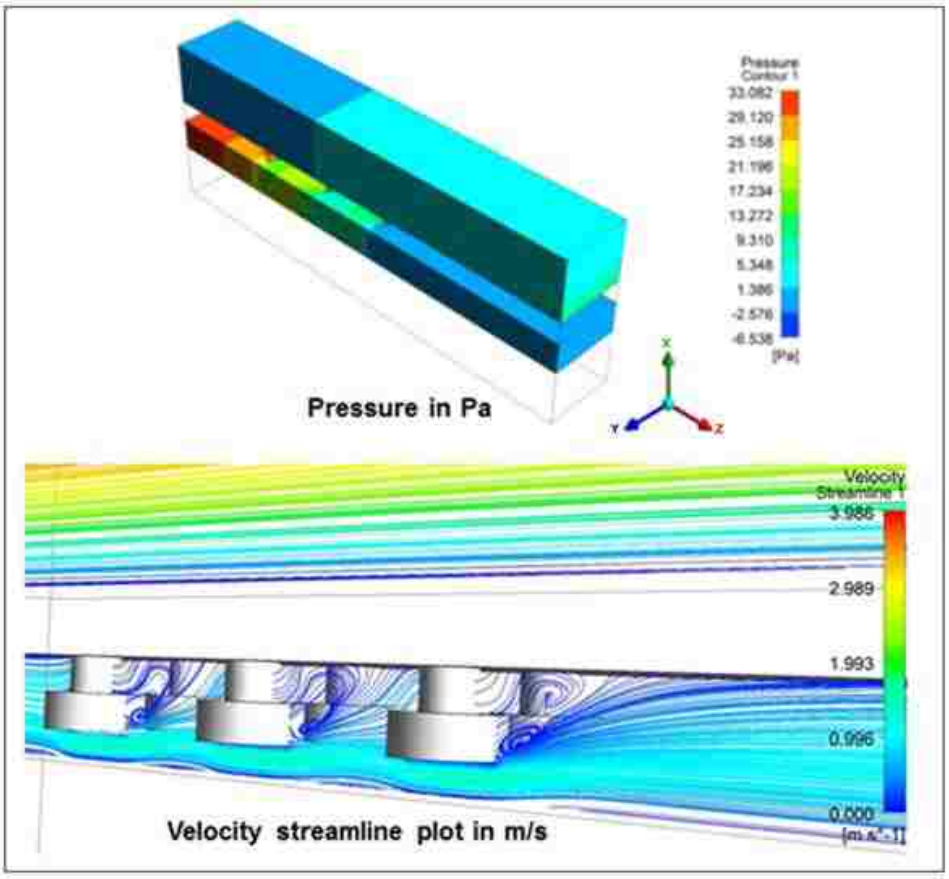

Figure 3.28. Pressure contour and velocity streamline for single channel model with straight inverted bolt fins at z=-0.0002 m.

Figure 3.29 shows the velocity streamline for large cylinder along the y-plane. The fluid flows uniformly until it reaches the fins and boundary layer separation starts at the origin of the fins. Horseshoe vortex is formed on the sides leading to the vortex shedding at the wake of the cylinder. Unlike the bolt fins it is found that the recirculation which is formed at the rear of the cylinder is not symmetrical. One reason for this formation is due to the weak incoming flow which is not strong enough to produce more recirculation. Since the aspect ratio H/d of the large cylinder is around 2.666 (H/d≤3~4) the shear layer formed reattaches to the wall at the rear end of the cylinder. The

recirculation zone is located at 0.00148 m and the reattachment region of the shear layers is located at 0.00216 m.

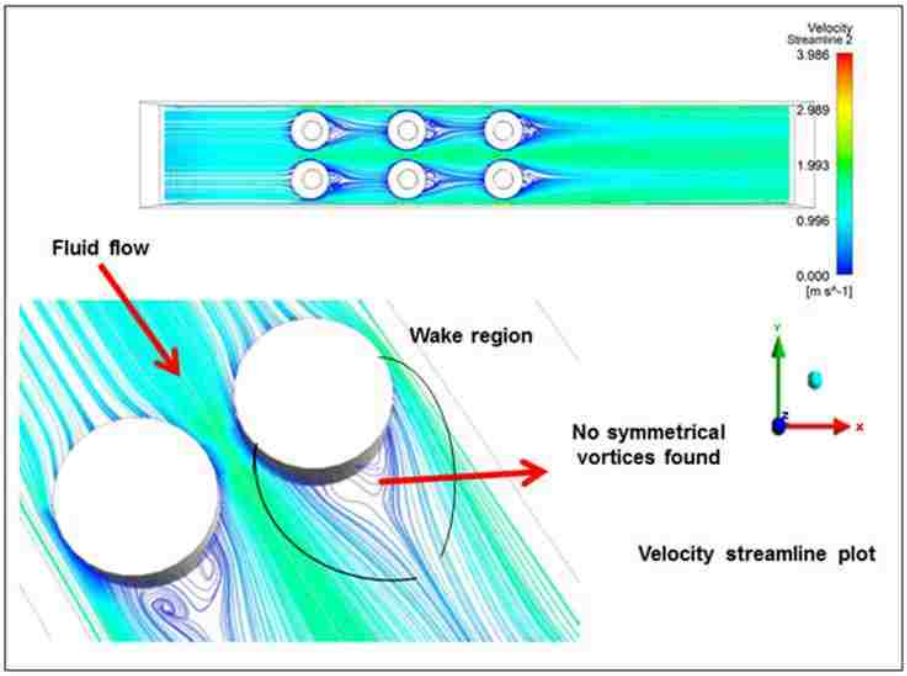

Figure 3.29. Streamline for the large cylinder along the y-plane at y=-0.00014 m for single channel model with straight inverted bolt fins.

Figure 3.30 shows the velocity streamline for the small cylinder. It can be found that after the boundary layer separation vortex shedding takes place. Symmetrical twin vortices are formed at the rear of the cylinder. Here vortex A rotates in the clockwise direction and vortex B rotates in the anticlockwise direction. The aspect ratio is H/d=1.333 and the shear layer reattaches at the rear end of the first fin or at the beginning of the next fin.

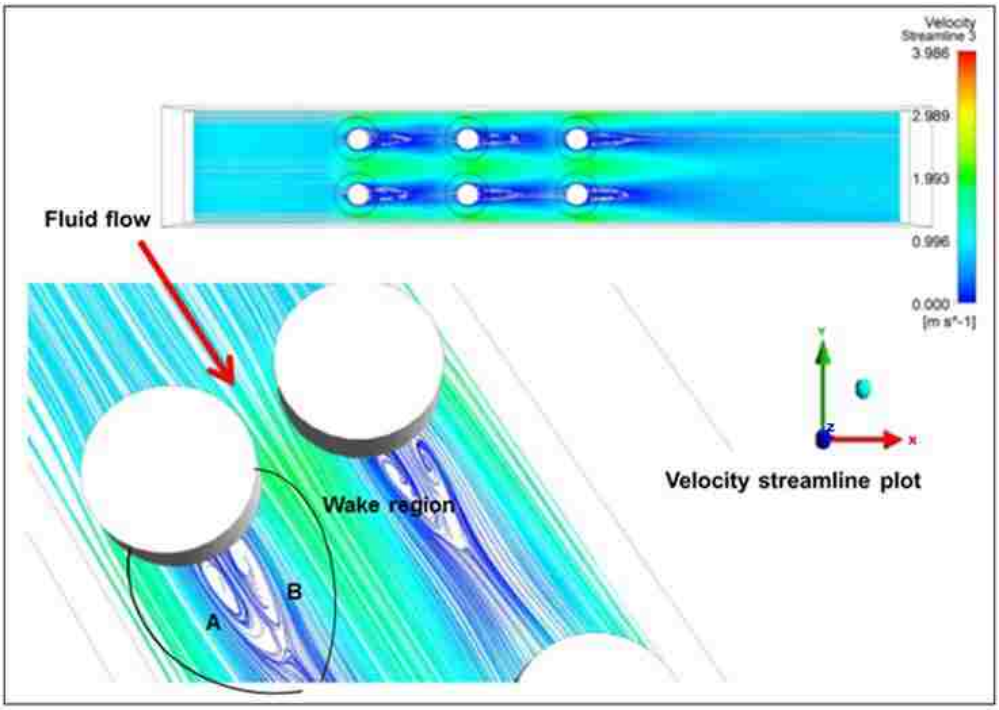

Figure 3.30. Streamline for the small cylinder along the y-plane at y=-1.336·10^{-6} m.

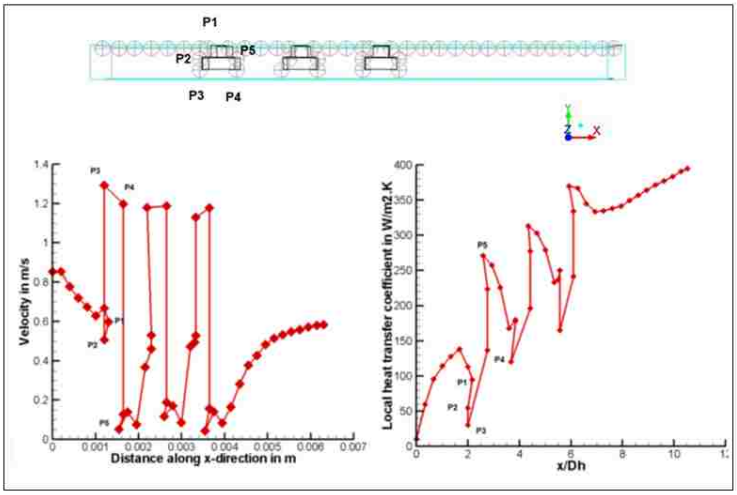

Figure 3.31. Velocity and local heat transfer coefficient for single channel model with straight inverted bolt fins.

Figure 3.31 shows the velocity and local heat transfer coefficient plot for inverted

bolt fins. It is noticed that for the cylindrical fins, three induced vortices influence fluid flow and heat transfer. They are flow separation/reattachment, downward/upward flow and vortex shedding. Pressure and velocity does not fluctuate much from the inlet to the fins origin. At the stagnation point P2, the pressure is high and the velocity is low. The pressure decreases and the velocity increases as the fluid flow around the sides of the cylinder. When the fluid reaches the rear of the cylinder, the pressure starts to build up in the wake region due to adverse pressure gradient. Hence the velocity decreases at P5 and the pressure increases. The process repeats till the end of the third fins. The heat flux is given by the following equation:

$$q'' = h\Delta T \tag{3.10}$$

The heat flux increases with increase in the heat transfer coefficient. The heat flux is high at the upper wall and it decreases at points P3, P4, etc. The local heat transfer coefficient increases from the inlet and it reaches minimum at P3. As the heat flux is higher near the hot wall higher heat transfer coefficient is obtained at points closer to the hot wall. The heat transfer coefficient decreases at points away from the wall where the temperature difference is high.

3.5.6 Case 6 and Case 7 (Single channel model with eyelid type fin and ripsaw fan type fin)

Sharp elliptical or eyelid type of fin is selected for Case 6 and ripsaw type of finis selected for Case 7. Due to the streamlined nature of the fins of Case 6 the flow is smooth and no recirculation is formed. Moderate heat transfer and pressure drop are obtained from this fin arrangement. The ripsaw fins are arranged in a circular shape like a fan as shown in Case 7. This arrangement of the fins has the highest surface area

density of all the cases. The heat transfer obtained is small due to the formation of primary vortices near each fin ends and the solid wall. In the first circular fin, a vortex is formed between the fin and the solid boundary surface. This vortex stagnates the flow in the corner due to the high pressure and low velocity region which leads to decrease in temperature. Due to the stagnation the velocity of the flow also reduces around the corners thus decreasing the heat transfer. This process repeats for other fins and at the end of the third fin a horseshoe vortex is formed where the boundary layer undergoes three-dimensional separation due to the adverse pressure gradient produced by the fins. The streamline for Case 6 and Case 7 are shown in Figure 3.32 and Figure 3.33, respectively.

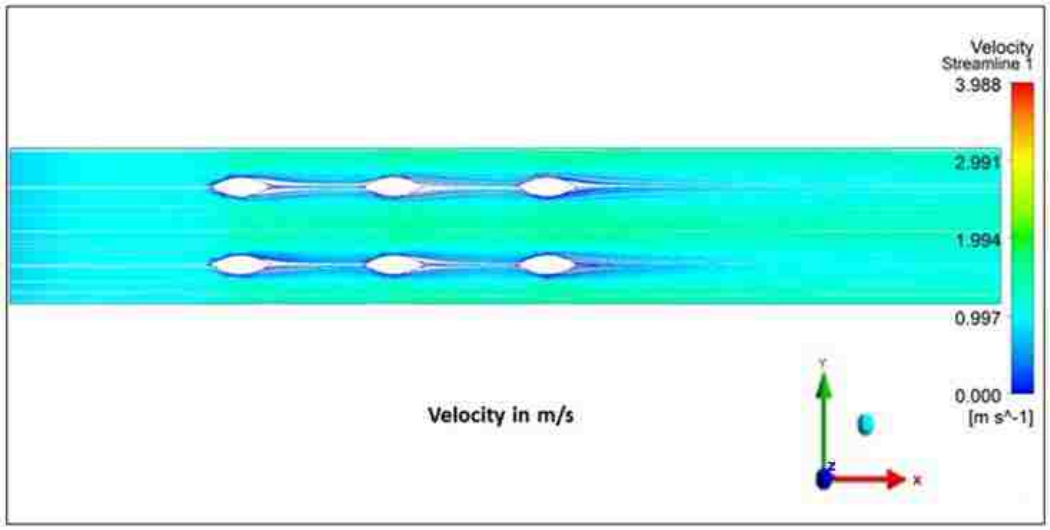

Figure 3.32. Streamline for single channel model with eyelid type fin at y=0.00015 m.

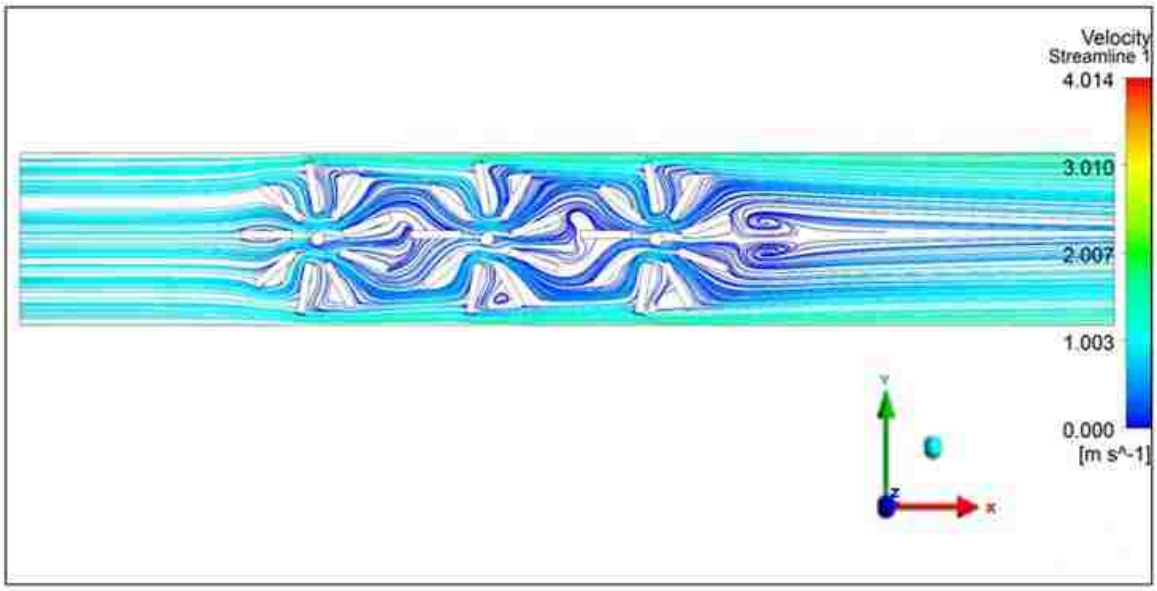

Figure 3.33. Streamline for single channel model with straight ripsaw fan type fin design at y=-5.002·10^{-5} m.

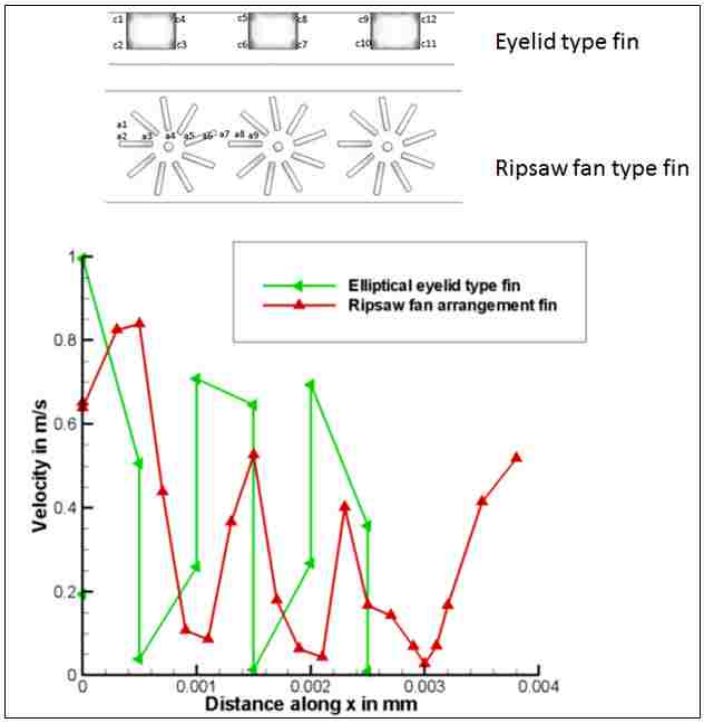

Figure 3.34. Velocity for single channel model with eyelid fin and ripsaw fan type fins.

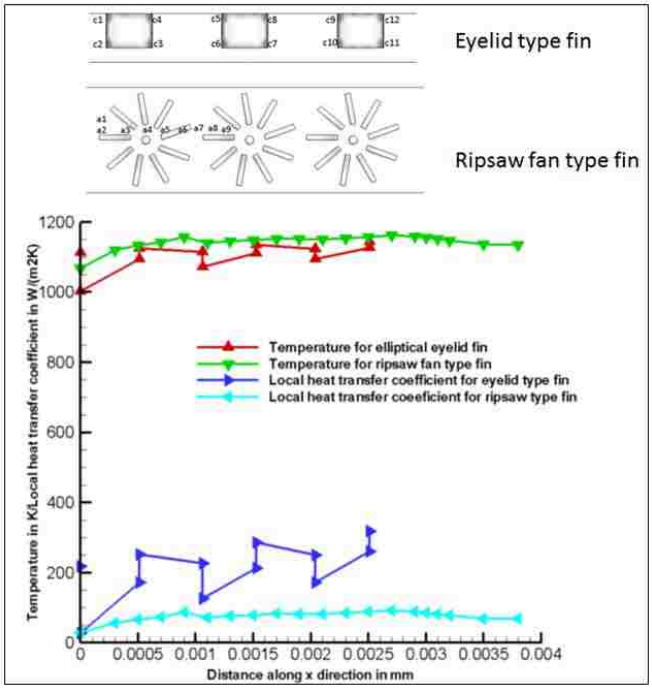

Figure 3.35. Heat transfer coefficient for single channel model with eyelid fin and ripsaw fan type fin.

The velocity, temperature and local heat transfer coefficient for Case 6 and Case 7 are shown in Figure 3.34 and Figure 3.35, respectively. The velocity decreases and the pressure increases near the fin ends. Farther from the fins the velocity is stable without much fluctuation. Due to the streamlined nature of the eyelid type fin there is no recirculation formed for the eyelid type fin (Case 6) and due to the vortex formation irregular velocity is obtained for Case7.

The local heat transfer coefficient for elliptical eyelid fin increases near the upper wall and there is a drop in the heat transfer coefficient at the lower end of the fins where the heat transfer from the fluid is low. The local heat transfer coefficient for ripsaw fan arrangement fins increases almost linearly from a1 to the outlet. This is due to the fact

that the local heat transfer coefficient is calculated at a distance from the fins along the fluid. Highest pressure drop and lowest heat transfer are obtained for the ripsaw fin model shaped like a fan (Case7).

3.5.7 Case 8 (Single channel model with ripsaw fin design with 0.0002 m thickness)

Another type of fin to enhance heat transfer is modeled which is the ripsaw fin. Two types of ripsaw fins are designed. One is with a thickness of 0.0002 m and another is with a thickness 0.00005 m. This type of fin gives a good heat transfer coefficient with low pressure drop. The ripsaw fin with thickness of 0.0002 m has a pressure drop of 18.14 Pa and friction factor of 0.571. The heat transfer surface area is $2.24 \cdot 10^{-5}$ m^2 and the obtained average Nusselt number is 2.469. Figure 3.36 shows the pressure contour for the ripsaw fin with thickness of 0.0002 m.

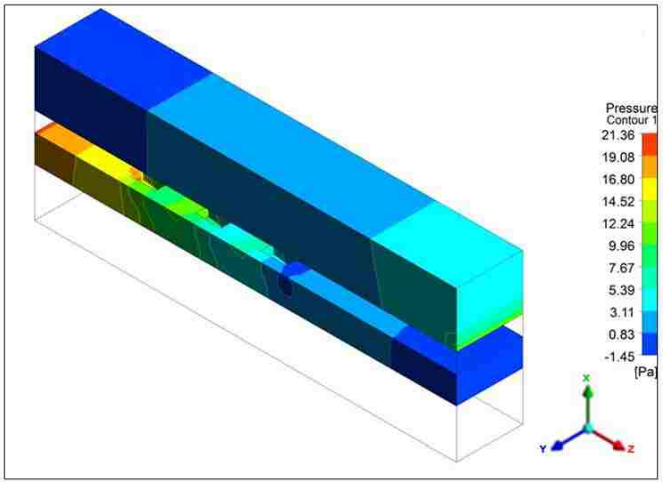

Figure 3.36. Pressure contour for single channel model with straight ripsaw fin design of 0.0002 m thickness.

Similar to the rectangular and triangular fins recirculation is formed behind the fins. Symmetrical vortices are formed in the wake region. The two vortices circulate in

the opposite direction. At the end of the fins the shear layer reattaches to the wall and boundary layer separation starts for the next fin. The recirculation occupies the entire length and height of the fin. The recirculation zone of the ripsaw fins is located at 0.00165 m and the reattachment region of the shear layers is located at 0.0023 m. Figure 3.37 shows the velocity streamline along the y and z-direction for ripsaw fin with thickness of 0.0002 m.

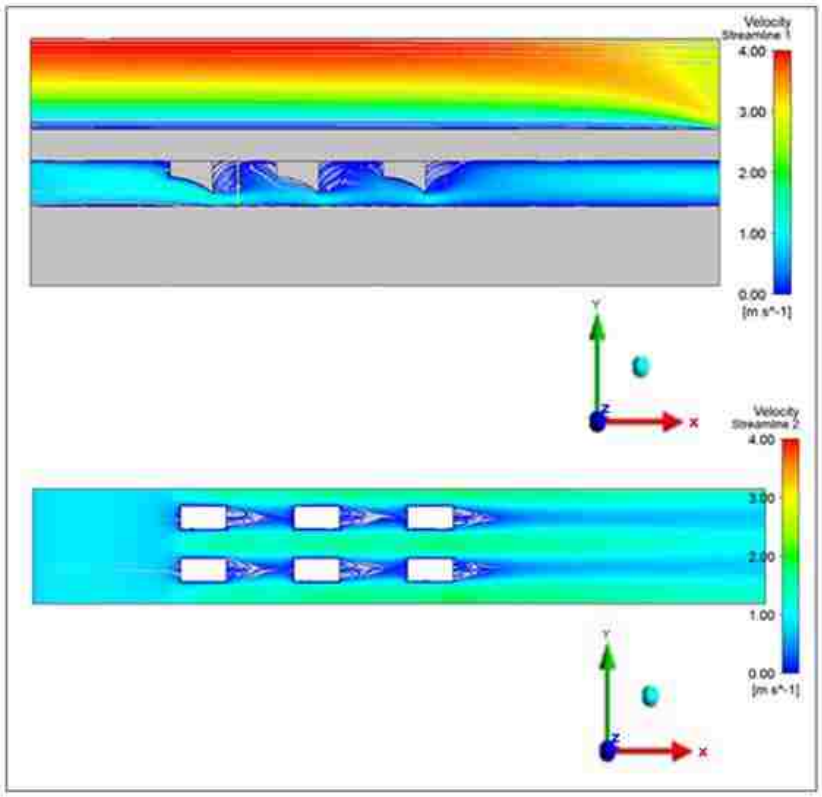

Figure 3.37. Velocity streamline in m/s for single channel model with straight ripsaw fins 1 at z=-0.00017 m and y=0.00013 m.

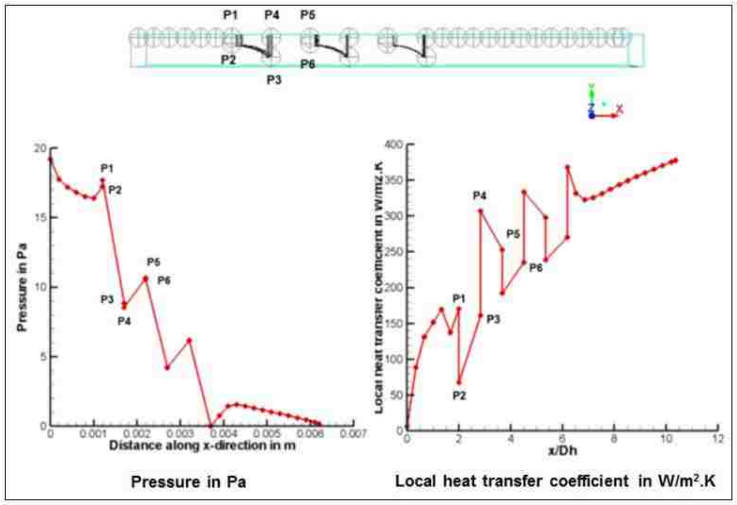

Figure 3.38. Pressure and local heat transfer coefficient for the ripsaw fin with thickness of 0.0002 m.

Figure 3.38 shows the pressure distribution and the local heat transfer coefficient along the ripsaw fin with thickness of 0.0002 m. The obtained pressure drop and heat transfer coefficient for the ripsaw fin with thickness of 0.0002 m are less compared to the standard rectangular fins. Uniform pressure distribution is obtained from the inlet to the point where the fins start. At the stagnation point P1, P2 the pressure increases and the velocity decreases. As the fluid flows towards the sides of the fins the pressure decreases due to the absence of obstacles and the velocity increases. The velocity is high at P4 and the pressure is low at that point. As the fluid reaches the wake region there is an adverse pressure gradient and the recirculation is formed. At this point the pressure increases and the velocity decreases and after this point the shear layer reattaches to the wall. The process repeats till the end of the third fin and thereafter the velocity and the pressure becomes stable. Similarly the local heat transfer coefficient increases from the inlet and it reaches the maximum at P1 near the origin of the fins. Away from wall the heat flux

decreases due the fluid mixing resulting in the decrease of the local heat transfer coefficient. The heat transfer coefficient then increases and it reaches maximum at P4 at the rear of the fins in the wake region. Points which are closer to the hot solid wall have higher heat transfer coefficient and less temperature difference than those which are away from the wall. Hence the ripsaw fins with 0.0002 m thickness have a good heat transfer rate with reasonable pressure drop.

3.5.8 Case 9 (Single channel model with ripsaw fins with 0.00005 m thickness)

Another case with ripsaw fin thickness of 0.00005 m is studied to enhance the heat transfer rate. The fins are very thin and in order to be symmetrical 12 fins are equally placed in a uniform arrangement. The heat transfer surface area of the ripsaw fin with thickness 0.00005 m is $2.24 \cdot 10^{-5}$ m^2. The total heat transfer surface area is more than triangular fins but less than other fins. The pressure drop and friction factor for this case is 15.01 Pa and 0.472, respectively. The obtained heat transfer coefficient is better than the other fins. The average Nusselt number obtained is 3.050. The pressure contour for the ripsaw fin with thickness of 0.00005 m is shown in Figure 3.39.

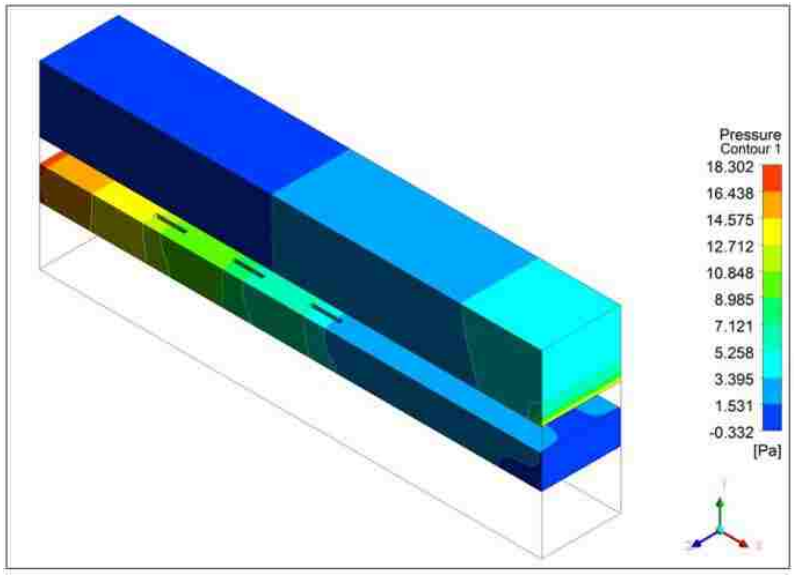

Figure 3.39. Contour for pressure in a single channel model with ripsaw fin with thickness of 0.00005 m.

Figure 3.40 shows the streamline velocity for the ripsaw fin design with 0.00005 m thickness. Since the fins are extremely thin no recirculation in between the fins. The fluid flows without much fluctuations from the inlet along the fins till it reaches the outlet.

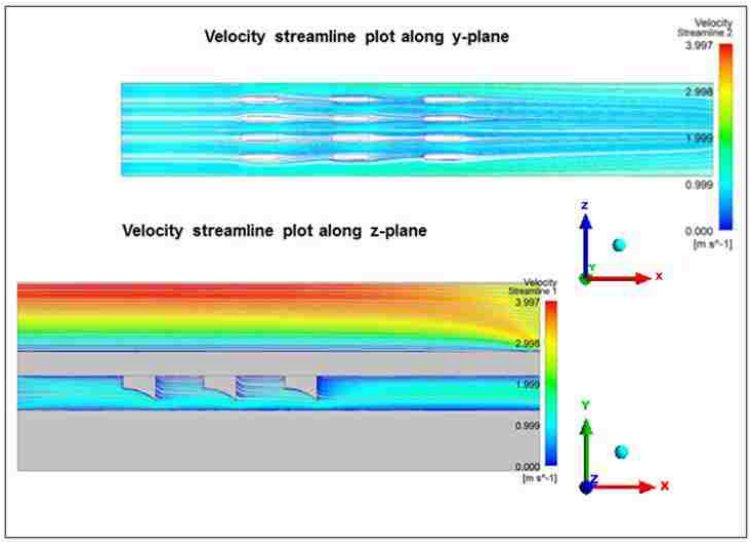

Figure 3.40. Streamline velocity for a single channel model with ripsaw fins with thickness 0.00005 m at y=1.336·10^{-6} m and z=0.00027 m.

There is no recirculation formed in the wake region of the fins. The advantage of using this type of fins is that the pressure drop and the friction factor obtained is less due to the absence of vortices. The heat transfer coefficient obtained is better compared to other fins.

Table 3.2 shows the values of heat transfer rate, dimensionless numbers like the Nusselt number, the Schmidt number, the Colburn j-factor and the friction factor. The Schmidt number which is the ratio of the viscous diffusion rate to the mass diffusion rate is calculated based on the average temperature of the reacting channel. The Schmidt number is given by the following equation.

$$Sc = \frac{\mu}{\rho D_{AB}} \tag{3.10}$$

The diffusivity of the mixture is calculated using the Chapman-Enskog kinetic theory. The corresponding formula for D_{AB} is given below.

$$D_{AB} = 0.0018583\sqrt{T^3\left(\frac{1}{M_A}+\frac{1}{M_B}\right)}\frac{1}{p\sigma_{AB}^2\Omega_{D,AB}} \tag{3.11}$$

where T is the average temperature in K, p is the operation pressure, M_A and M_B are the molecular weight of species A and B, $\sigma_{D,AB}$ is the Lennard-Jones characteristic length and $\Omega_{D,AB}$ is the collision integral used in the Lennard-Jones potential.

The obtained Schmidt number is found to be similar for all the fin types studied here. The heat transfer surface area is the highest for ripsaw fan type fin and the lowest for base case without fins.

Table 3.2

Fluid flow and heat transfer results for uniform arrangement of fins

	Uniform arrangement							
Types	Rectangle fins	Triangle fins	Inverted bolt fins	Bolt fins	Eyelid type fin	Ripsaw fan type fin with thickness 0.00005 m	Ripsaw fin with thickness 0.0002 m	Ripsaw fin with thickness 0.00005 m
Heat transfer rate (W)	0.476	0.472	0.471	0.510	0.464	0.497	0.410	0.471
Heat transfer surface area (m^2)	$2.21\cdot10^{-5}$	$2.16\cdot10^{-5}$	$2.28\cdot10^{-5}$	$2.21\cdot10^{-5}$	$2.08\cdot10^{-5}$	$8.76\cdot10^{-5}$	$2.24\cdot10^{-5}$	$2.23\cdot10^{-5}$
Heat transfer coefficient ($W/m^2\cdot K$)	215.85	216.58	232.03	229.63	206.08	56.644	172.70	211.18
Average Nusselt number	3.086	3.097	3.318	3.328	2.946	0.810	2.469	3.050
Colburn j factor	0.016	0.016	0.017	0.017	0.015	0.004	0.012	0.015
Schmidt number	0.316	0.316	0.316	0.313	0.316	0.314	0.320	0.316
Friction factor f	0.645	0.530	0.988	0.700	0.456	0.809	0.571	0.472

From Table 3.2 it can be seen that the friction is very high for the ripsaw fan type fin with thickness of 0.00005 m. Due to high recirculation and shape of the fin the obtained friction factor is very high compared to other fins. The ripsaw fin with thickness of 0.00005 m has the least friction factor due to the absence of recirculation and less thickness. Due to the increase in heat transfer surface area the inverted bolt fins have the highest heat coefficient compared to other fins. Even though the ripsaw fan type fin with thickness of 0.00005 m has the highest surface area the formation of vortices near the fin ends and the walls decrease the heat transfer coefficient to minimum value compared to the other fins.

Table 3.3 shows the pressure drop in the reacting flow and the temperature differences between the inlet and the outlet of the reacting and the helium channel. The inverted bolt fins have the highest pressure drop which is 31.4 Pa and eyelid type fins have the lowest pressure drop which is 14.50 Pa. The reason for the high pressure drop in the inverted bolt fins is due to the formation of the vortices. The eyelid type fin has low pressure drop due to its streamlined body and hence the flow is smooth without any recirculation. The obtained pressure drop for all the cases is found to be less. The obtained average Nusselt number for all the fin models is found to be less than the standard Nusselt number value of 4.0. The low value of the Nusselt number is due to the properties of the mixture fluid flowing inside the cold flow channel. Another study is carried out by using air as the fluid for the cold channel in the rectangular fin model and it is found that the obtained average Nusselt number is 6.147.

The effectiveness of heat exchanger is calculated according to the number of transfer units (NTU) method. There is a little variation in the heat transfer and

effectiveness obtained for all the cases. Due to the smaller length of the channel (0.0064648 m) the effectiveness obtained is less. A parametric study is done by increasing the channel length of the heat exchanger channel from 0.0064648 m to 0.064648 m and it is found that the effectiveness is increased to above 80%. But the pressure drop varies a lot for the different types of fins. Since the length of the heat exchanger is small (6.4648 mm) the heat transfer rates and the obtained Nusselt number are similar. When the heat exchanger is scaled up for the industrial use the heat transfer rates will change for different types of fins and the pressure drop will also increase. Hence considering the scaling up of heat exchangers the ripsaw fin with thickness of 0.00005 m is taken to be the good design as it gives reasonable heat transfer with minimal pressure drop.

Table 3.3

Pressure drop and the temperature difference between the inlet and the outlet of the flow channels

	ΔP in reacting flow channel (Pa)	ΔT in reacting flow channel (K)	ΔT in helium flow channel (K)	Temperature gradient in reacting flow channel ($K \cdot mm^{-1}$)	Mass diffusivity in the reacting channel D_{AB} ($m^2 \cdot s^{-1}$)	Effectiveness ε
Rectangular fins	20.48	132.33	53.22	20.47	$6.26 \cdot 10^{-6}$	0.533
Triangular fins	16.84	131.25	51.72	20.30	$6.25 \cdot 10^{-6}$	0.528
Inverted bolt fins	31.40	131.04	60.71	20.27	$6.25 \cdot 10^{-6}$	0.527
Bolt fins	22.24	141.95	57.52	21.95	$6.30 \cdot 10^{-6}$	0.571
Eyelid type fins	14.50	128.99	56.96	19.95	$6.24 \cdot 10^{-6}$	0.519
Ripsaw fan type fin	25.72	138.31	50.15	21.39	$6.28 \cdot 10^{-6}$	0.557
Ripsaw fin with thickness of 0.0002 m	18.14	114.12	53.88	17.65	$6.18 \cdot 10^{-6}$	0.459
Ripsaw fin with thickness of 0.00005 m	15.01	131.08	57.89	20.27	$6.25 \cdot 10^{-6}$	0.528

3.5.9 Conclusion

It can be seen that though the flow velocity and the Reynolds number are same for all the cases studied in this research the values of pressure drop and the Nusselt number are different due to the type of fins. It can be seen that ripsaw fins with fan type arrangement has the maximum surface area density with the minimum heat transfer and maximum pressure drop. Such types of fin arrangement are not good because it requires more operating cost. Rectangular and triangular fins are found to be a good design with a better effectiveness. Bolt fins and inverted bolt fins have good heat transfer rate but the obtained pressure drop are very high. Ripsaw fin with thickness of 0.00005 m is found to be the best design with good heat transfer and reasonable pressure drop.

3.6 Staggered Arrangement

In this research another study is done to enhance the heat transfer rate by arranging the fins in the staggered manner. The single channel model with rectangular fins, triangular fins, inverted bolt fins and ripsaw fin with thickness of 0.00005 m are studied in this research. The fluid flow and heat transfer results are discussed in detail in the following.

3.6.1 Case 1 (Single channel model with staggered rectangular and triangular fins)

The dimensions of the rectangular and triangular fins are the same as the ones used in the uniform arrangement. The uniform arrangement has 6 fins and the staggered arrangement has 7 fins. The heat transfer surface area for the staggered rectangular fins is $2.25602 \cdot 10^{-5}$ m^2 and triangular fins is $2.2058 \cdot 10^{-5}$ m^2. The obtained heat transfer rate is also high for the staggered arrangement. The obtained pressure drop for the staggered

rectangular and triangular fins is 28.41 Pa and 23.07 Pa, respectively. Due to the staggered arrangement of the fins there is more recirculation and hence higher pressure drop and friction factor are obtained. There is a significant increase in the friction factor for both the fins. The friction factor for rectangular fin is 0.894 and the friction factor for the triangular fin is 0.725. The average Nusselt number and the Colburn j-factor for the rectangular and triangular fins are 3.205, 0.016, and 3.235, 0.016, respectively. The Schmidt number for staggered rectangular and triangular fins is 0.316 and 0.316, respectively. Since the plots for rectangular and triangular fins are similar, figures are shown only for rectangular fins. Figure 3.41 shows the pressure and temperature contour for the staggered rectangular fins.

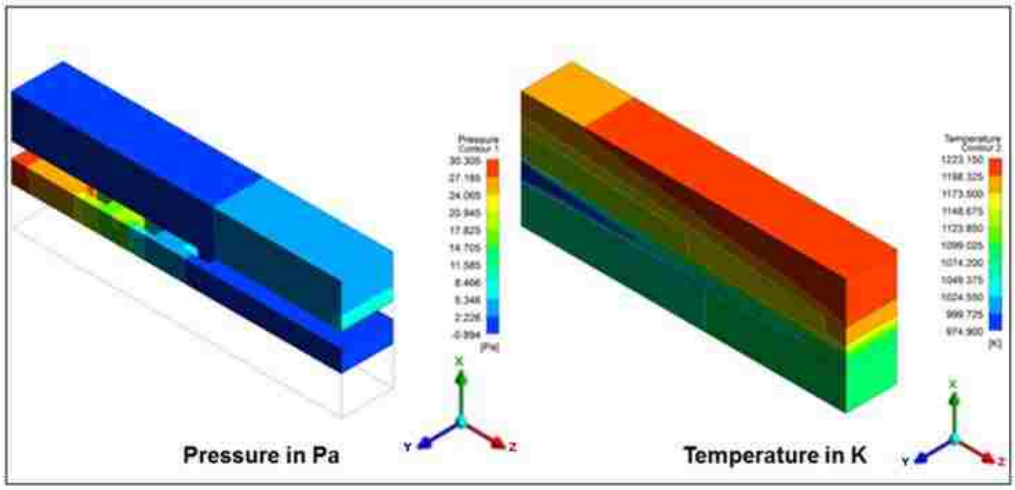

Figure 3.41. Pressure and temperature contour for single channel model with staggered rectangular fins.

Flow over staggered rectangular plates produces recirculation zones where the fluid separates and form vortices. In the wake which is formed downstream of the fin the

heat transfer is decreased due to the flow disturbances caused by the fins. Relatively low heat transfer distributions are found immediately behind the fin because of flow recirculation with low local velocity. The strong recirculation zone is found behind the fins where the shear layer separates and rolls into vortices. There is no secondary vortex and only one recirculation zone is formed in the wake region. The length of the recirculation region increases with the increase in the Reynolds number. The recirculation region is located at 0.00154 m and the reattachment region of the shear layers is located at 0.00210 m. The velocity streamline for the staggered rectangular fins is shown in Figure 3.42.

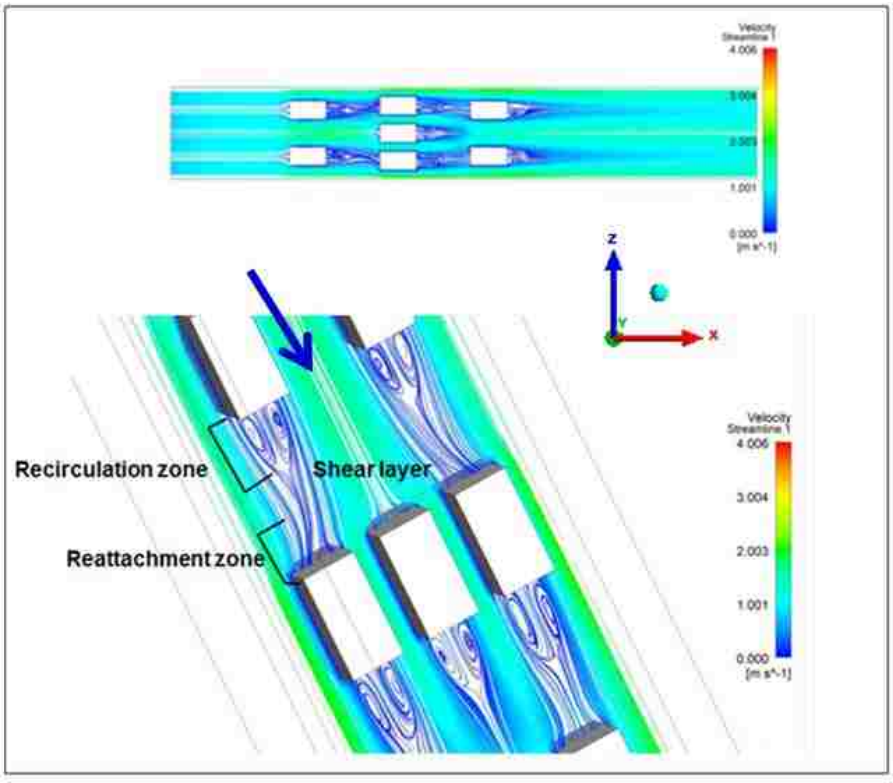

Figure 3.42. Velocity streamline for single channel model with staggered rectangular fins along y-plane at y=0.003 m.

The velocity streamline along the z-plane from Figure 3.43 shows the recirculation zone behind the fins. It can be seen that recirculation zone for the first and the third plane are formed at the rear end of the second row of fins or the before the start of the third row of fins. This is due to the staggered arrangement of the fins. The z-plane is created at a distance of three-fourth of the first and the third fin and near the edge of the second fin. The vortex is formed in the wake region immediately behind the first and the third fin. Since the fin thickness is very small behind the second fin no vortices are formed behind the second fins. The shear layers continue from the second fin and they separate and form recirculation zone before the start of the third fin for the first and the third z-plane. Another vortex is formed in the wake region of the third fin and thereafter the shear layers reattach and the flow becomes uniform.

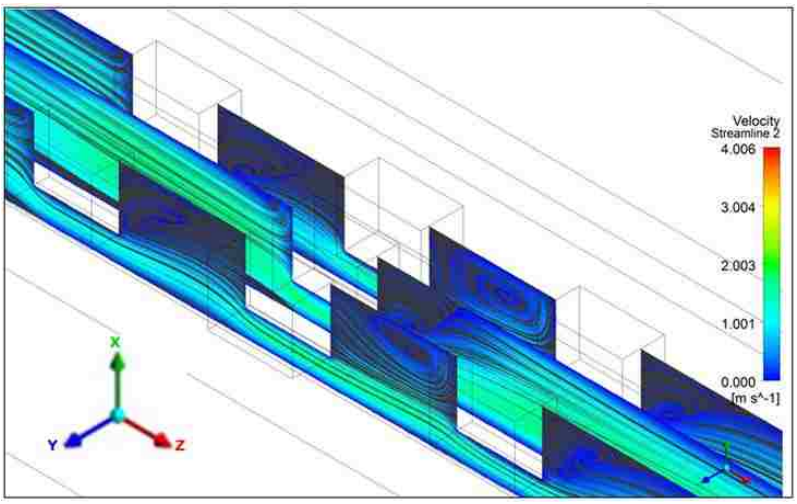

Figure 3.43. Velocity streamline for single channel model with staggered rectangular fins along z-plane at z=0.0015 m.

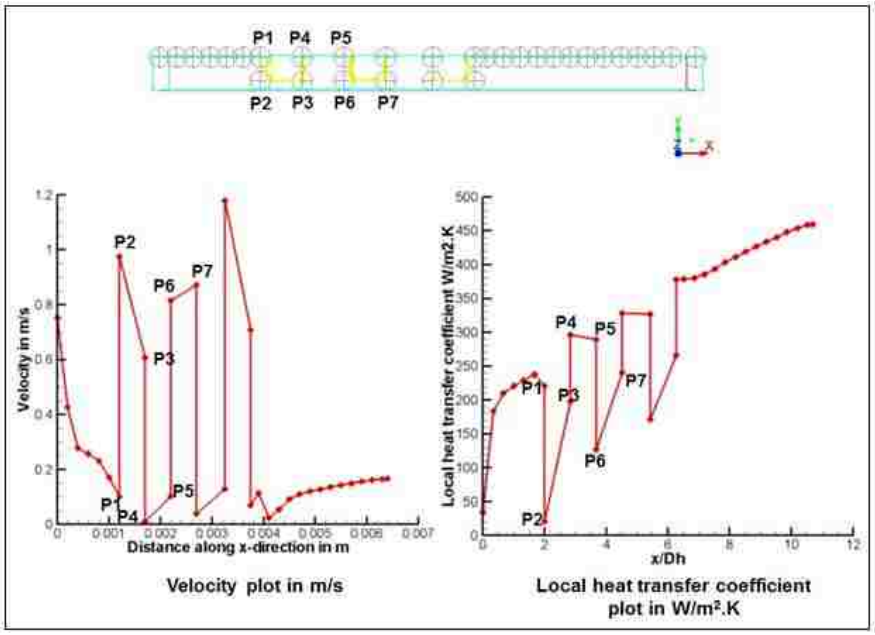

Figure 3.44. Velocity and local heat transfer coefficient for single channel model with staggered rectangular fins.

Figure 3.44 shows the velocity and local heat transfer coefficient for the single channel model with staggered rectangular fins. The velocity of the fluid decreases from 0.800 m/s and it reaches minimum at the stagnation point P1. The velocity reaches maximum at P2 where the fluid flows without any disturbance and is about 0.975 m/s. The velocity decreases as the fluid travels to the wake region of the fins. The velocity starts decreasing from P3 and becomes minimum at P4. Again the velocity increases and it becomes maximum at P7. The process repeats till the end of the third fin and then the velocity becomes stable till the fluid reaches the outlet. The increase in pressure drop due to the generation of vortex in the wake region is observed similar to the uniform arrangement of the fins. The heat transfer coefficient is high at a point near to the hot solid wall. The heat transfer rate is greatly enhanced due to the fin arrangement and due

to the increase in the total heat transfer surface area caused by the fins. The heat flux is high near the wall and decrease near the bottom region of the fins. The heat transfer coefficient is low at fluid points near the fin bottom. The reason is due to the points are placed away from the hot solid wall and the heat is dissipated by the moving fluid. The temperature difference is high at points away from the wall and the heat flux is less at these points. After the end of the third fin the heat transfer coefficient increases without much fluctuation till it reaches the outlet. There is increase in heat transfer as the fluid reaches the outlet due to the counterflow arrangement of the heat exchangers.

3.6.2 Case 2 (single channel model with inverted bolt fins)

The inverted bolt fins gives a good heat transfer rate compared to all the other cases studied here. The obtained pressure drop for inverted bolt fin case is 31.64 Pa and the friction factor obtained is 0.996. Due to the recirculation and the vortex formed in the fins the obtained pressure drop and the friction factor for the fins are relatively high. The obtained maximum velocity in the fins is 2.027 m/s and the average inlet velocity is 0.8 m/s. The obtained average Nusselt number for the staggered inverted bolt fins is 3.418 and the Colburn j-factor is 0.017. The obtained Schmidt number for the staggered inverted bolt fins is 0.315. The pressure that drives the fluid is the static pressure and the resistance offered to the fluid by the tube causes the pressure drop as the fluid moves towards the exit. Figure 3.45 shows the velocity and pressure contour for the single channel model with staggered inverted bolt fins.

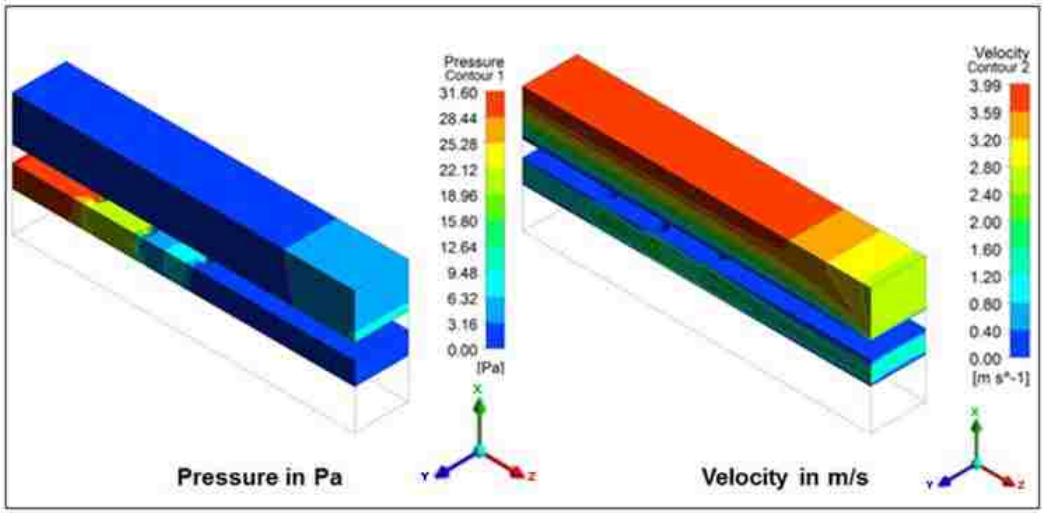

Figure 3.45. Pressure and velocity contour for single channel model with staggered inverted bolt fins.

The streamline velocity for the staggered inverted bolt fin is shown in Figure 3.46. Horseshoe vortices are formed around the cylinder and the pressure increases at the stagnation point. As the fluid flows around the cylinder shear layer separates and forms vortices behind the fins. Recirculation zone occurs at the wake region behind the cylinder. The vortices formed are symmetrical and there are two vortices one rotating in clockwise and the other in counter clockwise direction. Since there are three large cylinders in the second row, the vortices formed are not symmetrical. From Figure 3.46 the vortices can be found in the wake region on the first and third row of the fins but no recirculation is found in the second row of the fins. Along the middle z-plane strong recirculation zone is found in the wake region. Since there are more recirculation zones found in the staggered arrangement the obtained pressure drop and friction is high compared to the uniform arrangement. The recirculation region of the staggered inverted

bolt fins is located at 0.000957 m and the reattachment region of the shear layer is located at 0.00197 m.

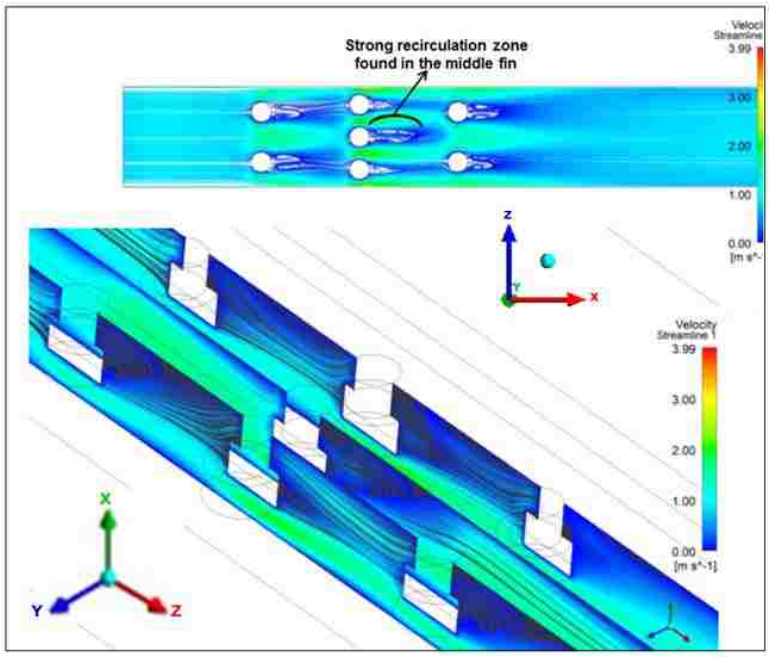

Figure 3.46. Velocity streamlines for the single channel model with staggered rectangular fins at y=0.003 m and z=0.0048 m.

Figure 3.47 shows the temperature plot along the y-plane. The temperature increases along the axial direction of the fluid flow. The solid temperature line plot shows the temperature distribution at various places along the surface. Due to the counterflow arrangement the temperature increases as the fluid moves from inlet to the outlet.

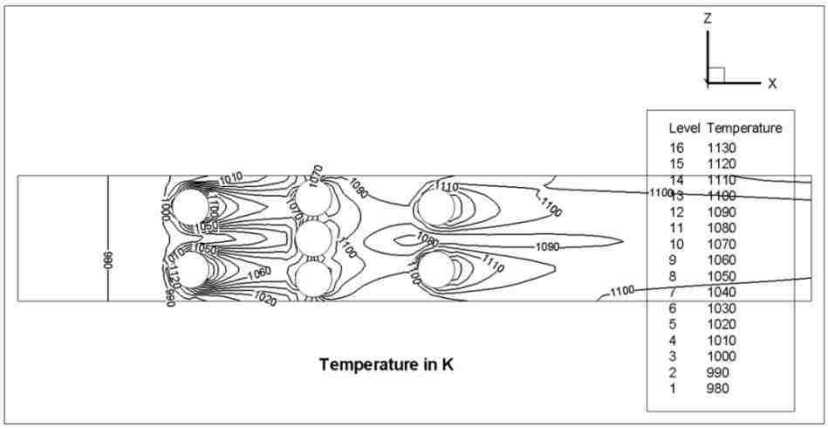

Figure 3.47 Temperature in K along y=0.00302037 m for a single channel model with staggered inverted bolt fins.

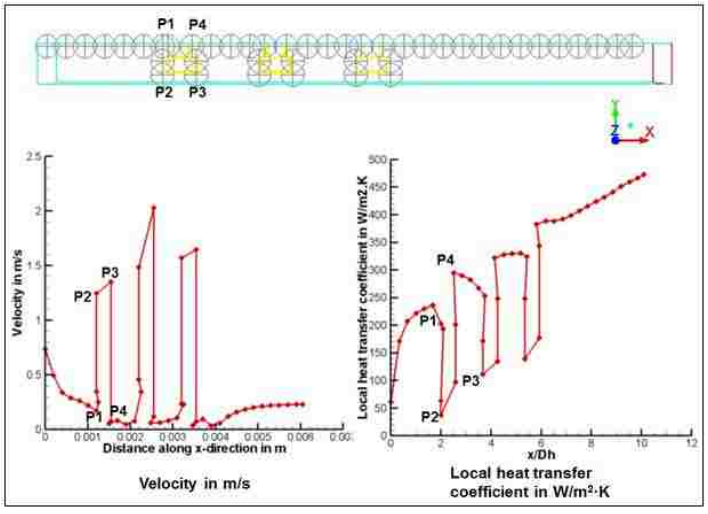

Figure 3.48. Velocity and local heat transfer coefficient for single channel model with staggered inverted bolt fins.

Figure 3.48 shows the velocity and heat transfer coefficient plot for the staggered inverted bolt fins. The velocity of the fluid decreases and it reaches minimum at P1. P1 is the point where the pressure is high and the velocity is low. The velocity increases from P2 and it becomes high at P3. The pressure is low at P2 and it starts increasing as the fluid travels to the rear of the cylinder. The velocity is minimum at P4 and the

pressure is high at the point due to the adverse pressure gradient. Also the increase in pressure is due to the formation of the recirculation zone in the wake of the fins. Again as the fluid moves towards the second fin the velocity increases and the pressure decreases until it reaches the wake region of the fins. The velocity is maximum at the end of the second fin due to the staggered arrangement of the fins and there is more space for the fluid to flow without any disturbance. The local heat transfer coefficient is high at points (P1, P4, etc.) near the top solid wall. The heat flux is high at the top solid wall and it decreases at places away from the top solid wall or near the bottom region of the fins. After P4 the local heat transfer coefficient decreases due to the recirculation formed in the wake region of the fins. The local fluid velocity is low at these points which decrease the heat transfer rate. The temperature and local heat transfer coefficient are low at points (P2, P3 etc.) away from the hot solid wall. After the third fin the local heat transfer coefficient increases without much fluctuation till it reaches the outlet.

3.6.3 Case 3 (Single channel model with staggered ripsaw fin of thickness 0.00005 m)

The single channel model with staggered ripsaw fins of thickness 0.00005 m gives a good heat transfer rate with reasonable pressure drop. The obtained pressure drop and friction factor are 16.59 Pa and 0.522, respectively. The pressure drop increases by about 1.4 Pa between the uniform and the staggered arrangement of the fins. The obtained heat transfer rate for the staggered ripsaw fin is 0.483 W and the average Nusselt number is 3.404. The obtained Colburn j-factor is 0.017. The average heat transfer coefficient increases from 211.18 $W \cdot m^{-2} \cdot K^{-1}$ to 223.61 $W \cdot m^{-2} \cdot K^{-1}$. The Schmidt number obtained is 0.315. Figure 3.49 shows the contour of pressure and the velocity for the single channel model with staggered ripsaw fins with thickness of 0.00005 m.

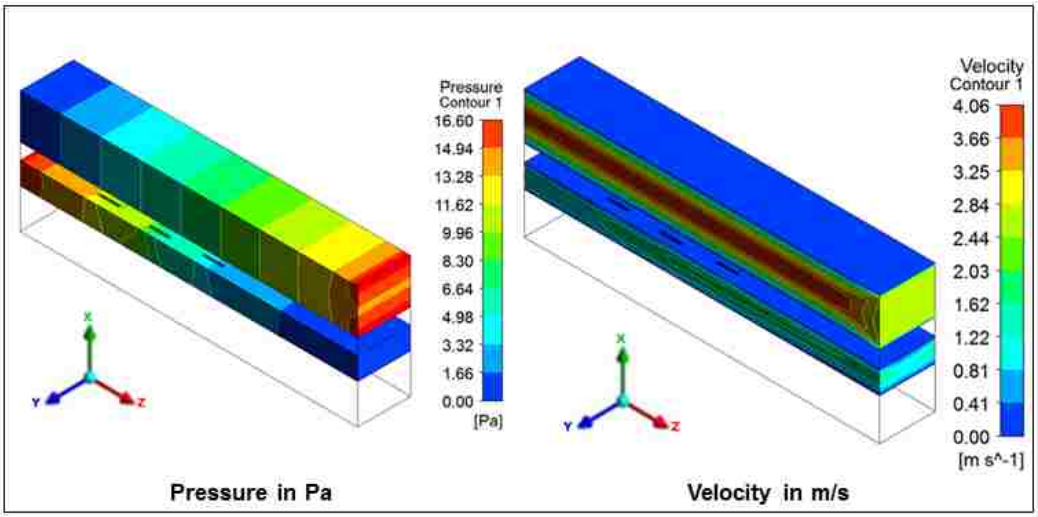

Figure 3.49. Pressure and velocity contour for single channel model with staggered ripsaw fins with thickness of 0.00005 m.

The obtained velocity streamlines show that there is no recirculation formed in the wake region. Since the fins are extremely thin and placed close to each other there are no vortices formed in this type of fin arrangement. The heat transfer rate is increased by the increase in the heat transfer surface area. Figure 3.50 shows the velocity streamline along the y and z-planes.

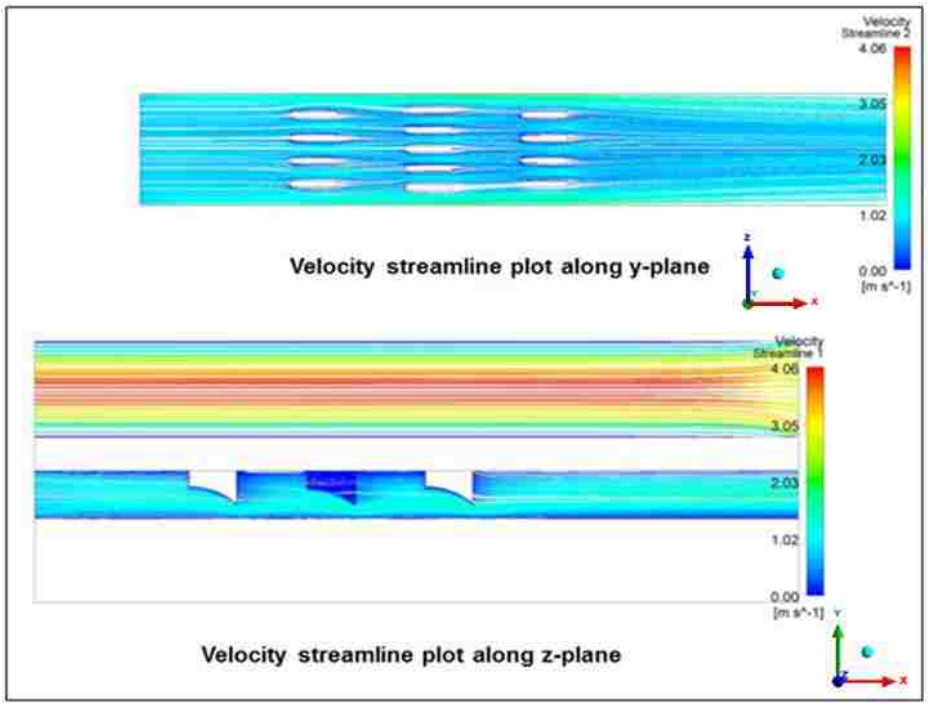

Figure 3.50. Velocity streamline for single channel model with staggered ripsaw fin with thickness of 0.00005 m at y=0.0037 m and z=0.0047 m.

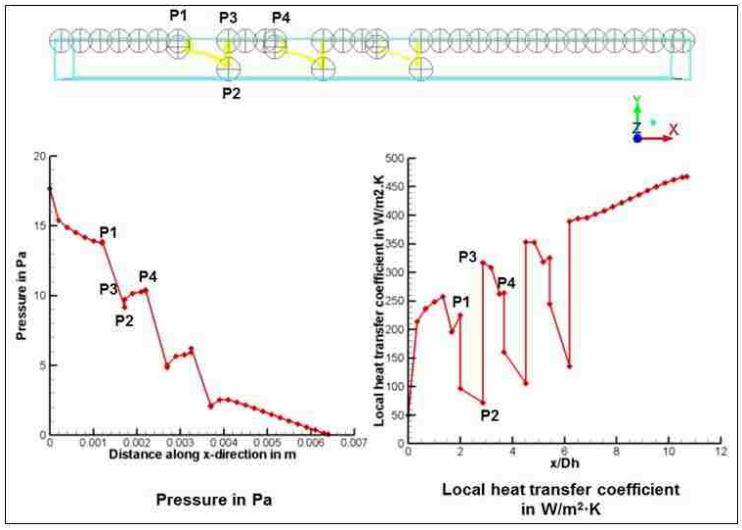

Figure 3.51. Pressure and local heat transfer coefficient for staggered ripsaw fin with thickness 0.0005 m.

Figure 3.51 shows the pressure and local heat transfer coefficient for the staggered ripsaw fins with thickness of 0.00005 m. The pressure changes decreases from the inlet until it reaches the fins at P1. At this point the velocity is negligible due to the stagnation region and after this point the fluid flow around the fins and the flow separation starts. The pressure is low at P2 since there is no obstacle and the velocity is high at this point. As the fluid reaches the rear of the fins there will be a wake region where the pressure increases. Even though there is no recirculation zone in this fin arrangement the pressure increases behind the fins and the velocity decreases due to the obstacles and the narrow space between the fins. This process continues until the fluid reaches the third fin and the flow becomes increases till it reaches the outlet. Due to the resistance offered to the flow the pressure decreases as the fluid moves from the inlet to the outlet. The local heat transfer coefficient is high at points near the hot solid wall and is low at P2 away from the wall. In between P3 and P4 the local heat transfer coefficient decreases due to the decrease in local fluid velocity. The local heat transfer coefficient does not change a lot after the third fin and till the fluid reaches outlet.

Table 3.4 shows the fluid flow and heat transfer values for the staggered arrangement of different fins. It has been found that the heat transfer and pressure drop increases for the staggered arrangement of the fins. It can be seen that the heat transfer rate is higher for ripsaw fin with thickness of 0.00005 m compared to the other cases. The obtained average Nusselt number is the highest for the inverted bolt fins and least for the ripsaw fins. The rectangular and triangular fins have similar values for the average Nusselt number and pressure drop. The Schimdt number is calculated based on the average temperature and it is found to be similar for all the cases studied. Due to the

increase in pressure drop the friction factor is found to be the highest for inverted bolt fins followed by the rectangular fins. The ripsaw fin with thickness of 0.00005 m has the least friction factor.

Table 3.4

Fluid flow and heat transfer values for the staggered flow arrangement

Staggered arrangement				
Types	Rectangle fins	Triangle fins	Inverted bolt fins	Ripsaw fin with thickness 0.00005 m
Heat transfer rate (W)	0.481	0.478	0.482	0.494
Heat transfer surface area (m^2)	$2.256 \cdot 10^{-5}$	$2.205 \cdot 10^{-5}$	$2.233 \cdot 10^{-5}$	$2.262 \cdot 10^{-5}$
Heat transfer coefficient ($W/m^2 \cdot K$)	224.16	226.28	239.04	223.61
Average Nusselt number	3.205	3.235	3.418	3.197
Colburn *j* factor	0.016	0.016	0.017	0.016
Schimdt number	0.316	0.316	0.315	0.315
Friction factor *f*	0.894	0.725	0.996	0.522

There is a little in increase in pressure drop compared to the uniform arrangement of the fins. The ripsaw and the inverted bolt fins do not have noticeable increase in pressure drop. All the obtained pressure drop values are good for safe operation. Due to the smaller heat transfer surface area the effectiveness obtained is also less. There is increase in the effectiveness of the heat exchanger and the ripsaw fin with thickness of 0.00005 m is found to have the highest effectiveness. Table 3.5 shows the pressure drop and temperature values for the staggered arrangement.

Table 3.5

Pressure drop and temperature difference between the inlet and the outlet for the flow channels

	ΔP in reacting flow channel (Pa)	ΔT in reacting flow channel (K)	ΔT in helium flow channel (K)	Temperature gradient in reacting flow channel (K/mm)	Mass diffusivity in the reacting channel D_{AB} ($m^2 \cdot s^{-1}$)	Effectiveness ε
Rectangular fins	28.41	135.13	55.58	20.90	$6.25 \cdot 10^{-6}$	0.544
Triangular fins	23.03	132.89	52.72	20.55	$6.26 \cdot 10^{-6}$	0.535
Inverted bolt fins	31.64	134.22	58.26	20.76	$6.27 \cdot 10^{-6}$	0.540
Ripsaw fin with thickness of 0.00005 m	16.59	137.35	59.85	21.24	$6.28 \cdot 10^{-6}$	0.553

3.6.4 Conclusion

The obtained average Nusselt number is higher for inverted bolt fins which is 3.418 followed by triangular fins which is 3.235. The obtained pressure drop for the rectangular fins is higher compared to the triangular fins for similar heat transfer rate. For similar heat transfer rate the obtained pressure drop which is 16.59 Pa is less for the ripsaw fins compared to the other fins. Hence ripsaw fin with thickness of 0.00005 m is considered to be the best design with less pressure drop and reasonable heat transfer rate.

3.7 Fins Arranged on the Top and the Bottom Solid

In this study the fins are arranged on both the top and the bottom solid regions to enhance the heat transfer. It is found that since the bottom solid region doesn't have any heat input and the heat transfer is only from top solid region there is a little increase in heat transfer rate compared to the uniform and staggered arrangement. But the pressure

drop obtained is higher compared to the other two arrangements because there is an increase in heat transfer surface area and more flow disturbances produced by the fins.

3.7.1 Case 1 (Single channel model with rectangular fins)

In this study the rectangular fins are arranged on both the top and bottom solid regions. The heat transfer surface area of the rectangular fin arrangement is $2.47602 \cdot 10^{-5}$ m^2. The pressure drop obtained for this model is 56.49 Pa which is twice higher than the uniform and staggered arrangement. The friction and Colburn j-factor is 1.778 and 0.01609, respectively. Due to the top and bottom arrangement there is strong flow disturbance which results in the increase of pressure drop. Figure 3.52 shows the pressure and velocity contour for the single channel model with rectangular fins arranged on the top and the bottom solid regions.

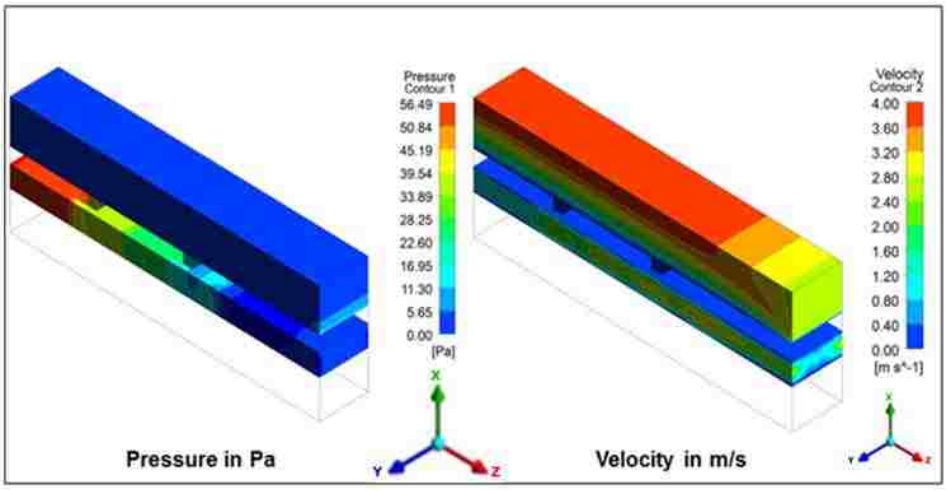

Figure 3.52. Pressure in Pa and velocity in m/s contour for single channel model with rectangular fins arranged on the top and bottom solid regions.

The horseshoe vortex is formed at the beginning of the fins and it extends along the sides. Recirculation is formed behind the fins in the wake region. The shear layer separates and form twin vortices where one vortex rotates in the clockwise direction and the other in the opposite direction. In Figure 3.53, recirculation can be seen clearly in the second and the fourth row of fins but not in the first and the third row. The y-plane is taken at a distance from three-fourth of the top fin and from one-fourth of the bottom fin. Hence more recirculation is found on the top fins. From the streamline along the z-plane recirculation can be found alternately along the top and the bottom fins. Since the Reynolds number is only 244 there is no secondary vortex formed. The recirculation region is located at 0.00108 m and the reattachment region of the shear layer is located at 0.00201 m.

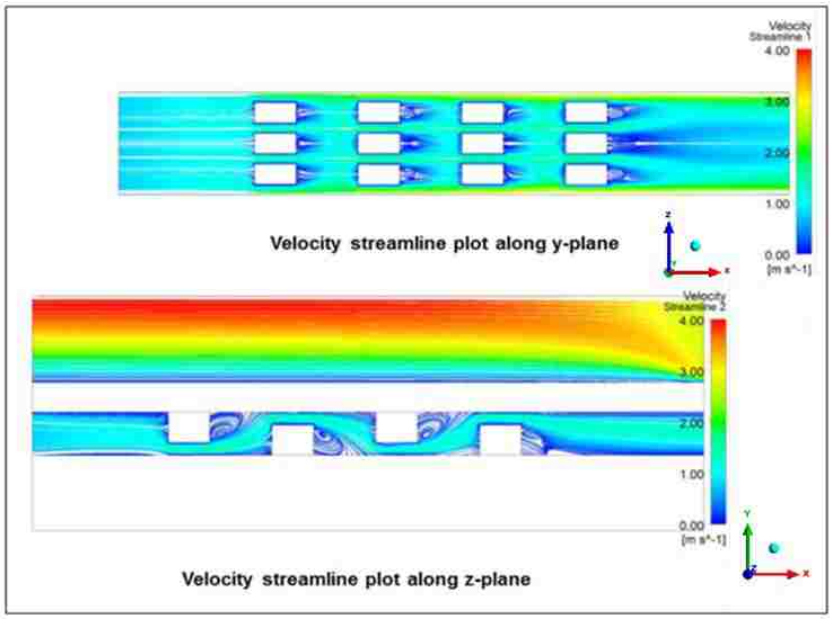

Figure 3.53. Velocity streamline for the single channel model with rectangular fins arranged on the top and bottom solid regions at y=0.0032 m and z=0.0053 m.

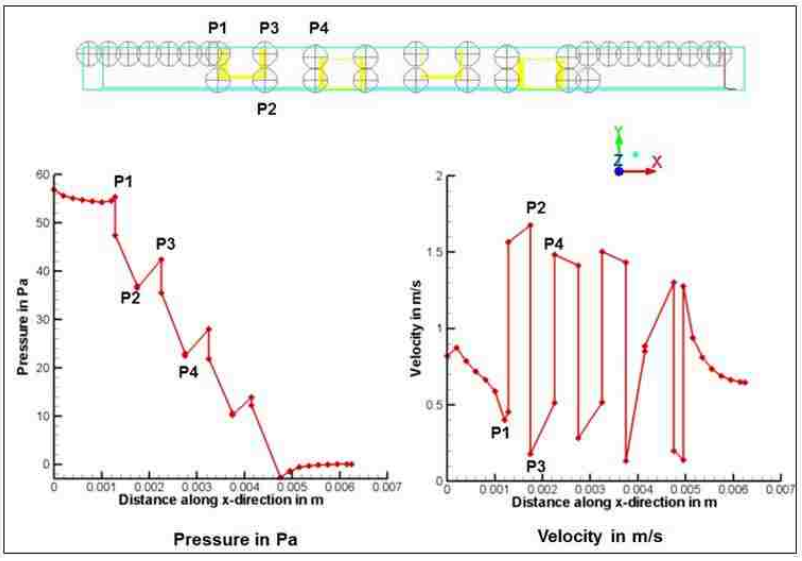

Figure 3.54. Pressure and velocity for single channel model with rectangular fins arranged on the top and bottom solid regions.

Figure 3.54 shows the top and bottom arrangement of rectangular fins for pressure and velocity plots. The pressure decreases uniformly from inlet to P1 where the fins start. Pressure is high at P1 and it starts decreasing and reaches minimum at P2. Similarly velocity is low at point P1 and increases as the fluid flow around the fins and becomes maximum at P2. Recirculation zone is formed behind the top fin and adverse pressure gradient is formed. Hence pressure increases at P3 and the velocity is minimum at P3. The bottom fin starts and the pressure is low at P4 where there is no obstacle and the velocity increases. The pressure decreases as the fluid travels to the rear of the fins. The process continues till the end of the fourth fin and the pressure and velocity becomes uniform till it reaches the outlet.

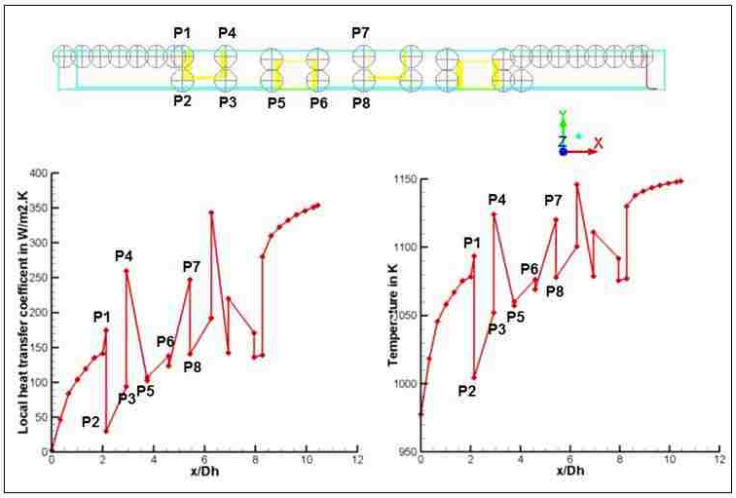

Figure 3.55. Temperature and local heat transfer coefficient of single channel model with rectangular fins arranged in the top and bottom solid regions.

Figure 3.55 shows the temperature and the local heat transfer coefficient for the rectangular fins. The temperature and the local heat transfer coefficient increases until it reaches P1. The local heat transfer coefficient decreases at P2, P3 which are placed away from the hot solid wall. The temperature becomes high at P4. The fins placed on the bottom solid are away from the heat source and hence the temperature and the local heat transfer coefficient at P5 and P6 are small. The heat flux is high at the upper solid wall and it decreases away from the hot wall. The temperature increases at P7 where the top fin start and again decreases at P8. Away from the wall the temperature difference increases resulting in the decrease of the heat transfer coefficient. The process repeats till the end of the fins and the temperature and the local heat transfer coefficient increases till the fluid reaches the outlet. Due to the increase in the heat transfer surface area, the obtained heat transfer rate is high compared to the uniform and staggered arrangement of rectangular fins.

3.7.2 Case 2 (Single channel model with triangular fins)

Two rows with three triangular fins arranged in alternate manner along the top and bottom solid regions are studied. Similar to the top and bottom rectangular fins six fins are arranged on the top solid surface and six fins are arranged on the bottom solid surface. The heat transfer surface area of triangular fins is smaller than rectangular fins. The heat transfer surface area for the top and bottom fin arrangement is $2.342 \cdot 10^{-5}$ m^2. The pressure drop and the friction factor for this model are 34.04 Pa and 1.073, respectively. The average Nusselt number and the Colburn j-factor is 3.099 and 0.016, respectively. The obtained heat transfer rate and the pressure drop is less than the rectangular fins. The pressure and velocity contour is shown in Figure 3.56.

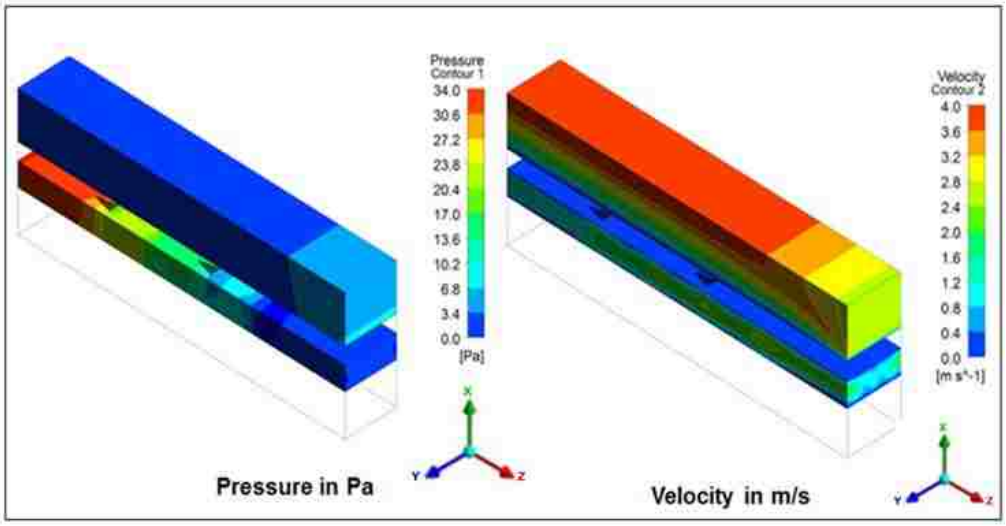

Figure 3.56. Pressure and velocity distribution for single channel model with triangular fins arranged on the top and bottom solid regions.

Figure 3.57 shows the velocity streamline for the triangular fins along y and z-planes. The obtained streamlines are similar to the rectangular fins. Recirculation zone

is found in the wake region forming symmetrical twin vortices behind each fin. The recirculation region is located at 0.00123 m and the reattachment region is located at 0.00207 m.

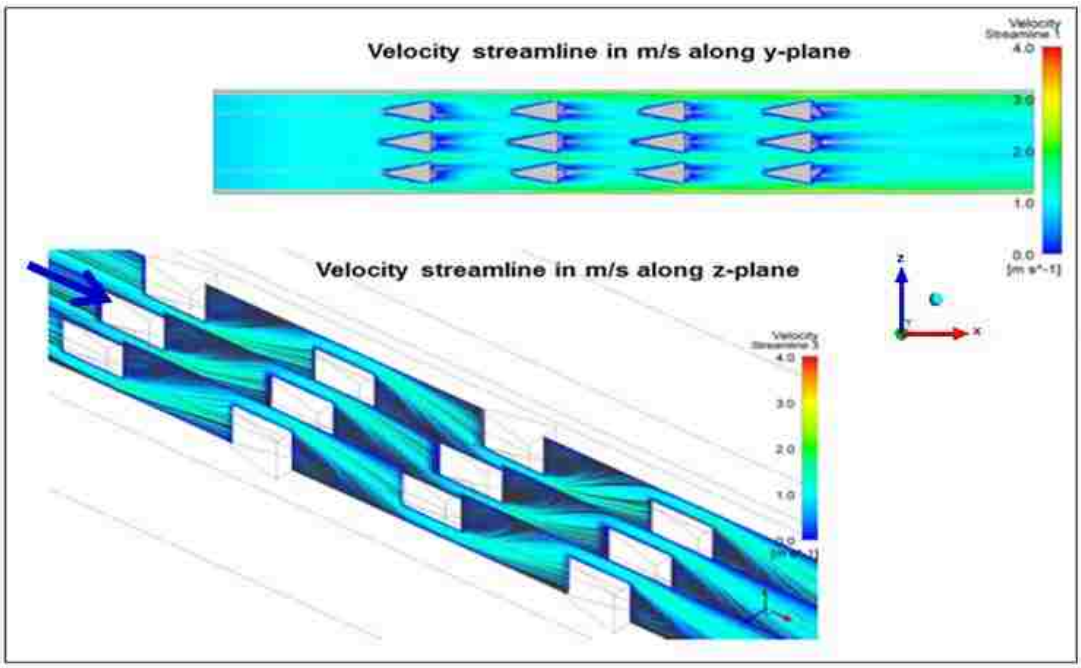

Figure 3.57. Velocity streamline for single channel model with triangular fins arranged on the top and bottom solid regions at y=0.0045 m and z=0.0059 m.

It can be seen that recirculation zone is formed behind the top and bottom fins alternately. Since the Reynolds number is low there is no formation of secondary vortex. Though the bottom solid does not have any heat input the heat transfer rate of this model is more than the uniform and staggered triangular fin arrangement. The increase in heat transfer is due to the increase in heat transfer surface area. The pressure, velocity and local heat transfer coefficient plot for the triangular fins are similar to the rectangular fin model and hence not shown in this study.

3.7.3 Case 3 (Single channel model with inverted bolt type fins)

It has been found that the inverted bolt type fins has the best heat transfer coefficient for both uniform and staggered arrangement. The obtained heat transfer rate is higher than the triangular and rectangular fins for the uniform and staggered inverted bolt fins. The heat transfer surface area is $2.438 \cdot 10^{-5}$ m^2 which is higher than all the fins. The only disadvantage of this fin type is the high pressure drop and the friction factor. Due to the complex design and arrangement horseshoe vortices are formed which increases the pressure drop and the friction factor. The obtained local heat transfer coefficient and the average Nusselt number are 221 $W \cdot m^{-2} \cdot K^{-1}$ and 3.16, respectively. The pressure and velocity for the inverted bolt fin are similar to the rectangular and triangular fins. The velocity streamline plot for the inverted fin mounted on the top and the bottom solids is shown in Figure 3.58. A strong horseshoe vortex is formed in front of the cylindrical fins and fluid flows around the cylinder to the rear side. The shear layers starts to separate and recirculation zone is formed in the rear side of the top fins for the top fins and in the rear side of the bottom fins for the bottom fins. The recirculation zone covers almost three-fourth of the space between the fins and the shear layers reattach to the wall after the wake region. Again flow separation occurs and this results in periodic breaking of the boundary layer thus enhancing the heat transfer. The recirculation region is located at 0.00123 m and the reattachment region of the shear layer is located at 0.001978 m.

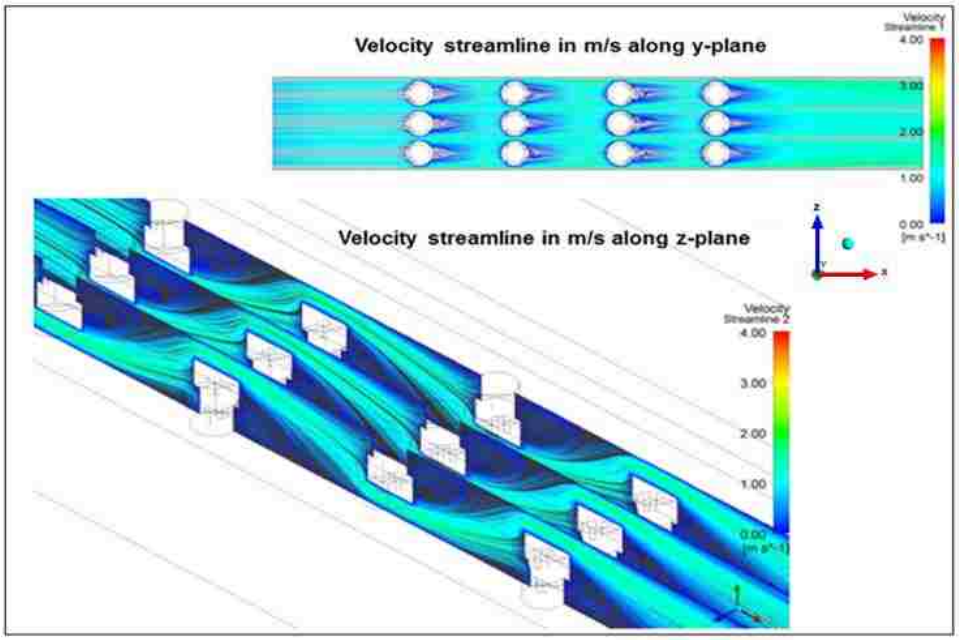

Figure 3.58. Velocity streamline for the single channel model with inverted bolt fins arranged on the top and bottom solid regions at y=0.0036 m and z=0.0045 m.

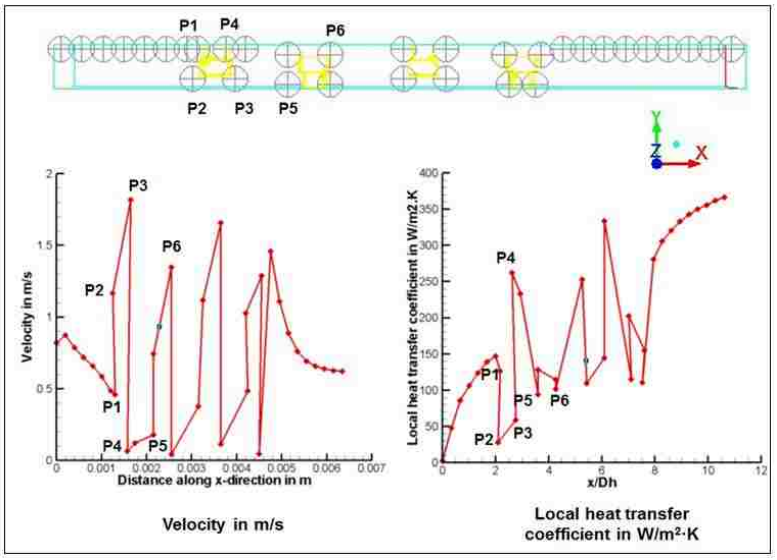

Figure 3.59. Velocity and local heat transfer coefficient for the single channel model with inverted bolt fins arranged on the top and bottom solid regions.

Figure 3.59 shows the velocity and local heat transfer coefficient. The velocity along the flow is uniform till it reaches the fins. The velocity is low at P1 and the pressure is high. The velocity increases at P2 as the fluid flow around the fins and it reaches a maximum at P3. The pressure is least at this point. Recirculation takes place at the rear of the fins and the velocity is minimum at P4 and the pressure is maximum at P4. The fluid then flows through the bottom fins and the velocity is minimum at P5 and pressure is high at this point. The fluid velocity then reaches maximum at P6 and the pressure is minimum at P6. The process continues until it reaches the fourth row of the fins and it becomes stable after the end of the fins. The local heat transfer coefficient is high for the top fins which are in contact with the solid wall. The temperature and local heat transfer coefficient is low at P2, P3, P5, etc. which are away from the hot solid surface. After the fourth tow of the fin the temperature increases without much fluctuation till reaches the outlet.

3.7.4 Case 4 (Single channel model with ripsaw fin thickness of 0.00005 m)

The last model studied in this research is the ripsaw fin thickness of 0.00005 m arranged on the top and bottom solid regions. The heat transfer surface area is $2.371 \cdot 10^{-5}$ m^2. This type of arrangement has no recirculation due to their shape. As a result of this the obtained pressure drop and the friction factor is also less. The obtained friction factor and the pressure drop is 0.589 and 18.73 Pa, respectively. The obtained average heat transfer coefficient and the average Nusselt number is 211.43 $W \cdot m^{-2} \cdot K^{-1}$ and 3.023, respectively. The streamline velocity plot shows that there is no recirculation and the streamlines are parallel to the flow direction. The obtained velocity and local heat

transfer coefficient are similar to the other fins explained above. Figure 3.60 shows the velocity streamline along the y and z-planes.

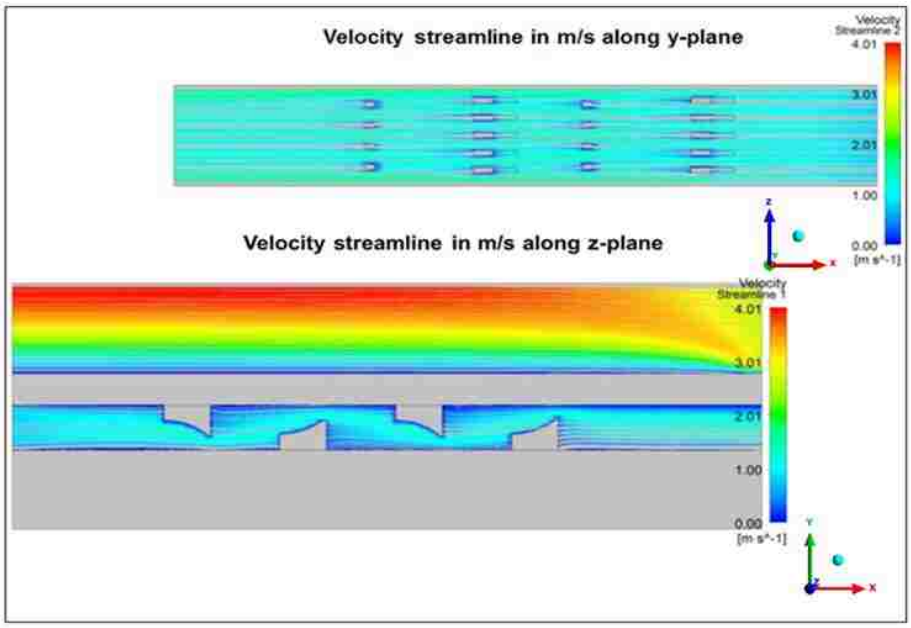

Figure 3.60. Velocity streamline for single channel model with ripsaw fin of thickness 0.00005 m arranged on the top and bottom solid regions at y=0.0032 m and y=0.0046 m.

The pressure, temperature and local heat transfer coefficient plots are similar to the other fin types. The velocity is low and the pressure is high at the stagnation point and in the recirculation region. The temperature and the local heat transfer coefficient are high at places near the top solid wall and low at regions away from the hot solid wall.

From the results it is found that there is not significant increase in heat transfer between the uniform arrangement and the top and bottom fin arrangement. The reason is because the bottom solid has no heat input and the heat is transferred only from the top solid. In staggered fin arrangement there are 7 fins attached to the top solid and hence

there is more heat transfer. However in the top and bottom arrangement there are only 6 fins placed in the hot solid wall and 6 placed in the cold solid wall. Hence the obtained heat transfer is less than the staggered arrangement of the fins. In real case, the channel arrangement is periodic and the hot helium fluid flows below the cold solid wall and heat transfer will be increased by having fins on both the solid walls. However in the current study the hot flow channel is present only above the reacting channel and hence the heat transfer obtained is less. The obtained average Nusselt number and the Colburn j factor is similar to the uniform fin arrangement. The friction factor is increased and the ripsaw fin with thickness of 0.00005 m is found to have the lowest friction factor. Table 3.6 shows the fluid flow and heat transfer results for the top and bottom arrangement of the fins.

Table 3.6

Fluid flow and heat transfer results for the top and bottom fin arrangement

Top and bottom fin arrangement				
Types	Rectangle fins	Triangle fins	Inverted bolt fins	Ripsaw fin with thickness 0. 00005 m
Heat transfer rate (W)	0.484	0.474	0.485	0.475
Heat transfer area (m^2)	$2.476 \cdot 10^{-5}$	$2.342 \cdot 10^{-5}$	$2.438 \cdot 10^{-5}$	$2.371 \cdot 10^{-5}$
Heat transfer coefficient ($W/m^2 \cdot K$)	215.35	216.76	221	211.43
Average Nusselt number	3.079	3.099	3.16	3.023
Colburn *j* factor	0.016	0.016	0.080	0.015
Schimdt number	0.315	0.316	0.315	0.316
Friction factor *f*	1.778	1.073	1.644	0.589

The effectiveness of the heat exchanger increases for the top and bottom arrangement. The pressure drop increases due to the presence of fins on both the top and bottom solids. In this arrangement recirculation and vortices are formed which increases the pressure drop and friction factor. The pressure drop is the highest for rectangular fins and least for the ripsaw fins. Hence ripsaw fin with thickness of 0.00005 m is considered to be the best design because it gives good heat transfer with minimum pressure drop.

The obtained effectiveness is around 52 to 54% for all the fin designs. The heat transfer surface area is less and hence the effectiveness of the heat exchanger is less. However another study is done for the staggered arrangement of the rectangular, triangular and ripsaw fins with thickness of 0.00005 m by increasing the channel length of the heat exchanger. The length of the heat exchanger channel with staggered rectangular, triangular and ripsaw fin with thickness of 0.00005 m is increased from 0.0064648 m to 0.064648 m. The heat transfer area of the long staggered rectangular fins is $2.44 \cdot 10^{-4}$ m^2, triangular fins is $2.35 \cdot 10^{-4}$ m^2 and the ripsaws with thickness of 0.00005 m is $2.4354 \cdot 10^{-4}$ m^2. The obtained heat exchanger effectiveness for rectangular fin is 80.15%, triangular fin is 87.25% and ripsaw fins with thickness of 0.00005 m is 92.13%. Table 3.7 shows the pressure drop and temperature difference for the top and bottom arrangement.

Table 3.7

Pressure drop and temperature difference between the inlet and the outlet for the top and bottom fins

	ΔP in reacting flow channel (Pa)	ΔT in reacting flow channel (K)	ΔT in helium flow channel (K)	Temperature gradient in reacting flow channel ($K \cdot mm^{-1}$)	Mass diffusivity in the reacting channel D_{AB} ($m^2 \cdot s^{-1}$)	Effectiveness ε
Rectangular fins	56.49	134.75	57.84	20.84	$6.27 \cdot 10^{-6}$	0.542
Triangular fins	34.08	131.86	55.95	20.39	$6.26 \cdot 10^{-6}$	0.531
Inverted bolt fins	52.22	134.86	58.43	20.86	$6.27 \cdot 10^{-7}$	0.543
Ripsaw fin with thickness of 0.00005 m	18.73	132.09	56.35	20.43	$6.26 \cdot 10^{-7}$	0.532

3.7.5 Conclusion

The average Nusselt number and pressure drop for rectangular, triangular, inverted bolt type and ripsaw fins with thickness of 0.00005 m for the top and bottom fins are 3.079, 3.099, 3.201, 3.023 and 56.49 Pa, 34.08 Pa, 52.22 Pa and 18.73 Pa, respectively. The inverted bolt fins have the highest average Nusselt number followed by the triangular fins. The values of the average Nusselt number for the triangular and the rectangular fins are very close. But the pressure drop for the rectangular fin which is 56.49 Pa is almost twice that of the triangular fin which is 34.08 Pa. Eventhough the obtained average Nusselt number for the ripsaw fin with 0.00005 m thickness which is $\overline{Nu}$ = 3.026 is less compared to the other fins, the obtained pressure drop for the ripsaw fins is the least of all the four fins which is 18.73 Pa. Hence the ripsaw fin thickness of 0.00005 m is selected as the best design with good heat transfer rate of 0.475 W and minimum pressure drop of 18.73 Pa.

3.8 Parametric Study for Straight Ripsaw Fin with Thickness of 0.00005 m

The mass flow rate of the hot and the cold fluid channel is fixed and the analysis is carried out under laminar flow. In order to study the effect of mass flow rate on the heat exchanger, a parametric study is carried out by changing the mass flow rate for the hot and the cold channel for the uniform arrangement of the ripsaw fins with thickness of 0.00005 m. It is well known that the Reynolds number increases by increasing the mass flow rate and the flow changes from laminar to turbulent flow. The flow becomes turbulent as the Reynolds number exceeds 2000 and standard k-epsilon model is used for the last two parametric study points. Extensive literature search has been carried out to select the type of turbulence model used for the parametric study. It is found that k-epsilon model is used for low pressure gradient compared to other models. Since the obtained pressure gradient is relatively low, k-epsilon model is used for the parametric study. The obtained numerical results in this study are compared with the published computational and experimental work done by other researchers. From the study carried out by Monteiro et al. [34], Dong et al. [76], Lu et al. [77], Paeng et al. [78] and Lacovides et al. [79] it is shown that standard k- epsilon model is more suitable to predict the fluid flow in the Reynolds number range from 1000 to 5000 for the compact plate fin heat exchangers. Hence k-epsilon model is used for the parametric study in the turbulent flow region. The governing equation for the turbulent kinetic energy k and its rate of dissipation ε are given as follows:

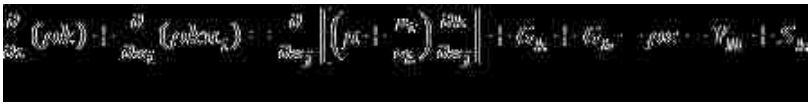

(3.11)

(3.12)

Here [redacted] represents the generation of turbulence kinetic energy due to mean velocity gradients, [redacted] is the generation of turbulence kinetic energy due to buoyancy, [redacted] represents the ratio of fluctuating dilatation incompressible turbulence to overall dissipation rate. [redacted], [redacted] are constants, [redacted], [redacted] are turbulent Prandtl numbers for k and [redacted] and [redacted], [redacted] are user-defined source terms.

It is well known that the pressure drop increases with increasing the Reynolds number and the reverse happens with the friction factor. In the laminar zone the friction factor decreases with increasing the Reynolds number (f=64/Re). The standard friction factor correlation for laminar flow is f=64/Re. Hence it is used to find the friction factor in the laminar flow for the parametric study. The correlation equation proposed by Manson [72] is used for the turbulent region. It is not always possible to predict the friction factor in the transition region. As the flow becomes turbulent the relative roughness factor increases with decreasing the friction factor. It has been found that the Reynolds number has very little effect on the friction factor as the flow becomes more turbulent. The friction factor and pressure drop for the uniform arrangement of ripsaw fin with thickness 0.00005 m is 0.472 and 15.01Pa, respectively. The above values are obtained for the Reynolds number of 244 and mass flow rate of $3.148 \cdot 10^{-6} kg \cdot s^{-1}$. Figure 3.61 shows the effect of the Reynolds number on the friction factor, the pressure drop and the average Nusselt number.

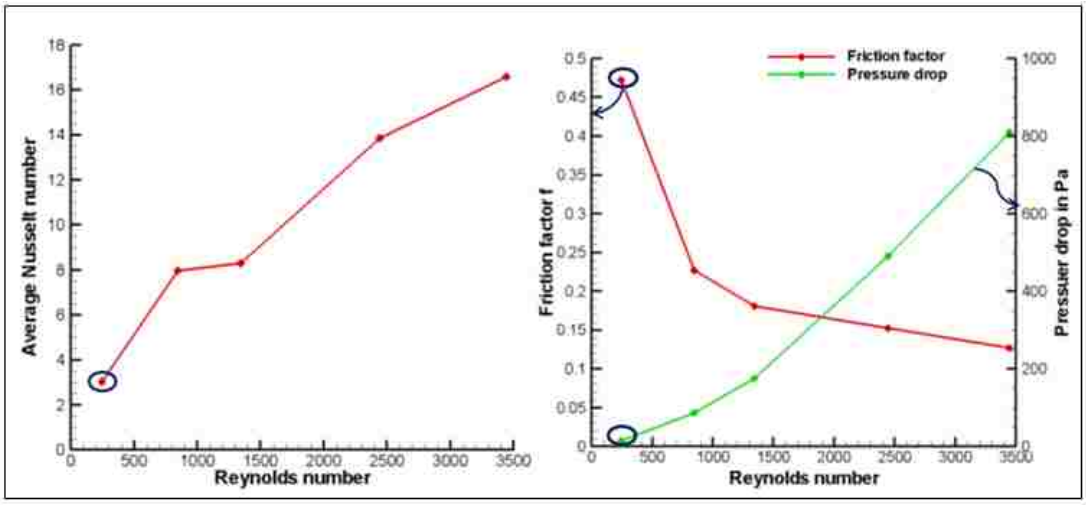

Figure 3.61. Parametric study for uniform arrangement of ripsaw fin with thickness of 0.00005 m.

The energy balance is done for all the cases studied and satisfying results are obtained. Rectangular, triangular, inverted bolt and ripsaw fins with thickness of 0.00005 m gives good fluid flow and heat transfer results. The ripsaw fins with 0.00005 m thickness is selected as the best design since it gives high heat transfer rate with less pressure drop.

3.9 Semi-Analytical Modeling

Semi-analytical study was carried out for the rectangular channel without fins and the obtained results are compared with the numerical results from ANSYS FLUENT.[13] The length of the rectangular channel is 0.006 m and the width is 0.003 m. The Dirichlet boundary condition is applied at the inlet and the Neumann boundary condition is applied at the bottom wall. A no slip boundary condition is applied to walls. Constant heat flux is applied at the top wall and the temperature at the outlet is determined by semi-

analytical method. The inlet temperature is 975 K and constant heat flux of 1000 $W \cdot m^{-2}$ is applied at the top wall. The geometry is segregated into 6 parts and the problem is solved per meter length. The geometry is shown in Figure 3.62.

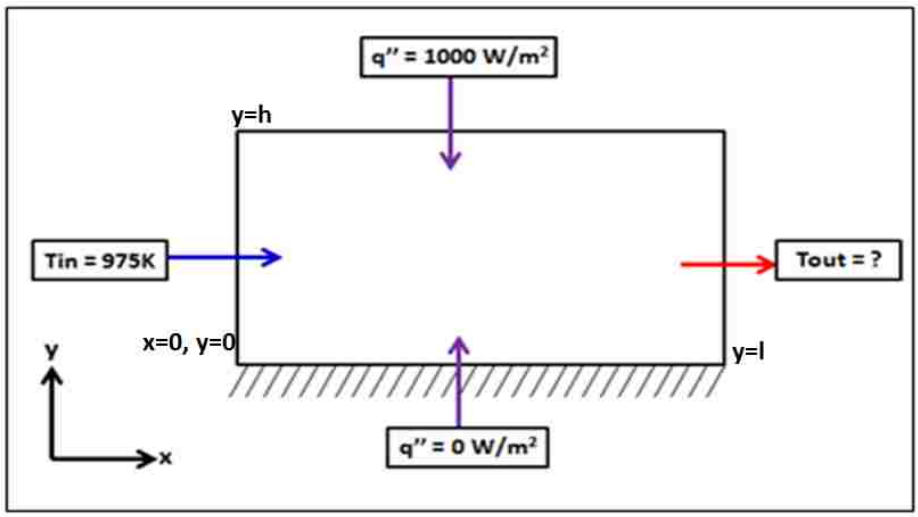

Figure 3.62. Geometry of the rectangular channel.

3.9.1 Continuity equation

The continuity equation is first solved for the problem. The problem studied here is two-dimensional, steady, laminar and incompressible flow. The continuity equation is given by

$$\frac{\partial u}{\partial x} + \frac{\partial v}{\partial y} = 0 \tag{3.13}$$

The fluid flows parallel to the x-direction and hence y=0 and v=0. The continuity equation reduces to

$$\frac{\partial u}{\partial x} = 0 \tag{3.14}$$

3.9.2 Momentum equation

The momentum equation for the two-dimensional flow is given by

$$u\frac{\partial u}{\partial x}+v\frac{\partial u}{\partial y}=-\frac{1}{\rho}\frac{\partial P}{\partial x}+\frac{\mu}{\rho}\left(\frac{\partial^2 u}{\partial x^2}+\frac{\partial^2 u}{\partial y^2}\right) \tag{3.15}$$

$$u\frac{\partial v}{\partial x}+v\frac{\partial v}{\partial y}=-\frac{1}{\rho}\frac{\partial P}{\partial y}+\frac{\mu}{\rho}\left(\frac{\partial^2 v}{\partial x^2}+\frac{\partial^2 v}{\partial y^2}\right) \tag{3.16}$$

After applying the direction of the fluid path and cancelling out the other terms the momentum equation reduces to

$$\frac{\partial P}{\partial x}=\mu\frac{\partial^2 u}{\partial y^2} \tag{3.17}$$

The boundary condition is u=0 at y=0 and u=0 at y=h. No slip boundary condition is applied at the walls. Integrating and applying the boundary condition the above equation reduces to the Poiseuille's flow equation with no-slip boundary condition.

$$u=\frac{1}{2\mu}\left(\frac{\partial P}{\partial x}\right)(y^2-yh) \tag{3.18}$$

3.9.3 Energy equation

$$u\frac{\partial T}{\partial x}+v\frac{\partial T}{\partial y}=\frac{k}{\rho C_P}\left(\frac{\partial^2 T}{\partial x^2}+\frac{\partial^2 T}{\partial y^2}\right) \tag{3.19}$$

After applying along the fluid region the equation reduces to

$$u\frac{\partial T}{\partial x}=\frac{k}{\rho C_P}\left(\frac{\partial^2 T}{\partial x^2}+\frac{\partial^2 T}{\partial y^2}\right) \tag{3.20}$$

The initial analysis involves the semi-analytical method where the profile for the temperature along the x-direction is obtained from FLUENT. The geometry is divided into 6 parts for 0.006m length and the temperature profile is obtained along the x-direction for every 0.001 m length. Figure 3.63 shows the subdivided geometry.

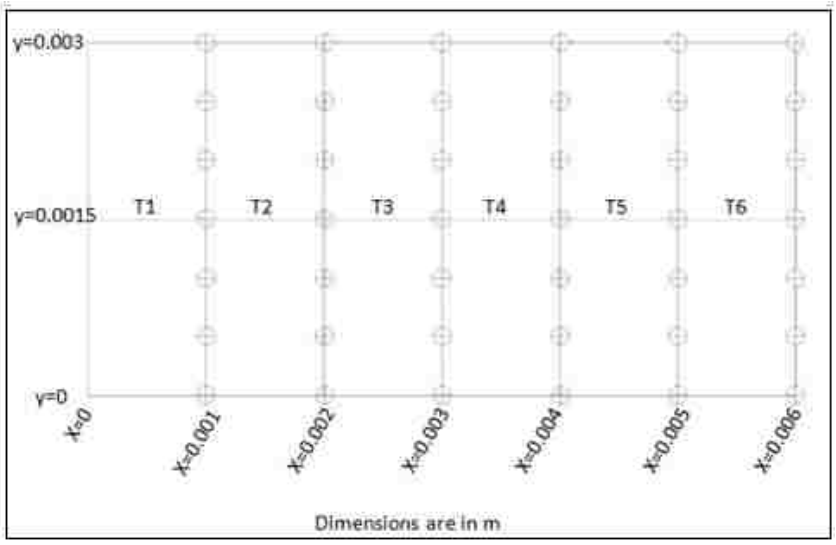

Figure 3.63. Subdivided geometry for the rectangular channel.

The velocity profile u, from the momentum equation is applied in the energy equation is solved. The obtained energy equation will become the linear second order differential equation.

$$\left[\frac{1}{2\mu}\left(\frac{\partial P}{\partial x}\right)\left(y^2 - yh\right)\right]\left(\frac{\partial T}{\partial x}\right) = \frac{k}{\rho C_P}\left(\frac{\partial^2 T}{\partial x^2} + \frac{\partial^2 T}{\partial y^2}\right) \tag{3.21}$$

The temperature profile is obtained from FLUENT at x=0.001 m to 0.006 m. Figure 3.64 shows the temperature obtained from FLUENT.

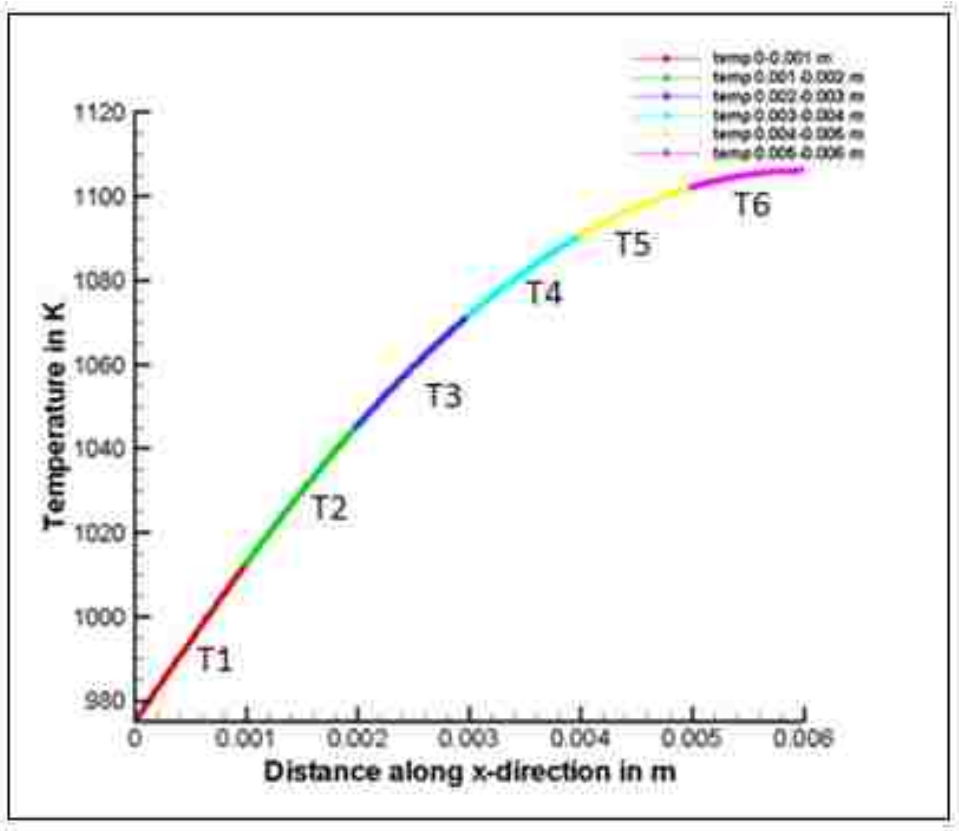

Figure 3.64. Temperature profile obtained from FLUENT.

The obtained temperature at the outlet from the semi-analytical method is compared with the results from the FLUENT. It is found that the minimum error percentage is 3% and the maximum error percentage is around 13%. The error increases with the number of divisions in the geometry. Table 3.8 shows the semi-analytical and the FLUENT results and Table 3.9 shows the obtained percentage of error between the semi-analytical and FLUENT.

Table 3.8

Temperature results for the model

x	0.001		0.002		0.003		0.004		0.005		0.006	
y	Numerical	Analytical	Numerical	Analytical	Numerical	Analytical	Numerical	Analytical	Numerical	Analytical	Numerical	Analytical
0	1007.46	1040.29	1037.74	1087.59	1063.38	1125.9	1081.79	1164.21	1093.26	1202.52	1240.83	1097.25
0.0005	1007.86	1040.53	1038.44	1088.33	1064.23	1126.89	1082.6	1165.20	1093.97	1203.51	1241.81	1097.72
0.001	1009.25	1041.28	1040.73	1090.57	1066.96	1129.89	1085.57	1168.20	1096.96	1206.51	1244.81	1100.74
0.0015	1011.93	1042.52	1044.88	1094.32	1071.72	1134.88	1090.40	1173.19	1102.34	1211.50	1249.81	1106.14
0.002	1016.58	1044.26	1051.49	1099.56	1078.44	1141.87	1098.11	1180.18	1109.60	1218.49	1256.80	1113.41
0.0025	1023.52	1046.50	1060.22	1106.30	1087.64	1150.86	1107.42	1189.16	1118.97	1227.47	1265.78	1122.78
0.003	1033.36	1049.24	1070.81	1114.53	1098.42	1161.84	1118.27	1200.15	1129.81	1238.46	1276.77	1133.61

Table 3.9

Obtained percentage error between the semi-analytical modeling and the numerical result

	Error %					
y	0.001	0.002	0.003	0.004	0.005	0.006
0	3.257	4.803	5.878	7.618	9.993	13.115
0.0005	3.241	4.804	5.887	7.620	10.012	13.126
0.001	3.173	4.789	5.897	7.610	9.985	13.088
0.0015	3.022	4.731	5.893	7.592	9.902	12.988
0.002	2.723	4.571	5.881	7.473	9.812	12.877
0.0025	2.245	4.346	5.812	7.378	9.696	12.736
0.003	1.536	4.082	5.773	7.321	9.616	12.628

CHAPTER 4

STEADY AND TRANSIENT STATE STRUCTURAL ANALYSIS

In this study three-dimensional model is created to simulate, analyze and calculate the induced stresses due to the applied load. In the FEA model, the component is divided into number of elements and each element consists of number of nodes. It is easy to extract the state of stresses at each node or element and use the values obtained to calculate the factor of safety according to the Coulomb-Mohr failure criteria.

4.1 Principal Stress

Brittle materials are used extensively in engineering applications and hence an appropriate failure criterion has to be determined to calculate the failure strength of the brittle materials. In a material the normal stress σ and the shear stress τ vary with direction specified by the angle θ relative to the originally chosen x-y coordinate system. The coordinate axes rotation for the maximum and minimum values of σ is given by the following equation.

$$\tan 2\theta_p = \frac{2\tau_{xy}}{\sigma_x - \sigma_y} \tag{4.1}$$

At certain angle θ_p, the shear stress τ_{xy} becomes zero. The angle is found by setting τ_{xy} to zero in the above shear transformation equation. The angle θ_p defines the principal directions where the only stresses are the normal stresses. These stresses are called the principal stresses and are found from the original stresses. The maximum and minimum principal normal stresses are given by

$$\sigma_1, \sigma_2 = \frac{\sigma_x + \sigma_y}{2} \pm \sqrt{\left(\frac{\sigma_x - \sigma_y}{2}\right)^2 + \tau_{xy}^2} \tag{4.2}$$

The transformation to the principal directions is shown in Figure 4.1.

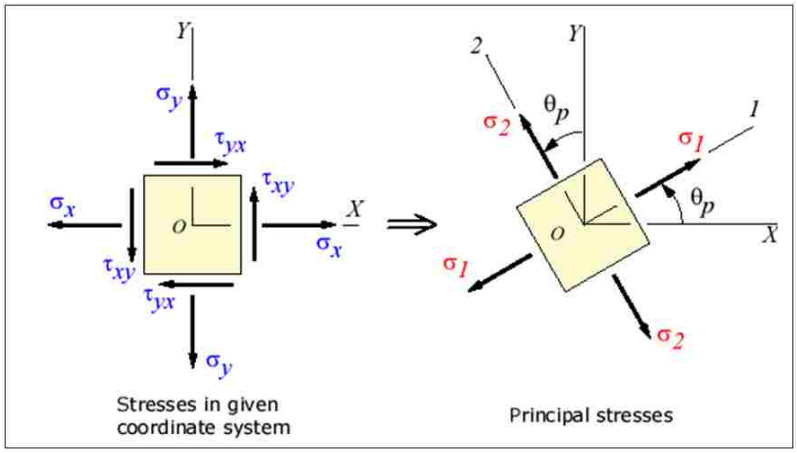

Figure 4.1. Principal normal stresses (Dowling [80]).

The shear stress is zero on the planes where the normal principal stresses occur.

The maximum shear stress is given by

$$\tan 2\theta_s = -\frac{\sigma_x - \sigma_y}{2\tau_{xy}} \tag{4.3}$$

The corresponding shear stress is given by

$$\tau_3 = \sqrt{\left(\frac{\sigma_x - \sigma_y}{2}\right)^2 + \tau_{xy}^2} \tag{4.4}$$

This is the maximum shear stress in the x-y plane and is called the principal shear stress.

4.2 Coulomb-Mohr Failure Criterion

In the Coulomb-Mohr (C-M) failure criterion, fracture is hypothesized to occur on a given plane in the material when a critical combination of shear and normal stress acts on this plane. The mathematical function giving the critical combination of stresses is assumed to be a linear relationship.

$$|\tau| + \mu\sigma = \tau_i \tag{4.5}$$

where τ and σ are the stresses acting on the fracture plane and μ and τ_i are constants for a given material. The equation forms a line on a plot of σ versus $|\tau|$ as shown in Figure 4.2. The intercept with τ axis is τ_i and the slope is $-\mu$ where both τ_i and μ are defined as positive values.

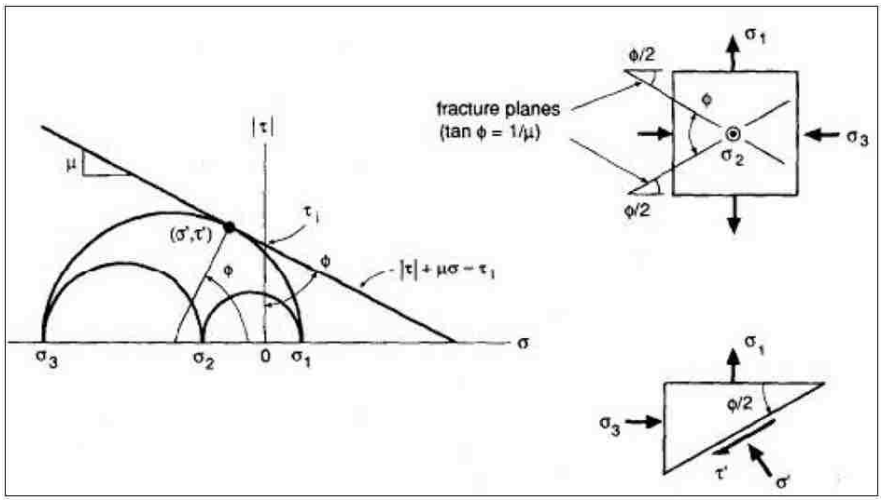

Figure 4.2. Coulomb-Mohr fracture criterion as related to the Mohr's circle (Dowling [80]).

Now consider a set of applied stresses which can be specified in terms of the principal stresses σ_1, σ_2, σ_3 and plot the Mohr's circles for the principal planes on the

same axes. The failure condition is satisfied if the largest of the three circles is tangent to (just touches) to the line. If the largest circle does not touch the line, a safety factor greater than unity exist. Intersection of the largest circle and the line is not permissible as this indicates that failure has already occurred. The line is therefore used to represent the failure envelope for the Mohr's circle. In particular the fracture is expected to occur on a plane that is related to the plane where the maximum principal stress acts by a rotation $\phi/2$ in either direction. The angle ϕ is related to the constant μ by the following equation.

$$\tan\phi = \frac{1}{\mu} \tag{4.6}$$

The C-M theory can be expressed in terms of the principal normal stresses and is given by the equations shown below.

$$\sigma' = \frac{\sigma_1 + \sigma_3}{2} + \left|\frac{\sigma_1 - \sigma_3}{2}\right| \cos\phi \tag{4.7}$$

$$|\tau'| = \left|\frac{\sigma_1 - \sigma_3}{2}\right| \sin\phi \tag{4.8}$$

where σ_1 and σ_3 are assumed to be the maximum and minimum principal normal stresses respectively. The ultimate strength in tension σ_{ut} and ultimate strength in compression σ_{uc} are given below.

$$\sigma_{ut} = \frac{2\tau_u}{1+m} \tag{4.9}$$

$$\sigma_{uc} = \frac{-2\tau_u}{1-m} \tag{4.10}$$

where the new constants m and τ_u are defined as the following

$$m = \frac{\mu}{\sqrt{1+\mu^2}} = \cos\phi \tag{4.11}$$

$$\tau_u = \frac{\tau_i}{\sqrt{1+\mu^2}} = \tau_i \sin\phi \tag{4.12}$$

The C-M criterion with a positive value of μ is consistent with a number of observations that are typical of brittle materials. The difficulties with the C-M theory can be avoided by using the criterion only where the behavior is dominated by compressive stresses. The maximum normal stress criterion is then used where the behavior is dominated by tension. The combined criterion is called the modified Mohr fracture criterion. It has been assumed that m is constant, that is the Mohr failure envelope is straight line. This may not be true for all stress states in real materials and hence caution is needed in employing this idealization.

From the finite element analysis model it will be applicable to extract the nodal solution of the first, second and third principal stresses σ_1, σ_2, σ_3 and determine the state of stress at each node. The output of using the Coulomb-Mohr failure criterion is the factor of safety. The value of the factor of safety must be more than one to prove that the component is safe under this state of stress. Based on the Coulomb-Mohr failure criterion, calculation of the factor of safety depends on the calculated principal stresses σ_1, σ_2, σ_3, the ultimate tensile strength and the ultimate compressive strength. The latter two parameters change with temperature. The component will be safe if the maximum allowable values of the two principle stresses should fall into any one of the four categories as shown in Table 4.1

Table 4.1

Criterion requirements for different cases of principal stresses (Dowling [80])

Case	Principal Stresses	Criterion requirements
Both in tension	$\sigma_1 > 0 , \sigma_3 > 0$	$\sigma_1 > \sigma_{ut} , \sigma_3 > \sigma_{ut}$
Both in compression	$\sigma_1 < 0 , \sigma_3 < 0$	$\sigma_1 > \sigma_{uc} , \sigma_3 > \sigma_{uc}$
σ_1 in tension, σ_3 in compression	$\sigma_1 > 0 , \sigma_3 < 0$	$\frac{\sigma_1}{\sigma_{ut}} + \frac{\sigma_3}{-\sigma_{uc}} < 1$
σ_3 in tension, σ_1 in compression	$\sigma_1 < 0 , \sigma_3 > 0$	$\frac{\sigma_1}{-\sigma_{uc}} + \frac{\sigma_3}{\sigma_{ut}} < 1$

From the finite element analysis model the temperature distribution of the solid part is imported to ANSYS static structural from ANSYS FLUENT. The strength of the heat exchanger material varies with temperature for ceramic (SiC) material. The ultimate tensile and compressive strength varies with the absolute temperature in K according to the equation mentioned below.

$$\sigma_{ut} = (0.0142857)T + 200 \text{ MPa} \tag{4.13}$$

$$\sigma_{uc} = -3\sigma_{ut} \text{ MPa} \tag{4.14}$$

4.3 Steady State Structural Analysis

The geometry of the ceramic plate-fin heat exchanger with different fin designs was shown in the previous chapters. A computational model for single channel is developed to reduce computation load and time. A uniform mass flow rate distribution is assumed for all the plate channels. In this study fluid/thermal analysis of the heat exchanger and the decomposer is carried out in ANSYS FLUENT and stress analysis of

the solid structure is carried out in steady structural analysis of ANSYS. The temperature and pressure distribution of the solid geometry is imported to ANSYS steady structural from ANSYS FLUENT.

4.3.1 Geometry and mesh generation.

The selection of element type plays an important role in determining the stress analysis. The meshing was done in ANSYS WORKBENCH 14.5. Unlike the traditional ANSYS, the ANSYS WORKBENCH has an inbuilt element selection method. It selects appropriate solid elements based on the geometry of the model. Quadratic hexahedron type element or SOLID 186 is chosen for this geometry. SOLID186 is a higher order 3-D 20-node solid element that exhibits quadratic displacement behavior. The element is defined by 20 nodes having three degrees of freedom per node: translations in the nodal x, y, and z directions. The structural geometry of SOLID 186 is shown in Figure 4.3.

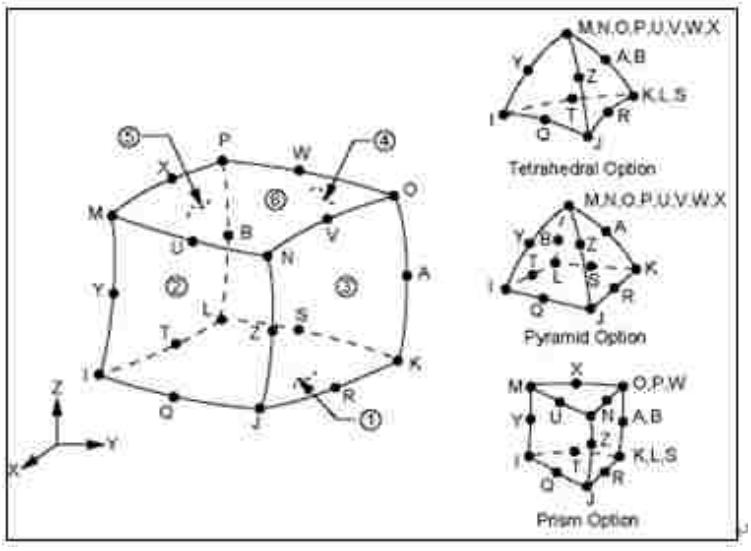

Figure 4.3. ANSYS 20 nodes solid structural element types.

The mesh independent study is done for the solid regions of the ripsaw fin design with thickness of 0.00005 m and from the study 210,901 nodes and 46,502 elements are selected for further meshing. The mesh is mainly refined near the walls where the solid and the fluid regions are in contact. The meshing for the geometry is shown in Figure 4.4.

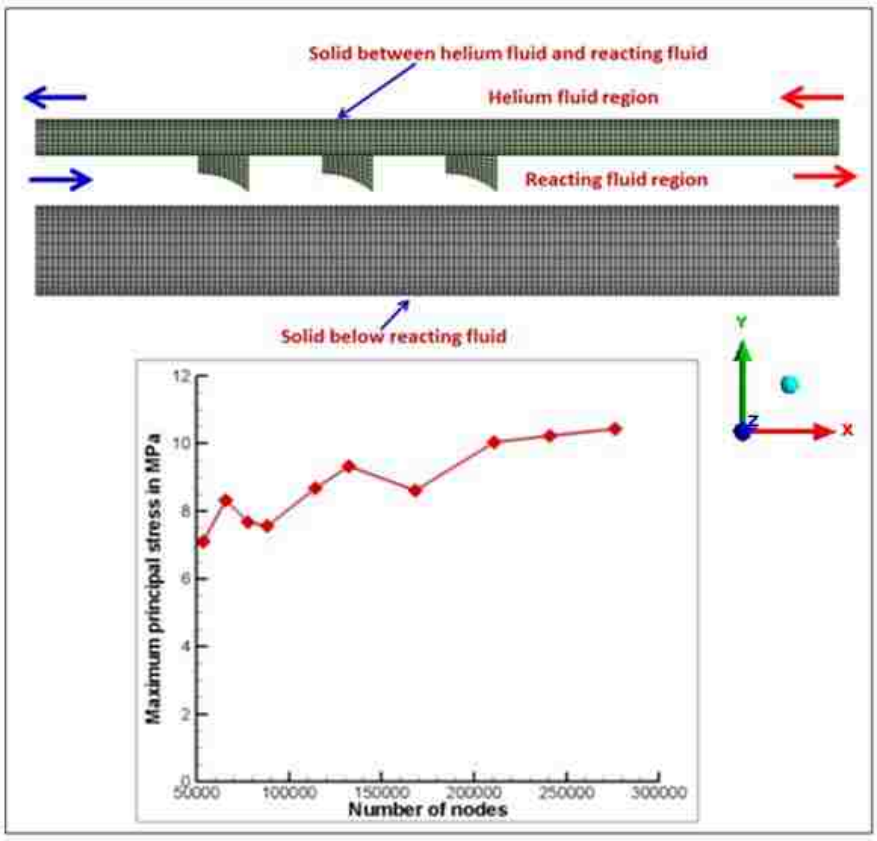

Figure 4.4. Meshing and grid independent study.

4.3.2. Material properties.

Due to the high temperature and the corrosive nature of the plate fin heat exchanger and decomposer the choices of materials that can be used are limited. Corrosive tests indicated that all common metals typically used for constructing high

temperature heat exchangers exhibited very high corrosion rates and were unacceptable for use in this process. Hence silicon carbide is chosen as the material for the solid regions. Silicon carbide is also called carborundum, a black (and green) hex crystal which is extremely hard and sharp with excellent physical and chemical properties. Silicon carbide offers good heat-resistance, heat-conductibility, aseismatic properties, very high wear resistance and has low dilatability. Silicon carbide is quite stable chemically. It can be anti-acid and anti-alkali and it will not react with fuming nitric acid, boiling sulfuric, hydrochloric or hydrofluoric acid. These unique properties of silicon carbide make it an ideal material to be used in a variety of industrial applications today. The material properties of silicon carbide vary with temperature. The equation given below represents the polynomial interpolation of the thermal conductivity of SiC with temperature (Munro [70]):

$$k_{SiC} = 1.9477 \cdot 10^{2} - 3.60612 \cdot 10^{1} \cdot T + 3.30843 \cdot 10^{4} \cdot T^{2} - 1.46006 \cdot 10^{-7} \cdot T^{3} + 2.7588 \cdot 10^{11} \cdot T^{4} \quad (4.15)$$

where T is the absolute temperature in K. Table 4.2 shows the material properties of silicon carbide at different temperatures.

Table 4.2

Material properties of silicon carbide (Green, 1998)

Silicon carbide				
Temperature (°C)	20	500	1000	1200
Density ($kg \cdot m^{-3}$)	3180	3160	3140	3110
Coefficient of thermal expansion (m^{-1})	$1.1 \cdot 10^{-6}$	$4.4 \cdot 10^{-6}$	$5.0 \cdot 10^{-6}$	$5.2 \cdot 10^{-6}$
Youngs modulus (Pa)	$4.15 \cdot 10^{11}$	$4.04 \cdot 10^{11}$	$3.92 \cdot 10^{11}$	$3.87 \cdot 10^{11}$
Poisson's ratio	0.160	0.159	0.157	0.157
Ultimate tensile strength (MPa)		217.47		
Ultimate compressive strength (MPa)		652.42		

4.3.3 Boundary and operating conditions.

The boundary conditions for the temperature and pressure are received from CFD results for heat transfer analysis of the heat exchanger. Thermal load is exported from ANSYS FLUENT (ANSYS [13]) and is applied in the ANSYS steady state structural module for all the fin cases studied here. Studies are carried out for three different fin arrangements namely straight, staggered and top and bottom. In high temperature heat exchangers thermal loads are found to produce higher stresses compared to the mechanical loads. Hence structural analysis is done for three different loads as described below.

1. Imported thermal load and uniform pressure of 1.5 MPa
2. Imported thermal and pressure loads from FLUENT
3. Only pressure load

The applied displacement boundary condition is same for different fin designs, fin arrangements and loads. The solid surface on side of the symmetry is restricted along z-direction, the bottom surface of both the solid regions is restricted along the y-direction. The fins are not restricted and the restriction boundary condition is applied only on the bottom surface for the solid region which is in between the helium and the reacting fluid. A whole restriction is applied along the two vertices at the outlet region of the two solid surfaces. The displacement restrictions are shown in Figure 4.5, Figure 4.6 and Figure 4.7.

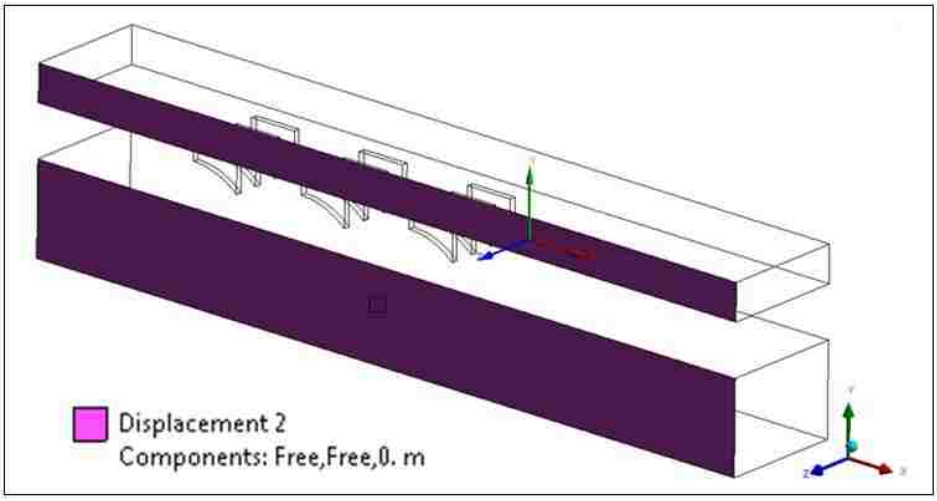

Figure 4.5. Displacement restrictions along z-direction.

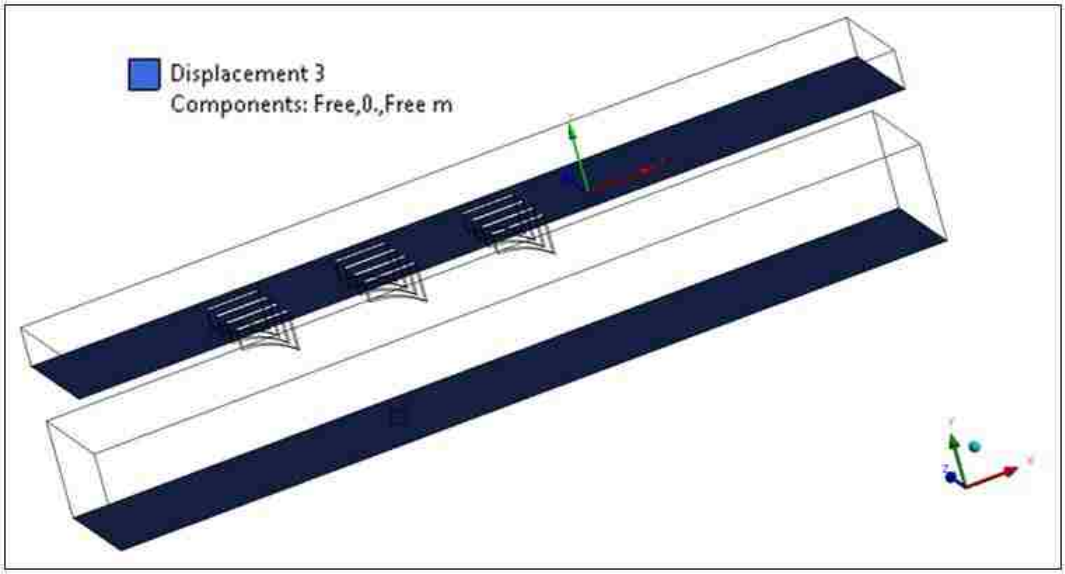

Figure 4.6. Displacement restrictions along y-direction.

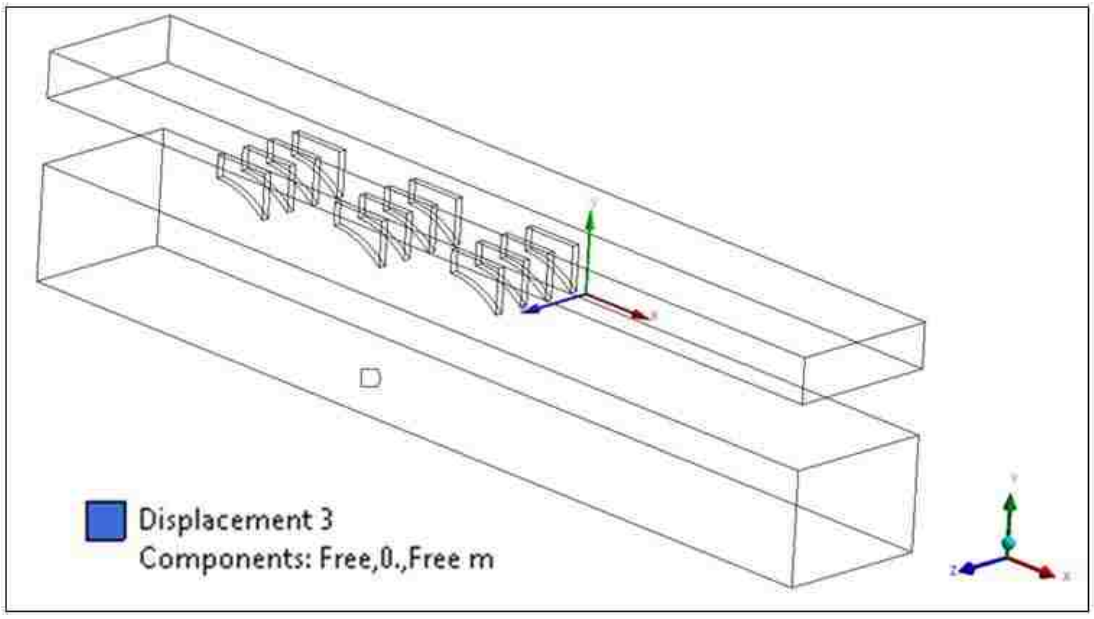

Figure 4.7. Whole body restriction along vertices.

4.4 Imported Thermal Load and Uniform Pressure of 1.5 MPa

The thermal load is imported to the steady state structural module of the ANSYS workbench. The fluids flow in a counterflow manner and hence the temperature of the solid region increases along the axial direction. The temperature gradient is higher for the top solid region with fins than the bottom solid region due to the flow of hot fluid above the top solid region with fins. In addition to that silicon carbide has higher value of thermal conductivity than the thermal conductivity of the fluids. Hence the temperature of the solid part of the decomposer changes in the direction of the flow. It has been found that the thermal conductivity of SiC is around two orders of magnitude higher than the thermal conductivity of fluid. The imported thermal loads for the solid regions for the rectangular, triangular, inverted bolt and ripsaw fin with thickness of 0.00005 m are shown in Figure 4.8, Figure 4.9, Figure 4.10 and Figure 4.11, respectively.

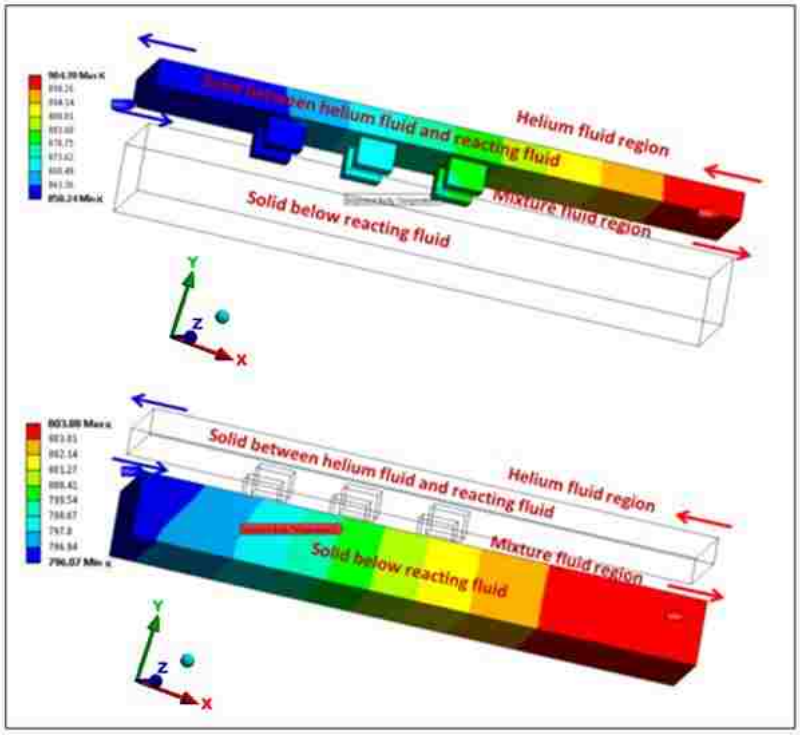

Figure 4.8. Imported thermal load in K for the single channel model with rectangular fins.

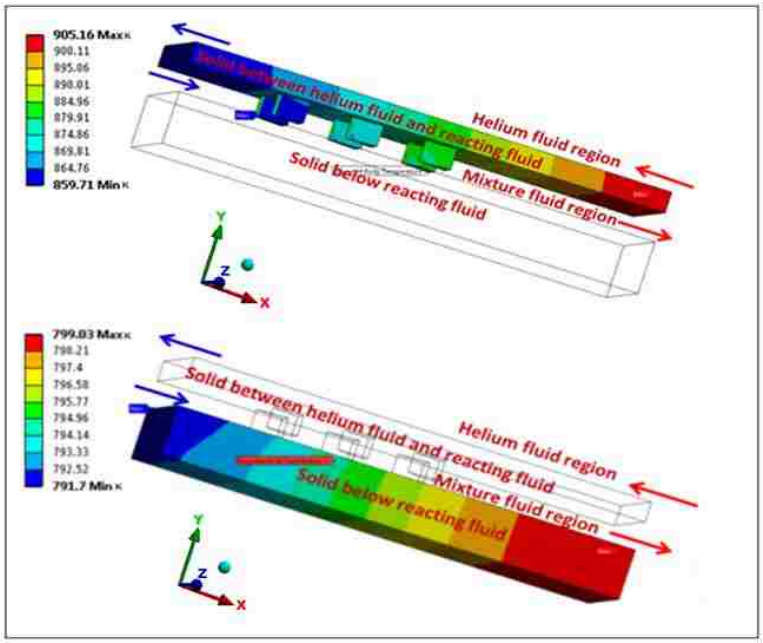

Figure 4.9. Imported thermal load in K for the single channel model with triangular fins.

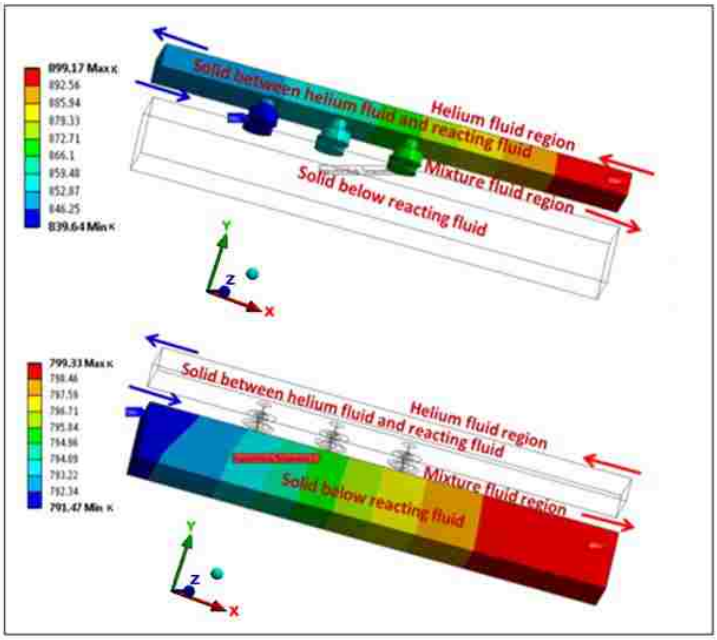

Figure 4.10. Imported thermal load in K with the single channel model for inverted bolt fins.

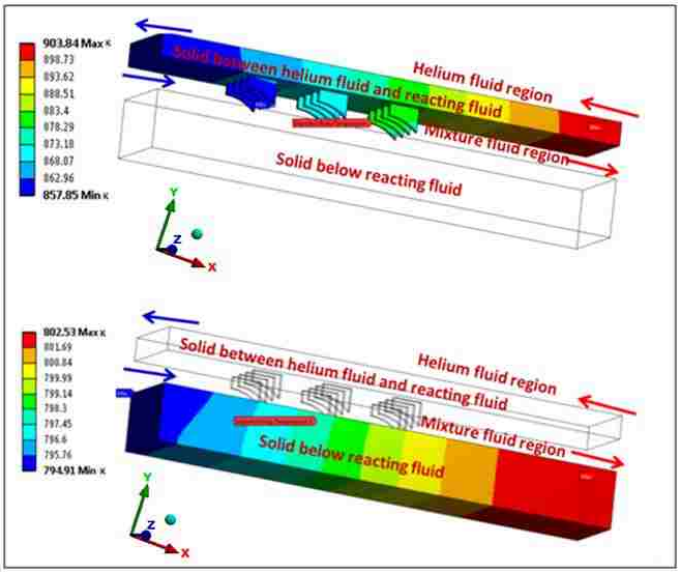

Figure 4.11. Imported thermal load in K with the single channel model for ripsaw fins of 0.00005 m thickness.

The heat transfer analysis in the FLUENT [13] is carried out at an operating pressure of 1.5 MPa. Hence in the initial study uniform pressure of 1.5 MPa is applied to all solid surfaces that are in contact with the fluid. Figure 4.12 shows the pressure load on the straight rectangular fin arrangement.

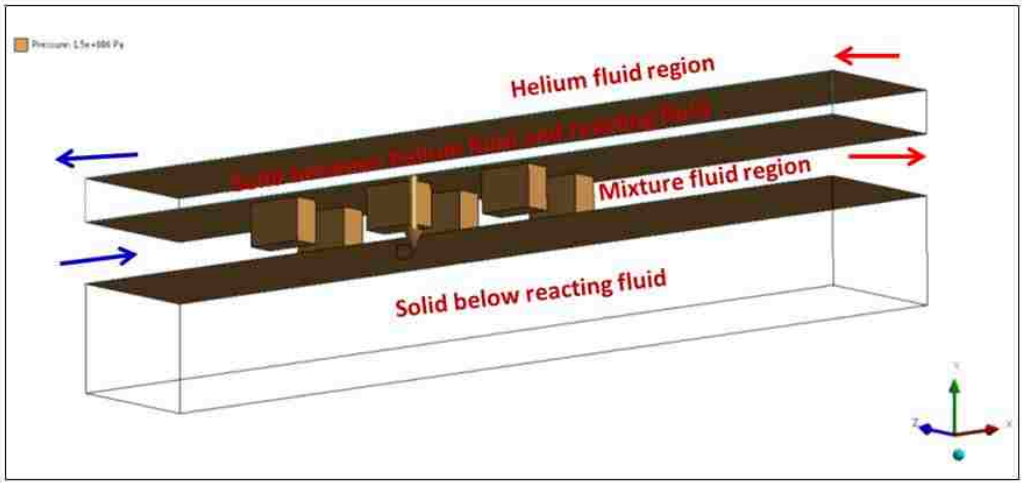

Figure 4.12. Uniform pressure load of 1.5 MPa.

4.4.1 Case 1 (single channel model with rectangular fins)

The maximum principal stress obtained for the single channel model with rectangular fins is 9.247 MPa and the minimum principal stress obtained is 0.3696 MPa. Tensile stress for the first principal stress is significantly above the other two principal stresses. However all the stresses obtained are significantly lesser than the ultimate tensile and compressive strength. It can be seen from Figure 4.13 the stress is high at the point of contact between the fins and the rectangular solid surface. The model will fail first at this point where the principal stress is high. Also the stress increases near the places where there is full body restriction. Since the full body restriction is applied at a

point near the outlet the body deforms along the negative x-direction. The deformation obtained is more on the first fin followed by the second and the third fin. Similarly the principal stress is high on the first fin and it decreases on the second and the third fins. The minimum principal stress is also higher near the fin contact points. Due to the presence of the fins more stress variations are found in the top solid region. The stress is almost uniform for the bottom solid. The obtained maximum principal stress of staggered rectangular fins is 8.89 MPa and the top and bottom rectangular fins are 10.28 MPa. The obtained stresses are similar to the straight arrangement and the stresses are high near the contact points between the fins and the solid surface.

The factor of safety is calculated based on the Coulomb-Mohr failure criterion. The minimum factor of safety obtained is 23.51. The factor of safety is high and hence the material is safe under application of the thermal and mechanical loads for the single channel model with rectangular fins. The minimum factor of safety is 24.43 for staggered arrangement and 21.13 for the top and bottom arrangement. The maximum principal stress obtained for the single channel model with rectangular fins for straight, staggered and top and bottom arrangement are shown in Figure 4.13, Figure 4.14 and Figure 4.15, respectively.

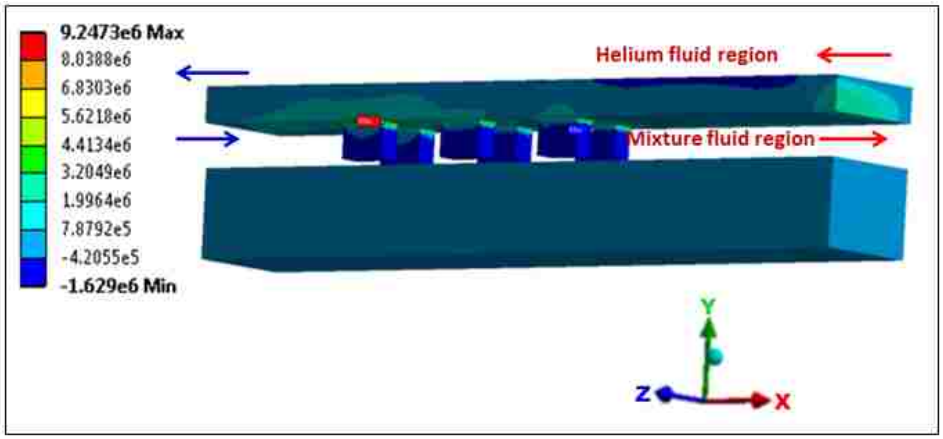

Figure 4.13 .Maximum principal stress (Pa) for single channel model with straight rectangular fins.

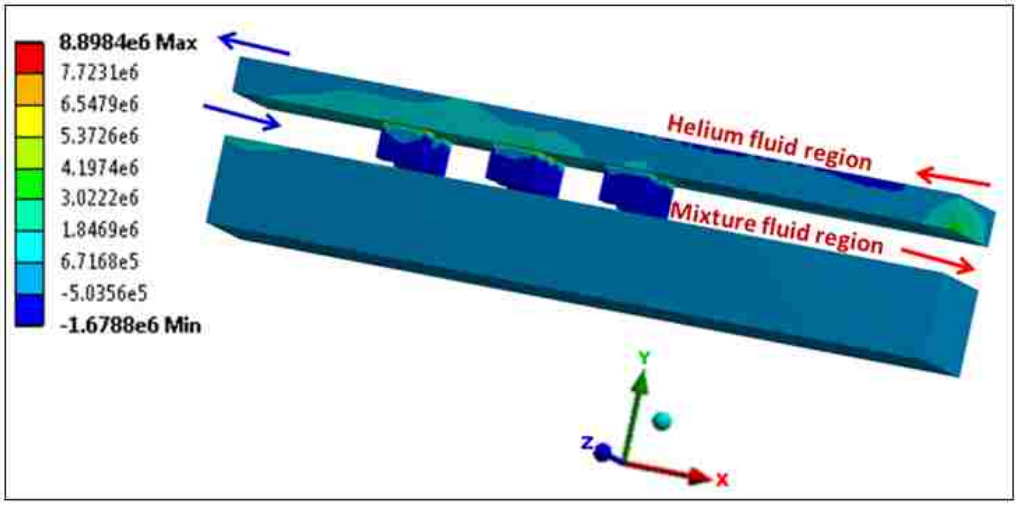

Figure 4.14. Maximum principal stress (Pa) for single channel model with staggered rectangular fins.

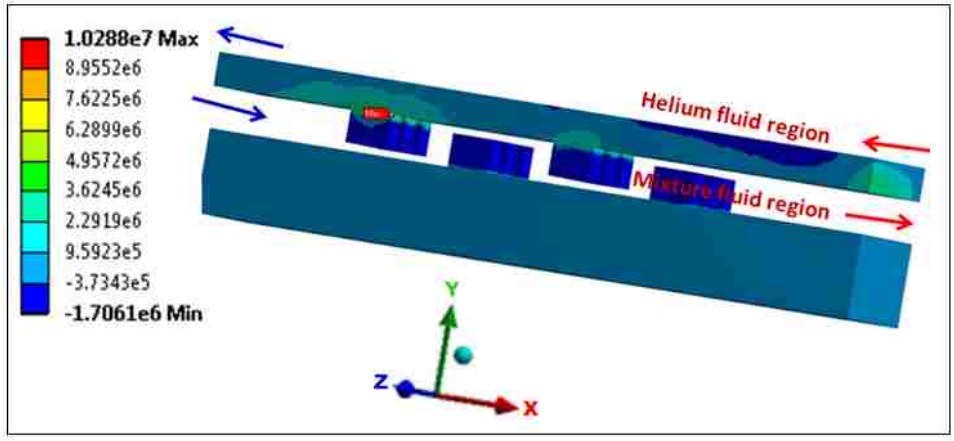

Figure 4.15. Maximum principal stress (Pa) for single channel model with top and bottom arrangement of rectangular fins.

Figure 4 16, Figure 4.17 and Figure 4.18 show the total deformation formed of the rectangular fin channel. The deformation of the solid is high near the inlet of the mixture channel and the outlet of the helium fluid because there are no displacement restrictions at that end. The whole body restriction is applied at points near the outlet of the mixture flow and the inlet of the helium flow channel. Hence deformation is high at the free ends and low at the region of the fixed displacement. The obtained deformation is higher for the case with thermal load compared to the case with only mechanical load. The maximum deformation of 0.0272 mm is obtained due to the high temperature gradient as well the free end which allows the material to expand freely along the axial direction. The total deformation obtained for the staggered and top and bottom rectangular fin arrangement is 0.02718 mm and 0.02702 mm, respectively. The obtained thermal deformation is around 0.027 mm for all fin designs and fin arrangements and it is higher than the deformation produced by the mechanical loads.

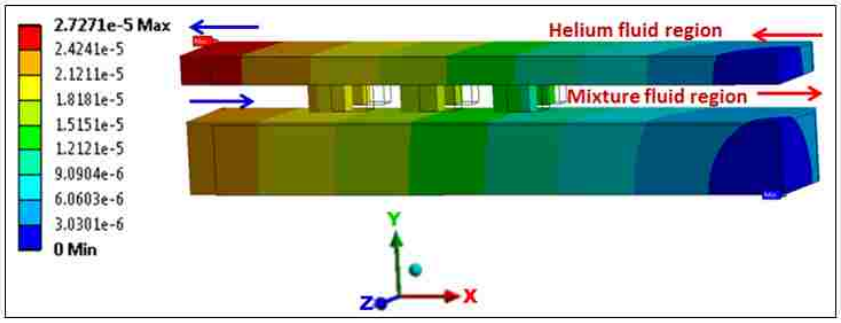

Figure 4 16. Total deformation (m) for single channel model with straight rectangular fins.

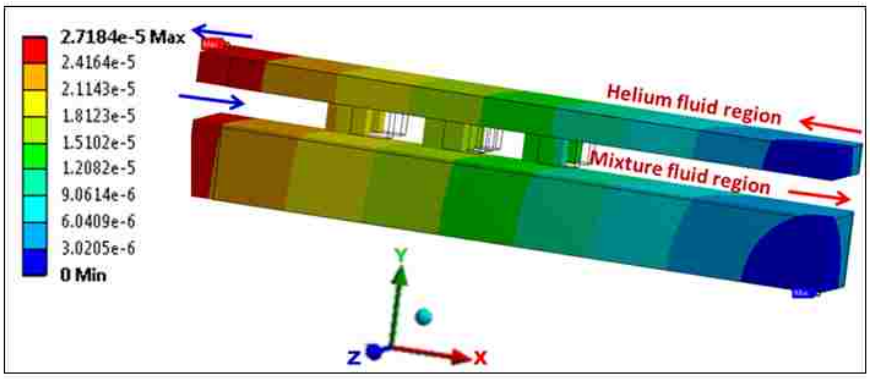

Figure 4.17. Total deformation (m) for single channel model with staggered rectangular fins.

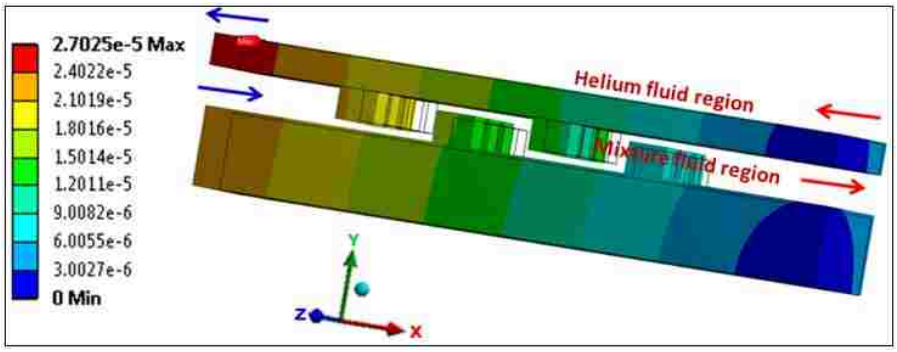

Figure 4.18. Total deformation (m) for single channel model with top and bottom rectangular fins.

4.4.2 Case 2 (Single channel model with triangular fins)

The thermal load for the triangular fins shown in Figure 4.9 is imported into ANSYS steady structural module from FLUENT [13] and uniform pressure of 1.5 MPa is applied for the mechanical load. The maximum principal stress for the straight triangular fin is 16.632 MPa and the minimum principal stress is 4.565 MPa. Due to the sharp corners found in the triangular fins the stress obtained is higher compared to the rectangular fins. The maximum principal stress for the staggered and top and bottom fin arrangement is 22.36 MPa and 15.368 MPa, respectively. The minimum factor of safety is 13.07 for straight triangular fins, 9.72 for staggered triangular fins and 14.15 for top and bottom triangular fins. The obtained safety factor is lesser than all the other fin designs. The reason for the low factor of safety is due to the formation of high thermal stress and increase in temperature difference between the fins and the contact surface. Figure 4.19, Figure 4.20 and Figure 4.21 show the maximum principal stress for uniform, staggered and top and bottom fin arrangement, respectively.

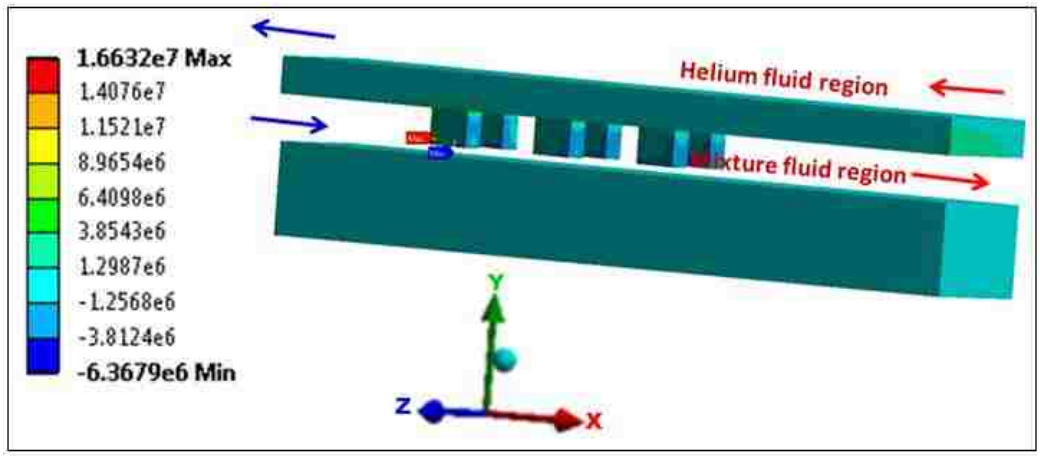

Figure 4.19. Maximum principal stress (Pa) for single channel model with straight triangular fins.

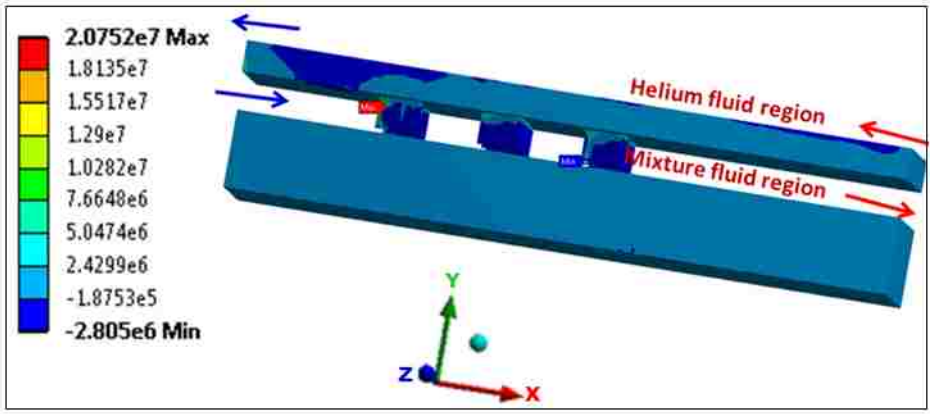

Figure 4.20. Maximum principal stress (Pa) for single channel model with staggered triangular fins.

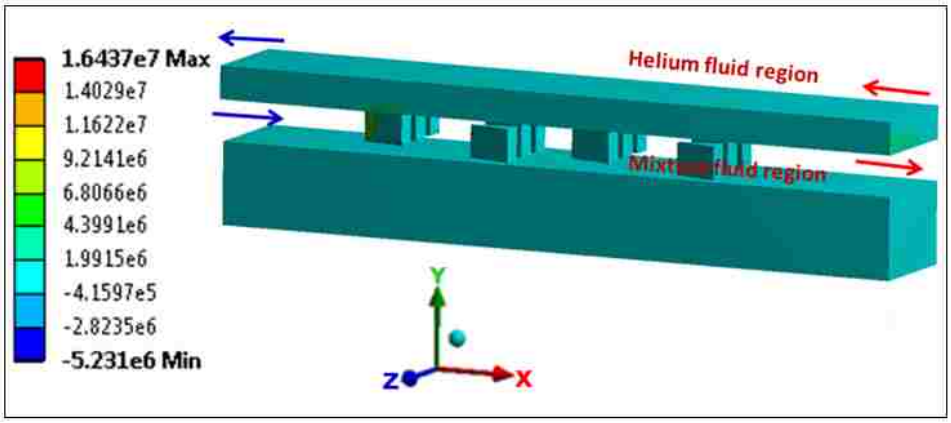

Figure 4.21. Maximum principal stress (Pa) for single channel model with top and bottom triangular fin arrangement.

The total deformation of 0.0272 mm obtained for all the triangular fin arrangements are similar to the rectangular fins and the material deforms along the free end of the solid surface. Figure 4.22, Figure 4.23 and Figure 4 24 show the total deformation obtained for the single channel model for uniform, staggered and top and bottom triangular fins, respectively.

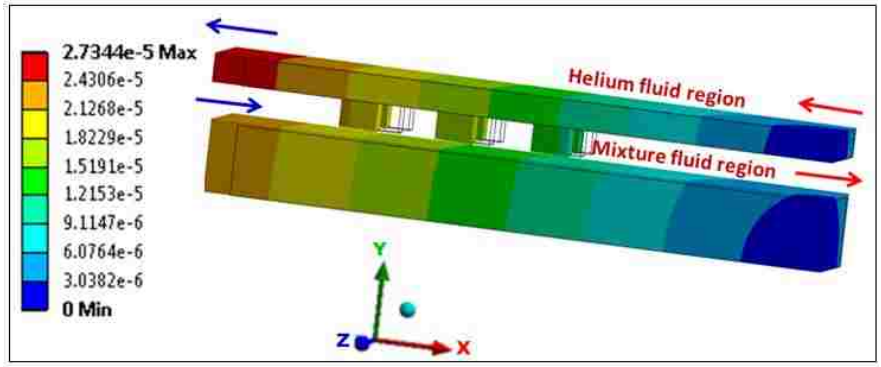

Figure 4.22. Total deformation (m) for single channel model with uniform triangular fins.

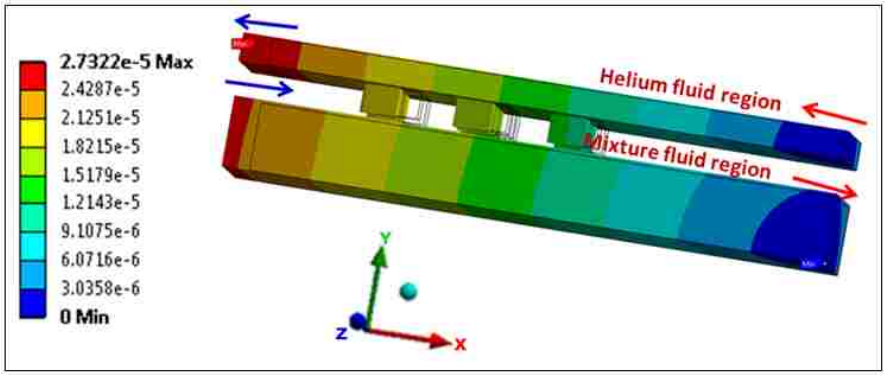

Figure 4.23. Total deformation (m) for single channel model with staggered triangular fins.

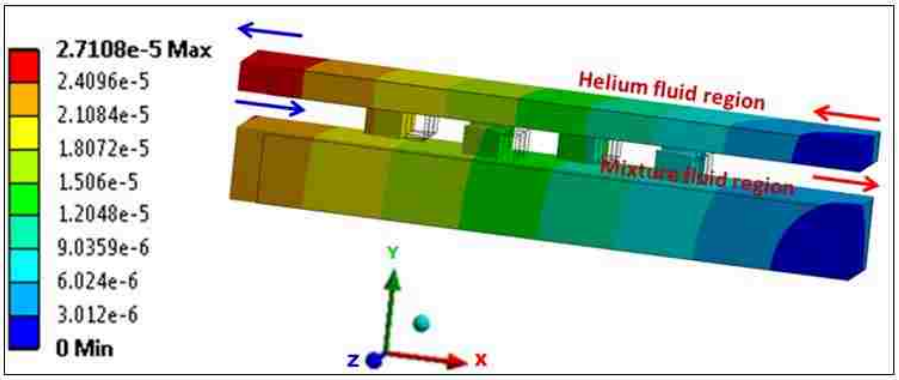

Figure 4 24. Total deformation (m) for single channel model with top and bottom triangular fins.

4.4.3 Case 3 (Single channel model with inverted bolt fins)

The maximum principal stress obtained for the straight inverted bolt fins is 9.465 MPa, staggered inverted bolt fins is 6.158 MPa and the top and bottom arrangement of the inverted bolt fins is 7.839 MPa. The stress obtained is similar to the rectangular fins. Figure 4.25, Figure 4.26 and Figure 4.27 show the maximum principal stress for the single channel model with straight inverted bolt fins, staggered inverted bolt fins and top and bottom arrangement of the inverted bolt fins, respectively. From the results it can be seen that the stresses are high near the first row of fin and near the fixed point restriction. The whole body restriction is applied near the outlet of the cold fluid flow and hence the material expands freely along the negative x-direction. Due to the expansion in the negative x-direction and the restriction on one side of the symmetrical solid surface the principal stress is maximum for the first fin. The safety factor for the straight fin arrangement is 22.97, staggered fin arrangement is 35.30 and top and bottom fin arrangement is 27.74. Since the stress obtained is less for the staggered fins the safety factor is high compared to the other two arrangements and hence it is relatively a good design. But the disadvantage in using this type of fins is the high friction factor and pressure drop. The total deformation obtained for all the three fin arrangements is 0.027 mm. The material expands freely in the free end along the negative x-direction. Since the total deformation obtained is similar to the rectangular and triangular fins figures are shown only for the principal stress.

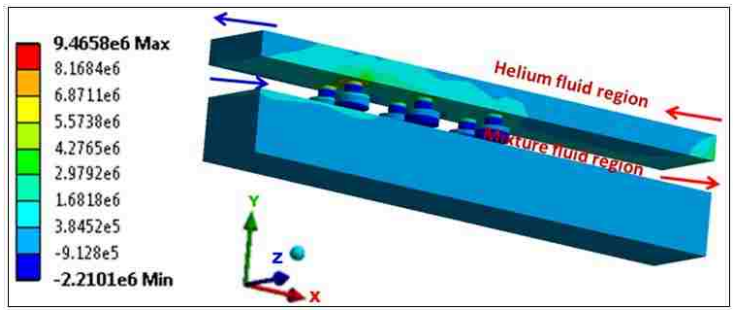

Figure 4.25. Maximum principal stress (Pa) for single channel model with straight inverted bolt fins.

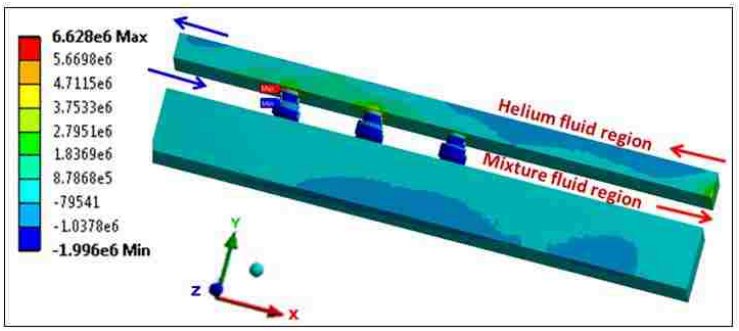

Figure 4.26. Maximum principal stress (Pa) for single channel model with staggered inverted bolt fins.

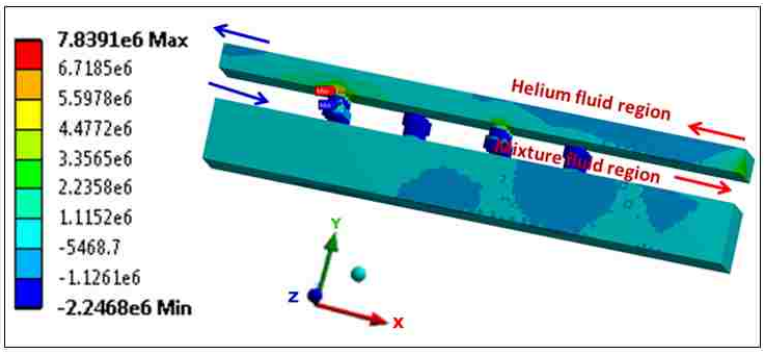

Figure 4.27. Maximum principal stress (Pa) for single channel model with top and bottom arrangement of inverted bolt fins.

4.4.4 Case 4 (Single channel model with ripsaw fins)

The maximum thermal stress for the ripsaw fins with thickness of 0.00005 m is 10.042 MPa for straight arrangement, 9.903 MPa for staggered ripsaw fin arrangement and 11.438 MPa for top and bottom ripsaw fin arrangement, respectively. The stresses obtained are higher than the rectangular and the inverted bolt fins. However they are less than the triangular fin arrangement. This design model is selected as the best design because the stress obtained is not very high and they produce good heat transfer with the minimum pressure drop and the friction factor. The obtained safety factor is 21.80, 21.95 and 19.01 for straight ripsaw fin, staggered ripsaw fin and top and bottom fin arrangement, respectively. The safety factor is less for the top and bottom fin arrangement due to the presence of more fins and the thickness of the fins. The decrease in safety factor is due to the increase in temperature difference and induced stress between the contact surface of the fins and the solid surface. The total deformation obtained for both the fins are similar around 0.027 mm. Figure 4.28, Figure 4.29 and Figure 4.30 show the maximum principal stress for the ripsaw fin with thickness of 0.00005 m for straight, staggered and top and bottom fin arrangement, respectively.

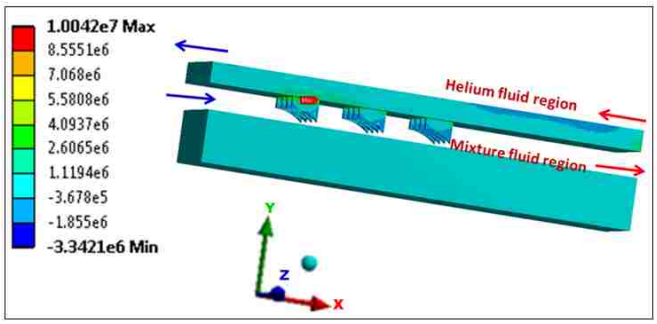

Figure 4.28. Maximum principal stress (Pa) for straight ripsaw fin with thickness of 0.00005 m.

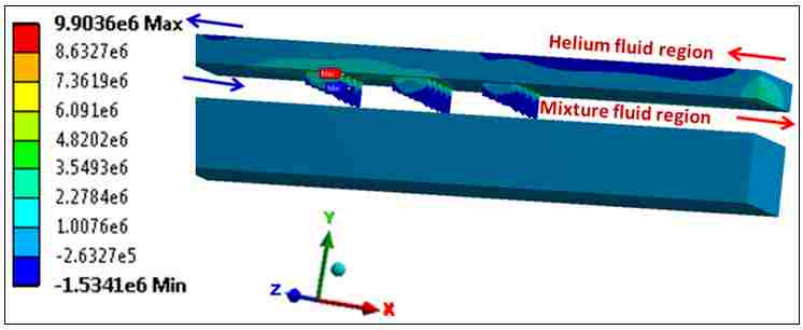

Figure 4.29. Maximum principal stress (Pa) for staggered ripsaw fin with thickness of 0.00005 m.

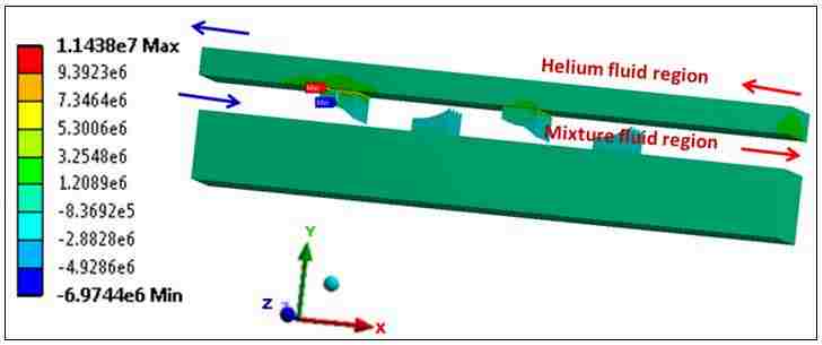

Figure 4.30. Maximum principal stress (Pa) for top and bottom arrangement of ripsaw fin with thickness of 0.00005 m.

4.4.5 Case 6 (Single channel model with ripsaw fin with thickness of 0.0002 m, bolt fins, ripsaw fin fan type arrangement)

Bolt fins have the lowest principal stress and the highest safety factor. The maximum principal stress obtained for straight bolt fin is 5.038 MPa and the safety factor is 45.389, respectively. Even though the stress obtained is less and the model is best compared to other fins the pressure drop and the friction factor are high. Another study has been done by increasing the thickness of the ripsaw fins (0.00005 m) to four times the

fin thickness (0.0002 m). The maximum principal stress for the ripsaw fin with thickness of 0.0002 m is 7.100 MPa and the safety factor is 30.63. The ripsaw fin fan type arrangement has the maximum principal stress of 7.922 MPa and the safety factor is 28.283.

Table 4.3 shows the maximum principal stress and the safety factor for all the models with imported thermal load and uniform pressure of 1.5 MPa. The minimum principal stress for staggered and top and bottom ripsaw fin with thickness of 0.00005 m is negative indicating the formation of compressive stress.

Table 4.3

Principal stress and safety factor for all fin designs with imported thermal load and uniform pressure of 1.5 MPa

Imported thermal and pressure load of 1.5 MPa				
Fins	Maximum principal stress (MPa)	Minimum principal stress (MPa)	Total deformation (mm)	Safety factor
Straight rectangular fin	9.247	0.369	0.027	23.51
Staggered rectangular fin	8.898	0.565	0.027	24.43
Top and bottom rectangular fin	10.288	0.572	0.270	21.13
Straight triangular fin	16.632	4.565	0.027	13.07
Staggered triangular fin	20.619	5.242	0.027	10.54
Top and bottom triangular fin	15.368	1.227	0.027	14.15
Straight inverted bolt fins	9.465	3.428	0.026	22.97
Staggered inverted bolt fins	6.628	1.574	0.026	32.81
Top and bottom inverted bolt fins	7.839	1.642	0.026	27.74
Straight ripsaw fin thickness of 0.00005 m	10.085	-0.124	0.027	21.80
Staggered ripsaw fin thickness of 0.00005 m	9.903	-0.145	0.027	21.95
Top and bottom ripsaw fin with thickness of 0.00005 m	11.438	3.282	0.027	19.01

The worst safety factor is obtained at the point of contact between the fins and the solid surface. Triangular fins have the least value of safety factor and the value of the safety factor is more than 10 for all the other fin designs. The mesh nodes and elements are selected after the grid independent study. Due to the higher temperature difference the temperature gradient obtained is higher for the solid region located below the helium fluid. The temperature gradient and grid dimensions for all the fin designs and arrangements are shown in Table 4.4.

Table 4.4

Temperature gradient and grid dimensions for all the models

Imported thermal and uniform pressure of 1.5 MPa				
Fins	Mesh nodes	Mesh elements	Solid between helium and mixture temperature gradient ($K \cdot mm^{-1}$)	Solid below mixture temperature gradient ($K \cdot mm^{-1}$)
Straight rectangular fin	209,569	46,430	7.138	1.208
Staggered rectangular fin	210,457	46,598	7.520	1.619
Top and bottom rectangular fin	215,234	47,544	7.618	1.466
Straight triangular fin	209,569	46,430	7.138	1.208
Staggered triangular fin	210,457	46,598	7.520	1.619
Top and bottom triangular fin	212,715	46,954	7.613	1.446
Straight inverted bolt fin	216,492	47,706	9.208	1.215
Staggered inverted bolt fin	241,375	53,534	7.701	1.529
Top and bottom inverted bolt fins	243,020	54,156	8.145	1.396
Straight ripsaw fin thickness of 0.00005 m	210,901	46,502	6.821	1.410
Staggered ripsaw fin thickness of 0.00005 m	212,590	46,844	7.096	1.426
Top and bottom ripsaw fin with thickness of 0.00005 m	217,118	47,676	7.036	1.127

4.5 Imported Thermal Load and Imported Pressure Load from FLUENT

The thermal and the pressure loads are imported from FLUENT. The pressure load is applied to all the surfaces that are in contact with the fluid. The imported pressure load is similar for all the fin designs and arrangements and hence only top and bottom arrangement of ripsaw fin with thickness of 0.00005 m is shown in Figure 4.31.

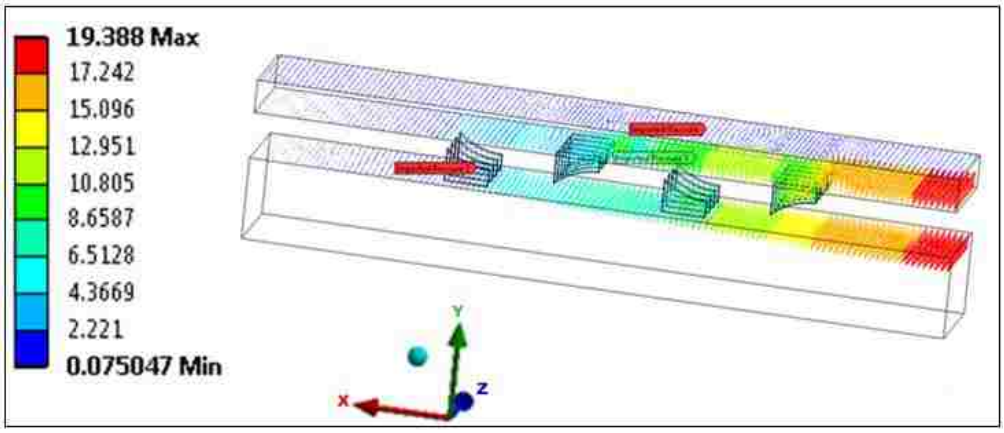

Figure 4.31. Imported pressure load (Pa) for top and bottom ripsaw fin arrangement from FLUENT [13].

The maximum principal stresses obtained for straight, staggered and top and bottom rectangular fin arrangements are 8.198 MPa, 8.898 MPa and 9.221 MPa, respectively. Figure 4.32 shows the maximum principal stress for the top and bottom rectangular fins. From the results it can be seen that the obtained principal stress with the imported pressure load is less than or equal to the stress obtained for the rectangular fins with uniform pressure of 1.5 MPa. The safety factor obtained for straight rectangular fin, staggered rectangular fin and top and bottom arrangement fin is 26.55, 24.23 and 23.58, respectively. It is found that unlike the thermal load, the pressure load does not have

much impact on the stresses produced. The stress obtained is almost similar for the model with imported thermal load and uniform pressure of 1.5 MPa and for the model with imported thermal and pressure loads.

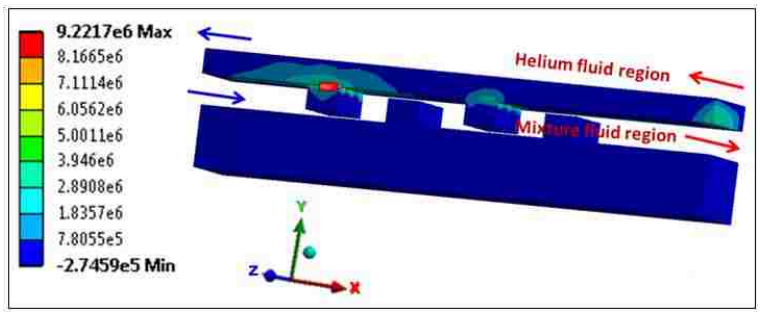

Figure 4.32. Maximum principal stress (Pa) for single channel model with top and bottom rectangular fins.

From Figure 4.32 it can be seen that the stress is high on the top solid surface with fins. The stress is minimum on the bottom solid surface with fins. One reason for this occurrence is due to the high thermal gradient on the top solid surface compared to the bottom surface. The temperature gradient for the top solid surface is 7.618 $K \cdot mm^{-1}$ and the bottom solid surface is 1.466 $K \cdot mm^{-1}$. Since thermal load is more significant than the pressure load more stress variation is found on the top solid surface with fins.

The maximum principal stress obtained for the triangular fin with the imported pressure load is slightly higher than those obtained using uniform pressure load of 1.5 MPa. The maximum principal stress for the straight triangular fin is 18.115 MPa, staggered triangular fin is 22.360 MPa and top and bottom triangular fin arrangement is 16.437 MPa. Due to the sharp edges in the triangular fin the pressure drop and the friction factor are also high. The triangular fin is not a good design since it has higher

stress, high pressure drop and friction factor. The minimum safety factor for the straight, staggered and top and bottom arrangement is 12.004, 9.725 and 13.230, respectively. The safety factor is less due to the increase in temperature difference and induced stress between the fins and the solid surface. Figure 4.33 shows the maximum principal stress for the top and bottom arrangement of the triangular fins.

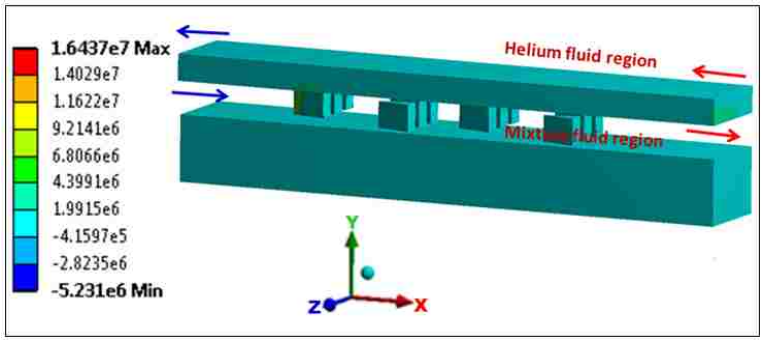

Figure 4.33. Maximum principal stress (Pa) for the single channel model with top and bottom triangular fin arrangement.

The maximum principal stress of the straight, staggered and top and bottom inverted bolt fins are 9.465 MPa, 6.158 MPa and 9.309 MPa, respectively. The safety factor obtained is 22.97, 35.30 and 27.74, respectively which are similar to the stress obtained from uniform pressure of 1.5 MPa. The total deformation of all the three arrangements is around 0.026 mm. Figure 4.34 shows the maximum principal stress for the top and bottom arrangement of the inverted bolt fins.

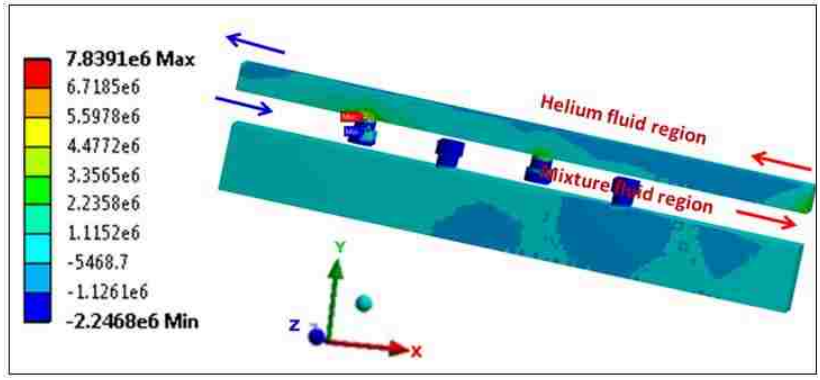

Figure 4.34. Maximum principal stress (Pa) for single channel model with top and bottom arrangement of inverted bolt fins.

The maximum principal stress of the straight, staggered and top and bottom ripsaw fin with thickness of 0.00005 m is 10.042 MPa, 9.038 MPa and 11.438 MPa, respectively. The safety factor obtained is 21.65, 24.06 and 18.83, respectively. The stress obtained is similar to the model with imported thermal load and uniform pressure of 1.5 MPa. The total deformation obtained is around 0.0272 mm. Due to the shape of the fins and their sharp corners the stress obtained are higher than rectangular and inverted bolt fins. However the factor of safety is high and the model is safe to work under high pressure and temperature. Figure 4.35 shows the maximum principal stress for the top and bottom arrangement of the ripsaw fins with thickness of 0.00005 m. As mentioned before due to the higher temperature gradient for the top solid surface higher stress is found in the top solid surface. Figure 4.36 shows the total deformation for the top and bottom arrangement of the ripsaw fins.

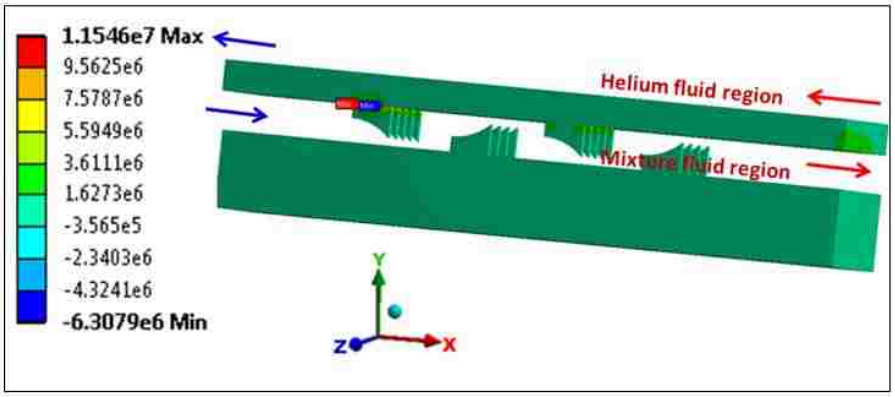

Figure 4.35. Maximum principal stress (Pa) for the single channel model with top and bottom ripsaw fins.

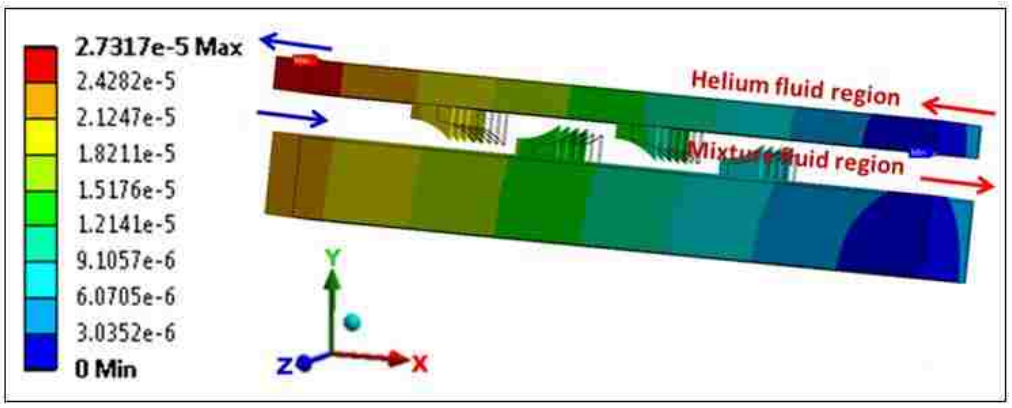

Figure 4.36. Total deformation (m) for the single channel model with top and bottom ripsaw fins.

From the results it is observed that inverted bolt fins and rectangular fins have lower stress followed by ripsaw fins with thickness of 0.00005 m. The minimum safety factor is around 11 to 15 for all the models except triangular fins. The obtained worst safety factor for the triangular fins is 9.119. The triangular fins have the highest stress and the lowest safety factor. Table 4.5 shows the principal stress and the safety factor for all the fin designs.

Table 4.5

Principal stress and safety factor for all fin designs

Imported thermal and pressure load				
Fins	Maximum principal stress (MPa)	Minimum principal stress (MPa)	Total deformation (mm)	Safety factor
Straight rectangular fin	8.189	1.691	0.0272	26.55
Staggered rectangular fin	8.898	0.565	0.0271	24.53
Top and bottom rectangular fin	9.221	1.791	0.0270	23.58
Straight triangular fin	18.115	5.595	0.0274	12.00
Staggered triangular fin	22.360	6.559	0.0273	9.72
Top and bottom triangular fin	16.437	2.519	0.0271	13.20
Straight inverted bolt fins	9.465	3.428	0.0269	22.97
Staggered inverted bolt fins	6.158	2.806	0.0269	35.30
Top and bottom inverted bolt fins	9.309	2.972	0.0269	23.36
Straight ripsaw fin thickness of 0.00005 m	10.042	1.140	0.0270	21.65
Staggered ripsaw fin thickness of 0.00005 m	9.038	1.123	0.0274	24.04
Top and bottom ripsaw fin with thickness of 0.00005 m	11.546	4.072	0.0273	18.83

4.6 Imported Pressure Load

Another study is done to study the effect of only pressure load on the heat exchanger model. It is found that the mechanical stresses obtained using the imported pressure boundary condition from FLUENT is negligible compared to the thermal stresses. Due to lower stress very high value of the safety factor is obtained. The total deformation obtained is very small and is almost negligible. Hence it can be concluded that the high temperature loads are the main reason to cause high stress rather than the pressure loads in the high temperature plate-fin heat exchanger. Figure 4.37 shows the maximum principal stress for the top and bottom ripsaw fins. It can be seen that the maximum stress is found on the fixed full body restriction point.

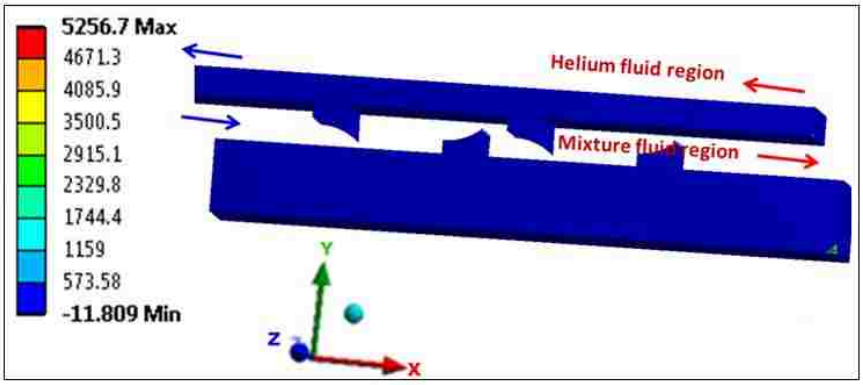

Figure 4.37. Maximum principal stress (Pa) for single channel model with top and bottom ripsaw fins.

The total deformation for the top and bottom ripsaw fins is shown in Figure 4.38. The deformation obtained is different from the thermal deformation. The imported pressure is applied on the top and the bottom surface of the top solid and on the top surface of the bottom solid region. More deformation is found in the bottom solid region. Due to the applied pressure direction the bottom solid is deformed along the positive axial direction and the top solid is deformed along the negative axial direction.

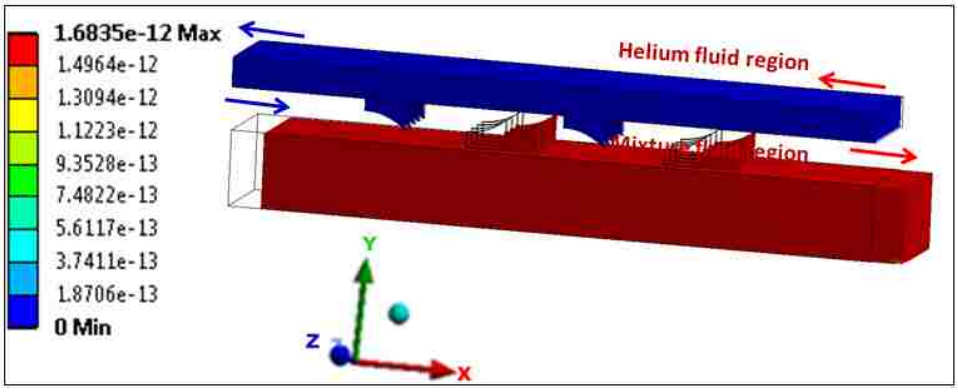

Figure 4.38. Total deformation (m) for single channel model with top and bottom ripsaw fins.

Table 4.6 shows the principal stress and deformation obtained for the models with imported pressure load. The staggered triangular fin and the straight inverted bolt fins have negative minimum principal stress indicating the obtained stress is compressive.

Table 4.6

Principal stress and total deformation for all fin designs

Fins	Maximum principal stress (MPa)	Minimum principal stress (MPa)	Total deformation (m)
Straight rectangular fin	0.026	$2.64 \cdot 10^{-07}$	$2.06 \cdot 10^{-09}$
Staggered rectangular fin	0.026	$2.67 \cdot 10^{-07}$	$4.66 \cdot 10^{-06}$
Top and bottom rectangular fin	0.017	$9.16 \cdot 10^{-06}$	$5.72 \cdot 10^{-09}$
Straight triangular fin	0.026	$2.64 \cdot 10^{-07}$	$2.06 \cdot 10^{-09}$
Staggered triangular fin	0.066	$8.09 \cdot 10^{-06}$	$5.32 \cdot 10^{-09}$
Top and bottom triangular fin	0.012	$8.95 \cdot 10^{-06}$	$3.89 \cdot 10^{-09}$
Straight inverted bolt fins	0.566	-1.30	$4.65 \cdot 10^{-06}$
Staggered inverted bolt fins	0.008	$2.80 \cdot 10^{-06}$	$3.18 \cdot 10^{-09}$
Top and bottom inverted bolt fins	0.017	$6.10 \cdot 10^{-06}$	$5.77 \cdot 10^{-09}$
Straight ripsaw fin thickness of 0.00005 m	0.003	$4.86 \cdot 10^{-07}$	$1.11 \cdot 10^{-09}$
Staggered ripsaw fin thickness of 0.00005 m	0.003	$5.89 \cdot 10^{-07}$	$1.13 \cdot 10^{-09}$
Top and bottom ripsaw fin with thickness of 0.00005 m	0.005	$3.69 \cdot 10^{-06}$	$1.68 \cdot 10^{-09}$

4.7 Transient Analysis of All the Fins

The thermal performance of the industrial heat exchangers is evaluated by analyzing the heat exchangers in the transient state. The transient analysis is carried out when the conventional steady state testing procedures becomes impossible or not

feasible. Due to the presence of very small channels the stress analysis evaluation of the high temperature heat exchanger in the transient state has become particularly important. In any heat exchanger the maximum stress occurs at the startup and shut down conditions. Hence it is very important to find the maximum principal stress and the factor of safety at the start up and shut down process in addition to the steady state conditions. The factor of safety for the transient state is calculated from the stresses based on the Mohr-Coulomb failure criteria. From the previous studies it is found that the proposed design is safe at the steady state operating conditions. The fluid flow and heat transfer analysis is carried out under the transient state condition in FLUENT. The results for 0, 10, 50, 80 and 100 seconds are calculated and the obtained heat transfer results are imported to ANSYS structural module to calculate the induced stress and the factor of safety at different time steps. Figure 4.39 shows the setup of the above model in the ANSYS WORKBENCH. The results obtained at each time step is imported to the ANSYS structural setup and the structural analysis is carried out.

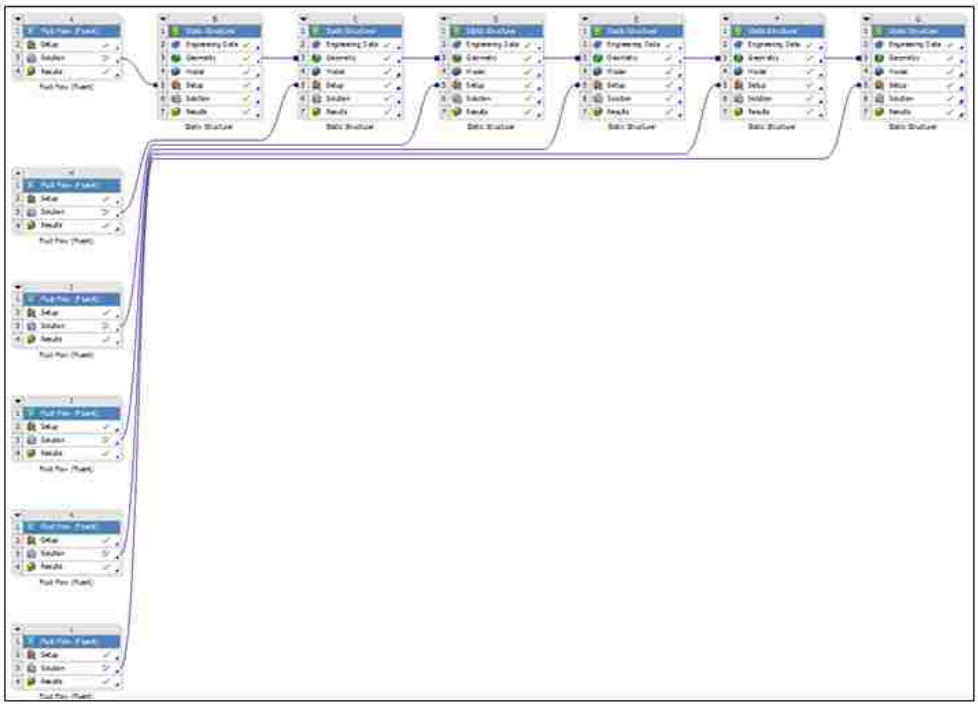

Figure 4.39. Fluid-structure interaction setup in ANSYS WORKBENCH.

4.7.1 Startup process

The transient regime started from no flow conditions at room temperature of 293.15 K. Initially at 0 second there is no fluid flow or applied pressure in all the channels in the case. After sometime hot helium with temperature of 1223.15 K is allowed to flow inside the helium channel. In this study the principal stress and the factor of safety is calculated at 0^{+}, 10, 50, 80 and 100 seconds after the beginning of the helium flow, respectively.

4.7.2 Calculation at 0^{+} seconds

In the beginning after 0^{+} second fluid flow and applied pressure is allowed to flow in all the channels. Since the temperature gradient is low on all the channels, less stress

is produced. Hence the lower value of principal stress and the higher value of safety factor are obtained. Figure 4.40 and Figure 4.41 show the maximum principal stress for the triangular fins for straight, top and bottom arrangement type at 0^+ sec.

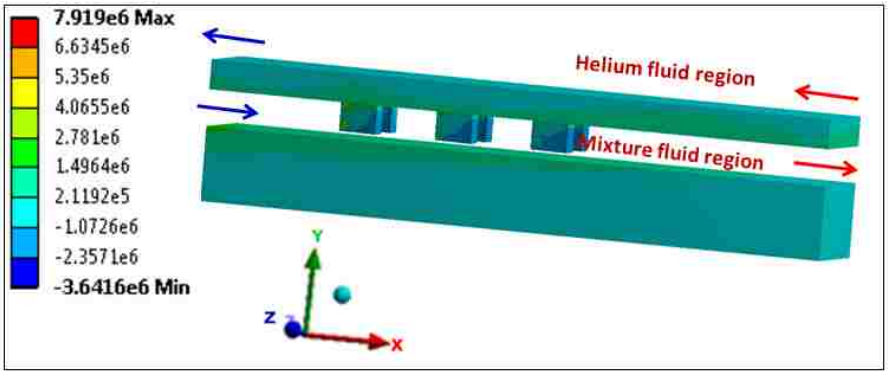

Figure 4.40. Maximum principal stress (Pa) for single channel model with straight triangular fins at 0^+ second.

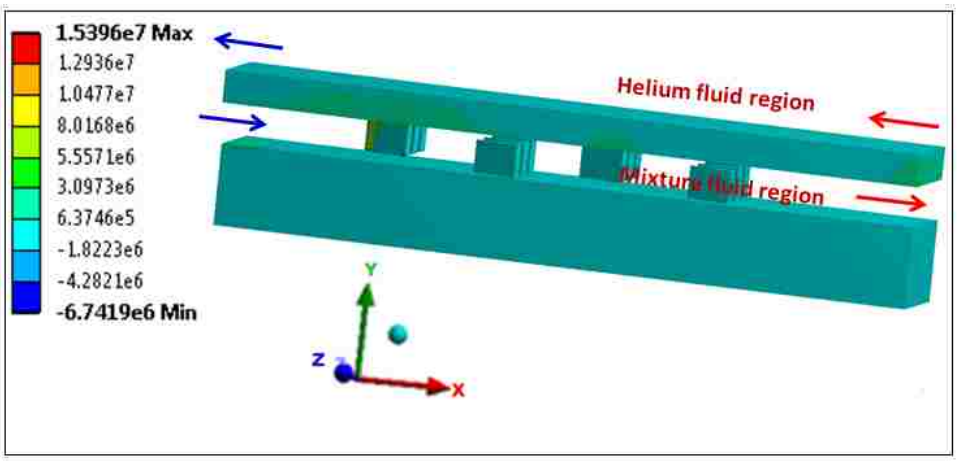

Figure 4.41. Maximum principal stress (Pa) for single channel model with top and bottom rectangular fins at 0^+ second.

Table 4.7 shows the maximum principle stress and safety factor for all the fin designs and different arrangements. In the beginning at 0 second there is no flow of hot fluid and applied pressure along the channels. At 0^+ second the hot fluid flows into the channels and uniform pressure of 1.5 MPa is applied. However the flow of hot fluid has just began the obtained temperature difference and the induced stress between the fins and the contact surface is small. Due to the decrease in the principal stress a high value of safety factor is obtained at the initial time of 0^+ second. From Table 4.7 it can be seen that maximum principal stress of 7 MPa is obtained for most of the fin designs and arrangements. The uniform arrangement of ripsaw fins with thickness of 0.00005 m gives the maximum stress and the inverted bolt fins gives the minimum stress similar to the steady state structural results.

Table 4.7

Maximum principal stress and safety factor for all fin designs at 0^+ second

Fins	Maximum principal stress (MPa)	Safety factor
Straight rectangular fin	7.159	30.37
Staggered rectangular fin	7.068	30.76
Top and bottom rectangular fin	7.964	27.30
Straight triangular fin	7.919	27.46
Staggered triangular fin	7.858	27.67
Top and bottom triangular fin	7.762	28.01
Straight inverted bolt fins	4.523	48.08
Staggered inverted bolt fins	3.437	63.25
Top and bottom inverted bolt fins	6.616	32.87
Straight ripsaw fin thickness of 0.00005 m	8.247	26.36
Staggered ripsaw fin thickness of 0.00005 m	6.516	33.37
Top and bottom ripsaw fin with thickness of 0.00005 m	8.217	26.46

4.7.3 Calculation at 10 seconds

The helium and the other chemicals with the applied pressure load of 1.5 MPa has been flowing to into the channel for the past 10 seconds. At this point the induced stresses produced starts increasing which in turn decreases the factor of safety. The reason for the increase in the stress is due to the increase in the temperature difference. As the hot fluid and the cold fluid flows inside the heat exchanger channel the heat transfer starts which helps in increasing the temperature difference between the solid regions. It is already known that the temperature loads has a significant impact on the stresses induced and hence increase in the temperature gradient increases the stress produced in the heat exchanger. Table 4.8 shows the maximum principal stress and the safety factor for the fins designs at 10 seconds.

Table 4.8

Maximum principal stress and safety factor for all fins at 10 seconds

Fins	Maximum principal stress in MPa	Safety factor
Straight rectangular fin	7.956	27.33
Staggered rectangular fin	7.452	29.18
Top and bottom rectangular fin	8.125	26.76
Straight triangular fin	12.753	20.22
Staggered triangular fin	9.156	23.75
Top and bottom triangular fin	13.752	15.81
Straight inverted bolt fins	5.056	43.01
Staggered inverted bolt fins	4.321	50.32
Top and bottom inverted bolt fins	6.750	32.21
Straight ripsaw fin thickness of 0.00005 m	8.604	25.27
Staggered ripsaw fin thickness of 0.00005 m	6.878	31.61
Top and bottom ripsaw fin with thickness of 0.00005 m	8.535	25.47

4.7.4 Calculation at 50 seconds

Figure 4.42 and Figure 4.43 show the maximum principal stress of the straight triangular fins and the top and bottom triangular fins, respectively. The principal stress obtained is associated with the applied thermal and pressure load after 50 seconds from the beginning of the helium flow. The first principal stress after 50 seconds is increased when compared to the value of the principal stress at 10 seconds due to the increase in the temperature gradient within the channel walls. The safety factor is decreased a little but the model is still under the safe limit for the high temperature application.

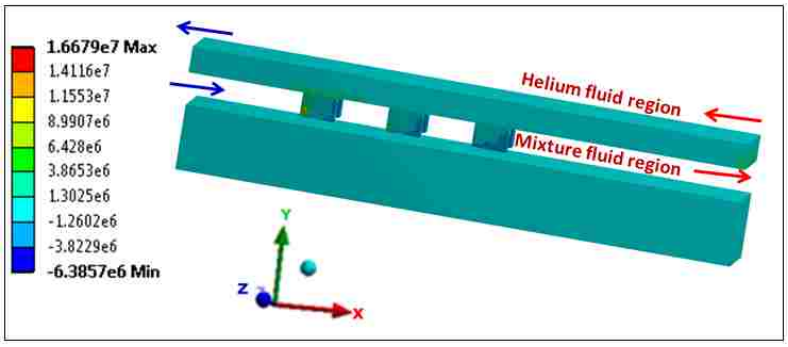

Figure 4.42. Maximum principal stress (Pa) for the straight triangular fins at 50 seconds.

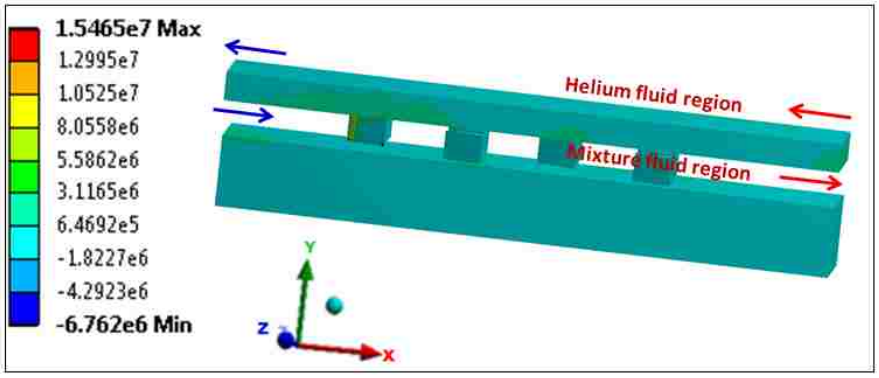

Figure 4.43. Maximum principal stress (Pa) for the top and bottom triangular fins at 50 seconds.

Table 4.9 shown below gives the maximum principal stress and the factor of safety at 50 seconds.

Table 4.9

Maximum principal stress and safety factor for all fins at 50 seconds

Fins	Maximum principal stress in MPa	Safety factor
Straight rectangular fin	8.234	26.41
Staggered rectangular fin	8.343	26.07
Top and bottom rectangular fin	9.785	22.22
Straight triangular fin	16.679	13.04
Staggered triangular fin	14.734	14.76
Top and bottom triangular fin	15.642	13.90
Straight inverted bolt fins	7.589	28.66
Staggered inverted bolt fins	6.395	34.00
Top and bottom inverted bolt fins	7.053	30.83
Straight ripsaw fin thickness of 0.00005 m	9.732	22.35
Staggered ripsaw fin thickness of 0.00005 m	7.956	27.33
Top and bottom ripsaw fin with thickness of 0.00005 m	9.752	22.30

4.7.5 Calculation at 80 seconds

In this high temperature heat exchanger the thermal load is a significant factor that influences the stresses produced in the heat exchanger. As the time increases, the temperature difference increases which in turn increase the induced stress. The increase in the principal stress decreases the safety factor for the model. Table 4.10 shows the maximum principal stress and the factor of safety at 80 seconds.

Table 4.10

Maximum principal stress and safety factor for all fin designs at 80 seconds

Fins	Maximum principal stress in MPa	Safety factor
Straight rectangular fin	9.056	24.01
Staggered rectangular fin	8.952	24.29
Top and bottom rectangular fin	10.262	21.19
Straight triangular fin	16.765	16.85
Staggered triangular fin	16.855	12.90
Top and bottom triangular fin	16.651	15.95
Straight inverted bolt fin	7.987	27.23
Staggered inverted bolt fin	6.976	31.17
Top and bottom inverted bolt fin	7.865	27.65
Straight ripsaw fin thickness of 0.00005 m	9.815	22.16
Staggered ripsaw fin thickness of 0.00005 m	8.728	24.92
Top and bottom ripsaw fin with thickness of 0.00005 m	10.556	20.60

4.7.6 Calculation at 100 seconds

As expected it is found that with increase in time the induced stress decreases. The first principal stress obtained is minimum and the factor of safety is high. At this stage fully developed condition is reached and the temperature no longer changes. Hence constant stress is obtained and there is no change in the value of the stress with increase in time. Table 4.11 shows the maximum principal stress and the factor of safety at 100 seconds.

Table 4.11

Maximum principal stress and factor of safety for all fin designs at 100 seconds

Fins	Maximum principal stress in MPa	Safety factor
Straight rectangular fin	9.865	22.04
Staggered rectangular fin	9.015	24.12
Top and bottom rectangular fin	11.010	19.75
Straight triangular fin	17.158	12.67
Staggered triangular fin	18.756	11.59
Top and bottom triangular fin	16.756	12.98
Straight inverted bolt fin	8.919	24.38
Staggered inverted bolt fin	7.015	31.00
Top and bottom inverted bolt fin	7.913	27.48
Straight ripsaw fin thickness of 0.00005 m	10.015	21.71
Staggered ripsaw fin thickness of 0.00005 m	9.016	24.12
Top and bottom ripsaw fin with thickness of 0.00005 m	11.952	18.20

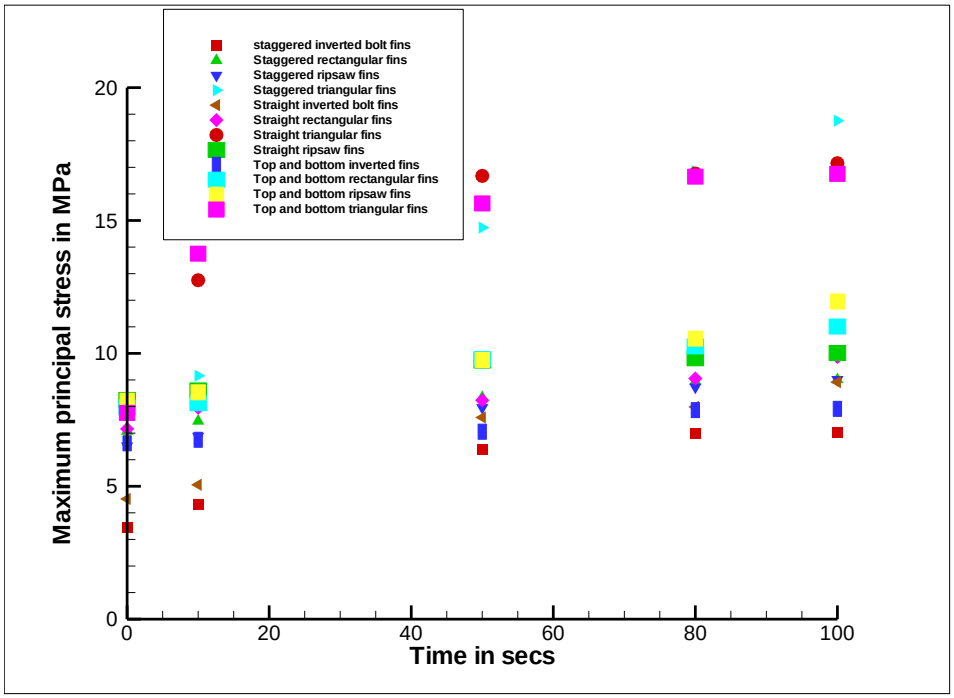

Figure 4.44 Time vs. the principal stress for all the fin designs in transient analysis.

Figure 4.44 shows the maximal principal stress in MPa for all fin designs and fin arrangements. From the results it is found that the straight triangular fins have the maximum stress followed by the top and bottom triangular fins. The straight inverted bolt fins and the staggered inverted bolt fins have the least value of the principal stress. Hence the principal stress is maximum for triangular fins and minimum for inverted bolt fins. However both triangular and inverted bolt fins produce the high pressure drop and the friction factor. Hence it is not reasonable to select the inverted bolt fins even though they have the least stress value. The ripsaw fins produce a reasonable value of the principal stress and the safety factor. Also they give good heat transfer rate with the minimum pressure drop and the friction factor. Similar to the steady state the worst safety factor is obtained for the triangular fins. The critical area in the model where the failure occurs is at the area where the fins are attached to the solid surface. The safety factor is minimum at these areas for both steady and transient states and for all fin designs. Hence ripsaw fin design is selected as the best fin design for the heat exchanger.

CHAPTER 5

MODELING OF FLOW WITH CHEMICAL REACTIONS

In this chapter three-dimensional study is carried out to calculate the decomposition percentage of sulfur trioxide to sulfur dioxide and oxygen. Parametric studies are carried out to enhance the decomposition percentage of sulfur trioxide. In order to save computational time only a single channel model is developed to calculate the chemical reactions and all the geometrical parameters used in this calculation are similar to the previous chapters.

5.1 Geometry and Boundary Conditions

The geometry of the model is similar to the geometry used in the previous chapters and chemical reaction is alone added in this chapter. Since the mass flow rate is assumed to be uniform a single channel model is developed to investigate the chemical reactions taking place inside the heat exchanger and the decomposer. Figure 5.1 shows the geometry and the calculation domain of the plate fin heat exchanger and decomposer.

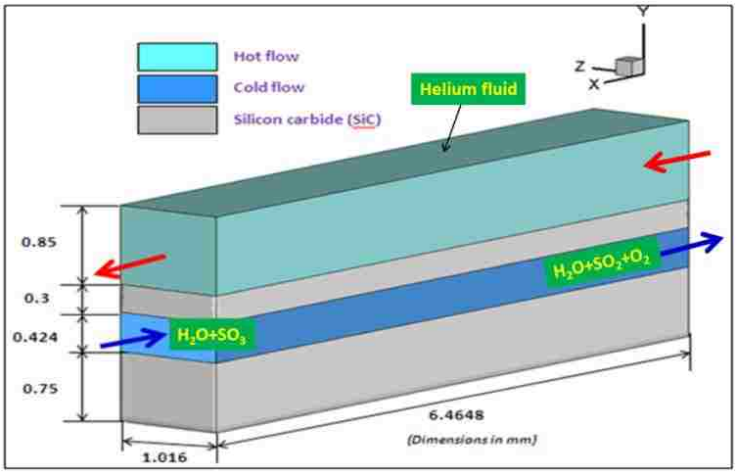

Figure 5.1. Geometry of the heat exchanger and decomposer.

5.2 Material Properties and Boundary Conditions

The density and specific heat of SiC are 3130 $kg \cdot m^{-3}$ and 1200 $J \cdot kg^{-1} \cdot K^{-1}$. The thermal conductivity of SiC varies with temperature (973 K-1223 K) and is given by the following equation (Munro [70]):

$$k_{SiC} = 1.9477 \cdot 10^{2} - 3.60612 \cdot 10^{1} \cdot T + 3.30843 \cdot 10^{4} \cdot T^{2} - 1.46006 \cdot 10^{-7} \cdot T^{3} + 2.7588 \cdot 10^{11} \cdot T^{4} \tag{5.1}$$

The properties of the reacting fluid mixture such as density, viscosity, heat capacity and thermal conductivity are obtained from FLUENT. The mixed properties for each of the component are calculated from FLUENT. The thermal conductivity and molecular viscosity of the mixture calculated based on the kinetic theory are given by the following equation:

$$\lambda = \sum_{i} \frac{X_i \lambda_i}{\sum_{j} X_j \eta_{ij}} \tag{5.2}$$

$$\mu = \sum_{i} \frac{X_i \mu_i}{\sum_{j} X_j \eta_{ij}} \tag{5.3}$$

where

$$\eta_{ij} = \frac{\left[1 + \left(\frac{\mu_i}{\mu_j}\right)^{\frac{1}{2}} \left(\frac{M_j}{M_i}\right)^{\frac{1}{4}}\right]^2}{\left[8\left(1 + \frac{M_i}{M_j}\right)\right]^{\frac{1}{2}}} \tag{5.4}$$

The density of the mixture is calculated using the following equation:

$$\rho = \frac{p_{op}}{RT \sum_{i} \frac{Y_i}{M_i}} \tag{5.5}$$

The specific heat of the mixture is calculated based on the average mass fraction of the pure species heat capacities. The mixture specific heat capacity is given by the following equation.

$$c_p = \sum_i Y_i c_{p,i} \tag{5.6}$$

The mass diffusion coefficients are calculated using the kinetic theory which is given by the following Chapman-Enskog formula:

$$D_{ij} = 0.0188 \frac{\left[T^3 \left(\frac{1}{M_i} + \frac{1}{M_j} \right) \right]^{1/2}}{p_{abs} \sigma_{ij}^2 \Omega_D} \tag{5.7}$$

Ω_D is the function of the quantity T_D^*, where

$$T_D^* = \frac{T}{(\varepsilon / k_B)_{ij}} \tag{5.8}$$

$(\varepsilon / k_B)_{ij}$ for the mixture is the geometric average:

$$(\varepsilon / k_B)_{ij} = \sqrt{(\varepsilon / k_B)_i (\varepsilon / k_B)_j} \tag{5.9}$$

For the mixture, σ_{ij} is calculated as the arithmetic average of the individual σ

$$\sigma_{ij} = \frac{1}{2} (\sigma_i + \sigma_j) \tag{5.10}$$

5.3 Chemical Reactions and Kinetics

The wall surface reaction model was implemented to determine the mass fraction of SO_3, SO_2 and O_2 as a result of sulfur trioxide decomposition: $SO_3 \rightarrow SO_2 + 0.5O_2$. The chemical reaction is highly temperature and pressure dependent.

Assuming that the reaction is the first order homogeneous reaction (Spewock [68]), the rate equation for the reaction is written as:

$$R_{rxn} = -kC_{SO_3} \tag{5.11}$$

The reaction rate constant (k) is obtained by using the Arrhenius equation (Scot [69]):

$$k = Ae^{\left(\frac{-E_a}{RT}\right)} \tag{5.12}$$

A platinum catalyst is used to enhance the decomposition. The activation energy, E_a and pre-exponential factor, A for the chemical reaction is obtained from the experimental data of Ginosar [51]. For the 1 wt % Pt catalyst pre-exponential factor A is 0.16 $1 \cdot s^{-1}$ and E_a is 32.67 $kJ \cdot mol^{-1}$. There are both exothermic and endothermic reactions in the mechanism and the heat generated or consumed by these reactions needs to be accounted for in the energy equation.

5.4 Calculation of Results

Flow calculations of sulfur trioxide decomposition ($SO_3 \rightarrow SO_2 + 0.5O_2$) for single channel geometry with platinum catalyst are performed. In the reacting channel as the decomposition takes place sulfur trioxide is decomposed to sulfur dioxide and oxygen. In the reacting channel mass fraction of SO_3 decreases and mass fraction of SO_2 and O_2 decreases as the fluid flows from inlet to the outlet of the channel. The mass fraction of SO_3 and H_2O at the inlet of the reacting channel are 0.8163 and 0.1837, respectively. The obtained decomposition percentage of sulfur trioxide is less due to the smaller length of

the reacting channel of 0.0064648 m. The decomposition percentage of sulfur trioxide is around 16 % for all the fin designs and arrangements.

Figure 5.2 shows the pressure distribution for the staggered rectangular fin arrangement. The pressure decreases from inlet to the outlet for the reacting fluid region and the helium fluid flow region. The pressure obtained for the straight, staggered and top and bottom rectangular fin are 21.90 Pa, 30.93 Pa and 59.07 Pa, respectively. Figure 5.3 shows the temperature distribution and the temperature increases along the axial direction.

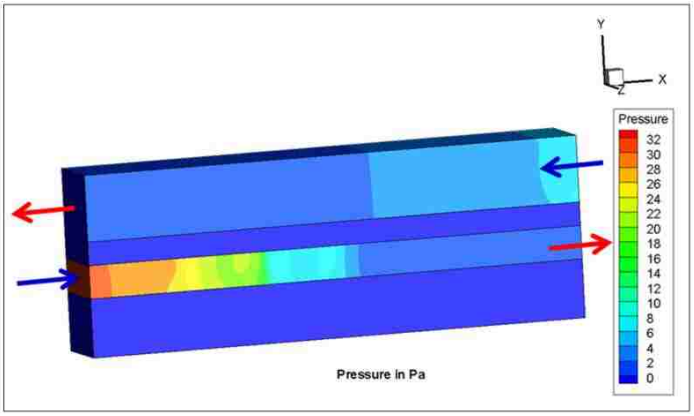

Figure 5.2. Pressure distribution in Pa for single channel staggered rectangular model.

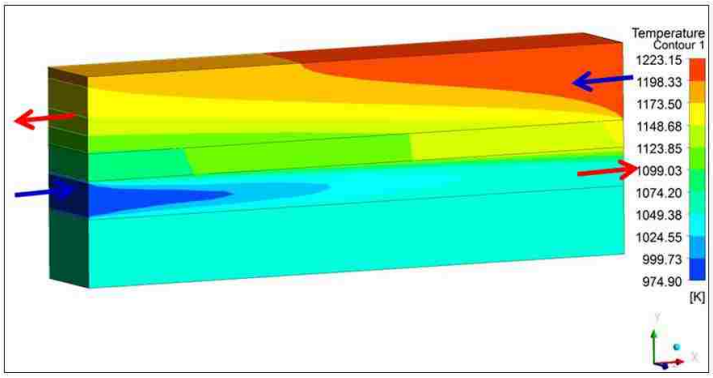

Figure 5.3. Temperature distribution in K for single channel model with staggered rectangular fins.

Figure 5.4, Figure 5.5 and Figure 5 6 show the mass fraction of SO_3, SO_2 and O_2, respectively It can be found that the mass fraction of SO_3 decreases and the mass fraction of SO_2 and O_2 increase as the fluid moves along the axial direction.

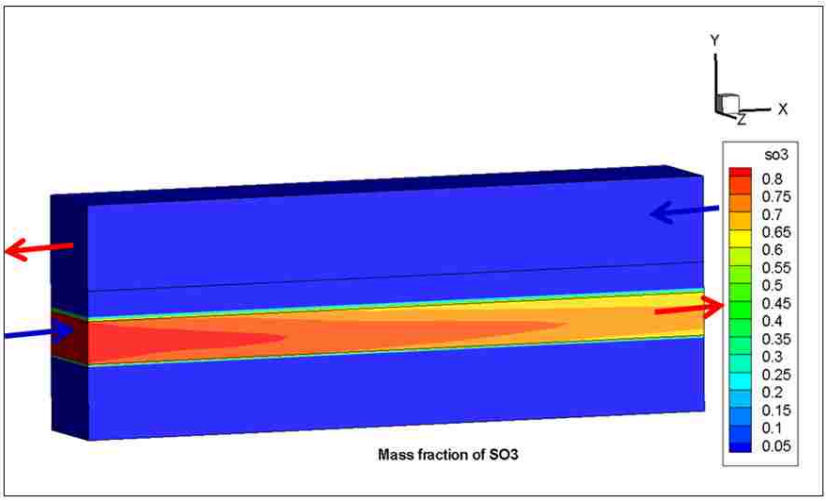

Figure 5.4. Mass fraction of SO_3 for single channel model with staggered rectangular fins.

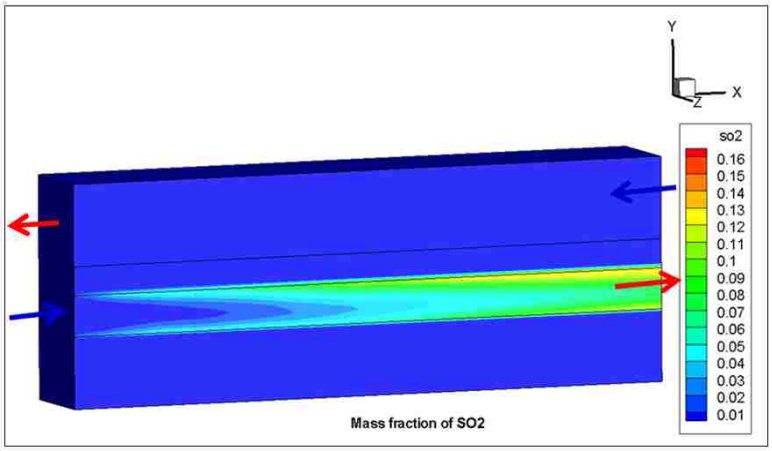

Figure 5.5. Mass fraction of SO_2 for single channel model with staggered rectangular fins.

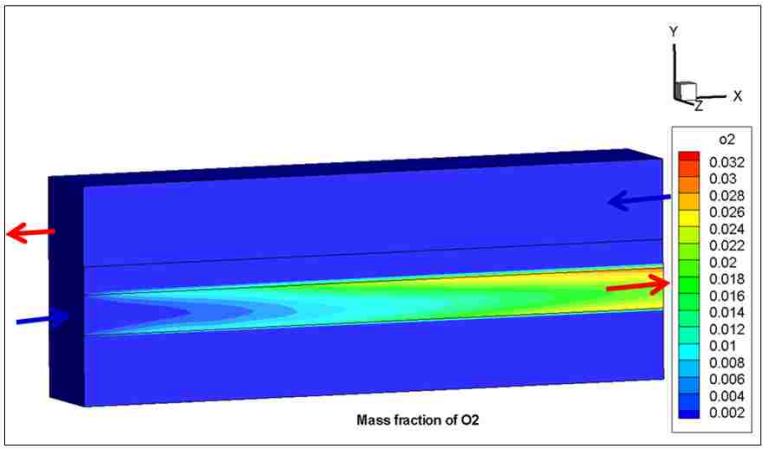

Figure 5 6. Mass fraction of O_2 for single channel model with staggered rectangular fins.

Due to the wall surface reaction the mass fraction of sulfur dioxide and oxygen are higher near the wall. The decomposition percentage of sulfur trioxide for single channel model with straight, staggered and top and bottom rectangular fins are 15.85%, 16.15%, 18.5%, respectively.

The ripsaw fin design is considered to be the good design since it gives less pressure drop and friction factor and reasonable heat transfer rate. The pressure distributions for the straight, staggered and top and bottom rip saw fins are 15.61 Pa, 16.74 Pa, 20.55 Pa, respectively. The decomposition percentages of sulfur trioxide for straight, staggered and top and bottom fins are 15.98%, 15.58%, 16.52%, respectively. The pressure distribution, mass fraction of SO_3 and SO_2 for top and bottom ripsaw fins are shown in Figure 5.7, Figure 5.8 and Figure 5.9, respectively.

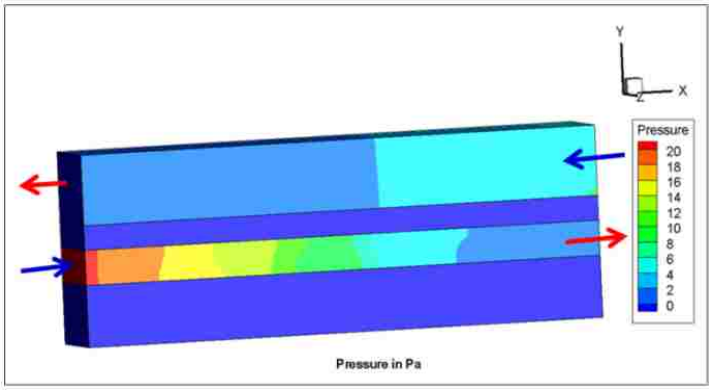

Figure 5.7. Pressure distribution in Pa for single channel model with top and bottom ripsaw fins.

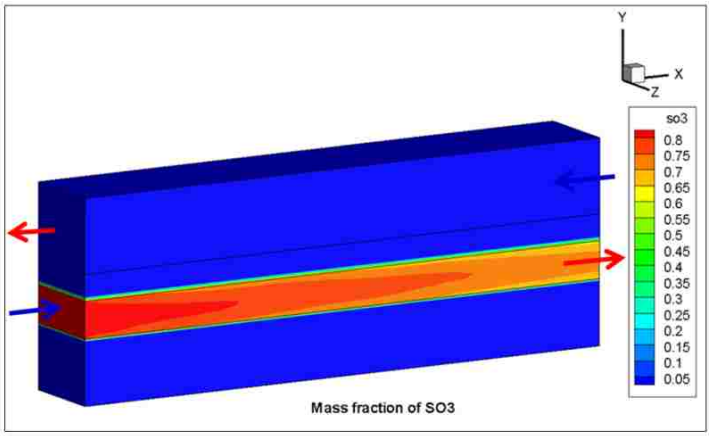

Figure 5.8. Mass fraction of SO_3 in single channel model with top and bottom ripsaw fins.

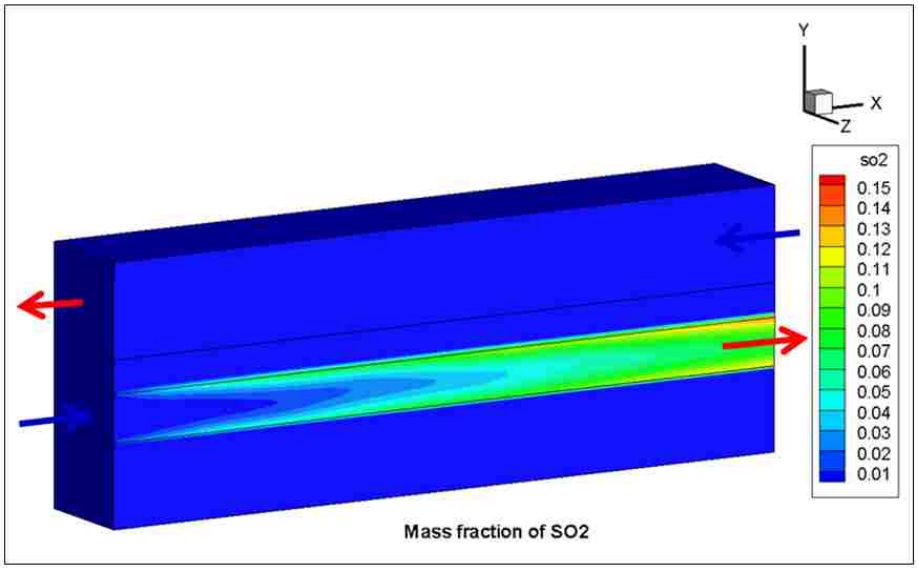

Figure 5.9. Mass fraction of SO_2 for a single channel model with top and bottom ripsaw fins.

It can be seen from the above figures that the mass flow rate of the reaction products of SO_2 and O_2 are higher near the walls when compared to the core flow area of the channel. Since wall surface reaction is used for the model the chemical decomposition occurs only in the surface regions. Table 5.1 shows pressure drop, decomposition percentage of sulfur trioxide and temperature gradient for all the fin design configurations and arrangements.

Table 5.1

Fluid flow and chemical decomposition results for all fin designs

Fins	Pressure drop (Pa)	% decomposition of SO_3	Temperature gradient ($K \cdot mm^{-1}$)
Straight rectangular fins	21.90	15.85	23.32
Staggered rectangular fins	30.93	16.15	16.31
Top and bottom rectangular fins	59.07	18.50	18.75
Straight triangular fins	19.93	16.57	22.90
Staggered triangular fins	22.66	15.37	17.07
Top and bottom triangular fins	38.30	18.56	17.74
Straight inverted bolt fins	38.36	16.81	21.33
Staggered inverted bolt fins	35.19	15.42	19.35
Top and bottom inverted bolt fins	59.70	17.95	18.31
Straight ripsaw fins	17.60	15.98	19.37
Staggered ripsaw fins	16.74	15.58	17.50
Top and bottom ripsaw fins	20.55	16.52	18.12

From Table 5.1 it can be seen that the inverted bolt fins has the highest pressure drop and ripsaw fins has the lowest pressure drop. The decomposition percentage obtained for sulfur trioxide is around 15 to 18% for all the models. Top and bottom triangular fins have the highest decomposition percentage of SO_3 which is 18.56% due to the higher temperature gradient along the reacting channel. The ripsaw fins have decomposition percentage of around 15 to 16% and has the lowest pressure drop.

5.5 Parametric Studies

A parametric study is carried out by increasing the length of the heat exchanger and decomposer ten times to the original length of 0.064648 m. The pressure obtained for the long staggered rectangular channel is 320 Pa and the velocity is 0.8075 $m \cdot s^{-1}$. Figure 5.10 shows the pressure distribution in Pa for the long staggered rectangular fins.

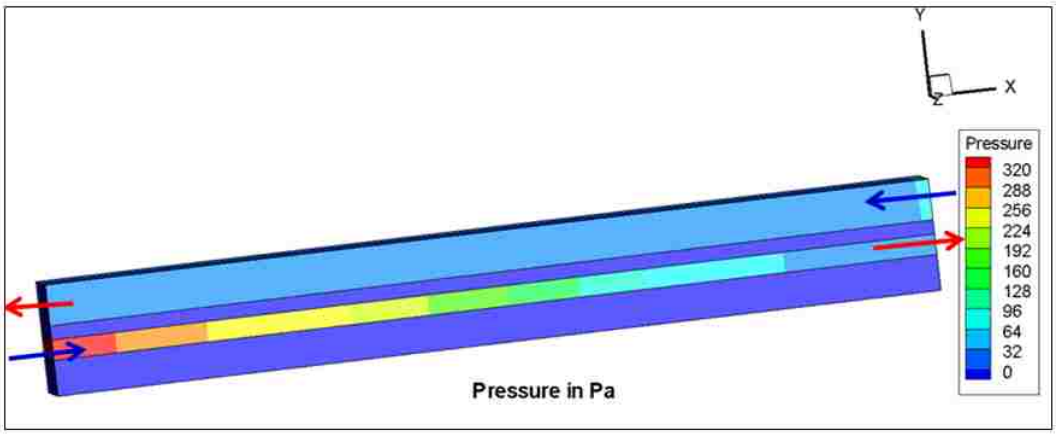

Figure 5.10. Pressure distribution in Pa for long staggered rectangular fins.

In the reacting channel the mass fraction of sulfur trioxide decreases and the mass fraction of sulfur dioxide and oxygen increase from inlet to the outlet. The decomposition mainly takes along the wall boundary surface compared to the core fluid area. The decomposition percentage of sulfur trioxide is 78.43%. The reason for the increase in the decomposition percentage of SO_3 is due to the increase in the residence time. The residence time increases from 0.008 seconds (0.0064648 m length of the channel) to 0.08 seconds (0.064648 m length of the channel). Due to the increase in the residence time the reacting fluid has more time to interact with the platinum catalyst and the decomposition percentage of sulfur trioxide increases. The mass fraction of SO_3,

$SO_2$and O_2 for long staggered rectangular fins is shown in Figure 5.11, Figure 5.12 and Figure 5.13, respectively.

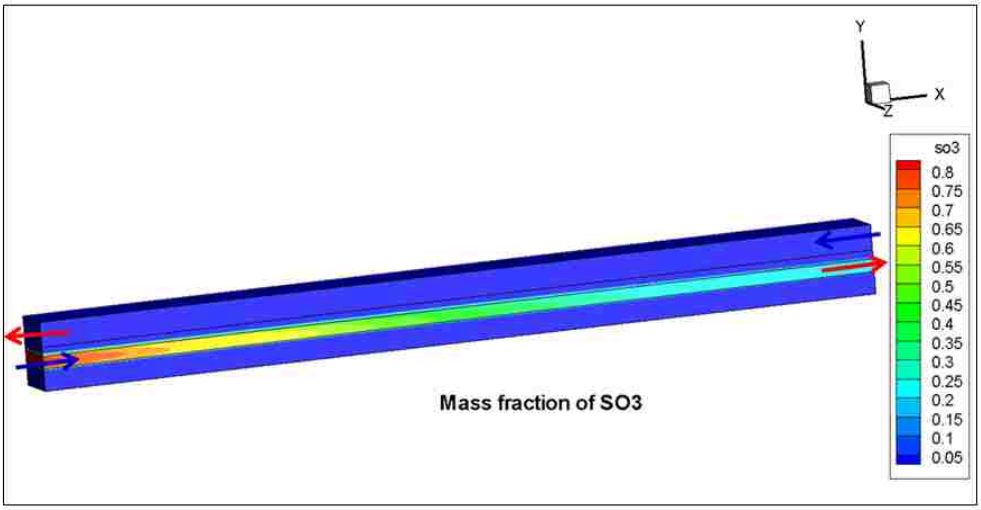

Figure 5.11. Mass fraction of SO_3 for single channel model with long staggered rectangular fins.

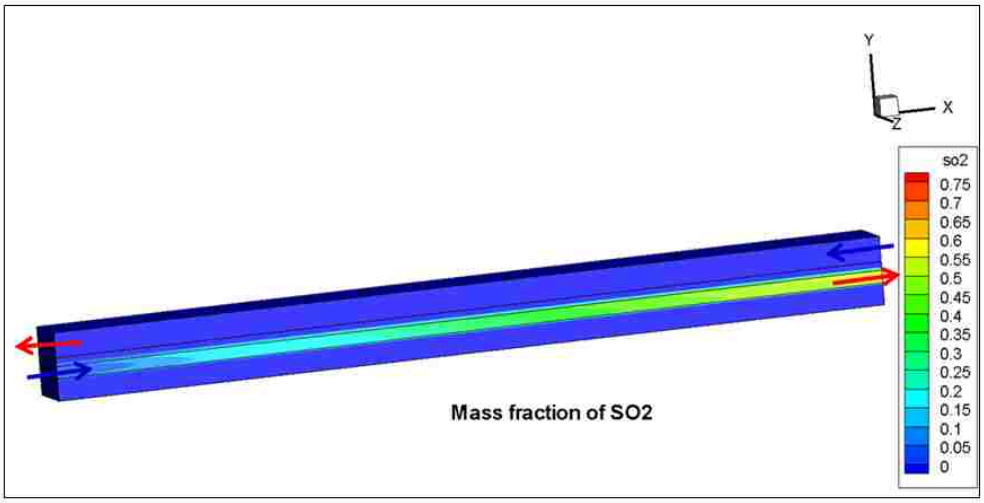

Figure 5.12. Mass fraction of SO_2 for single channel model with long staggered rectangular fins.

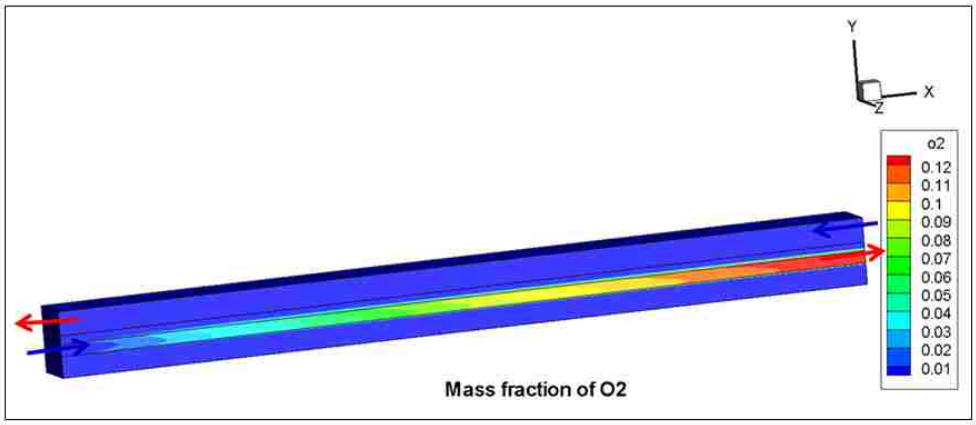

Figure 5.13. Mass fraction of O_2 for a single channel model with long staggered rectangular fins.

Similarly the channel length of the triangular and the ripsaw fins are increased from the original length of 0.0064648 m to 0.064648 m ten times. The heat transfer surface area of triangular and ripsaw fins are $2.35 \cdot 10^{-5}$ $m^2$and $2.435 \cdot 10^{-5}$ m^2, respectively Due to the increase in the length and the heat transfer surface area the effectiveness of the fins also increases. The effectiveness of the triangular and ripsaw fins are 87.25% and 92.13%, respectively. The decomposition percentage of SO_3 for triangular and ripsaw fins are 82% and 85.16%, respectively. The pressure drop for ripsaw fins is 120.64 Pa and for the triangular fins is 252.01 Pa. Hence it is found that less pressure drop, high heat transfer and decomposition percentage of SO_3 is obtained for ripsaw fins.

Another parametric study has been carried out for the top and bottom ripsaw fins by increasing the mass flow rate. The decomposition percentage of sulfur trioxide increases significantly as the operating pressure of the reacting flow increases. Figure 5.14 shows the parametric study for the different operating pressures.

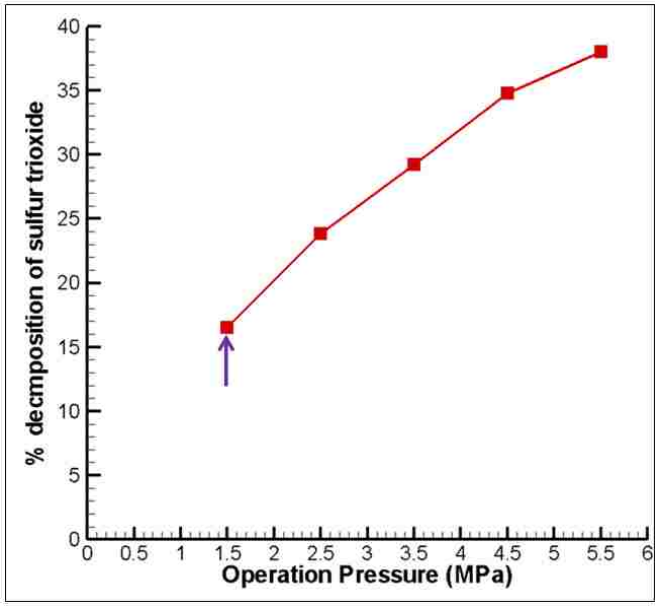

Figure 5.14. Percentage decomposition of SO_3 vs operation pressure for top and bottom ripsaw fins for channel length of 0.0064648 m.

The parametric study for the top and bottom ripsaw fins is carried to find decomposition percentage of sulfur trioxide for different mass flow rates. It can be found that the decomposition percentage of SO_3 decreases with increase in the mass flow rate. As the mass flow rate increases the velocity increase thus reducing the residence time. The decrease in residence time decreases the decomposition percentage of sulfur trioxide. Figure 5.15 shows the decomposition percentage of SO_3 for different mass flow rates.

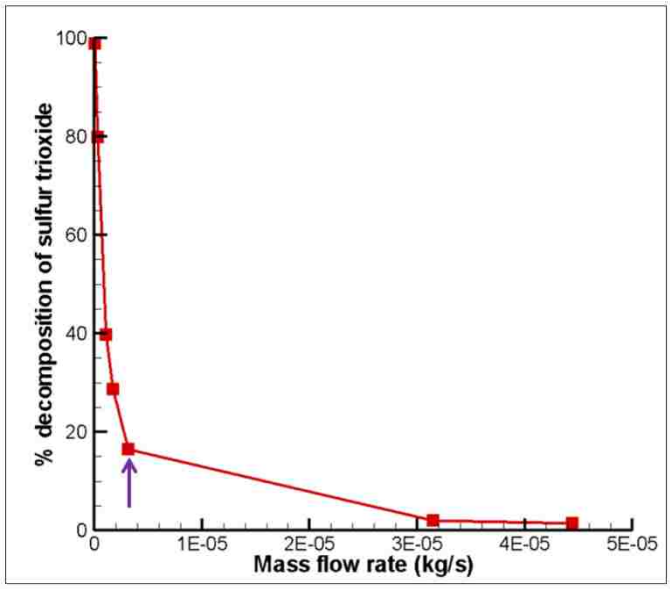

Figure 5.15. Percentage decomposition of SO_3 versus different mass flow rates of the reacting channel for top and bottom ripsaw fins for channel length of 0.0064648 m.

The production or throughput of sulfur dioxide for different mass flow rates is studied. It is found that as the mass flow rate of the reacting channel increases the residence time decreases leading to the decrease in the production of sulfur dioxide. Another study on the production of sulfur dioxide for different operation pressure is carried out. The sulfur dioxide production or throughput increases with increase in the residence time of fluid flow in the reacting channel. Figure 5.16 and Figure 5.17 show the sulfur dioxide production for different mass flow rates and different operating pressures, respectively.

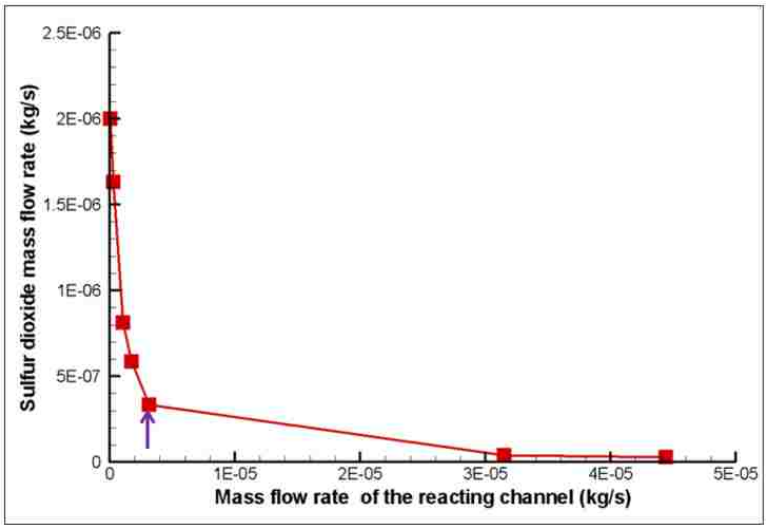

Figure 5.16. Sulfur dioxide production or throughput vs mass flow rate of the reacting channel for channel length of 0.0064648 m.

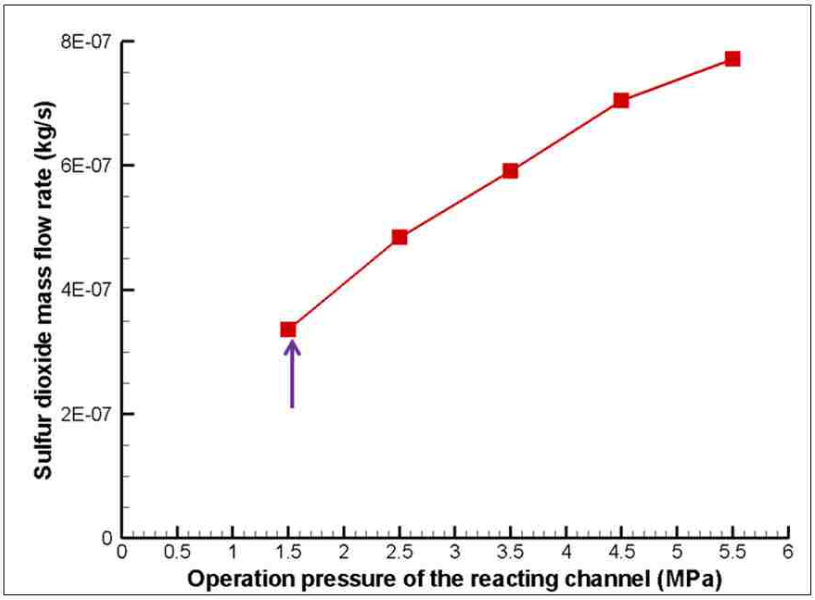

Figure 5.17. Sulfur dioxide production or throughput vs operating pressure of the reacting channel for channel length of 0.0064648 m.

CHAPTER 6

CONCLUSIONS AND FUTURE WORKS

6.1 Conclusions

In this dissertation, numerical analysis on three-dimensional ceramic plate fin high temperature heat exchanger and decomposer is carried out to study the fluid flow, heat transfer, structural analysis and chemical reactions. The computational model used for the fluid flow and heat transfer analysis is validated by comparing with the empirical correlation done by the other researchers.

The fluid flow and heat transfer analysis for nine different fin designs arranged in a uniformly are studied. The friction factor for the rectangular fin design and ripsaw fin design are validated with the friction factor correlation proposed by Manson [72]. The friction factor correlation was proposed for the Reynolds number above and below 3500 and from the results it is found that the obtained numerical result is in good agreement with the published empirical result for the rectangular and ripsaw fins. Similarly the heat transfer result for the rectangular and ripsaw fins with thickness of 0.00005 m is validated with the empirical correlation proposed by Wieting [73]. Weiting [73] proposed an empirical correlation equation for the Colburn factor for laminar and turbulent flows. The obtained numerical result for the Colburn factor is in good agreement with the published result by Wieting [73]. Recirculation is found at the wake region of the fins for rectangular, triangular and inverted bolt fins. Due to the presence of recirculation the pressure drop and the friction factor is high for these fins. The eyelid type fin does not have any recirculation and has less pressure drop and friction factor due to the streamlined nature of the fins. The ripsaw fins with thickness of 0.00005 m does not

have any recirculation due to their small thickness and hence they have lower pressure drop and friction factor. The average Nusselt number for the straight arrangement ripsaw fin with thickness of 0.00005 m is 3.050. The pressure drop and the friction factor for the model are 15.01 Pa and 0.472, respectively. The ripsaw fin design is considered to be the best design because it gives lower pressure drop and friction factor with good heat transfer rate. Another study is carried out by arranging the fins in a staggered manner and the fins are placed on the top and bottom surfaces of the solid surfaces. The study is carried out on rectangular fins, triangular fins, inverted bolt fins and ripsaw fins with thickness of 0.00005 m. The pressure drop and the friction factor are more for top and bottom arrangement due to the increase in the number of fins. Due to the placement of the fins on the top and bottom surfaces there is increase in flow disturbances due to the more recirculation regions which in turn increases the pressure drop. The heat transfer rate and the average Nusselt number obtained are similar for both the fin arrangements. The staggered arrangement has more number of fins in the upper solid surface compared to the top and bottom arrangement. Since the heat is transferred from the helium fluid to the top solid surface the heat transfer obtained for staggered and top and bottom fins are similar. Though there are fewer fins on the top solid surface compared to the staggered arrangement the heat transfer surface area is higher for the top and bottom fins are more. Hence the heat transfer surface area is little higher or similar to the staggered arrangement. For both the fin arrangements ripsaw fin design gives the minimum pressure drop and friction factor and inverted bolt fins has the maximum pressure drop and friction factor.

Structural analysis is carried out for the steady and transient state on four different fin design configurations, three different arrangements (straight, staggered and top and bottom) and three different load conditions (imported thermal load and uniform pressure of 1.5 MPa, imported thermal and pressure load and imported pressure load). From the study it is found that the thermal stresses are more significant than the mechanical stresses. The principal stress obtained for all the models is similar for the case with imported thermal load and uniform pressure of 1.5 MPa and for the case with imported thermal and pressure loads. The imported thermal and pressure loads are exported from ANSYS FLUENT and are imported to ANSYS steady structural module to find the thermal stress. The principle stress obtained for the case with imported pressure load is very less and the deformation is almost negligible. The safety factor obtained for all the models is greater than 1. Hence all the models are safe to work at high temperature and corrosive environment assuming the material has been perfectly manufactured without any cracks or flaws. In the transient analysis it is found that the stresses are high at heat exchanger startup and shutdown stages. The triangle fins have the highest principal stress and the lowest safety factor. The inverted bolt fins have the lowest principal stress and the highest safety factor. However from the fluid and heat transfer results it can be seen that pressure drop is high for both triangular and inverted bolt fins and hence these two types of fin designs cannot be selected as the good design. The rectangular fins have the minimum stress followed by the ripsaw fins. Since the stress limits for the ripsaw fins are within the safety limit and the fluid and heat transfer results are also better the ripsaw fin design is considered to be the best design.

Another study is carried out to study the decomposition percentage of sulfur trioxide using wall surface chemical reactions. The study is carried out on four types of fin design configuration and three different arrangements. The obtained decomposition percentage of SO_3 for all the fin designs and arrangements are in the range of 15% to 18%. The reason for the low decomposition percentage is due to the length of the heat exchanger which is only 0.0064648 m. The extremely small length of the heat exchanger reduces the residence time to 0.008 seconds. Due to the smaller residence time the incoming sulfur trioxide fluid has less time to interact with the platinum catalyst which reduces the decomposition percentage of sulfur trioxide. A parametric study has been carried out by increasing the length of the heat exchanger to ten times the original length of 0.064648 m. The decomposition percentage of sulfur trioxide is increased to 80%. Increasing the length of the heat exchanger increases the residence time to 0.08 seconds which in turn increases the decomposition percentage of sulfur trioxide. The decomposition percentage of sulfur trioxide and the throughput obtained for sulfur dioxide increases by increasing the operating pressure of the reacting channel. From the study it is found that the ripsaw fin design with thickness of 0.05 mm has the maximum decomposition percentage of sulfur trioxide, minimum pressure drop, good heat transfer rate and high safety factor. Hence ripsaw fin design is considered to be the good design compared to all the other fin designs studied in this research.

6.2 Recommendations and Future Research

In this dissertation only the helium fluid channel and the reacting channel are considered for study. The recuperating channel can be modeled for the above shown fin configurations to find the decomposition percentage of sulfur trioxide. The Arrhenius constants like the activation energy and the pre-exponential factors are obtained from the experimental study by Ginosar [51]. The constants were calculated for different models. Hence an experimental study can be done to evaluate the Arrhenius constant for the model discussed in this research.

Silicon carbide is the only material used in this study for the structural analysis calculation. There are different ceramic materials and high temperature alloys used at high temperature and corrosive environment. Hence a study can be carried out by using different materials for the above models in order to find their resistance to high temperature and corrosive environment. Also for the hot fluid channel the helium fluid can be replaced by other fluids and check their heat transfer effectiveness.

APPENDIX

NOMENCLATURE

A	pre-exponential factor in Arrhenius equation, s^{-1}
A	total inlet area, m^2
A_s	cross-sectional area, m^2
$A1$	constant in the polynomial equation
C	molar concentration, $mol \cdot L^{-1}$
C_p	specific heat constant pressure, $J \cdot kg^{-1} \cdot K^{-1}$
C_2	inertial resistance factor
D_{AB}	mass diffusivity of the binary mixture, $m^2 \cdot s^{-1}$
$D_{i,m}$	diffusion coefficient for species i in the mixture, $m^2 \cdot s^{-1}$
D_h	hydraulic diameter, m
Ea	activation energy, $kJ \cdot mol^{-1}$
G	mass velocity, $kg \cdot s^{-1} \cdot m^{-2}$
G_k	generation of turbulence kinetic energy due to mean velocity gradients
G_b	generation of turbulence kinetic energy due to buoyancy
f	friction factor
h_x	local heat transfer coefficient, $W \cdot m^{-2} \cdot K^{-1}$
$\bar{h}$	average heat transfer coefficient, $W \cdot m^{-2} \cdot K^{-1}$
j	Colburn factor
K	thermal conductivity of the fluid, $W \cdot m^{-1} \cdot k^{-1}$
k	first order reaction rate, s^{-1}
L	length of the channel, m

M	molecular weight, $g \cdot mol^{-1}$
m	constant in Coulomb-Mohr criterion
$\dot{m}$	mass flow rate, $kg \cdot s^{-1}$
Nu_x	local Nusselt number
$\overline{Nu}$	average Nusselt number
ΔP	pressure drop, Pa
Pr	Prandtl number
p	static pressure, Pa
q''	heat flux, $W \cdot m^{-2}$
R	gas constant, $J \cdot K^{-1} \cdot mol^{-1}$
Re	Reynolds number
R_{rxni}	net rate of production of species i by chemical reaction, $kg \cdot m^{-3} \cdot s^{-1}$
S_i	net rate of production of species i by chemical reaction, $kg \cdot m^{-3} \cdot s^{-1}$
S_h	heat of chemical reaction, $kg \cdot K \cdot s^{-1} \cdot m^{-3}$
Sc	Schmidt number
t	time, s
t	fin thickness used in Wieting [73], mm
T	temperature, K
T_b	bulk temperature of the fluid, K
T_i	inlet temperature of the mixture, K
T_o	outlet temperature of the mixture, K
T_w	wall temperature, K
U	velocity magnitude, $m \cdot s^{-1}$

u_i mean velocity component (i = 1,2,3), $m \cdot s^{-1}$

u_j mean velocity component (j = 1,2,3), $m \cdot s^{-1}$

u_k mean velocity component (k = 1,2,3), $m \cdot s^{-1}$

v volumetric flow rate, $ml \cdot min^{-1}$

v_n normal velocity component, $m \cdot s^{-1}$

w_i length coordinate i (x, y, z), m

w_j length coordinate j (x, y, z), m

w_k length coordinate k (x, y, z), m

X_i mass concentration of species, *i*

Greek

α permeability, m^2

α aspect ratio used in Wieting [73]

β constant for pressure gradient

λ aspect ratio

μ dynamic viscosity, $kg \cdot m^{-1} \cdot s^{-1}$

μ slope of the Coulomb-Mohr circle

μ_t turbulent viscosity, $kg \cdot m^{-1} \cdot s^{-1}$

υ kinematic viscosity, $m^2 \cdot s^{-1}$

ρ density, $kg \cdot m^{-3}$

σ Lennard-Jones characteristic length, Å

ϕ_i mole fraction of species *i*

δ_{ij} Kronecker delta

$\sigma_{D,AB}$ mass diffusivity of the species *A* and *B*, $m^2 \cdot s^{-1}$

$\Omega_{D,AB}$	Collision integral used in Lennard-Jones potential
σ_k	turbulent Prandtl number
σ_e	turbulent Prandtl number
σ_{ut}	ultimate tensile strength, MPa
σ_{uc}	ultimate compressive strength
σ_x, σ_y	Principal stress along direction x and y
τ_i	shear stress acting along i, MPa
τ_u	constant used in Coulomb-Mohr criterion

BIBLIOGRAPHY

[1] Odum, H. T. (1998). Energy evaluation. *International Workshop on Advances in Energy Studies: Energy Flows in Ecology and Economy.* Porto Venere, Italy.

[2] Vitart, X., Le Duigou, A., & Carles, P. (2006). Hydrogen production using the sulfur-iodine cycle coupled to a VHTR: An overview. *Energy Conversion and Management, 47*, 2740-2747.

[3] Thomas. (2006). Hydrogen production via thermochemical cycle. *Hydrogen Fuel Cell*.

[4] Norman, J. B. (1981). Thermochemical water splitting for hydrogen production. GRI-80/0105.

[5] Picard, P. (2005). *DOE Hydrogen Program Review for Sulfur-Iodine Thermochemical Cycle.* Sandia National Lab, Presentation for Project PD27.

[6] Hesselgreaves, J. E. (2001). *Compact heat exchangers selection, design and operation.* Oxford, UK: Elsevier Science Ltd.

[7] Shah, R. &. (1983). *Compact and enhanced heat exchangers in heat exchangers: Theory and practice.* Washington DC.

[8] Najafi, H. N. (2011). Energy and cost optimization of a plate and fin heat exchanger using genetic algorithm. *Applied Thermal Engineering, 31*(10), 1839-1847.

[9] Sahin, B. O. (2008). Horseshoe vortex studies in the passage of a model plate-fin-and-tube heat exchanger. *International Journal of Heat and Fluid Flow, 29*, 340-351.

[10] Zhang, L. (2009). Flow maldistribution and thermal performance deterioration in a cross-flow air to air heat exchanger with plate-fin cores. *International Journal of Heat and Mass Transfer, 52*(19-20), 4500-4509.

[11] Kayansayan, N. (1994). Heat transfer characterization in plate-fin tube heat exchangers. *International Journal of Refrigeration, 17*, 49-57.

[12] Ismail, S. L. (2009). Numerical study of flow patterns of compact plate-fin heat exchangers and generation of design data for offset and wavy fins. *International Journal of Heat and Mass Transfer, 52*, 3972-83.

[13] ANSYS Inc. (2011). *ANSYS 14.5 user's guide.*

[14] Ranganayakulu, C. & Seetharamu. K.N. (1999). The combined effects of wall longitudinal heat conduction, inlet fluid flow non-uniformity and temperature non-uniformity in compact tube-fin heat exchangers: a finite element method. *International Journal of Heat and Mass Transfer, 42*, 263-73.

[15] Fernandez-Seara, J. D. (2013). Pressure drop and heat transfer characteristics of a titanium brazed plate-fin heat exchanger with offset strip fins. *Applied Thermal Engineering, 51*, 502-511.

[16] Dubrovsky, E. (1995). Experimental investigations of highly effective plate-fin heat exchanger surfaces. *Experimental Thermal and Fluid Sciences, 10*, 200-220.

[17] Jiao, A. &. (2005).). Effects of distributor configuration on flow maldistribution in plate-fin heat exchangers. *Heat Transfer Engineering, 26*(4), 19-25.

[18] Wen, J. & Liu. (2004). Study of Flow Distribution and Its Improvement on the Header of Plate-fin Heat Exchanger. *Cryogenics, 44*(11), 823-831.

[19] Leu, J. S. (2004). Heat transfer and fluid flow analysis in plate fin and tube heat exchangers with a pair of block shape vortex generators. *J Eng Thermophys, 47*(19-20), 4327-38.

[20] Sinha, A. R. (2013). Effects of different orientations of winglet arrays on the performance of plate-fin heat exchangers. *International Journal of Heat and Mass and Transfer, 57*(1), 202-214.

[21] Manglik, R. M. &. Bergles, A. E. (1995). Heat transfer and pressure drop correlations for the rectangular offset strip fin compact heat exchanger. *Experimental Thermal and Fluid Science, 10*, 171-80.

[22] Bhowmik. H., &. Lee.K. (2008). Analysis of heat transfer and pressure drop characteristics in an offset strip fin heat exchanger. *International Communications in Heat and Mass Transfer, 36*(3), 259-263.

[23] Martinez, E., Vicente, W., Soto, G., & Salinas, M. (2010). Comparative analysis of heat transfer and pressure drop in helically segmented finned tube heat exchangers. *Applied Thermal Engineering, 30*, 1470-1476.

[24] Ma, T., Wang, Q. W., Zeng, M., Chen, Y., Liu, Y., & Nagarajan, V. (2012). Study on heat transfer and pressure drop performances of ribbed channel in the high temperature heat exchanger. *Applied energy, 99*, 393-401.

[25] Yakut, K. Alemdaroglu, N., Sahin, B., & Celik, C. (2006). Optimum design-parameters of a heat exchanger having hexagonal fins. *Applied Energy, 83*(2), 82-98.

[26] Naik, S., & Probert, S.D. (1988). Thermal-hydraulic characteristics of a heat exchanger: the vertical rectangular fins being aligned parallel to the mean air-flow in the duct. *Applied Energy, 29*, 217-252.

[27] Dong, J., Chen, J., Chen, J., Zhang, W., & Zhou, Y (2007). Heat transfer and pressure drop correlations for the multi-louvered fin compact heat exchangers. *Energy Conversion and Management, 48*(5), 1506-1515.

[28] Ngo, T. L., Kato, Y., Nikitin, K., & Ishizuka, T. (2007). Heat transfer and pressure drop correlations of microchannel heat exchangers with S-shaped and zigzag fins for carbon dioxide cycles. *Experimental Thermal and Fluid Science, 32*(2), 560-570.

[29] Alm, B., Knitter, R., & Haußelt, J. (2008). Development of a Ceramic Micro Heat Exchanger Design, Construction, and Testing. *Chemical Engineering and Technology, 28*, 1554-1560.

[30] Peng, X. F., & Peterson, G.P. (1996). Convective Heat Transfer and Flow Friction for Water Flow in Microchannel Structures. *International Journal of Heat and Mass Transfer, 39*, 2599-2608.

[31] Kang, S. &.Tseng, S.C. (2007). Analysis of Effectiveness and Pressure Drop in Micro Cross-Flow Heat Exchanger. *Applied Thermal Engineering, 27*, 877-885.

[32] Meschke, F., Riebler, G., Hessel, V., Schurer, J., & Baier, T. (2005). Hermetic Gas-Tight Ceramic Microreactors. *Chemical Engineering and Technology, 28*, 465-473.

[33] Schulte-Fischedick, J., Dreibigacker, V., & Tamme, R. (2007). An innovative ceramic high temperature plate-fin heat exchanger for EFCC processes. *Applied Thermal Engineering, 27*(8-9), 1285-94.

[34] Monteiro, D. &. B., & Batista De Mello, P.E. (2012). Thermal performance and pressure drop in a ceramic heat exchanger evaluated using CFD simulations. *Energy, 45*, 489-496.

[35] Brown, Besenbruch, L.C., Lentsch, G.E., Schultz, K.R., Funk, J.F., Pickard, P.S., Marshall, A.C., & Showalter, S.K. (1999-2003). *High Efficiency Generation of Hydrogen Fuels using Nuclear Power.* General Atomics. USA: Final Technical Report .

[36] Giaconia, A. Caputo., G., Ceroli, A., Diamanti, M., Barborossa, V., Tarquini, P., & Sau, S. (2007). Experimental study of two phase separation in the Bunsen section of the sulfur–iodine thermochemical cycle. *International Journal of Hydrogen Energy, 32*(5), 531-536.

[37] Huang, C. T.-Raissi, A. (2005). Analysis of Sulfur-Iodine Thermochemical Cycle for Solar Hydrogen Production. Part I: Decomposition of Sulfuric Acid. *Solar Energy, 78*(5), 632-646.

[38] Barbarossa, V. Brutti, S, Diamanti, M, Sau, S, & De Maria, G. (2006). Catalytic Thermal Decomposition of Sulphuric Acid in Sulphur–Iodine Cycle for Hydrogen Production. *International Journal of Hydrogen Energy, 31*, 883-890.

[39] Lin, S. S., & Flaherty, R. (1983). Design Studies of Sulfur Trioxide Decomposition Reactor for the Sulfur Cycle Hydrogen Production Process. *International Journal of Hydrogen Energy, 8*(8), 589-596.

[40] Kuchi, G., Ponyavin, V., Chen, Y., & Sherman, S. (2008). Numerical modeling of high-temperature shell-and-tube heat exchanger and chemical decomposer for hydrogen production. *International Journal of Hydrogen Energy, 33*(20), 5460-5468.

[41] Brecher, L., Spewock, S., &Warde, C., (1977) The Westinghouse Sulphur Cycle for the thermochemical decomposition of water,*International Journal of Hydrogen Energy*, 2: 7-15, Pergamon Press ltd. 1977

[42] Ozturk, T., Hammache, A., & Bilgen, E., A. (1994). New Process for Oxygen Generating Step for the Hydrogen Producing Sulfur-Iodine Thermochemical cycle. *Chemical Engineering research and Design, 72*(42), 241-250.

[43] Perkins, C. &. Weimer, A.W. (2004). Likely Near-Term Solar-Thermal Water-splitting technologies. *International Journal of Hydrogen Energy, 29*, 1587-1599.

[44] Kubo, S., Nakajima, H., Kasahara, S., Higashi, S., Masaki, T., Abe, H., & Onuki, K. (2004). A Demonstration Study on a Closed-Cycle Hydrogen Production by the Thermochemical Water-Splitting Iodine - Sulfur Process. *Nuclear Engineering and Design, 33*(1-3), 347-354.

[45] Wang, L., Ping, Z.,Zhichao, W.,Songzhe, C., Jingming, X., Jing, C. (1971). *Catalytic hydrogen iodide decomposition over carbon nanotubes supported Pt catalysts.* Institue of Nuclear and New Energy Technology.

[46] Kane, C., &. Revankar., S. T. (2008). Sulfur-Iondine Thermochemical Cycle: HI decomposition flow sheet analysis. *International Journal of Hydrogen Energy, 33*(21), 5996-6005.

[47] Wong, B., Buckinham, R., T.,Brown, L., C., Russ, B., E., Besenbruch, G., E., Kaiparambil, A., Santhakrishnan, R., & Ajith Roy, B. (2007). Construction Materials Development in Sulfur-iodine Thermochemical Water splitting process for hydrogen production. *International Journal of Hydrogen Energy*, *32*, 497-504.

[48] Ponyavin, V., Chen, Y., Mohamed, T., Trabia, M.B., Hechanova, A.E., & Wilson, M. (2012). Design of a compact ceramic high-temperature heat exchanger and chemical decomposer for hydrogen production. *Heat Transfer Engineering, 33*(10), 853-70.

[49] Liberatore, R., Lanchi, M., Caputo, G., Felici, C., Giaconia, A., Sau, S., & Tarquini, P. (2012). Hydrogen production by flue gas through sulfur–iodine thermochemical process: Economic and energy evaluation. *International Journal of Hydrogen Energy, 37*(11), 8939-8953.

[50] Subramanian, S., Ponyavin, V., DeLosier, C., R., Chen, Y., & Hechanova, A., E. (2005). Design Considerations for Compact Ceramic Offset Strip-fin High Temperature Heat Exchangers. *Proceedings of the ASME Turbo Expo*, (pp. 989-996).

[51] Ginosar, D. M. (2005). *Activity and Stability of Catalysts for the High Temperature Decomposition of Sulfuric Acid.* Idaho National Laboratory Report.

[52] Gelbard, F., Vernon, M., Moore, R., Parma, E., Stone, H., Andazola, J., Naranjo, G., Reay, A., & Salas, F. (2006). *Operational Characteristics and Performance of a Pressurized and Integrated H2SO4 Decomposition Section.* Sandia National Lab Report.

[53] Nagarajan, V. , Ponyavin, V., Chen, Y., Vernon, M. E., Pickard, P., Hechanova, A., E. (2008). Numerical study of sulfur trioxide decomposition in bayonet type heat exchanger and chemical decomposer with porous media zone and different packed bed designs. *International Journal of Hydrogen Energy, 33*, 6445-55.

[54] Nagarajan, V., Ponyavin. V., Chen, Y., Vernon, M. E., Pickard, P., & Hechanova. A. E. (2009). CFD modeling and experimental validation for sulfur trioxide decomposition in bayonet type heat exchanger and chemical decomposer for different packed bed designs. *International Journal of Hydrogen Energy, 34*, 2543-2557.

[55] Barreau, A., Hernandez. R., O'Toole, B. J., & Trabia, M. B. (2011). Failure strength of silicon carbide ceramic disks under biaxial flexure when exposed to elevated temperatures and concentrated sulfuric acid. *International SAMPE Technical Conference.*

[56] Borger, A., Supancic, P., & Danzer, R. (2002). The ball on three balls test for strength testing of brittle discs: Stress distribution in the disc. *Journal of the European Ceramic Society, 22*(9-10), 1425-36.

[57] Danzer, R., Supancic, P., Harrer, W. (2006). Biaxial tensile strength test for brittle rectangular plates. *Journal of the Ceramic Society of Japan, 114*(1335), 1054-60.

[58] Lamon, J. (1993). Probabilistic failure predictions in ceramics and ceramic matrix fibre-reinforced composites. *Ceramic Engineering and Science Proceedings, 17*(7-8 Pt 1), 326.

[59] Thulukkanam, K. (2000). Plate Heat Exchanger and Spiral Plate Heat Exchanger. In *Heat Exchanger Design Handbook.* Eastern Hemisphere Distribution.

[60] Cheresources.com., *Plate and Frame Heat Exchanger*.

[61] Thermal Heat Transfer Systems, Inc., *Spiral Heat Exchanger*.

[62] Alfa Biz Limited., Brazed plate heat exchanger. China.

[63] Heatric. Inc.,*Printed Circuit Heat Exchanger*.

[64] Lytron Total ThermalSoultions, Inc., *Plate Fin Heat Exchanger*.

[65] *SOLIDWORKS 2013.,* SOLIDWORKS Corp.

[66] Nagarajan, V., Chen, Y., Wang, Q., & Ma, T. (2014). Hydraulic and thermal performances of a novel configuration of high temperature ceramic plate-fin heat exchanger. *Applied Energy, 113*, 589-602.

[67] Patankar, S. (1980). *Numerical Heat Transfer and Fluid Flow.* New York.

[68] Spewock, , S., Brecher, L.E., & Talko, F. (1976). The Thermal Catalytic Decomposition of Sulfur Trioxide to Sulfur Dioxide and Oxygen. *Proceedings of 1st World Hydrogen Energy Conference,* (pp. 9A-53).

[69] Scott, F. H., (1999). *Elements of Chemical Reaction Engineering.* New Jersey: Prentice Hall.

[70] Munro, R. G. (1997). Material properties of sintered a-SiC. *26,* pp. 1195-1203. American Institute of Physics and American Chemical Society.

[71] Green, D. J. (1998). *An introduction to the mechanical properties of ceramics.* The press syndicate of the University of Cambridge.

[72] Manson, S. V. (1950). *Correlations of heat transfer data and friction data for interrupted plate fins staggered in successive rows*. Washington DC: National Advisory Committee for Aeronautics.

[73] Wieting, A. R. (1975). Empirical correlations for heat transfer and flow friction characteristics of rectangular offset-fin-plate-fin heat exchanger. *ASME, Int J. Heat Transfer, 97*, 480-490.

[74] Taha, M. (2007). *Applying of mechanical failure criteria of brittle material to the design of high temperature heat exchanger.* Las Vegas: Master Thesis, University of Nevada.

[75] NIST. (2009). *Structural and ceramics database.* National Institute of Standards and Technology.

[76] Dong, J., Chen, J., Zhang, W., & Hu, J. (2010). Experimental and numerical investigation of thermal-hydraulic performance in wavy fin-and-flat tube heat exchangers. *Applied Thermal Engineering, 30*, 1377-1386.

[77] Lu, C., Huang, J., Nien, W.C., & Wang, C. (2011). A numerical investigation of the geometric effects on the performance of plate finned-tube heat exchanger. *Energy Conversion and Management, 52*, 1638-1643.

[78] Paeng, J.G., Kim, K.H., & Yoon, Y.H. (2009). Experimental measurement and numerical computation of the air side convective heat transfer coefficients in a plate fin-tube heat exchanger. *Journal of Mechanical Science and Technology, 23*, 536-543.

[79] Lacovides, H., Kelemenis, G., & Raisee, M. (2003). Flow and heat transfer in straight cooling passages with inclined ribs on opposite walls: an experimental and computational study. *Experimental Thermal and FLuid Science, 27*, 283-294.

[80] Dowling, N. E. (1993). *Mechanical behavior of material, engineering method for deformation fracture and fatigue.* Prentice-Hall, Inc., .

VITA

Graduate College

University of Nevada, Las Vegas

Vijaisri Nagarajan

Local Address:

4248, Cottage Circle, Apt #4,

Las Vegas, NV 89119

Degrees:

Master of Science, Mechanical Engineering, 2008

University of Nevada, Las Vegas

Bachelor of Engineering, Mechanical Engineering, 2005

Anna University, India

Publications:

- Nagarajan, V., Ponyavin, V., Chen, Y., Vernon, M., Picard, P., Hechanova, A., E. (2007). "CFD modeling of bayonet type high temperature heat exchanger and chemical decomposer with different packed bed designs". *Proceedings of the 2007*

ASME International Mechanical Engineering Congress and Exposition, November 11-15, Seattle, Washington

- Nagarajan, V., Ponyavin, V., Chen, Y., Vernon, M., Picard, P., Hechanova, A., E. (2007). Extended abstract on "Numerical study of sulfur trioxide decomposition in bayonet type heat exchanger and chemical decomposer", November 4–9, *AIChE Annual Meeting*, Salt lake City, Utah
- Nagarajan, V., Ponyavin, V., Chen, Y., Vernon, M., Picard, P., Hechanova, A., E. (2008). "Numerical study of sulfur trioxide decomposition in bayonet type heat exchanger and chemical decomposer with porous media zone and different packed bed designs". *International Journal of Hydrogen Energy*,33 6445-6455
- Nagarajan, V., Ponyavin, V., Chen, Y., Vernon, M., Picard, P., Hechanova, A., E. (2009). "CFD modeling and experimental validation of sulfur trioxide decomposition in bayonet heat exchanger and chemical decomposer for different packed bed designs". *International Journal of Hydrogen Energy*, 34, 2543-2557
- Ma, T., Wang, Q-W., Zeng, M., Chen, Y., Liu, Y., Nagarajan, V. (2012). "Study on heat transfer and pressure drop performances of ribbed channel in the high temperature heat exchanger". *Applied Energy*, 99, 393-401
- Nagarajan, V., Chen, Y., Hung, T-C., Wang, Q., Ponyavin, V. (2014). "Numerical modeling of bayonet type heat exchanger and decomposer for the decomposition of sulfuric Acid to sulfur dioxide". *Heat Transfer Engineering*, 35, 589-599
- Nagarajan, V., Chen, Y., Wang, Q., Ma, T. (2014). "Hydraulic and thermal performances of a novel configuration of high temperature ceramic plate-fin heat exchanger". *Applied Energy*, 113, 589-602

- Nagarajan, V., Chen, Y., Wang, Q., Ma, T. (2014). ”Numerical analysis of steady state and transient state structural analysis of high temperature ceramic plate fin heat exchanger”. *Nuclear Engineering and Design*,(Submitted, in review process)
- Nagarajan, V., Chen, Y., Wang, Q., Ma, T. (2014). “Numerical analysis of fluid flow and heat transfer for different fin designs and arrangements of ceramic plate fin high temperature heat exchanger”. *Applied Thermal Engineering*, (Submitted, in review process)